Doping of Organic Semiconductors: Electrostatic Tuning and Stabilization of Nanoparticle Dispersions

To obtain the academic degree of
Doctor Engineer (Dr.-Ing.)
From the Department of
Electrical Engineering and Information Technology
Karlsruhe Institute of Technology (KIT)

approved
Dissertation
by

M.Sc. Jonas Armleder
born in Öhringen

Date of oral exam:	08.12.2025
First Examiner:	Apl. Prof. Dr. Alexander Colsmann
Second Examiner:	Prof. Dr. Wolfgang Wenzel

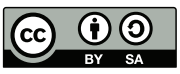

Doping of Organic Semiconductors: Electrostatic Tuning and Stabilization of Nanoparticle Dispersions

Zur Erlangung des akademischen Grades eines
DOKTORS DER INGENIEURWISSENSCHAFTEN (Dr.-Ing.)
von der KIT-Fakultät für
Elektrotechnik und Informationstechnik
des Karlsruher Instituts für Technologie (KIT)

angenommene
Dissertation
von

M.Sc. Jonas Armleder
geb. in Öhringen

Tag der mündlichen Prüfung:	08.12.2025
Hauptreferent:	Apl. Prof. Dr. Alexander Colsmann
Korreferent:	Prof. Dr. Wolfgang Wenzel

Kurzfassung

Organische Halbleiter haben sich aufgrund ihrer mechanischen Flexibilität, chemischen Einstellbarkeit und ihres Potenzials für eine kostengünstige Herstellung als vielversprechende Alternative zu herkömmlichen anorganischen Materialien herausgebildet. Sie haben beachtliche Fortschritte ermöglicht, wie etwa organische Solarzellen mit Wirkungsgraden von über 20 % sowie organische Fotodioden mit Empfindlichkeiten, die mit denen anorganischer Bauelemente vergleichbar sind. Diese Eigenschaften eröffnen zum Beispiel Anwendungen in der flexiblen Elektronik, in durchsichtigen Solarzellen und in Bildsensoren. Die Lösungsmittelverarbeitung hat sich als praktikable Alternative zur Vakuumprozessierung etabliert. Üblicherweise werden organische Halbleiter jedoch in giftigen und umweltschädlichen Lösungsmitteln gelöst, was sowohl ökologische als auch wirtschaftliche Bedenken aufwirft. Eine umweltfreundliche Alternative stellen Nanopartikeldispersionen in Medien wie Wasser oder Ethanol dar. Zur Stabilisierung dieser Dispersionen sind Oberflächenladungen erforderlich, die beispielsweise durch elektronische Dotierung eingebracht werden können.
Diese Arbeit bringt das Gebiet der Dotierung in der organischen Elektronik durch die Bearbeitung mehrerer zentraler Herausforderungen voran. Zunächst wurde ein neues Modell für die Bindungsenergie des ganzzahligen Ladungsübertragungskomplexes entwickelt, das orientierungsabhängige Polarisationswirkungen sowie das Quadrupolmoment des Dotiermoleküls berücksichtigt. Es zeigt sich, dass das Quadrupolmoment des Dotanden die Beweglichkeit der Ladungsträger deutlich beeinflussen kann, potenziell um mehr als zwei Größenordnungen. Das Modell ermöglicht eine präzise rechnergestützte Vorhersage, wie die elektrostatischen Eigenschaften des Dotierstoffs den Ladungstransport beeinflussen, und liefert damit wertvolle Erkenntnisse für die Materialgestaltung. Zusätzlich wurde eine neuartige spektroskopische Methode entwickelt, mit der die Polaronenausbeute in organischen Dispersionen bestimmt werden kann. Im Gegensatz zu herkömmlichen Ansätzen erfordert diese Methode keine Vorkenntnis der Absorptionsspektren des Wirtsmaterials und ermöglicht dadurch ein rasches Prüfen neuer Halbleiter.
Im Bereich organischer Fotodetektoren zeigt diese Arbeit, dass umweltfreundliche Nanopartikeldispersionen zur Herstellung von Fotodetektoren eingesetzt werden können, deren Detektivität mit der von modernen organischen und anorganischen Fotodioden vergleichbar

ist. Damit unterstreicht sie das Potenzial nanopartikelbasierter Beschichtungsverfahren, schädliche Lösungsmittel zu ersetzen, ohne die Bauelementleistung zu beeinträchtigen. Weiterhin werden organische Solarzellen mit lichtabsorbierenden Schichten vorgestellt, die aus durch n-Dotierung stabilisierten organischen Nanopartikeldispersionen prozessiert wurden. Insbesondere konnten n-dotierte Nanopartikel aus dem niedermolekularen Halbleitermaterial Y6 hergestellt werden, einem weit verbreiteten Akzeptormaterial in modernen organischen Solarzellen. Elektrophoresemessungen bestätigten, dass diese Nanopartikel negativ geladen sind. Darüber hinaus ermöglichte die gleichzeitige Stabilisierung von PIDT-T8BT die Herstellung donorakzeptorhaltiger Dispersionen, die sich für die Bauelementfertigung eignen. Während die ersten Bauelemente einen Wirkungsgrad von 0,8% erreichten, könnten weitere Verbesserungen bei der Kompensation der n-Dotierung innerhalb der lichtabsorbierenden Schicht sowie bei der Optimierung der Mikrostruktur zu Leistungssteigerungen führen.

Zusammenfassend leistet diese Arbeit Fortschritte in der elektronischen Dotierung organischer Halbleiter, indem sie ein verbessertes Rechenmodell bereitstellt, eine neuartige Methode zur Bestimmung der Polaronenausbeute entwickelt und die Anwendung n-dotierter Nanopartikeldispersionen in Solarzellen demonstriert. Diese Beiträge erweitern nicht nur das grundlegende Verständnis, sondern eröffnen auch praxisnahe Wege zu nachhaltigeren und effizienteren organischen elektronischen Bauelementen. Die entwickelten Methoden können darüber hinaus für ein Hochdurchsatzprüfen neuer Kombinationen aus Dotierstoff und Wirtsmaterial eingesetzt werden.

Abstract

Organic semiconductors have emerged as a promising alternative to traditional inorganic materials because of their mechanical flexibility, chemical tunability, and potential for low-cost fabrication. They have demonstrated significant achievements, such as organic solar cells (OSCs) exceeding 20% power conversion efficiency (PCE) and organic photodiodes with detectivities comparable to their inorganic counterparts. These properties enable applications, *e.g.*, in flexible electronics, transparent solar cells, and imaging sensors.
Solution processing emerged as a viable alternative to vacuum processing. While organic semiconductors are traditionally dissolved in toxic and environmentally harmful solvents, raising economic and environmental concerns, nanoparticle dispersions in eco-friendly media such as water or ethanol present an alternative. One method to stabilize these dispersions requires surface charges, which can be introduced via electronic doping.
This thesis advances the field of doping in organic electronics by addressing several key challenges. First, a new model for the integer charge transfer complex (ICTC) binding energy was developed, incorporating orientation-dependent polarization effects and the quadrupole moment of the dopant molecule. It was revealed that the quadrupole moment of the dopant can significantly influence charge carrier mobility, potentially by more than two orders of magnitude. The model enables accurate *in-silico* predictions of how dopant electrostatics influence charge carrier transport, providing valuable insights for material design. Additionally, a novel UV-Vis spectrometry method was established to determine polaron yield efficiencies in organic dispersions. Unlike traditional methods, this approach does not require prior knowledge of the absorption spectra of the host, facilitating the rapid screening of new semiconductors.
In the realm of organic photodetectors, this research demonstrates that eco-friendly nanoparticle dispersions can be used to fabricate photodetectors with detectivities comparable to state-of-the-art organic and inorganic photodetectors. These findings emphasize the potential of the nanoparticle-based fabrication route to replace harmful solvents while maintaining high device performance.
This work reports on OSCs with photoactive layers processed from organic nanoparticle dispersions stabilized by n-doping. Specifically, n-doped nanoparticles were successfully

synthesized from the small molecule semiconductor Y6, which is a widely used acceptor in state-of-the-art OSCs. Electrophoresis measurements confirmed that these nanoparticles carry a negative charge. Furthermore, co-stabilization of PIDT-T8BT enabled the formation of donor-acceptor dispersions suitable for device fabrication. While the initial devices achieved a PCE of 0.8%, further improvements in compensating the n-doping within the photoactive layer and optimizing the microstructure hold promise for performance gains. In summary, this research advances electronic doping in organic electronics by improving computational modeling, developing a novel polaron yield quantification method, and demonstrating the new application of n-doped nanoparticle dispersions in solar cells. These contributions not only advance the fundamental understanding, but also provide practical pathways toward more sustainable and efficient organic electronic devices. The methods developed can be used in high-throughput screening of new dopant-host systems.

Publications

Publications in peer-reviewed journals

- Armleder, J.; Neumann, T.; Symalla, F.; Strunk, T.; Olivares Peña, J. E.; Wenzel, W.; Fediai F. Controlling doping efficiency in organic semiconductors by tuning short-range overscreening. *Nat. Commun.* **2023**, *14*, 1356. DOI: 10.1038/s41467-023-36748-x.

- Bruder, J.; Fischer, K.; Armleder, J.; Müller, E.; Da Roit, N.; Behrens, S.; Peng, Y.; Wenzel, W.; Röhm, H.; Colsmann, A. Photocatalytic hydrogen generation in surfactant-free, aqueous organic nanoparticle dispersions. *Small* **2024**, *20*, 2406236. DOI: 10.1002/smll.202406236.

- Fischer, K.; Fichtelmann, F.; Bruder, J.; Armleder, J.; Röhm, H.; Colsmann, A. Fabrication of organic solar cells from surfactant-free aqueous nanoparticle dispersions. *Energy Technol.* **2025**, 2500074. DOI: 10.1002/ente.202500074.

Publications in preparations

- Armleder, J.; Fischer, K.; Bruder, J.; Colsmann, A. Quantifying the Polaron Yield Efficiency in p-Doped Organic Nanoparticle Dispersions. *In preparation*

- Armleder, J.; Fischer, K.; Bruder, J.; Röhm, H.; Colsmann, A. High-Detectivity Organic Photodiodes from Eco-friendly Nanoparticle Dispersions. *In preparation*

Talks at international conferences

- Armleder, J..; Strunk, T.; Symalla, F.; Friederich, P.; Olivares Peña, J.E.; Neumann, T.; Wenzel, W.; Fediai, A. Computing Charging and Polarization Energies of Small Organic Molecules Embedded into Amorphous Materials with Quantum Accuracy. *E-MRS Fall Meeting* **2021**. Symposium G, Session "Materials modeling for nanoelectronics", Number G.8.4.

- Armleder, J..; Fischer, K.; Bruder, J.; Colsmann, A. An Efficient UV-VIS Spectroscopic Approach for Quantifying the Doping Efficiency in p-Doped Organic Nanoparticle Dispersions. *E-MRS Spring Meeting* **2024**. Symposium T, Session "T09_Doping in organic semiconductors IIIb", Number 1603.

Talks and poster presentations on expert symposiums

- Armleder, J..; Manger, F.; Marlow, P.; Fischer, K.; Koppitz, M.; Gärtner, S.; Sprau, C.; Colsmann, A. Electrostatically Stabilized Organic Nanoparticle Dispersions for Organic Solar Cells. Poster presentation. *Joint Lab Virtual Materials Design Statustreffen* **2022**, Karlsruhe, Germany.

- Armleder, J..; Manger, F.; Marlow, P.; Fischer, K.; Koppitz, M.; Gärtner, S.; Sprau, C.; Colsmann, A. Eco-friendly Fabrication of Organic Solar Cells from Nanoparticle Dispersions. Poster presentation. *MaTeLiS Materials Day* **2022**, Karlsruhe, Germany.

- Armleder, J..; Manger, F.; Marlow, P.; Fischer, K.; Koppitz, M.; Gärtner, S.; Sprau, C.; Colsmann, A. Eco-friendly Fabrication of Organic Solar Cells from Nanoparticle Dispersions. Poster presentation. *9. Jahrestagung des KIT-Zentrum Energie* **2022**, Karlsruhe, Germany.

- Armleder, J..; Manger, F.; Marlow, P.; Fischer, K.; Koppitz, M.; Gärtner, S.; Sprau, C.; Colsmann, A. Electrostatically Stabilized Organic Nanoparticle Dispersions for Organic Solar Cells. Poster presentation. *Virtual Materials Design CECAM Workshop* **2022**, Karlsruhe, Germany.

- Armleder, J..; Manger, F.; Marlow, P.; Fischer, K.; Röhm, H.; Sprau, C.; Colsmann, A. Eco-friendly Fabrication of Organic Solar Cells from Nanoparticle Dispersions. Poster presentation. *MaTeLiS Materials Day* **2023**, Karlsruhe, Germany.

- Armleder, J..; Punjabi, D.; Mushtaq, A.; Özdemir, A.; Holzhauer, L.; Colsmann, A.; Wenzel, W.; Jung, N. Virtual Design of Organic Semiconductor Materials. Talk. *Joint Lab Virtual Materials Design Statustreffen* **2023**, Karlsruhe, Germany.

- Armleder, J..; Özdemir, A.; Holzhauer, L.; Colsmann, A.; Wenzel, W.; Jung, N. Advancing Electron Transport Materials: Integrating Multiscale Simulations and Experimental Validation. Poster presentation. *Virtual Materials Design Statustreffen* **2023**, Karlsruhe, Germany.

Teaching and supervised scientific work

- Teaching assistant for the lecture “Elektronische Eigenschaften für Festkörper”, Materialwissenschaft und Werkstofftechnik, 2022
- Nils Bischof, *Stabilisierung organischer Nanopartikel mittels Trifluormethyl substituierter Molybdän-Tris(Dithiolen)-Komplexe*, Bachelorarbeit in Elektro- und Informationstechnik, 2023
- Nils Klein, *Elektronenblockschichten fur nanopartikuläre organische Photodetektoren*, Bachelorarbeit in Materialwissenschaft und Werkstofftechnik, 2023
- Raphael Hörner, *Stabilisierung von J71:Y6 Nanopartikeldispersionen mit Cobalt(III)-TFSI-Salzen für organische Solarzellen*, Masterarbeit in Elektro- und Informationstechnik, 2024

Contents

1 Introduction

Organic semiconductors have rapidly emerged as a promising alternative to inorganic semiconductor technologies. They can be deposited on plastic foils, allowing the fabrication of electronic devices with high mechanical flexibility [1]. The conjugated small molecules or polymers, mainly composed of carbon, can be chemically tailored to adjust electronic properties for targeted applications, such as specific emission or absorption spectra. In addition, thin functional layers reduce material consumption and allow low-cost production. Large-area printing techniques, such as roll-to-roll processing or spray-coating, further support economical manufacturing. Today's organic devices can compete with inorganic counterparts in several performance metrics. Organic solar cells have achieved power conversion efficiencies (PCE) that exceed 20% [2] and have been shown to exhibit low energy payback time [3–6]. Their tunability for specific colors and semitransparency enables innovative applications such as integration into windows, facades, and greenhouses. Organic photodiodes already exhibit detectivities comparable to those of their inorganic counterparts, with the added advantage of an easily tunable spectral response. They are currently used in image sensors, health monitoring, machine vision systems, night-time surveillance, and biomedical imaging [7, 8]. Despite these achievements, organic electronics still face critical challenges such as thermal instability, limited conductivity, and particularly the high costs of materials, along with manufacturing expenses.

One manufacturing approach is solution processing, which enables low-cost large-area fabrication [9, 10]. Stable inks are required, which typically involve dissolving organic semiconductors in solvents that are toxic and environmentally harmful. This increases costs because expensive solvent capture systems are required. An alternative to solution-based processing is the use of organic semiconductors in the form of nanoparticles dispersed in eco-friendly media, *i.e.* water or ethanol, eliminating the need for harmful solvents. The stability of these inks is based on surface charges that lead to particle repulsion. More than 4% PCE has been achieved with P3HT:fullerene stabilized by intrinsic charging of P3HT [11, 12]. Typically, polymers other than P3HT require extrinsic charging to form stable nanoparticle dispersions, which was shown to be possible by illumination or electronic doping [12, 13].

Electronic doping occurs by charge transfer between a dopant and organic host molecule, increasing the charge concentration on the host material. Not only does this help stabilize the dispersions, but it also addresses the problem of limited conductivity in organic layers. Furthermore, it allows tuning key electronic parameters such as the Fermi level and charge carrier mobility, which in turn improves interface energetics and transport in organic devices [14, 15]. Doping has led to various approaches to improve the performance of organic devices such as organic transistors and organic solar cells [16, 17].
Given the importance of doping, it is included in current computational models to allow predictions of doped organic electronic devices *in-silico* [18, 19]. However, implementations often lack a fundamental description of the process on a microscopic level. Current models often rely on simplified assumptions. For example, the binding energies of the integer charge transfer complex (ICTC) are considered fixed, and the amorphous orientations that lead to orientation-dependent polarization effects are neglected, which are inherent to real organic semiconductors [20, 21]. These simplifications do not allow for the predictive accuracy of *in-silico* doping studies [22].
To efficiently drive the research of doping-stabilized dispersions, a quantification of transferred charges from dopant to organic host is needed. For quantification, accurate electron paramagnetic resonance and facile UV-Vis methods have been established [23, 24]. Although many films and solutions have been characterized, UV-Vis methods typically require knowledge of the absorption spectra of the semiconductor materials in their neutral and charged states. These are often not known for new materials and are difficult to measure for dispersed semiconductors. Hence, a facile method is required to determine the number of charges transferred between the dopant and the nanoparticles to drive the fast development of stable inks based on new organic semiconductors.
Previously, the stabilization of organic nanoparticle dispersions has primarily employed p-doping (i.e., electron transfer from the organic host to the dopant). Materials with high ionization potentials (IP) require strong p-dopants. Even strong dopants with electron affinities of 5.87 eV may only weakly p-dope hosts with deeper IPs [25]. Many modern acceptor molecules used in organic photovoltaics exhibit a high electron affinity, which is a key requirement for efficient n-doping (i.e., electron transfer from the dopant to the organic host). Consequently, n-doping such acceptors could enable efficient charge transfer and facilitate stable dispersions.

The goal of this thesis is to advance the field of doping by: (i) Developing a new model of the ICTC binding energy incorporating orientation-dependent polarization energies. This enables *in-silico* analysis of how the dopant electrostatics influences charge transport

in an organic semiconductor. (ii) Developing a new UV-Vis spectrometry method for determining the polaron yield efficiency (PYE) of dopants in organic dispersions, and thus the number of transferred charges between host and dopant. In addition, a host-dopant pair that yields a high PYE is used to fabricate organic solar cells. (iii) Testing of n-doping for stabilization of organic nanoparticle dispersions and using these for the fabrication of organic solar cells.

Furthermore, organic photodiodes are fabricated using intrinsically stabilized P3HT:fullerene nanoparticles to explore new device architectures enabled by nanoparticle dispersions, and their performance is compared to state-of-the-art organic and inorganic photodiodes.

2 Physical fundamentals

In this section, the physical fundamentals are discussed. First, the principles of organic semiconductors are introduced, forming the basis for a subsequent discussion on organic nanoparticle dispersions and electronic devices. Specifically, organic solar cells (OSCs) and organic photodiodes (OPDs) are examined.

2.1 Organic semiconductors

Organic semiconductors are based on carbon atoms, which is why the electronic configuration of carbon is discussed and how it leads to molecular orbitals for bound carbon atoms. Various molecular properties are discussed, including the electrostatic field resulting from a molecule's nonuniform charge distribution, ionization potential, and electron affinity. Furthermore, charge carrier transport is examined along with the influence of electron-donating or electron-accepting entities, known as electronic dopants.

2.1.1 Electronic structure

The electronic configuration of a neutral carbon atom in its ground-state is $1s^2\,2s^2\,2p_x^1\,2p_y^1\,2p_z^0$. The $1s$ and $2s$ orbitals are fully occupied, whereas only two of the three $2p$ orbitals contain a single electron. Promoting an electron from the orbital $2s$ to the orbital $2p_z$ enables the formation of four covalent bonds. The energy required for this promotion can be compensated by interactions with the binding partners, leading to the formation of new hybrid orbitals through the mixing of the $2s$ and $2p$ orbitals. The mixing of four atomic orbitals results in the formation of four equivalent sp^3 hybrid orbitals. This occurs, for example, in ethane, where two carbon atoms form a single bond, and each carbon establishes three additional bonds with hydrogen atoms. Alternatively, combining the $2s$ orbital with only two $2p$ orbitals generates three planar sp^2 hybrid orbitals, while the non-hybridized $2p_z$ orbital orients perpendicularly to this plane, as observed in ethene. The number of hybrid orbitals and remaining non-hybridized p orbitals determines the types of molecular orbitals (MOs) and bonds formed between atoms. When neighboring carbon atoms possess sp^2 hybridized atomic orbitals (AOs), their overlap produces bonding (σ) and antibonding (σ^*) molecular orbitals, which exhibit rotational symmetry around

the bonding axis. The bonding and antibonding interaction arises from interference of the electronic wavefunctions. The remaining atomic p_z orbitals overlap to a lesser extent, forming π and π^* orbitals [26]. For diatomic carbon molecules, the highest occupied molecular orbital (HOMO) and the lowest unoccupied molecular orbital (LUMO) consist of π and π^* orbitals. To fully describe the electronic properties of the ground-state, the entire molecule must be considered, with all molecular orbitals up to the HOMO occupied by electrons, whereas states above the LUMO remain unoccupied. The molecular orbitals are solutions to the Schrödinger equation. Various approximations have been used to solve it for molecules, usually in the Born-Oppenheimer approximation, which assumes that the atom positions are fixed because they are much heavier and slower than electrons. Simple models approximate the molecular orbitals by linear combination of atomic orbitals (LCAO), whereas more accurate models describe the orbitals as a superposition of basis functions, such as density functional theory (DFT). [26]

Organic semiconductor molecules have conjugated bonds resulting in delocalized π electron orbitals, which especially contribute to electronic properties due to their energetic proximity to the energy gap. In polymers, the π orbitals can overlap, leading to splitting of the frontier orbitals, reducing the energy gap between HOMO and LUMO [27]. Ideally, overlapping leads to electron delocalization over the whole polymer.

The nonuniform spatial distribution of molecular orbitals leads to a nonuniform distribution of charge density in the molecule, which in turn results in a molecular electrostatic potential (MEP). This causes molecules to interact with each other through electrostatic interactions. The MEP, determined by the positively charged atomic nuclei and the negatively charged electrons occupying molecular orbitals, is the following:

$$V_{\mathrm{MEP}}(\vec{r}) = \frac{1}{4\pi\varepsilon_0}\left(\sum_k^{\text{nuclei}} \frac{Z_k}{|\vec{r}-\vec{r}_k|} - \int \frac{\rho(\vec{r}')}{|\vec{r}-\vec{r}'|}d\vec{r}'\right) \tag{2.1}$$

for a test charge located at position $\vec{r}$. Here, ε_0 is the vacuum permittivity, Z_k represents the charge of the nucleus k, while $\rho(\vec{r}')$ denotes the electron density. The molecular electrostatic potential, V_{MEP}, can be expressed using a multipole expansion, providing a more intuitive interpretation:

$$V_{\mathrm{MEP}}(\vec{r}) = \frac{1}{4\pi\epsilon_0}\left(\frac{q}{r} + \frac{\vec{\mu}\vec{r}}{r^3} + \frac{1}{2}\frac{\vec{r}Q\vec{r}}{r^5}\right), \tag{2.2}$$

where q represents the total charge of the molecule, $\vec{\mu}$ denotes the dipole moment, and Q corresponds to the quadrupole tensor. Higher-order terms in the expansion diminish more

rapidly with increasing distance r from the molecular origin, which shows that charged molecules ($q \neq 0$) generate particularly strong electrostatic fields.

The ionization potential (IP) and electron affinity (EA) are properties characterizing charge carrier transport. The vacuum IP is the energy needed to remove an electron from a neutral atom or molecule in its ground-state in vacuum. It is given by:

$$\mathrm{IP}^{\mathrm{g}} = E(N-1) - E(N), \tag{2.3}$$

where $E(N)$ and $E(N-1)$ represent the total energies of the neutral and cationic molecule, respectively. N is the number of electrons on the neutral molecule. The vacuum EA is defined as the energy gained when an additional electron is added to an isolated atom or molecule in its ground-state.

$$\mathrm{EA}^{\mathrm{g}} = E(N) - E(N+1), \tag{2.4}$$

where $E(N+1)$ represents the total ground-state energy of the anionic molecule. Adding or removing an electron to the frontier orbitals (HOMO/LUMO) induces structural changes in the molecule due to the resulting additional charge. As a result, IP and EA are defined in two different ways. The vertical IP (EA) is defined assuming that the molecular geometry remains fixed in its neutral-state conformation during transition to the cationic (anionic) state. In contrast, the adiabatic IP (EA) considers the relaxation of the molecular structure in the charged state, allowing it to reach its lowest energy [28].
The IP and EA can differ significantly between molecules in vacuum and those in a polarizing environment. Even for the same molecule embedded in two different solids, these energies can vary by as much as 0.6 eV [29, 30]. Equations 2.3 and 2.4 define how IP and EA are computed for isolated molecules in vacuum. For embedded molecules, these quantities are modified and determined by:

$$\mathrm{IP} = U^{+} - U^{0}, \tag{2.5}$$

$$\mathrm{EA} = U^{0} - U^{-}, \tag{2.6}$$

where U^0, U^+, and U^- denote the total energy of the system when the molecule of interest (for which IP/EA is of interest) is in its neutral, positively charged (cationic) and negatively charged (anionic) states, respectively. The intermolecular interactions of the environment

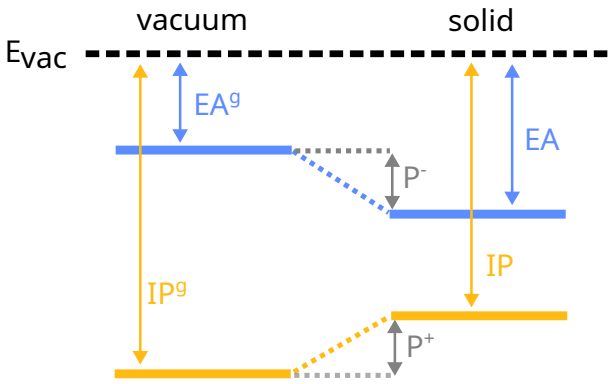

Figure 2.1: Shift of IP and EA in a polarizing environment. Compared to vacuum levels, the IP decreases and the EA increases.

influence these energies differently depending on the charge (0, +, -), which leads to an energy shift in IP and EA compared to their gas-phase energies [28]:

$$P^{(+)} = \mathrm{IP}^{\mathrm{g}} - \mathrm{IP} \tag{2.7}$$

$$P^{(-)} = \mathrm{EA} - \mathrm{EA}^{\mathrm{g}}, \tag{2.8}$$

where $P^{(+)}$ and $P^{(-)}$ represent the polarization energies. The resulting energy changes are shown in Figure 2.1. As a consequence, IP decreases, while EA increases, leading to a reduction in the transport energy, defined as $E_{\mathrm{T}} = \mathrm{IP} - \mathrm{EA}$, in the solid phase. Often, the dominant contribution to $P^{\pm}$ arises from electronic polarization, mainly due to the stabilizing effect of induced dipoles that form in response to the localized charge on a molecule [31, 32]. This stabilization energy can sometimes exceed the total polarization energy $P^{\pm}$, as other effects such as structural relaxation and charge delocalization generally reduce the overall contribution of polarization [33, 34].

2.1.2 Optical excitations

The absorption of a photon can excite an electron from the HOMO into an orbital of higher energy, leading to a bound electron-hole pair *i.e.* an exciton. In inorganic semiconductors, high dielectric screening leads to low binding energies E_{B}, which can be overcome at room temperature to form free charge carriers. In organic semiconductors, the dielectric permittivity is lower ($\epsilon_r = 3 - 4$) leading to less screening and Frenkel excitons, which have an E_{B} of several hundred meV. The minimal energy needed for the formation of an exciton is $\mathrm{IP} - \mathrm{EA} - E_{\mathrm{B}}$.
However, excitations with higher energies are also possible. The probability of optical transitions, considering the vibrational influence, is explained by the Franck-Condon

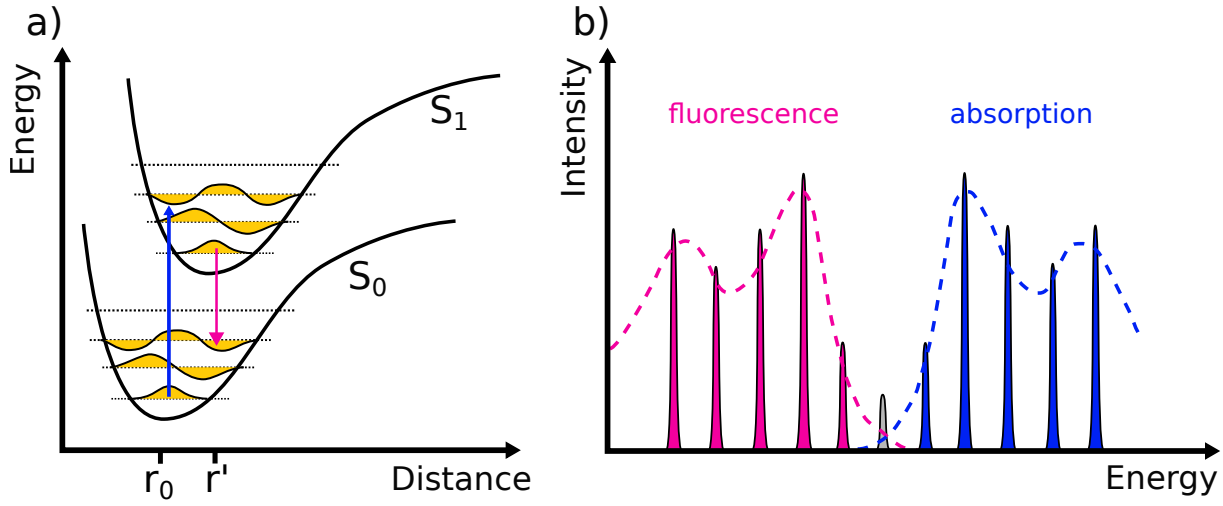

Figure 2.2: a) Vibrational splitting of the energy levels in the ground-state (S_0) and excited state (S_1) of a diatomic molecule. According to the Franck-Condon principle, electronic transitions occur vertically in this energy diagram. b) Schematic representation of the resulting emission and absorption spectra. In solutions or solids, these peaks are broadened, as indicated by the dashed line. Own schematic illustration inspired by [27, 35].

principle. A molecular ground-state is typically denoted S_0. The excited (singlet) states are denoted S_1, S_2,.... For each of these states, vibrations lead to the formation of vibrational states and the splitting of energy levels. This is illustrated for a diatomic molecule in Figure 2.2, the atom distance being the x-axis. The ground-state (S_0) and the excited state (S_1) also exhibit a shifted potential, corresponding to a different energy-favorable molecular structure for the various excited states. The Franck-Condon principle states that the molecular structure remains unchanged during an electronic transition, which implies a vertical transition of electrons in Figure 2.2. Excitation of an electron from a structurally relaxed molecule in the S_0 state will lead to an excited vibrational state in S_1. Since the lifetime of the S_1 state is several orders of magnitude longer than the energy loss to phonons, it is likely that the electron will relax into the vibrational state of the lowest energy of S_1. Then it transitions to an excited vibrational state of S_0, emitting a photon with energy lower than that initially absorbed. This effect is referred to as the *Stokes shift*, causing the emitted photons to have a lower energy than the absorbed photons, making organic semiconductors largely transparent to their own emitted light. In addition, if the organic material is in solution or solid form, the broadening of the spectral peaks leads to continuous emission and absorption.

2.1.3 Charge carrier transport

Macroscopically, charge transport in a semiconductor is described by the conductivity $\sigma = (p\mu_\mathrm{h} + n\mu_\mathrm{e})e$, where p (n) are the concentrations and μ_h (μ_e) are the mobilities of the holes (electrons). This shows that charge carrier transport requires free charge carriers, given by the following mechanisms: Charge carrier injection or extraction from an electrode, redox reactions between host and dopant molecules in an organic semiconductor, or the dissociation of a neutral excited state leading to charge separation between neighboring molecules. The mobility μ_h or μ_e defines the proportional relationship between the velocity of the hole or electron and the applied electric field.
The mechanism of charge carrier transfer is influenced by the arrangement of molecules. In molecular crystals, orbital overlap results in band formation. However, due to weak interactions between neighboring sites, only narrow bands with bandwidths ranging from 50 to 500 meV [26] form. Although band transport is feasible at temperatures above approximately room temperature, intra- and intermolecular vibrations disrupt the coherence between adjacent sites, making band transport ineffective. Challenges such as brittleness and the consequently required thick layers have shifted research interest toward amorphous films. In amorphous polymers, conformational disorder restricts coherence to only a few repeat units. Over this limited distance, a charge can move coherently before hopping to the next conjugated segment. Therefore, it is more practical to consider such a conjugated segment as a single transport unit, often termed a chromophore. The Su-Schrieffer-Heeger model, a one-dimensional semiconductor band model, describes charge carrier transport in polymers. In amorphous molecular films, spatial fluctuations in polarization create a random distribution of molecular energy levels. These energy levels are typically modeled using a Gaussian distribution. Charge carrier transport in these systems is governed by charge carrier hopping between molecular energy levels.
When the electronic orbitals of different molecules are weakly coupled, the charge hopping rate can be determined using Fermi's Golden Rule:

$$\omega = \frac{2\pi}{\hbar} \sum_i \sum_f p_i \left|\langle \Psi_f | H | \Psi_i \rangle\right|^2 \delta(E_f - E_i), \tag{2.9}$$

where ω represents the hopping rate for an electron transferring from one molecule to another. The index i sums up all possible electronic states in molecule A, while f runs over all available states in molecule B. p_i denotes the occupation probability of the initial state i, followed by the matrix element that quantifies the coupling between the wavefunctions of states f and i. These matrix elements vary depending on whether energy or charge

transfer is considered. The function δ enforces the resonance condition between the initial and final states, ensuring energy conservation, where E_f and E_i correspond to the energies of the final and initial states, respectively. Two common approximations of equation 2.9 include the Miller-Abrahams approach and the Marcus theory. Marcus theory is based on the premise that charging a molecule induces conformational changes. To illustrate this, two molecules, A and B, are considered, where molecule A carries an additional electron, placing it in a distinct conformational state. This structural adjustment alters the electronic state energies and, consequently, modifies the energy barrier for electron transfer. However, because molecular conformational reorganization occurs on a slower timescale, molecule B cannot instantly adjust to facilitate charge transport. The Franck-Condon principle further suppresses transitions that occur during an intermediate conformational state. Marcus theory postulates that charge transfer occurs when the system fluctuates into a transient conformational state, where both molecules reach resonance in their charged states. This results in an energy barrier given by:

$$E_{\mathrm{T}} - E_{\mathrm{A}}, \tag{2.10}$$

where E_{T} represents the total energy of the system in the transition state and E_{A} denotes the energy of the initial state. To estimate the energy barrier, the following approximation is applied, assuming weak electronic coupling between the charge states on molecules A and B. Under this condition, the energy barrier is approximated and the electron charge hopping rate is given by:

$$\omega_{if} = \frac{2\pi}{\hbar}|J_{if}|^2 \frac{1}{\sqrt{4\pi\lambda k_{\mathrm{B}}T}} \exp\left(-\frac{(\lambda + \Delta E)^2}{4\lambda k_{\mathrm{B}}T}\right). \tag{2.11}$$

where λ is the reorganization energy, which is a measure of the energy change due to the geometric molecular rearrangement when an electron is added or removed, J_{if} is the transfer integral, and ΔE represents the energy difference between the initial and final states. The transfer integral J_{if} depends on the wavefunction overlap of the participating orbitals. Further discussion of its modeling is provided in Section 3.2.2.The energy difference ΔE corresponds to the variation in the Gibbs free energy of the system between the final and initial states, with additional details given in Section 3.3.1.

2.1.4 Electronic doping

Doping is understood through two mechanisms: ion pair formation, also considered as an integer charge transfer complex (ICTC) or a charge transfer complex (CTC) formation [17].

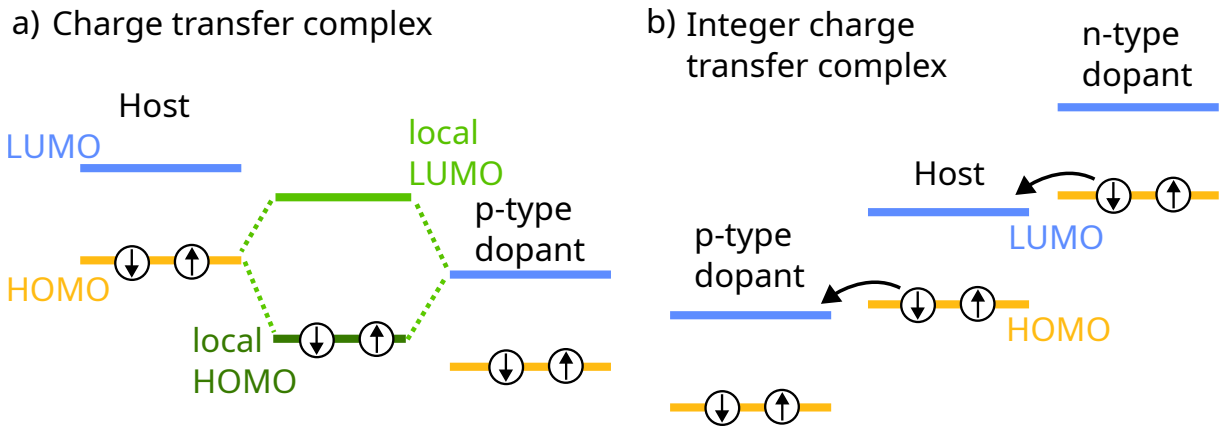

Figure 2.3: a) Energy level schematic of charge transfer complex (CTC) formation between a host and a p-dopant. The hybridization of the donor HOMO and dopant LUMO results in the formation of a new local HOMO and LUMO, leading to fractional charge transfer. b) Schematic representation of typical relative energy levels of a host, n-dopant, and p-dopant. Electron transfer between the host and dopant results in the formation of an integer charge transfer complex.

In the former, an integer elementary charge is transferred between donor and acceptor molecules, and in the latter, only a fraction of charge is transferred. This works by hybridization of the donor HOMO and the acceptor LUMO. New local HOMOs and LUMOs form, with their energy levels shown in Figure 2.3a. The bonding state has lower energy, while the antibonding state has higher energy. The fraction of charge transfer then depends on the energetic mismatch of the HOMO of the host and the LUMO of the dopant, as well as the spatial overlap of the individual orbitals [36]. CTCs have been observed, for example, for the widely used dopant 2,3,5,6-tetrafluoro-7,7,8,8-tetracyanoquinodimethane (F_4TCNQ) when doping 2,7-dioctyl[1]benzothieno[3,2-b][1]benzothiophene (C8-BTBT).[36, 37] An ICTC can be considered as the limiting case of an CTC.

A p-type molecular dopant triggers the formation of an ICTC if its LUMO is deep enough to enable charge transfer from the HOMO of another molecule. In the case of an n-type molecular dopant, the HOMO of the dopant must be shallow enough to donate an electron to the LUMO of another molecule. Figure 2.3b shows the energy levels of HOMO and LUMO of n-type and p-type dopants compared to a host organic semiconductor. In the following, only p-doping will be addressed, but the considerations can readily be transferred to n-doping. It is often assumed that the EA of the dopant only needs to be similar or greater than the IP of the host. This simplified picture has been shown to not even qualitatively explain the observed behavior of doped small molecules or oligomers[36, 38], because the electrostatic binding energy of ICTC V_C is not taken into account. V_C is the Coulomb interaction energy between the charge densities of the ionized host and dopant,

which on the one hand, stabilizes the ICTC, *i.e.*, aids dopant ionization. On the other hand, V_C poses a barrier that a charge carrier must overcome to be transported, which results in the conductivity to depend on V_C [14, 20, 39–44]. In addition, an important influence on the formation of ICTC is the polarization effect of the surrounding medium. The rate of dopant ionization depends on the energy difference of the system before and after ionization. Initially, the ICTC-participating molecules are neutral; upon ionization, they acquire opposite charges, forming a dipole. This dipole polarizes the surrounding medium, leading to a polarization energy that aids in dipole formation. A stronger polarizable medium (higher ϵ_r) increases the polarization energy, making the formation of ICTC more energetically favorable, as shown for monopoles [34, 45]. Experimentally, Barrett *et al.* demonstrated that ICTCs form more favorably in solvents of higher dielectric permittivity [46].

To quantify an amount of dopants, the dopant concentration, dopant weight ratio (DWR), or dopant molar ratio (DMR) is used. If not noted otherwise, the dopant concentration refers to the absolute concentration given in either $\mathrm{g\,L^{-1}}$ or $\mathrm{mol\,L^{-1}}$, the DMR (expressed in mol%) refers to the number of dopant molecules versus the number of doped semiconductor molecules (sum of the number of host and dopant molecules), the dopant weight ratio (DWR, expressed in wt%) refers to the weight of the dopant molecules versus the weight of the doped semiconductor (sum of the weight of host and dopant).

2.1.5 N-doping organic semiconductors

N-doping requires atoms or molecules with a high electron donating strength, which is why some of the first systematic n-doping was done with alkali metals. Because alkali metals have only one electron in the outermost s orbital, they can be removed with little energy. Potassium and sodium were used in the 1970s [47]. Lithium has especially played an important role due to deposition via lithium-containing layer such as lithium fluoride.[48] However, the general problem of atom doping is the diffusion of one layer into another that should not be doped [49]. This can, for example, cause luminescence quenching in organic light-emitting diodes (OLEDs) [48, 50]. Doping with molecules aids against diffusion because of their steric configuration. Molecular n-doping was first demonstrated in the year 2000.[51] Early n-dopants had the problem of being unstable in air, which drove the development of modified doping strategies. One strategy is to use n-type precursors that are themselves less sensitive to oxygen or not at all sensitive to oxygen and are activated in the host matrix via heat or illumination. Evaporation in vacuum leaves the dopant intact until it dopes the host semiconductor [52, 53]. A novel

approach is the use of air stable dimers that dissociate into n-dopants. They can typically be processed from solution and by evaporation. The dimers should be rather weakly bound to control the dissociation by small amounts of energy. Un *et al.* showed that (pentamethylcyclopentadienyl)(1,3,5-trimethylbenzene)ruthenium dimer ($(RuCp^*mes)_2$) strongly increased the conductivity of the polymer P(NDI2OD-T2) with high reproducibility, providing a clean reaction for n-doping. However, even higher conductivity was achieved employing the n-dopant N-DMBI-H which is less bulky than RuCp*mes, possibly leading to less perturbation of the ordered microstructure. This led to the development of (pentamethylcyclopentadienyl)(1,3,5-trimethylbenzene)ruthenium dimer ($(N\text{-}DMBI)_2$), which combines the properties of $(RuCp^*mes)_2$ and N-DMBI-H. $(N\text{-}DMBI)_2$ shows even higher conductivity than N-DMBI-H. Due to their straightforward use and air-stability, $(N\text{-}DMBI)_2$ and $(RuCp^*mes)_2$ are tested in Section 8 toward their use in the electrostatic stabilization of 2,2′-((2Z,2′Z)-((12,13-bis(2-ethylhexyl)-3,9-diundecyl-12,13-dihydro-[1,2,5]thiadiazolo[3,4-e]thieno[2′,3′′:4′,5′]thieno[2′,3′:4,5]pyrrolo[3,2-g]thieno[2′,3′:4,5]thieno[3,2-b]indole-2,10-diyl)bis(methanylylidene))bis(5,6-difluoro-3-oxo-2,3-dihydro-1H-indene-2,1-diylidene))dimalo-nonitrile (Y6) nanoparticles.

2.2 Organic nanoparticle dispersions

Most organic semiconductors dissolve only in heterocyclic, aromatic, or halogenated solvents such as chlorobenzene (CB) or chloroform ($CHCl_3$). Because these solvents can seriously harm health and present environmental risks [54–57], their use requires costly solvent recovery systems. An alternative approach toward more sustainable processing is to employ nanoparticle dispersions of the semiconductors in polar media, such as water or alcohols, where they are otherwise insoluble (nonsolvent). The photoactive layers of OSCs and photodiodes are processed of nanoparticle dispersions.

2.2.1 Nanoparticle formation

Nanoparticles in this work are obtained by nanoprecipitation (Section 4.1.1), which rapidly reduces the solubility of organic semiconductor in the medium, leading to supersaturation. The formation of nuclei that grow to particles is described by the classical nucleation theory (CNT) [58–61]. It describes that the supersaturated material clusters to solid material nuclei. These have a probability of dissolving again, which decreases for larger nuclei. At a critical size, the nuclei become thermodynamically stable. This size depends, among other parameters, on the surface energy and supersaturation of the semiconductor in the solution. During the nucleation process, the concentration of the solvated material

decreases. Although CNT describes the formation of particles, it does not produce accurate predictions for the final particle sizes[62], rather, it predicts only the minimal sizes. For the final nanoparticle size predictions, considerations of colloidal stability as described in the Derjaguin-Landau-Verwey-Overbeek (DLVO) theory have proven to be more useful [63–67].

2.2.2 Stabilization

The stability of an organic nanoparticle dispersion can be considered in the absence of growth processes that reduce stability. Known growth processes are Ostwald ripening, agglomeration, sedimentation, and coalescence [68]. Ostwald ripening is driven by the solubility difference between small and large particles, leading to small particles to be incorporated into larger particles [69]. Agglomeration describes particles sticking at each other, forming clusters of individual particles. Sedimentation is the formation of a solid phase that deposits out of the fluid through gravitational or other forces. Coalescence describes the merging of two or more particles into larger particles. Van der Waals forces and Brownian motion continuously lead to growth if not prevented. Particles can be stabilized by suspending them in a solution of depletants, which are non-adsorbing macromolecules. These form a depletion layer that leads to stabilization [70]. Steric stabilization is based on macromolecules attached to the particles by covalent binding or adsorption that prevent the particles from coming too close to each other [71]. Electrostatic stabilization is described by the DLVO theory. It describes the particle interaction by the sum of the attractive van der Waals force and the Debye–Hückel–screened electrostatic interaction as shown in Figure 2.4a. In [72] it is stated that the van der Waals force can be minimized by matching the surface energy of the particles and the dispersion medium, which leads to less agglomeration of the particles. A different approach is increasing the electrostatic repulsion, causing a barrier for particles that prevents agglomeration. To engineer the particle surface potential, illumination and electronic doping [12, 13, 73] have been used. As the kinetic energy of the particles in a dispersion is statistically distributed, some particles have a high enough energy to overcome the Coulomb barrier. This leads to agglomeration over time since there is no reverse process.
Figures 2.4b-d show the simulated influence of various parameters on the energetic potential of two particles. Figure 2.4b depicts the dependence on the Hamaker constant, which defines the strength of the van der Waals interaction between particles. Figure 2.4c shows that a higher surface potential leads to a higher barrier. Figure 2.4d shows that greater ion concentration in the dispersion leads to a reduced potential barrier, due

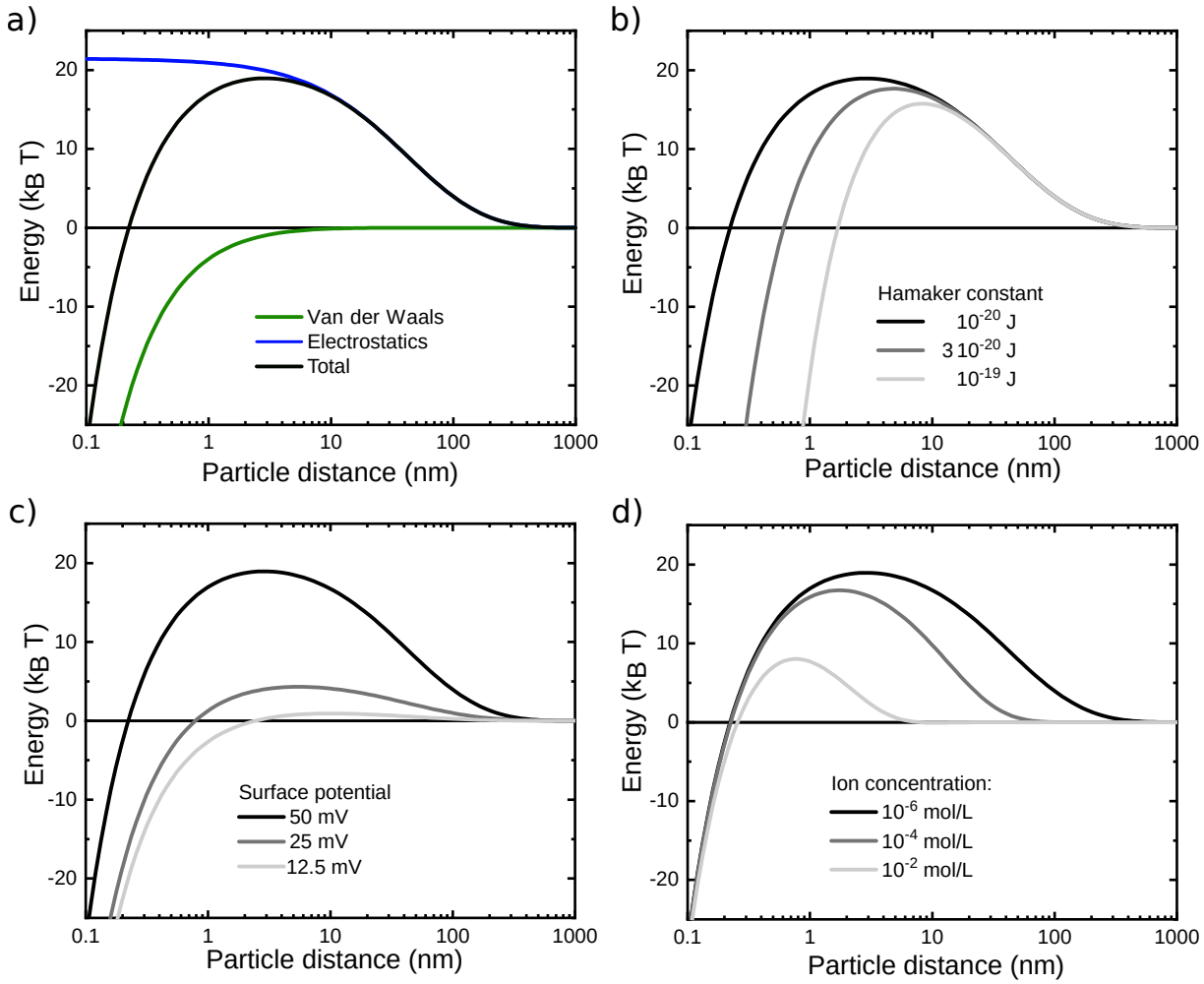

Figure 2.4: a) Potential energy of two particles with the same charge in the framework of DLVO theory, showing the contributions from attractive van der Waals forces, repulsive electrostatic interactions, and the resulting total energy. b)-d) Simulated influences of surface potential, Hamaker constant and ion concentration on the potential barrier between two particles. Published by Philipp Marlow under the licence CC BY-SA 4.0 [74]; language and visual appearance modified by the author.

to a decrease in the Debye-Hückel screening length. In [75] it is shown experimentally that ions added to a dispersion otherwise stable lead to larger particle sizes and flocculation.

The achievement of stable long-term dispersions can be achieved using ionic surfactants; however, after deposition, these surfactants persist in organic semiconductor devices, potentially limiting charge carrier transport and lowering device performance [76]. In this work, an alternative approach is pursued, the electrostatic stabilization of nanoparticle dispersions. Recently, photo- and electronic p-doping have been used to stabilize nanoparticle dispersions of semiconducting polymers for OSC applications. It occurred, that Poly(3-hexylthiophene-2,5-diyl) (P3HT) tends to self-charge, *i.e.* the formation of polarons on P3HT, and hence the corresponding nanoparticles carry positive charges which stabilize the dispersions against agglomeration [12]. Electrostatic stabilization can be enhanced by photoexcitation during nanoparticle formation [12]. Higher irradiance leads to smaller particles. Monochromatic illumination with a tuned wavelength shows that stabilization is increased in the wavelength regime where P3HT absorbs. Then it was shown that the p-dopant F_4TCNQ decreases the nanoparticle size of the P3HT dispersions. Since self-charging, to date, is a unique effect in P3HT, extrinsic charging was the key to stabilizing dispersions of other polymers. F_4TCNQ has been shown to aid in the stabilization of dispersions made of the following semiconductors [13]: Poly[[5,6-difluoro-2-(2-hexyldecyl)-2H-benzotriazole-4,7-diyl]-2,5-thiophenediyl[4,8-bis[5-(tripropylsilyl)-2-thienyl]benzo[1,2-b:4,5-b'] dithiophene-2,6-diyl]-2,5-thiophenediyl] (J71), (poly[[4,8-bis[(2-ethylhexyl)oxy]benzo[1,2-b:4,5-b′]dithiophene-2,6-diyl][3-fluoro-2-[(2-ethylhexyl)carbonyl]thieno[3,4-b]thiophenediyl]] (PTB7), Poly[4,8-bis(5-(2-ethylhexyl)thiophen-2-yl)benzo[1,2-b;4,5-b']dithiophen-2,6-diyl-alt-(4-(2-ethylhexyl)-3-fluorothieno[3,4-b]thiophen-)-2-carboxylat-2-6-diyl)] (PTB7-Th), Poly[(2,6-(4,8-bis(5-(2-ethylhexyl)thiophen-2-yl)-benzo[1,2-b:4,5-b']dithiophen))-alt-(5,5-(1',3'-di-2-thienyl-5',7'-bis(2-ethylhexyl)benzo[1',2'-c:4',5'-c']dithiophen-4,8-dion)] (PBDB-T) and Poly[(2,6-(4,8-bis(5-(2-ethylhexyl-3-fluoro)thiophen-2-yl)-benzo[1,2-b:4,5-b']dithiophen))-alt-(5,5-(1',3'-di-2-thienyl-5',7'-bis(2-ethylhexyl)benzo[1',2'-c:4',5'-c']dithiophen-4,8-dion)] (PBDB-T-2F). Some polymers require dopant concentrations that are higher than others to obtain the same nanoparticle size. With PTB7 and the acceptor [6, 6]phenyl-C_{71}-butyric acid methyl ester ($PC_{71}BM$) a stable ink was obtained for the processing of OSCs. Manger *et al.* stabilized a blend of J71 and Y6 using iodine as a dopant [73]. However, they found an excessive dopant weight ratio of 40 wt% (relative to the weight of J71) was needed to achieve dispersion concentrations of $0.5\,\mathrm{g\,L^{-1}}$.

2.3 Organic solar cells and photodiodes

This section focuses on the working principle of OSCs and photodiodes. In addition, important performance indicators are introduced.

2.3.1 Organic solar cells

OSCs utilize the photovoltaic effect to generate electrical power. Compared to inorganic SCs, OSC performs well in low light, can be lightweight and flexible, and can be designed to be semitransparent [77–79]. Organic light harvesting layers are typically only a few hundred nanometer thick, can be coated using roll-to-roll processes, and do not require very high fabrication temperatures, making them potentially inexpensive with low energy payback time [3, 80]. Recently, a single-junction OSC has been reported to show a power conversion efficiency (PCE) of over 20% on lab-scale [2].

The architecture of OSCs consists at least of an organic photoactive layer (responsible for absorbing light and exciton dissociation) and two electrodes on either side to collect the charge carriers. One of the electrodes is chosen to be transparent, so that photon can reach the photoactive layer. Depending on the application, the counter electrode is also transparent or reflecting (reflected photons pass through the photoactive layer a second time). Depending on the optical transitions of the photoactive layer semiconductors (see Section 2.1.2), photons are absorbed and excitons are created. The high absorption coefficients allow for thin photoactive layers. Organic semiconductors have a lower dielectric permittivity than common inorganic semiconductors, leading to high exciton binding energies. Thus, the dissociation of excitons into charge carriers by thermal energy is unlikely. The introduction of two organic semiconductors (donor and acceptor) in the photoactive layer with shifted energy levels makes exciton dissociation energetically favorable at the interface. The LUMO of the acceptor is deeper than the LUMO of the donor and the HOMO of the donor is shallower than the HOMO of the acceptor enabling energetically favorable exciton dissociation with the electron transferring from the donor to the acceptor and the hole from the acceptor to the donor. Excitons must reach an interface within their diffusion length (a few tens of nanometers) to dissociate [27]. This could, for example, be achieved by a bilayer architecture: a donor layer and an acceptor layer on top of each other. However, their thickness would need to be on the order of the exciton diffusion length L_D which is too small to efficiently absorb light. The solution is a bulk-heterojunction (Figure 2.5a), which is a mixed layer of donor and acceptor. Ideally, for efficient exciton dissociation in OSCs, the donor and acceptor materials should form

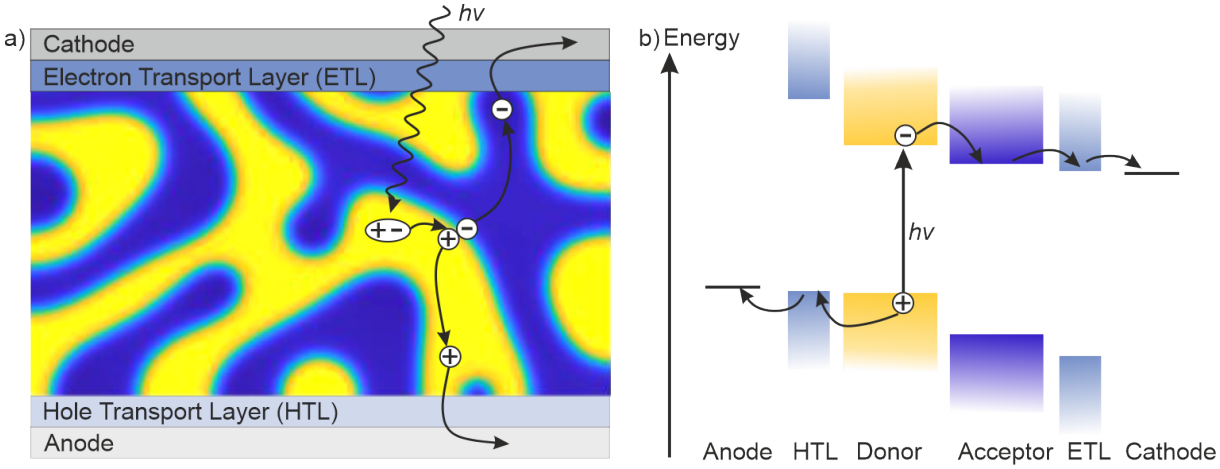

Figure 2.5: a) Schematic of the working principle of a BHJ in an OSC. An incident photon with energy $h\nu$ is absorbed by the photoactive layer, which consists of two materials: a donor and an acceptor. The generated exciton migrates to the donor-acceptor interface, where dissociation occurs due to the energy level offset (as shown in b). The resulting electron and hole are transported through the acceptor and donor phases to the cathode and anode, respectively, leading to charge extraction and photocurrent generation. Published by Philipp Marlow under the Licence CC BY-SA 4.0. [74]

pure domains with a size on the order of the exciton diffusion length (L_D). At the same time, these domains should remain connected to the electrodes so that the separated charge carriers can be efficiently transported and collected. The collection can be achieved by different Fermi levels: The cathode workfunction is similar to the LUMO of the acceptor and the anode workfunction similar to the HOMO of the donor. Another technique is to use hole transport layers (HTLs) or electron transport layers (ETLs) to align the energy levels for efficient charge carrier extraction. They can also be designed to be selective, allowing electrons to reach only the cathode and holes only the anode, thereby reducing recombination.

OSCs are typically characterized by their J-V curves, which show the measured current as a function of the applied voltage. An example (measured in the dark and under illumination) is shown in Figure 2.6. In the metal-insulator-metal model, the J-V characteristics in the dark show only very small currents for voltages below the built-in voltage, which is primarily determined by the electrode work-function difference, but can also be influenced by interfacial dipoles, contact layers, Fermi-level pinning, and (un)intentional doping [27]. In this case, the internal electric field counters charge carriers injection. Under illumination, charge carriers are photogenerated. However, the current that is extracted and measured depends strongly on the applied bias. For a voltage of $V = 0\,\mathrm{V}$, the OSC is short-circuited, which means that once the charge carriers reach the electrodes of the OSC, they contribute to the measured current (except for the low cable resistance). The current in this case is

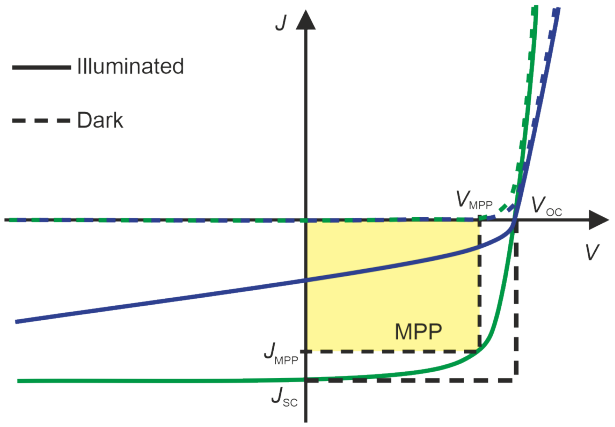

Figure 2.6: Example of the current density J versus applied voltage V of an OSC. The green line represents the characteristics of a well-performing solar cell, while the blue line corresponds to a less efficient solar cell. The performance of the solar cell is determined by the maximum power that can be harvested, indicated by the yellow square. The highest achievable current and voltage outputs are the short-circuit current density (J_{SC}) and the open-circuit voltage (V_{OC}). The maximum power the OSC can produce is given by $P_{\mathrm{MPP}} = V_{\mathrm{MPP}} \cdot J_{\mathrm{MPP}}$. Published by Karen Fischer under the Licence CC BY-SA 4.0. [81]

$I_{\mathrm{SC}} = A \cdot J_{\mathrm{SC}}$, with A being the area of the OSC. For a voltage of $V < 0\,\mathrm{V}$, an electric field is applied in a direction, which aids charge carriers to reach their respective electrode: holes the anode, electrons the cathode. This can reduce recombination and possibly increase J compared to J_{SC}. $V > 0\,\mathrm{V}$ decreases the built-in electric field, reducing the drift speed and increasing recombination, thus reducing J. At the open-circuit voltage $V = V_{\mathrm{OC}}$ the internal field decreases, so that all charge carriers recombine, leading to zero current. The power density that can be extracted from the OSC is given by $P(V) = V \cdot J(V)$, leading to a maximum power point (MPP) with $P_{\mathrm{MPP}} = V_{\mathrm{MPP}} \cdot J_{\mathrm{MPP}}$. J_{SC} is the highest photocurrent density, V_{OC} the highest voltage of the solar cell, generating a hypothetical maximum power $P_{\mathrm{max}} = V_{\mathrm{OC}} \cdot J_{\mathrm{SC}}$. Then the fill factor (FF) is defined as:

$$\mathrm{FF} = \frac{P_{\mathrm{MPP}}}{P_{\mathrm{max}}} = \frac{J_{\mathrm{MPP}} \cdot V_{\mathrm{MPP}}}{J_{\mathrm{SC}} \cdot V_{\mathrm{OC}}}. \tag{2.12}$$

The FF is often considered a quality factor, measuring the squareness of the J-V curve. A low FF results from poor charge carrier transport properties (low mobility) and recombination of charge carriers.

Different OSCs are often compared using their PCE, which is defined as the fraction of

the incident solar power $P_{\mathrm{in}} = 1000\,\mathrm{Wm}^{-2}$ (according to air mass (AM) 1.5G standard spectrum) converted into electrical energy:

$$\eta = \frac{P_{\mathrm{MPP}}}{P_{\mathrm{in}}} = \frac{V_{\mathrm{OC}} \cdot J_{\mathrm{SC}} \cdot \mathrm{FF}}{P_{\mathrm{in}}}. \tag{2.13}$$

The external quantum efficiency (EQE) and the spectral response (SR) provide insight into which wavelengths contribute to the generated current under illumination. The EQE is the ratio of the extracted charge carriers to the number of incident photons. The SR is the ratio of the generated current to the incident power on the device. Using the EQE, the spectral mismatch calculation factor (SMCF) can be computed to correct the recorded short-circuit current under a solar simulator for differences between the solar simulator and the real sunlight spectra (Section 4.3.1). Since the EQE depends on the applied bias, the SMCF also depends on it. However, this dependence is expected to be small; therefore, the SMCF is typically calculated at V=0. [27]

$$\begin{aligned}\mathrm{SMCF} = \frac{\frac{I_{\mathrm{DUT,Sim}}}{I_{\mathrm{DUT,AM1.5G}}}}{\frac{I_{\mathrm{Ref,Sim}}}{I_{\mathrm{Ref,AM1.5G}}}} &= \frac{\int \lambda \cdot \mathrm{EQE}_{\mathrm{DUT}}(\lambda) \cdot F_{\mathrm{Sim}}(\lambda)\mathrm{d}\lambda}{\int \lambda \cdot \mathrm{EQE}_{\mathrm{DUT}}(\lambda) \cdot F_{\mathrm{AM1.5G}}(\lambda)\mathrm{d}\lambda} \\ &\cdot \frac{\int \lambda \cdot \mathrm{EQE}_{\mathrm{Ref}}(\lambda) \cdot F_{\mathrm{AM1.5G}}(\lambda)\mathrm{d}\lambda}{\int \lambda \cdot \mathrm{EQE}_{\mathrm{Ref}}(\lambda) \cdot F_{\mathrm{Sim}}(\lambda)\mathrm{d}\lambda},\end{aligned} \tag{2.14}$$

with F_{Sim} and $F_{\mathrm{AM1.5G}}$ being the spectral irradiance of the solar simulator and the AM1.5G standard, respectively. This shows that the correction factor equals one if the EQE of the reference solar cell is equal to that of the device under test (DUT). Unless stated otherwise, the OSC data are presented without SMCF correction, as the correction did not significantly alter the device characteristics or comparative conclusions.

2.3.2 Organic photodiodes

Recent progress in wearables, disposable sensors [82] and implementations of image sensors [83–85], demands lower photodiode fabrication costs and new functionalities, including detection at low light intensities [86], narrowband and broadband spectral selectivity [87, 88], lightweight devices and mechanical flexibility [89, 90]. As silicon photodetectors require significant additional processing steps to meet these requirements, interest has shifted to OPDs that show chemical tunability, mechanical flexibility, and can be deposited by many different techniques [91]. OPDs rely on the same working principle as OSC; however, the architecture is optimized for other figures of merit, and they are usually operated under reverse bias to assist the extraction of charge carriers.

In an OPD, a signal must exhibit a stronger current than the noise current to be detected. The noise current is derived from the noise power spectral density (NSD), which is a Fourier-transformed quantity that represents the power spectral density (PSD) of the noise power. The noise current is the square root of the integrated NSD over a frequency bandwidth, making it a measurable quantity by measuring current fluctuations over time. The following terms contribute to the noise current in OPDs [92, 93]:

- The shot noise current originates from the quantum dynamics of charge carriers crossing a potential barrier and can be modeled as a Poisson process.

$$i_{\mathrm{sn}} = \sqrt{2qI_{\mathrm{D}}\Delta f}, \tag{2.15}$$

  with q being the elementary charge, I_{D} being the dark current and Δf the noise measurement bandwidth.

- The Johnson or Nyquist noise emerges by the thermal generation of charge carriers. It is given by

$$i_{\mathrm{jn}} = \sqrt{\frac{4k_{\mathrm{B}}T\Delta f}{R_{\mathrm{SH}}}}. \tag{2.16}$$

  k_{B} is the Boltzmann constant, T the temperature and R_{SH} the shunt resistance of the device.

- The flicker noise current i_{fn} has also been observed in OPDs. It is only relevant at low frequencies, and its PSD exhibits a dependence on $\frac{1}{f}$.

The total noise is

$$i_{\mathrm{n}} = \sqrt{i_{\mathrm{sn}}^2 + i_{\mathrm{jn}}^2 + i_{\mathrm{fn}}^2}. \tag{2.17}$$

Based on the noise current, the noise-equivalent power (NEP) and the specific detectivity D^* are defined. The NEP is the power required to have a signal-to-noise ratio (SNR) of one [93]:

$$\mathrm{NEP} = \frac{i_{\mathrm{n}}}{\mathrm{SR}}, \tag{2.18}$$

with SR being the spectral response, which is the current generated per incident illumination power. The specific detectivity is the inverse NEP, normalized by the detector area and bandwidth:

$$D^* = \frac{\sqrt{A\Delta f}}{\mathrm{NEP}}. \tag{2.19}$$

A is the light-absorbing area of the OPD. This makes D^* a better figure of merit to compare different OPDs. Assuming that the total noise current is dominated by shot noise, D^* yields

$$D^* = \frac{\mathrm{SR}\sqrt{A\Delta f}}{i_{\mathrm{sn}}} = \mathrm{SR}\sqrt{\frac{A}{2qI_D}} = \frac{\mathrm{SR}}{\sqrt{2qJ_{\mathrm{D}}}}. \tag{2.20}$$

Ignoring the contributions of flicker and thermal noise has been shown to overestimate D^* [7, 94–99]. However, under applied bias, the thermal noise generally becomes smaller than the shot noise [93] and for frequencies above 10 Hz, the flicker noise decreases to a steady limit, close to the shot noise, showing that the NEP for high frequencies is mainly shot noise limited [93, 100, 101]. Furthermore, care must be taken when using Equation 2.20 as comparing quantity because J_{D} depends on the applied electric field and the SR on the wavelength. OPDs are commonly operated under a reverse bias in the range of -1 to -5 V to enhance charge extraction and reduce recombination [102, 103]. The specific detectivity D^* is typically reported at the wavelength at which it reaches its maximum. The equation is widely used and thus enables a broad comparison of OPD performance [92].
Assuming shot noise as the primary noise mechanism, several strategies have been introduced to reduce the dark current (Figure 2.7a). OPDs with a planar heterojunction (PHJ) [97, 104] or sequentially solution-processed (SSP) photoactive layer [105, 106] can lead to pure phases at the electrodes, resulting in a higher energy barrier for charge carriers under reverse bias (Figure 2.7b). Thus, the dark current decreases. Another strategy is to introduce blocking layers between the photoactive layer and the electrode to increase charge carrier selectivity (Figure 2.7c) [107–110]. Some semiconductors even reduce charge carrier selectivity: Poly(3,4-ethylenedioxythiophene):Polystyrene sulfonate (PEDOT:PSS) has been shown to increase the dark current, as observed in [111].

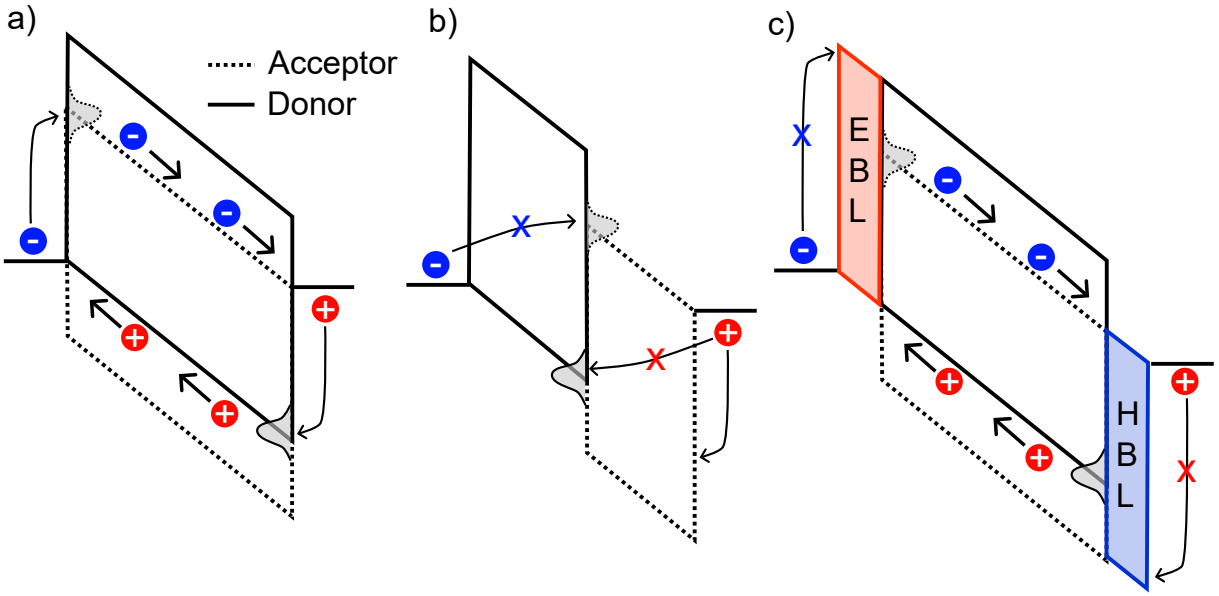

Figure 2.7: a) Dark current mechanism by injection under reverse bias: Electrons are injected into the LUMO of the acceptor and holes in the HOMO of the donor. b) Strategy to avoid dark current injection under reverse bias by pure material phases at the electrodes (planar heterojunction photoactive layer). Sequentially solution-processed photoactive layers can reduce the dark current as well while being partially mixed in the center of the photoactive layer. c) Blocking layers introduce barriers for charge carriers under reverse bias to reduce the dark current [92].

3 Simulation methods

This section describes the fundamentals of the simulation methods that are used and further developed in Section 5. The chapter focuses on a multiscale simulation workflow for organic electronic devices, initially developed in the group of Prof. Wolfgang Wenzel (Karlsruhe Institute of Technology) for single- or multi-component materials, and to some extent for doped materials with my active participation [22, 34]. The workflow begins by generating a force-field-like representation of molecules and assembling a digital morphology, in which the electronic properties of embedded molecules are simulated starting from quantum mechanical methods. This enables the calculation of rates that characterize the system dynamics, specifically the transport of charges and excitons. Kinetic Monte Carlo simulations utilize these rates to propagate the system in time.

3.1 Material deposition

The prediction of the formation of solid structures of atoms or molecules is a classical optimization problem. Several approaches have been introduced to model the morphologies of small molecules. The classical molecular dynamics (MD) and Monte Carlo (MC) methods require the evaluation of $O(N^2)$ energy terms, with N being the particle number, *i.e.* the system size, for each simulation step. The software Deposit [112] reduces the computational load to $O(N)$ by deposition of individual molecules in imitation of the experimental method of molecular beam epitaxy.

Single molecule deposition first requires the parametrization of molecular properties, which are then the input for the method. DFT simulations are used to relax the geometry and compute the molecular electrostatic potential (MEP). Atomic partial charges are fitted using the Merz-Singh-Kollmann scheme to reproduce the surrounding electrostatic potential [113, 114]. Lennard-Jones parameters, modeling the Pauli repulsion and van der Waals attraction between atoms, are inherited from a non-polarizable force field. Both the electrostatic potential and Lennard-Jones parameters form the non-bonded potential later used to determine energetically favorable conformations and positions of the molecule. If the molecules feature dihedrals, they are characterized during stepwise rotation, relax the rest of the molecule, and calculate the single-point energy by DFT. Figure 3.1a shows

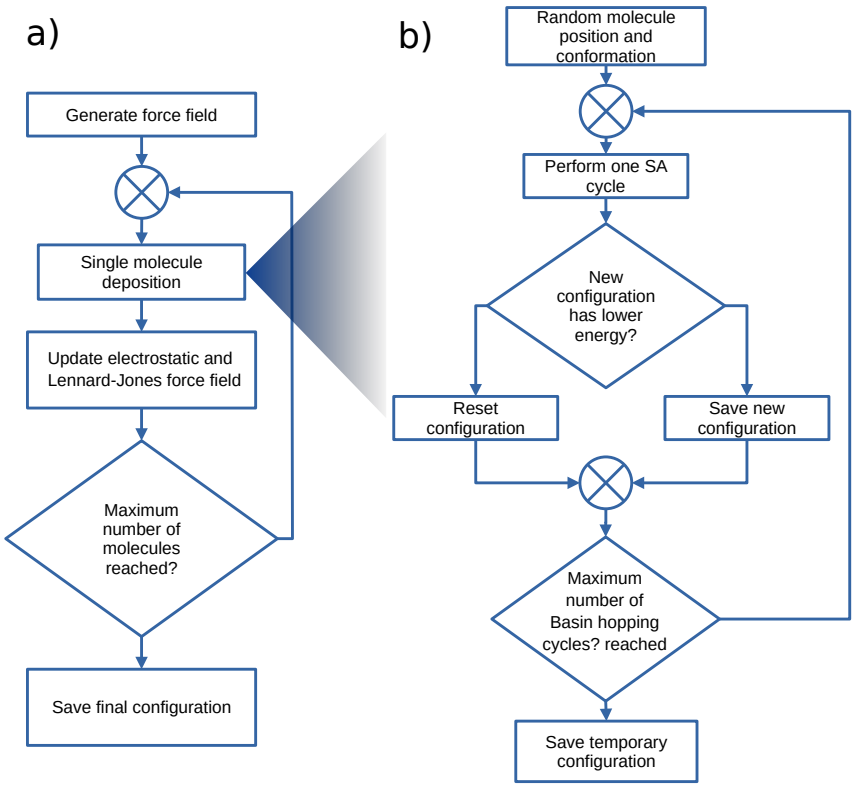

Figure 3.1: Algorithmic scheme of the software Deposit, simulating the assembly of organic small molecules. The process mimics molecular beam epitaxy by single molecule deposition via SA cycles. Own schematic illustration inspired by [112].

the general scheme of single molecule deposition. Together with an (optional) initial morphology, a force field representation is generated. On the basis of the Basin-hopping algorithm, a single molecule is deposited. The force terms in the morphology are updated including the new molecule atoms. This is repeated until the set number of molecules is deposited. Inspired by the Monte Carlo minimization, the Basin-hopping algorithm is an algorithm for global optimization in very high-dimensional landscapes [115]. It is based on sequentially finding the local minimum after perturbing the rigid body and dihedral variables till a set number of Basin-hopping cycles are reached. In Deposit, a new molecule starts with a random position and conformation, and then a simulated annealing (SA) cycle is performed to find a local minimum in the energy landscape. If this has a lower energy than the previous configuration, it is saved; otherwise, it is discarded. An SA cycle starts with a rigid body rotation/translation or dihedral rotation, drawn from a random Gaussian distribution with a standard deviation of 0.1 nm and $0.2\,\pi$, respectively. The move is accepted with a likelihood of $P = 1$ if $E_\mathrm{f} - E_\mathrm{i} < 0$ or $P = \exp(-(E_\mathrm{f} - E_\mathrm{i})/k_\mathrm{B}T)$ otherwise, where E_f is the configurational energy after and E_i before the move. The SA cycle terminates when it reaches the defined upper limit of Monte Carlo steps. During

deposition, periodic boundary conditions are applied in two axes (hereinafter labeled the x and y axes). In the direction of growth z, no periodicity is applied. In the case of electronically doped materials, the chance of deposited host or dopant molecules depends on the dopant molar ratio.
An important function to characterize amorphous structures is the radial distribution function (RDF), also called the pair correlation function $g(r)$. It explains how the particle number density changes depending on the distance r from a reference particle. Molecular RDFs approximate the molecules as one particle, here using its center of geometry as coordinate. $g(r)$ is calculated by counting the particles n_r in a spherical shell around a reference particle ($r \in [r, r + dr]$) and dividing it by the shell volume dV_r times bulk number density $\bar{n}$:

$$g(r) = \frac{dn_r}{dV_r \cdot \bar{n}}. \tag{3.1}$$

With regard to small molecule morphologies, the RDF provides information about local order and can be used to infer crystallinity, but it does not directly describe relative molecular orientations.
Another important parameter is the molecular density, summing up the element weight of atoms times the spatial frequency of occurrence in a unit volume. Density measurements are straightforward to perform, which facilitates direct comparisons between simulated morphologies and experimental results. The application of the Deposit method to various organic semiconductors showed good agreement with experimental densities. In addition, the lattice structure of Buckminsterfullerene (C_{60}) is predicted. [112]

3.2 Electronic characterization of morphologies

The previous section covered the computational simulation of a morphology but did not address the electronic structure. The following sections introduce a quantum embedding method for obtaining equilibrated charge density and computing transfer integrals and charge carrier transport energy levels.

3.2.1 Quantum embedding method QuantumPatch

The electronic structure of small molecules in organic semiconductors is primarily influenced by electrostatic interaction with the molecular electrostatic potential of other molecules (Section 2.1.1). The method is designed to simulate the equilibrated charge density of a system of molecules, *i.e.* how the charge density is distributed in the steady state. This

requires a model of the charge density and how it interacts with surrounding charges. There are fast and rather approximative methods, such as microelectrostatic or charge redistribution models that redistribute the polarized charge density along the molecular dipole or along bonds [116–118]. Typically, first-order principle methods are used to parametrize these models. Due to the simple nature of the models, they often have problems in expressing the correct polarization perpendicular to the dipole moment or the bonds. This leads to problems in particular for planar molecules. More complex methods often separate the simulation space into a "core" region and its surrounding. The quantum mechanics/molecular mechanics (QM/MM) methods treat the core region on a quantum mechanical level and the surrounding on a classical level with, e.g., polarizable force fields which are coupled. Because of computation time limitations and charge transfer between molecules, often only a few molecules form the core region and are treated quantum mechanically. This still leads to low predictability for molecules where the polarizability is not well represented by classical models. Full quantum mechanical approaches, Valence Bond Hartree-Fock (VBHF) [119, 120] and constrained DFT (CDFT) [121], employ HF or DFT for all molecules in modeling the molecular polarization response. Despite having high accuracy, they also have a high computational demand, scaling quadratically with the system size. VBHF and CDFT use artificially employed potentials to avoid charge transfer between the molecules, limiting their application to unknown molecular systems. As a compromise between QM/MM and full quantum mechanical approaches, the fully self-consistent quantum mechanical/quantum mechanical (QM/QM) method QuantumPatch has been developed [34, 122–124]. Even though every molecule is quantum mechanically treated, the computational cost grows only linearly with the number of molecules. Because no artificial constraints are imposed, the method is accurate and applicable to unknown systems.

The input of the method is a morphology (xyz-coordinates of atoms). Typically, a sphere around a core region or molecule constitutes the simulation volume. The use case of embedding methods is often to compute the properties of individual molecules embedded in the environment. The core region, in which these are extracted, can be modeled with more accurate DFT settings, such as a larger basis set. In OE, molecules are typically weakly coupled, so that exchange interactions and intermolecular contributions to the kinetic energy can be neglected, and intermolecular interactions are modeled as purely electrostatic. This leads to a diagonal Hamiltonian:

$$\hat{H}^{\mu} = \mathrm{diag}(\hat{H}_1^{\mu}(n_{\mathrm{tot}}^{\mu}(\vec{r})), ..., \hat{H}_N^{\mu}(n_{\mathrm{tot}}^{\mu}(\vec{r}))). \tag{3.2}$$

$\hat{H}_i^\mu(n_{\text{tot}}^\mu(\vec{r}))$ is the Hamiltonian describing the ith molecule depending on the total charge density $n_{\text{tot}}^\mu(\vec{r})$. $\mu \in [0, 1..., N_{\text{sf}}]$ is the self-consistency iteration step with a maximum of N_{sf}. The total charge density $n_{\text{tot}}^\mu(\vec{r})$ can be separated into the density of the ith molecule $n_i^\mu(\vec{r})$ and of the surrounding $n_{\text{env}}^\mu(\vec{r})$. In the first iteration, the molecular charge densities and so $n_{\text{env}}^\mu(\vec{r})$ are not known. For a first estimate, $\hat{H}_i^0(n_{\text{tot}}^0(\vec{r}))$ is solved for all molecules $i \in [1, ..., N]$ (N being the total number of molecules) with $n_{\text{env}}^0(\vec{r}) = 0$. Commonly, this type of calculation is referred to as an *in vacuo* calculation, *i.e.* using DFT as the method, it is referred as a vacuum single-point DFT calculation. For each molecule, this yields a first estimate of $n_i^\mu(\vec{r})$ yielding $n_{\text{env}}^\mu(\vec{r})$. Then, in the iteration steps $\mu \geq 1$, $\hat{H}_i^\mu(n_{\text{tot}}^{\mu-1}(\vec{r}))$ can be solved using the electron density of molecules surrounding the molecule i of the previous steps $n_{\text{tot}}^{\mu-1}(\vec{r})$. These self-consistent iterations are repeated till a steady-state is reached. The indicator of convergence is the total system energy; however, as illustrated in [34], parameters such as the dielectric constant require more self-consistent iteration steps. Practically, $n_{\text{tot}}^{\mu-1}(\vec{r})$ is represented by partial charges fitted using the Merz-Singh-Kollmann scheme [113].

3.2.2 Transfer integrals and reorganization energy

The transfer integrals, also denoted as electronic couplings, describe the overlap of molecular orbitals. They are necessary to calculate the charge carrier hopping rates and therefore fundamental to the simulation of charge carrier transfer in organic electronics. The transfer integral between two molecules is

$$J_{ij} = \frac{\hat{H}_{ij} - \frac{1}{2}(\hat{H}_{ii} + \hat{H}_{jj})S_{ij}}{1 - S_{ij}^2}, \tag{3.3}$$

where $S_{ij} = \langle \psi_i | \psi_j \rangle$ is the overlap matrix element of the extended HOMO (or LUMO) orbitals ψ_i and ψ_j, i as orbitals in the first and j of the second molecule. $\hat{H}_{ij} = \langle \psi_i | \hat{H}_{KS} | \psi_j \rangle$ is the effective one-electron Hamiltonian in a (neutral) dimer system $\hat{H}_{KS}$. As these values are used for simulating charge transfer in bulk materials, the orbitals of embedded molecules are of interest. To evaluate Equation 3.3, a morphology with equilibrated electronic structure is needed. The electron orbitals are equilibrated by the self-consistent quantum embedding scheme (Section 3.2.1). This shows that J_{ij} depends on the molecule, the electronic environment, the pair orientation, and the pair distance. Generally, the transfer integral decreases with increasing distance.

The reorganization energy λ of a particular molecule used in charge transfer compu-

tations between two molecules of the same type can be calculated by Nelson's four-point procedure: i) The total energy $E^1_{(0)}$ of the conformationally relaxed molecule is computed in the vacuum. ii) An electron is added to the molecule. The total energy $E^2_{(0)}$ is computed in the same molecular geometry used in (i). iii) The molecule is geometrically relaxed, then the total energy $E^2_{(1)}$ is computed. iv) Then the additional electron is removed and the total energy $E^1_{(1)}$ is computed in the geometry used in (iii). The reorganization energy is then given by

$$\lambda = \lambda_1 + \lambda_2 = (E^2_{(0)} - E^2_{(1)}) + (E^1_{(1)} - E^1_{(0)}). \tag{3.4}$$

As the reorganization energy depends on the total molecular energy, the molecule itself and its surrounding medium have influence on λ. In fact, the surrounding does not only electronically influence the total energy, but as the Nelson's four-point method requires several geometry relaxations, also the van der Waals interaction between molecules constrains the possible relaxed geometries. In general, the reorganization energy differs for hole and electron transport as they occupy different frontier orbitals.

3.2.3 IP/EA of embedded molecules and dielectric permittivity

As described in Section 2.1.1, the polarization energies $P^{(+)}/P^{(-)}$ are subtracted from or added to the vacuum IP/EA to obtain the respective bulk data. In general, $P^{(+/-)}$ depends on the specific *core* molecule under consideration, since different local environments in amorphous organic semiconductors lead to different polarization effects. The environment surrounding the core contributes to $P^{(+/-)}$ through an electrostatic interaction that scales with $1/R$, where R is the distance between the core and each neighboring molecule. This introduces a distance dependence on the polarization energy. $P^{(+/-)}(R)$ thereby represents the polarization energy for a core molecule that includes the surroundings within a radius R. The bulk polarization energy is then defined as $P^{(+/-)} = P^{(+/-)}(R = \infty)$. Because atomistic simulations can only be performed on finite volumes, it is practical to separate $P^{(+/-)}$ into two parts.

$$P^{(+,-)} = P^{(+,-)}_{\text{expl}}(R) + P_{\text{impl}}(R), \tag{3.5}$$

$P^{(+,-)}_{\text{expl}}(R)$ is the polarization contribution of molecules inside a sphere with radius R whose contribution is explicitly computed using an atomistic model, while $P^{(+,-)}_{\text{impl}}(R)$ is the polarization contribution of the environment outside the sphere with radius R, and it

is calculated by an implicit model based on classical electrostatics which can be applied to large R. The explicit part of the polarization energy is then given by:

$$P_{\mathrm{expl}}^{(+/-)}(R) = \Delta\Delta E_0^{(+/-)} + \Delta V_{\mathrm{env}}^{(+/-)}(R). \tag{3.6}$$

$\Delta\Delta E_0^{(+/-)}$ is the embedded internal molecular energy difference, *i.e.* the IP/EA change *only* of the core molecule during the embedding process, thus considering the change of conformation and charge density forced on the molecule by the environment. $\Delta V_{\mathrm{env}}^{(+/-)}(R)$ describes the change in electrostatic interaction (core molecule with the environment and environment with itself) and the internal energy of the environment upon charging the core molecule. For large R, local field effects have a reduced impact, enabling a macroscopic description based on classical electrostatic theory [34]:

$$P_{\mathrm{impl}} = \left(1 - \frac{1}{\epsilon_{\mathrm{r}}}\right) \frac{e^2}{8\epsilon_0 \pi R}, \tag{3.7}$$

with $\epsilon = \epsilon_0 \epsilon_{\mathrm{r}}$ being the dielectric permittivity, e the elementary charge. P_{impl} does not depend on the sign of the charge (+/-). Equation 3.7 predicts a linear dependence of $P_{\mathrm{expl}}^{(+/-)}$ on $1/R$ for large R. This can be used to extrapolate $P_{\mathrm{expl}}^{(+/-)}$ in $1/R$ linearly to $1/R = 0$ to incorporate the implicit polarization contribution and obtain the bulk $P^{(+/-)}$. By this scheme $P^{(+/-)}$ can be simulated. In practice, the explicit polarization energy is calculated for charge-equilibrated morphologies with the QuantumPatch method: One time the core molecule is charged, one time it is uncharged. Here, it is particularly important that the underlying QuantumPatch-engine, e.g. DFT or HF, captures the polarization of the molecules to achieve a correct polarization energy, but is still computationally cheap. DFT with the basis set def2-SVPD and functional BP86 [125] was shown to be a trade-off between precision and computational effort. Subtracting/adding $P^{+/-}$ to the vacuum IP/EA leads to the bulk IP/EA (Equation 2.7). The method to compute vacuum IP/EA is only applied to one molecule relaxed in vacuum. As a starting guess, the self-consistent eigenvalue scheme with the hybrid functional PBE0 [126] with def2-QZVP basis set is used to determine the vertical vacuum IP/EA (ev-GW:PBE0) as implemented in Turbomole [127]. An average error of 0.1 eV is reported for using the one-step GW method G_0W_0 [128].

For large R, the explicit quantum mechanical description and the implicit classical description yield the same results. Differentiating Equation 3.5 with respect to $1/R$ constitutes a

relation between dielectric permittivity ϵ_r and the slope of the explicit polarization energy $m = \frac{\partial P^{+/-}_\mathrm{expl}}{\partial(1/R)}$.

$$\epsilon_\mathrm{r} = -\frac{e^2/(8\pi\epsilon_0)}{e^2/(8\pi\epsilon_0) - m}. \tag{3.8}$$

Therefore, a linear fit can determine the dielectric permittivity ϵ_r. Two things have to be considered: 1. The implicit polarization correction does not depend on the sign of the charge. 2. The fluctuation of the RDF leads to fluctuations of the extracted ϵ_r. The first objective is addressed by taking the average over $P^{+}_\mathrm{expl}(1/R)$ and $P^{-}_\mathrm{expl}(1/R)$. The second objective is addressed by renormalizing the radius by the number of molecules $N(R)$ within a given polarization radius R:

$$\tilde{R} = \left[\frac{3}{4\pi} N(R)/n\right]^{1/3}, \tag{3.9}$$

n being the molecular number density of the morphology. However, the extracted ϵ_r of different core molecules vary, which is why a minimum of five core molecules are used to obtain the averaged results of Equation 3.8. It is noted that the determined dielectric permittivity does not include contributions by rotational, vibrational, or optically excited modes, as these are not captured in the self-consistent QP procedure.

3.2.4 ICTC binding energy V_C

ICTCs have been introduced in Section 2.1.4. They are characterized by their electrostatic binding energy V_C between ionized hosts and dopants. Accurate modeling of V_C is crucial as it influences the rate of dopant ionization and the charge carrier transport in a doped organic semiconductor.

In the following, an ICTC between a particular host molecule and p-dopant is considered. Before ionization, they are uncharged. Afterwards, the host is positively charged, and the dopant is negatively charged, with the additional charge occupying their frontier orbitals, their HOMOs and LUMOs. E^CT is the change in system energy upon charge transfer between host and dopant, also called charge transfer energy. E^CT is related to V_C and the particular IP of the host and EA of the dopant [129].

$$V_\mathrm{C} = E^\mathrm{CT} - (\mathrm{IP}_\mathrm{host} - \mathrm{EA}_\mathrm{dop}), \tag{3.10}$$

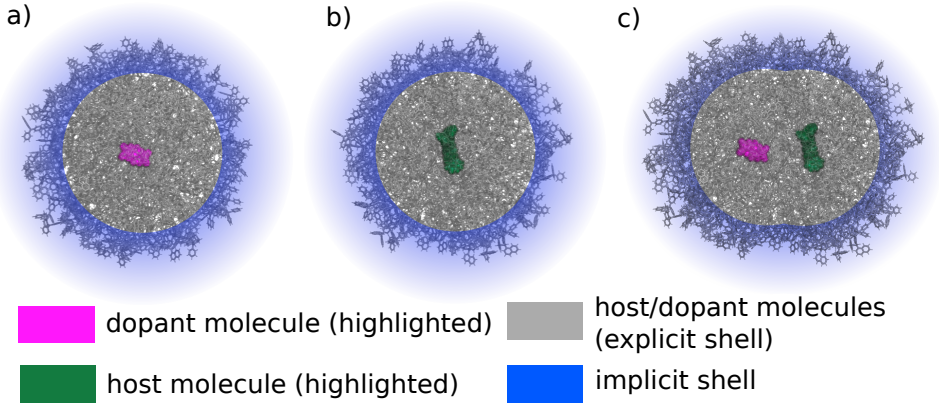

Figure 3.2: Visualization of the geometry to calculate ICTC binding energy, V_C. a) The EA of the dopant, b) the IP of the host and c) the system's energy difference upon dopant ionization (charge transfer energy) are computed. In a) and b) a sphere around the dopant/host is defined, in which the polarization influence is modeled explicitly by a quantum embedding method. In c) its a union of two spheres. Around the space, illustrated by the blue shading, the polarization contribution is added implicitly by the theory of classical electrostatics. Visualizations adapted from Armleder et al. [22], licensed under CC BY 4.0; modified by the author.

To obtain the *embedded* V_C, the charge transfer energy, IP, and EA of the embedded molecules must be calculated. IP and EA can be computed as described in Section 3.2.3. This method can also be altered to compute E^{CT}: The space is divided into two *shells*: (1) The explicit shell which is treated by explicit quantum embedding calculations. The space is the union of two spheres around the host-dopant pair (Figure 3.2c). (2) The implicit shell which is treated according to classical electrostatics, *i.e.* the space outside the union (analog to Section 3.2.3 for IP/EA). The explicit part of the ICT state energy E^{CT}_{expl} is given by the energy difference between the energies of the two systems:

$$E^{CT}_{expl} = E^{f}_{expl} - E^{i}_{expl}, \tag{3.11}$$

where E^{i}_{expl} is the energy of the uncharged (initial) and E^{f}_{expl} of the CT (final) state. In both cases, the energy contains the internal and Coulomb interaction energies for all molecules. For the initial state, the electron density of the molecules is equilibrated with all molecules being in the neutral state and for the final state with the host-dopant pair being ionized (the host is positively charged and the dopant is negatively charged). Charge equilibration is achieved using the QuantumPatch method described in Section 3.2.1. The implicit part of the energy P^{dip}_{impl} is derived using classical electrostatics (ICTC is approximated as a dipole):

$$P^{dip}_{impl} = \frac{1}{2\epsilon_0}\left(1 - \frac{1}{\epsilon_r}\right)\int_V \left|\vec{D}^{dip}(\vec{r})\right|^2 \mathrm{d}V, \tag{3.12}$$

where V describes the volume of the implicit space having a relative dielectric permittivity of ϵ_r and $\vec{D}^\mathrm{dip}$ is the electric displacement field produced by the ICTC. ϵ_r is computed beforehand using the QuantumPatch quantum embedding method according to Section 3.2.3. Using polar coordinates, the integral can be easily solved numerically. The final ICT state energy is thus given by:

$$E^\mathrm{CT} = E^\mathrm{CT}_\mathrm{expl} + P^\mathrm{dip}_\mathrm{impl}. \tag{3.13}$$

The basis set and functional used for individual single point computations are def2-SVPD[130] and BP86[125]. The explicit polarization shell has a radius of 30 Å.

3.3 Simulation of charge carrier transport hopping

Generated morphologies, as described in Section 3.1, have their electronic properties characterized as outlined in Section 3.2, providing the basis for computing charge carrier transport in organic electronic systems.
The morphology is hereby modeled at molecular resolution with a molecule represented as a site at the molecule's center of geometry. Atomistic models are transformed by positioning the sites at the molecule centers of geometry. Thus, periodic boundary conditions remain. Each site inherits a number of properties computed in advance in the electronic characterization. Which properties is detailed in the section below. Each site can host objects representing localized Frenkel excitons or charge carriers. The simulation process encompasses the creation, movement, and annihilation of these objects, with rates derived from microscopic parameters, as discussed in Section 3.3.1. Based on these rates, a rejection-free kinetic Monte Carlo (kMC) algorithm is used to propagate the system in time, as described in Section 3.3.2.

3.3.1 Microscopic Processes

In this work, the charge carrier transfer rate by hopping between the state Ψ_i of molecule i (site i) and Ψ_j of molecule j (site j) is given by:

$$\omega_\mathrm{if} = \frac{\pi}{\sqrt{\hbar^2 k_\mathrm{B} T \lambda}} J_\mathrm{if}^2 \exp\left(-\frac{(0.5(\Delta E_\mathrm{if} + \lambda + |\Delta E_\mathrm{if} + \lambda|))^2}{4\lambda k_\mathrm{B} T}\right), \tag{3.14}$$

with J_{if} denoting the electronic coupling and ΔE_{if} the energy difference between the initial and final states, determined by [131]:

$$\Delta E_{\text{if}} = -\Delta E_{\text{off}} + \Delta E_{\text{ext}} \pm e\vec{E}\vec{r}_{\text{if}}, \tag{3.15}$$

where ΔE_{off} denotes the difference in the charge carrier transport energy levels. Specifically, $\Delta E_{\text{off}} = \text{IP}_i - \text{IP}_f$ for hole transport and $\Delta E_{\text{off}} = \text{EA}_i - \text{EA}_f$ for electron transport. The charge carrier transport energy levels of the sites are typically modeled as Gaussian distributed with the standard deviation denoted as disorder. Microscopically, it arises from variations in molecular conformations and the local electrostatic environment. The term $E_{\text{if}}^{\text{ext}}$ captures the difference in the electrostatic interaction energy of the hopping charge carrier with its environment before and after hopping. Thus, it accounts for the Coulomb interaction between all electrons and holes in the given configuration. It varies dynamically with the position of the charge carriers and is evaluated via the Ewald summation [132]. Long distance Coulomb interactions between charge carriers are calculated from the interaction of point charges. Short distance Coulomb energies (nearest 250 neighbors) are drawn from tabulated Coulomb energy distributions derived from quantum embedding (including calculated electrostatic binding energy between ionized host and dopant molecules, Section 3.2.4). In the course of this work (Section 5) further parametrizations are developed. The final term is based on the potential energy generated by the charges in an external electric field. $\vec{r}_{if} = \vec{r}_i - \vec{r}_f$ describes the spatial displacement between the charge carriers before and after hopping.
Neutral dopants are described as excitons with zero excitation energy. The host-dopant activation process:

$$H + D \rightarrow H^+ + D^-, \tag{3.16}$$

is associated with the energy difference

$$\Delta E_{\text{ion}} = \Delta E_{\text{off}} + V_{\text{C}} + \Delta E_{\text{ext}} \pm e\vec{E} \cdot \vec{r}_{ij}, \tag{3.17}$$

where the energy difference $\Delta E_{\text{off}} = \text{IP}_{\text{h}} - \text{EA}_{\text{d}}$ (of the host h and the dopant d), and V_{C} is the attractive Coulomb energy between the ionized host-dopant pair. ΔE_{ext} is the electrostatic interaction energy between the ionized host-dopant pair and the charges in their environment.

3.3.2 Modeling with kinetic Monte Carlo

Kinetic Monte Carlo (kMC) is a Monte Carlo approach that simulates the time evolution of processes governed by transitions between discrete states with known transition rates. These rates, which cannot be determined by the kMC algorithm itself, must be obtained from prior knowledge, measurements, or separate calculations. In the context of this thesis, the charge carrier transport and the dopant ionization rate are calculated using Equation 3.14. The kMC simulation protocol was implemented by Symalla [131].

Because of the weak coupling between organic molecules, the system can be treated as a Markov chain, *i.e.* the probability rates for a given state to transition to a different state depend only on the current configuration, not on any previous states. In particular, a rejection-free kMC scheme [133] evolves the system in time. The state is specified by the positions of all particles. In a rejection-free kMC algorithm, the simulation begins at time $t = 0$ with an initial state k. The rate r_{ki} represents the probability per unit time of a transition from state k to state i. First, a random number, $u \in (0, Q_k]$, is generated to select the next state, with its upper bound given by $Q_k = \sum_{j=1}^{N_k} r_{kj}$, where r_{kj} are the transition rates from k to each possible state j and N_k is the number of possible transitions from state k. Defining $R_{k,i} = \sum_{j=1}^{i} r_{kj}$ as the cumulative distribution, the system moves to the state i that satisfies $R_{k,i-1} < u \leq R_{k,i}$. A second random number, $u' \in (0, 1]$, specifies the elapsed time step, $\Delta t = Q_k^{-1} \ln(1/u')$, which is added to the current time, $t \leftarrow t + \Delta t$. In the following discussion, the total rates for a specific process i are denoted as Γ^i. The total rate for charge transfer is given by $\Gamma^{\mathrm{ct}} = \sum_{i=1}^{n_c} \sum_{a=1}^{N_i^{\mathrm{cttargets}}} \omega_{i,a}^{\mathrm{ct}}$, where the index i runs through all charges n_c. $N_i^{\mathrm{cttargets}}$ is the number of sites accessible for hopping by charge i, and $\omega_{i,a}^{\mathrm{ct}}$ is the rate of each individual transition. The total rate for the system to move into another state is then

$$\Gamma^{\mathrm{total}} = \sum_i \Gamma^i. \tag{3.18}$$

An iteration of the kMC procedure is illustrated in Figure 3.3a. The system is prepared in a given state, and the individual rates for all processes and particles, denoted ω_i, are evaluated. The cumulative function $\omega_i^{\mathrm{cum}} = \sum_{j=1}^{i} \omega_j$ is then calculated. A uniformly distributed random number ω_{random} is drawn from the interval $(0, \omega_N^{\mathrm{cum}}]$, where N represents the total number of possible transitions. The system transitions to state i if:

$$\omega_{i-1}^{\mathrm{cum}} < u \leq \omega_i^{\mathrm{cum}}. \tag{3.19}$$

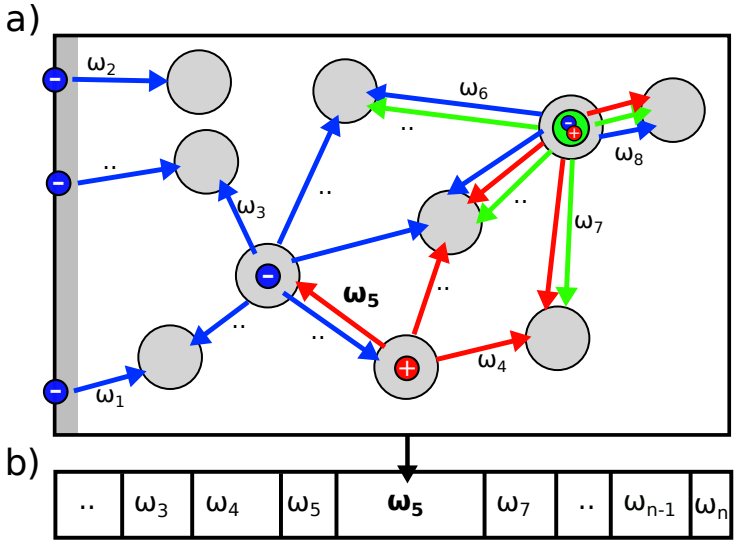

Figure 3.3: a) Scheme of the rejection-free kMC model of an amorphous small molecule organic semiconductor. The rates ω_i represent the individual processes for each charge carrier or exciton and event. b) shows the cumulative sum of all these rates; a uniform random number is drawn from $(0, \omega_n)$, and in the scenario depicted, ω_{random} falls within the interval selecting process number five for the next kMC step. Own schematic illustration inspired by [131].

The simulation proceeds until a stable current is observed, which is defined by a constant drift velocity. During the interval $t' - t$, the cumulative drift velocity is given by

$$v(t, t') = \frac{\sum_{i=1}^{n(t,t')} q_i \frac{\vec{F}_i}{F} \cdot \Delta\vec{R}_i}{t' - t}, \tag{3.20}$$

where $n(t, t')$ counts the Monte Carlo steps that contribute to charge carrier transport between times t and t'. The quantity q_i specifies the charge sign, $\Delta\vec{R}_i$ is the displacement in step i, and $\vec{F}$ is the applied electric field. The charge carrier mobility μ is then calculated using $\mu = \frac{\vec{v}}{\vec{E}}$. Two drift velocities serve as convergence criteria:
$v_1 = v(t_1, t_2)$ and $v_2(t_{\text{total}} - t_2) > d_{\text{min}}$. In every N_{iter} steps, the following conditions are checked: $\left|1 - \frac{v_2}{v_1} < c_{\text{DC}}\right|$ and $v_2(t_{\text{total}} - t_2) > d_{\text{min}}$, where c_{DC} is a convergence tolerance, d_{min} is the minimum hopping distance, t_{total} is the total simulation time, and $t_2 = \frac{2}{3} t_{\text{total}}$. The second condition prevents charges from being trapped for extended periods by requiring both v_1 and v_2 to be non-zero before reaching a steady state. Once both conditions are satisfied, the simulation is terminated. The parameter c_{DC} is chosen to balance computational cost and accuracy.

4 Experimental techniques

This section covers the experimental techniques used. First, the preparation of organic nanoparticle dispersions by nanoprecipitation is explained. Techniques to analyze the nanoparticle dispersions, *i.e.*, the measurement of the nanoparticle size by dynamic light scattering (DLS) and determining dispersion concentration by ultraviolet-visible (UV-Vis) absorbance spectrometry are described. Typically, these dispersions are used to process layers or fabricate whole devices, which is explained in the following section. Different techniques for analyzing the surface of the substrates are outlined. Further, the characterization of solar cells and photodiode characteristics are explained. The emphasis is placed on a highly accurate measurement setup that has been composed to increase the sensitivity of dark current measurements.

4.1 Preparation and analysis of dispersions

In this section, the synthesis by nanoprecipitation and characterization (DLS and UV-Vis absorbance spectrometry) of organic nanoparticle dispersions are introduced.

4.1.1 Preparation

This work relies on the nanoprecipitation method. Hence, an organic semiconductor, dissolved in a solvent, is mixed with a nonsolvent in which the organic semiconductor is not soluble. The solvent typically has a lower boiling point to enable its evaporation while keeping the semiconductor dispersed in the nonsolvent. Two common methods have been used for the nanoprecipitation of organic semiconductor applications. Continuous flow nanoprecipitation in a microfluidic system has been demonstrated to synthesize organic bulk-heterojunction nanoparticle dispersions. The solution is mixed with the nonsolvent in several mixing stages at a controlled flow rate. The inks exhibit excellent reproducibility and long-term stability, which is particularly important for upscaling of dispersion synthesis [81]. However, the microfluidic chip can clog and cleaning can be difficult, rendering the method unsuitable for testing new semiconductors that may have low colloidal stability or could contaminate the microfluidic chip.
Batch nanoprecipitation (hereafter nanoprecipitation) has lower reproducibility but is more

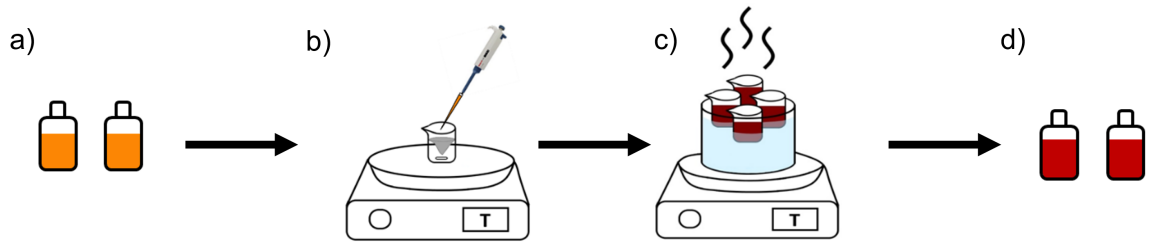

Figure 4.1: Schematic of the batch nanoprecipitation in a beaker. a) (Doped) organic semiconductor solution. b) Injection of the solution into a nonsolvent under stirring. This causes the organic material to nucleate and form nanoparticles. c) Volume reduction step that removes the solvent and increases the concentration of the dispersion. d) Nanoparticle dispersions left in the nonsolvent. Subsequently, a centrifugation removes larger agglomerates. Published by Karen Fischer under Licence CC BY-SA 4.0.

facile, rendering it the method of choice if only small dispersion volumes are needed or when working with new semiconductors. A scheme of the nanoprecipitation process is shown in Figure 4.1. Here, the organic semiconductor is dissolved in a transparent glass vial (4 mL). It may be doped to increase the charge density on the semiconductor. Then a specified amount from there is pipetted with an automatic pipette into a beaker with a defined volume of nonsolvent. The nonsolvent is stirred by a magnet at 800 rpm [74]. The solvent and nonsolvent are miscible; however, the solubility of the organic material rapidly reduces in the solvent-nonsolvent mixture, leading to nucleation and growth of the particles until the colloidal stability is reached. Illumination has a great influence on nanoparticle sizes [12], hence, in some experiments of this thesis, where indicated, a chip-on-board (COB) white light-emitting diode (LED, 2.1 cm·2.1 cm) illuminated the nonsolvent during injection with an electric power of 30 W. To fully extract the solvent, the beaker is positioned in a heated water bath. In addition, some of the nonsolvent is evaporated to increase the dispersion concentration. This step is referred to as volume reduction. Some dispersions show partial agglomeration, which can interfere with measuring the nanoparticle size or concentration. For this reason, all dispersions were centrifuged with a MiniSpin Plus by Eppendorf at 14,500 rpm for 2 minutes in 1.5 mL centrifugation tubes after volume reduction. This leads to sedimentation of agglomerates.

Small-angle neutron scattering and transient absorption have shown that P3HT:Indene-C_{60} bisadduct (P3HT:ICBA) nanoparticles synthesized by nanoprecipitation in a beaker are blend nanoparticles in which the two semiconductors are uniformly mixed [134]. Nanoparticles from synthesis methods other than nanoprecipitation can result in different semiconductor distributions. Miniemulsions often lead to core-shell particles, with the fullerene being surrounded by P3HT [135].

For this work, $CHCl_3$ (analytical grade) is used as a solvent and ethanol (EtOH, analytical

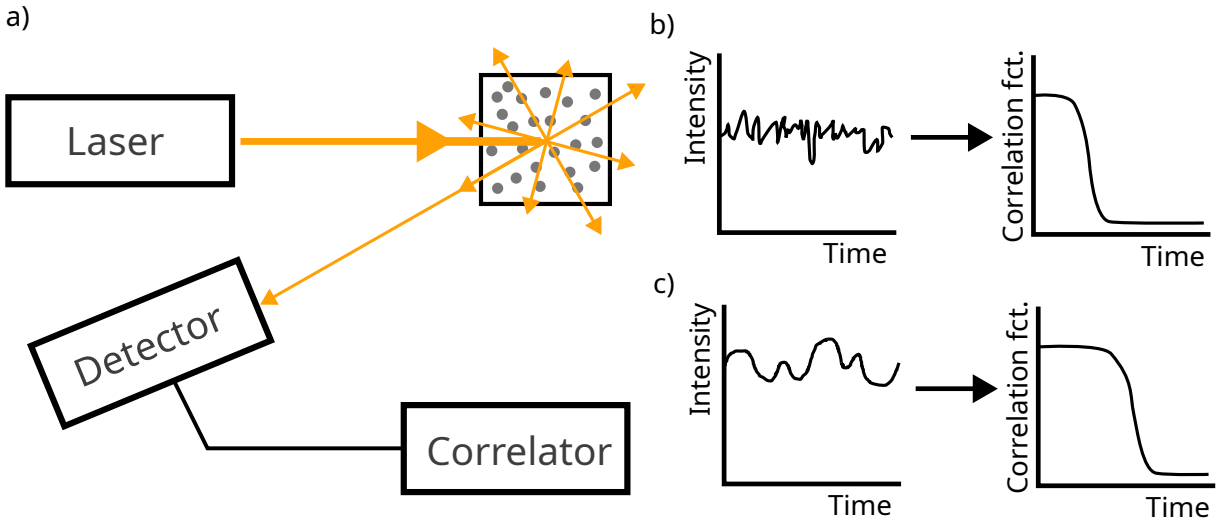

Figure 4.2: a) Schematic representation of dynamic light scattering for nanoparticle size determination. A laser beam is scattered by nanoparticles, and the intensity of the scattered light fluctuates over time due to Brownian motion. b) For smaller nanoparticles, the intensity fluctuations of the scattered laser occur on a shorter timescale compared to larger particles. (c) This is reflected in the autocorrelation function, where the decay occurs more rapidly for smaller particles.

grade, emsure) or acetonitrile (CH_3CN, 99.8% anhydrous) as a nonsolvent without further purification. Nanoprecipitations in borosilicate glass vials have been shown to lead to larger nanoparticles compared to those of high-density polyethylene (HDPE) vials. Washing the glass vials three times with EtOH leads to the same nanoparticle size. The hypothesis is that the anionic silicates are dissolved, which destabilizes the dispersions [74]. Because of its optical transparency, glass was still used but washed three times with the nonsolvent of the nanoprecipitation process. The time of dispersion in the glass beakers is limited to injection and volume reduction. Afterwards, the dispersions were stored in HDPE vials.

4.1.2 Dynamic light scattering

An unstable dispersion can often be directly identified by visible flocculations. However, below 10 µm, the flocculations are not visible to the naked eye, which requires a different technique to determine the nanoparticle size, which is connected to the colloidal stability according to the DLVO theory (Section 2.2.1).

DLS relies on the Brownian motion of particles (Section 2.2). A schematic is shown in Figure 4.2. In this work, the Zetasizer Nano ZS by Malvern Panalytical is used. A diluted dispersion is inserted into a cuvette and irradiated with a 633 nm laser beam. The Brownian motion of the nanoparticles causes light scattering. The ensemble of reflected photons interferes with each other, causing fluctuation in intensity. A detector records the time-resolved intensity at a specific angle (in frontscatter mode: $\theta = 13°$, in backscatter

mode: $\theta = 173°$). Smaller particles move faster than larger particles (having the same kinetic energy), leading to faster fluctuations in intensity. An autocorrelation function of intensity versus time $g^2(q;\tau)$ characterizes the dynamics of the fluctuations:

$$g^2(\tau) = \frac{\langle I(t)I(t+\tau)\rangle}{\langle I(t)\rangle^2}. \tag{4.1}$$

The brackets denote the expectation value over a defined time range. t and $t+\tau$ are the times at which the intensity fluctuations are compared. In the simplest case, the dispersion is monodisperse (particles are uniform) and can be described by a single exponential term:

$$g^2_{\text{mono}}(\tau) = B + \beta \cdot \exp(-\Gamma\tau), \tag{4.2}$$

with $\Gamma = 2Dq^2$, where B is the baseline, β is an instrument constant, D is the diffusion constant and q is the wave vector of the dispersion observed at the specific angle:

$$q = \frac{4\pi n_0}{\lambda} \sin\left(\frac{\theta}{2}\right), \tag{4.3}$$

with n_0 as the refractive index of the solvent and the incident laser wavelength λ. A fit determines the exponential decay rate Γ. Then, using the Stokes-Einstein-Sutherland equation, which describes the diffusion of spherical particles in a liquid with a low Reynolds number, the particle radius r can be calculated:

$$r = \frac{k_{\text{B}}T}{6\pi\eta D}, \tag{4.4}$$

with k_{B} being the Boltzmann constant, the temperature T and the viscosity η of the dispersion medium. r is also known as the hydrodynamic radius.
In most cases, samples are polydisperse. Then, a sum of exponential terms, each term representing the autocorrelation response of a specific size category, yields $g^2(\tau)$. However, fitting the individual decay rates is a mathematically ill-posed problem and can only distinguish between different particle sizes if their size distribution does not strongly overlap and their contribution to the recorded intensity is similar. The cumulant method is an established approach to solve this. A Gaussian distribution of particle sizes is assumed. The autocorrelation function is fitted using an exponential decay function that depends on the average decay rate multiplied by a power series containing cumulants. The average decay rate leads to the calculation of an average nanoparticle size, termed the Z-Average. The cumulants determine the polydispersity indices, which indicate the variance of the

size distribution. Often, just one polydispersity index is given, derived from the second and third order cumulants (denoted as PDI). Higher orders are only necessary for highly polydisperse samples. The cumulant method yields reproducible results. A PDI of 0 describes a monodisperse distribution. Up to 0.7, the cumulant method still yields the appropriate results but should be compared with a direct fit of $g^2_{\mathrm{mono}}(\tau)$ using size-related exponentials.
The size distribution of particles is weighted by the intensity of the scattered light. Particles with a size smaller than 1/10 of the incident wavelength exhibit Rayleigh scattering. Then, the intensity of scattered light depends on r^6, *i.e.*, larger particles are weighted much stronger in the size distribution than smaller particles. From this distribution, number- or volume-weighted distributions can be calculated. The exact particle radius can differ from the DLS-determined radii because particles are often surrounded by a thin layer of solvent molecules and particles can exhibit non-spherical shapes, introducing errors in the determined particle size. Still, the particle sizes are similar to sizes determined by microscopic measurement techniques such as atomic force microscopy (AFM), electron microscopy, or small-angle x-ray scattering.
In this work, nanoparticle dispersions are diluted to the order of $\mathcal{O}(10\,\mathrm{mg\,L^{-1}})$ to be measured by DLS, either in plastic or quartz cuvettes. At least eight measurements are taken, each recording the intensity fluctuations of the scattered laser beam for at least 8 s.

4.1.3 UV-Vis absorbance spectrometry

UV-Vis absorbance spectrometry has been proven to be a versatile method for characterizing organic nanoparticle dispersions. The absorption spectrum contains information about the concentration of individual constituents in the dispersion. Depending on the material, it can provide information about the microstructure, such as stacking. Especially when it comes to doping, it allows the distinction of dopants by their different absorbance signatures corresponding to their charging states. In Section 6, a method is developed that utilizes UV-vis recordings to determine the polaron yield efficiency (PYE), *i.e.* the actual number of charges transferred between the dopant and the host vs. the maximum number of charges available for transfer in organic dispersions.
In this work, an Agilent Cary 5000 ultraviolet-visible-near infrared (UV-Vis-NIR) spectrometer in two-beam operation mode is used. A light source generates light in the range of 175-3300 nm, which passes through a monochromator. A beam splitter separates the beam into two paths; one is directed through a sample, and the other follows a reference path. Behind both paths, photodetectors measure the intensities of the transmitted beams. The

ratio of the sample intensity I to the reference intensity yields I_0 the transmission of the sample. Beforehand, a calibration without a sample removes apparent absorbance features stemming from the measurement setup itself (e.g., differences in detector response). From the sample transmission T, the absorbance A is calculated as $A = -\log_{10}(T)$. While absorption refers to the decrease in the beam intensity by an absorbing physical process, absorbance also contains other contributions: attenuation of the beam intensity by interference, reflection, or scattering. Especially for thin films, these contributions play a role, which is why measuring with an integrating sphere is a better approximation of the absorption.
The Beer-Lambert law describes the attenuation of a beam intensity as it passes through a sample based on sample parameters:

$$-\log_{10}(I/I_0) = A = \varepsilon l c, \tag{4.5}$$

with ε being the molar absorption coefficient (MAC), l the path length through the sample, and c the concentration. Hence, by knowing the MAC (e.g. determined by a reference measurement with known concentration), the unknown concentration of a UV-Vis measured sample can be determined. In semiconductor mixtures, a fit using the spectra of individual reference solutions can yield individual contributions if no chemical reactions take place. To determine the concentration of a dispersion, it is redissolved in a solvent and compared to a reference with known concentration.

4.2 Preparation and analysis of thin layers

Here, the standard device fabrication and surface characterization are explained.

4.2.1 Fabrication

The following cleaning steps were performed in a cleanroom (Class 6, ISO 14644-1). In this work, glass substrates, quartz substrates, and glass substrates with a structured indium tin oxide (ITO) electrode were used to process individual layers or devices. The cleaning procedure was the same for all: First, they were cleaned with a glass cleaner and a Q-tip by swiping several times on the surface. Then an ultrasonic bath with acetone and 2-propanol was applied for 10 minutes. To remove organic residues, the substrates were treated with oxygen plasma (Diener Atto, 200 W, 2 min). The ITO-structured substrates have a size of $16 \times 16\,\mathrm{mm}^2$, the glass being 1.1 mm thick with an ITO layer on top. The ITO is structured to facilitate four equal devices in vertical architecture that can be contacted

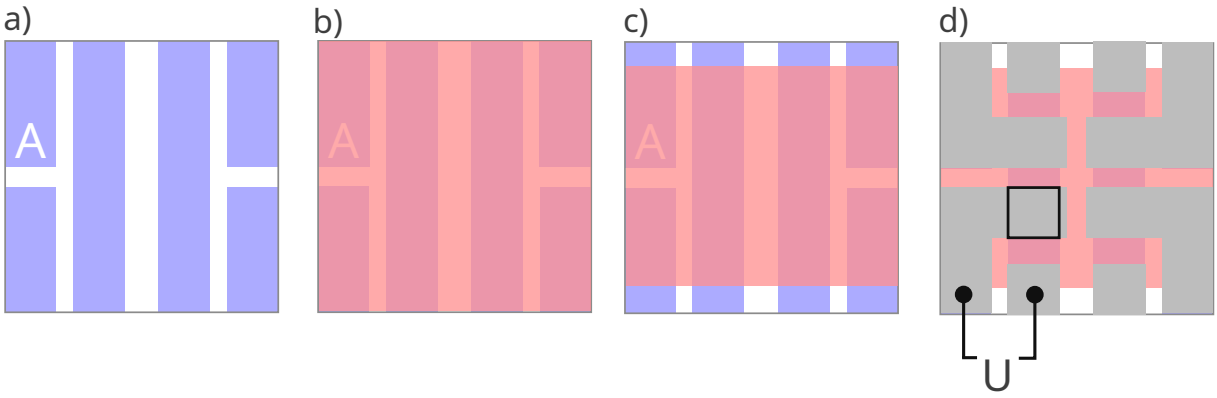

Figure 4.3: Schematics of device fabrication: a) ITO electrodes on a glass substrate. b) Deposition of transport layers and/or photoactive layer for OSCs and OPDs. c) Scratching removes the deposited layers in the upper and lower regions. The scratching step ensures electrical connection between the centered top contact areas and the underlying ITO strips. d) Evaporation of the top electrode. The black rectangle represents the photoactive area of the OSC, defined by the overlap between the ITO strip and the top electrode.

from the top. The dimensions of each device are $3 \times 3.5\,\mathrm{mm}^2$. Figure 4.3 shows (a) the ITO layout, (b) the deposited photoactive layer and/or transport layers, and (d) the respective top electrode layout. In the upper and lower parts of the top electrode, there are eight individual contact areas, two for each OSC. The photoactive and transport layers in the upper and lower areas are scratched (Figure 4.3c) to connect the centered ITO strips to the top contact in the center, forming the bottom contact of the device. The contact areas on the left and right form the top contact. The layout works because the conductivity of the organic photoactive and transport layers is much lower than that of the electrodes. Thus, charge transport occurs in the vertical direction, not laterally.
In this work, spincoating is used to deposit the organic semiconductors. It is a facile method that enables reproducible and homogeneous layers with defined thicknesses for many organic semiconductors. In static spincoating, the processing agent is cast onto the substrate, then the centrifugal motion starts with a specific acceleration until a defined speed is reached. Most of the solution is expelled from the substrate and the speed determines the wet-film thickness. Then, the wet film dries. This method is used for spincoating material with only one deposition step. In dynamic spincoating, the processing agent is cast onto an already rotating substrate. This enables faster deposition of several consecutive steps.

4.2.2 Surface profilometry

The thickness and roughness of the layers are crucial in thin-film devices. The thickness is determined using the Bruker Dektak XT tactile profiler. A stylus propagates along a

surface, recording the height. The stylus that touches the surface is made of diamond with 2 µm radius. The vertical resolution is 1 nm in the 65.5 µm range [136]. To measure the thickness of a layer, a step is scratched into the layer using a blunt metallic cannula without damaging the glass underneath. Only the total thickness can be measured. So, if the thickness of an individual layer in a stack is to be determined, the thickness of other layers must be measured separately and subtracted from the total thickness.

To analyze the surface roughness an atomic force microscopy (AFM, Dimension Icon, Bruker) is used. A tip is attached to a cantilever with a known spring constant. The tip moves along the surface, interacting with it via van der Waals and Coulomb forces. The distance to the surface is controlled by a piezo actuator and is either kept constant (contact mode) or oscillating, tapping the surface (tapping mode). Small changes in surface height cause deflection or torsion in the cantilever. A laser is directed onto the back of the cantilever, which reflects onto a four-quadrant photodiode. Thus, the movements of the tip are recorded digitally, and a height profile is generated. In this work, the AFM is utilized in tapping mode. The cantilever oscillates near its resonant frequency. The piezo actuators excite the cantilever, maintaining the amplitude. This method reduces the damage to the tip.

4.3 Solar cell and photodiode characterization

This section describes the electrical characterization of solar cells and photodiodes. To evaluate the solar cell performance under conditions similar to those of real-world applications, a solar simulator is used. In addition, the mechanisms of noise generation and suppression in photodiodes are discussed.

4.3.1 Solar simulator

The solar simulator used in this work produces a beam with a spectrum and power similar to that of sunlight at sea level. The sun power varies depending on the path length through the atmosphere. Power and solar spectra are classified into air mass (AM) classes. AM 1 describes light that travels through the air at a zenith angle of 0 °. Based on solar irradiance data in the United States, AM 1.5 has been established as a standard for solar cell testing [137]. This means that light travels 1.5 times farther through the atmosphere than at AM 1, corresponding to a zenith angle of 48.2 °. This standard is common for mid-latitude locations, where most solar panels are located. AM 1.5 Global (AM 1.5G) includes diffuse and scattered light according to the ASTM G173-03 standard. The irradiance is specified

as 1000 $\mathrm{Wm^{-2}}$. In this work, an AAA-class xenon solar simulator (Sciencetech Lightline AX-LA 200) was used. The three "A" ratings refer to (i) the spectral adaptation to AM 1.5G between 400 and 1100 nm, (ii) spatial uniformity and (iii) temporal stability of the irradiance. The solar simulator is calibrated to 1000 $\mathrm{W\,m^{-2}}$ using a reference silicon solar cell (Newport 91150-KG5). If the device under test exhibits a different SR from the reference cell, a spectral mismatch correction, using Equation 2.14, is applied using the measured EQE, as described below.

4.3.2 External quantum efficiency

The nature of the EQE and the SR are explained in Section 2.3.1. A high-pressure xenon lamp (USHIO 450 W UXL 451-O) is filtered by a monochromator (LOT Oriel Omni-lambda 300 with color filter wheel MSZ3122). The monochromatic beam is split, with one part going to a monitor photodiode and the other to the sample holder. The current generated by the sample and the monitor photodiode is converted into a measurable voltage by transimpedance amplifiers (Femto Messtechnik OE-200S). To calibrate the monochromatic beam on the sample holder, the current of a reference photodiode (Newport 818-UV-20925), I_{R}, with a known spectral response $\mathrm{SR_R}$, is recorded for a specific range of wavelengths. At that time also the current of the monitor photodiode is recorded, denoted as $I_{\mathrm{Monitor,R}}$. Then, the DUT is positioned in the sample holder, and its current is recorded as I_{DUT}. At the same time, the current of the monitor photodiode is recorded, denoted as $I_{\mathrm{Monitor,DUT}}$. As the current of the monitor photodiode is recorded during the measurement of reference and DUT, it is used to correct for temporal fluctuations in the beam intensity. The SR of the DUT is calculated as follows:

$$\mathrm{SR} = \frac{I_{\mathrm{DUT}}}{I_{\mathrm{R}}} \cdot \mathrm{SR_R} \cdot \frac{I_{\mathrm{Monitor,R}}}{I_{\mathrm{Monitor,DUT}}}. \tag{4.6}$$

Increasing the monochromator wavelength stepwise allows for determination of the SR at different wavelengths. To reduce noise and isolate the current generated by the monochromatic beam (e.g. excluding ambient illumination), the lock-in principle is used. The monochromatic beam is chopped into a rectangular waveform (Thorlabs MC2000B with the disc MC1F10, 373 Hz). A lock-in amplifier (Anfatec Instruments, eLockIn 203) isolates the current generated by the monochromatic beam from other sources.

5 Controlling charge transport by tuning the electrostatics of p-doped organic semiconductors

While the energetic landscape in intrinsic organic semiconductors is well understood, doped systems involve additional influences that impact charge transport. When a dopant is activated, it creates two charges: a free charge carrier on the host semiconductor and a counter-charge that remains on the dopant. The charged dopants generate a strong electric field because of their non-zero charge. The transport of charge carriers on the host semiconductor is crucial for determining the macroscopic electronic properties of a layer. The ICTC binding energy, which represents the Coulomb interaction between free charge carriers and charged dopants, has been shown to differ from a simple point-charge interaction [21, 138].

This section is based on work previously published in Armleder et al. [22]. The results are included here as part of the dissertation.

An accurate model for ICTC binding energy based on the quadrupole moment of the anionic dopant is developed. The quadrupole moment and its orientation relative to the host molecule are found to critically influence the conductivity in doped organic semiconductors. Specifically, a large positive quadrupole moment can cause overscreening in charge transfer complexes, potentially boosting the conductivity by several orders of magnitude and enabling the targeted design of highly conductive materials.

The investigation of the quadrupole moment was motivated by quantum-mechanical simulations using the QuantumPatch method, which showed that the Coulomb interaction energy between ionized host-dopant pairs deviates from the simple Coulomb energy between two point charges. As the dopant molecules were dipole-less, this motivated to look at the next electrostatic moment: the quadrupole moment.

5.1 Morphology of NPB doped with F_6TCNNQ

N,N′-Di(1-naphthyl)-N,N′-diphenyl-(1,1′-biphenyl)-4,4′-diamine (NPB) doped with Tetracyanoquinodimethane (TCNQ) derivatives represents a standard organic semiconductor system and therefore serves as an appropriate test system. The molecular structures of NPB, TCNQ, F_4TCNQ, 1,3,4,5,7,8-hexafluorotetracyanonaphthoquinodimethane (F_6TCNNQ)

are displayed in Appendix C.4. Using the multiscale approach described in Section 3, a morphology is created by Deposit (Section 3.1) that is the foundation for characterization of the electronic properties of the embedded molecules.
First, the molecules NPB and F_4TCNQ are parametrized. The vacuum conformation and conformations for various dihedral angles of the molecules are optimized regarding energy using DFT with the def2-SV(P) basis set [139] and the BP86 functional [125]. Atomic partial charges are calculated via an ESP fitting procedure. After that, within the Deposit method, the individual molecules to be deposited are annealed from 4,000 K to 300 K in 76 SA cycles, with each cycle consisting of 50,000 Monte Carlo steps. The energy between two Monte Carlo steps is calculated using the Lennard-Jones parameters and ESP charges. Two axes with periodic boundary conditions span the base area of the simulation box, with a size of $180 \times 180\,\text{Å}^2$. For doped NPB morphologies, 10,000 molecules are deposited (mainly NPB molecules, with the exact ratio of NPB molecules to dopants given by the DMR). This yields a length in growth direction of at least 240 Å, in which no periodic boundary conditions are applied.
An undoped NPB morphology is created to compare the density with the experimental data. For that, the atomic mass in the simulation box, containing the deposited molecules, is summed up and divided by the volume. A density of $1.13\,\text{g/cm}^3$ is obtained for a simulated morphology, very similar to the experimental density of $1.14\,\text{g/cm}^3$[140]. In the doping regime considered in this section (DMR <5%), the density of the doped morphologies deviates only slightly from the undoped morphologies. The density of the NPB morphology doped with 5% F_6TCNNQ, as shown in Figure 5.1a, is $1.14\,\text{g/cm}^3$, equal to the experimental density [140]. The figure depicts dopants (purple) that are distributed in the host NPB (grey). Depending on the molecular structure, preferred orientations or distances between molecules will arise. Given the molecular structure and orientation constraints, peaks in the RDF can be associated not only with preferred distances but also with orientations. Figure 5.1b shows the corresponding RDF only of NPB molecules to other NPB molecules. The RDF takes non-zero values for $r > 2\,\text{Å}$, which is the closest distance between two centers of geometries of host molecules. At $r = 6\,\text{Å}$, the first maximum appears, which can be attributed to $\pi - \pi$ stacking, also experimentally observed in thin films [141]. The RDF shows a local minimum and a second peak at $r = 12\,\text{Å}$, then becomes relatively constant. As the RDF peaks are rather broad and, for large r, become approximately 1 without strong fluctuations, the morphology is amorphous. Figure 5.1c shows the RDF of distances between F_6TCNNQ and NPB molecules. The RDF increases strongly, beginning at $r = 3\,\text{Å}$, it reaches the first peak at $r = 5\,\text{Å}$, and then decreases rapidly to 0.6. These sharp peaks show a high frequency of

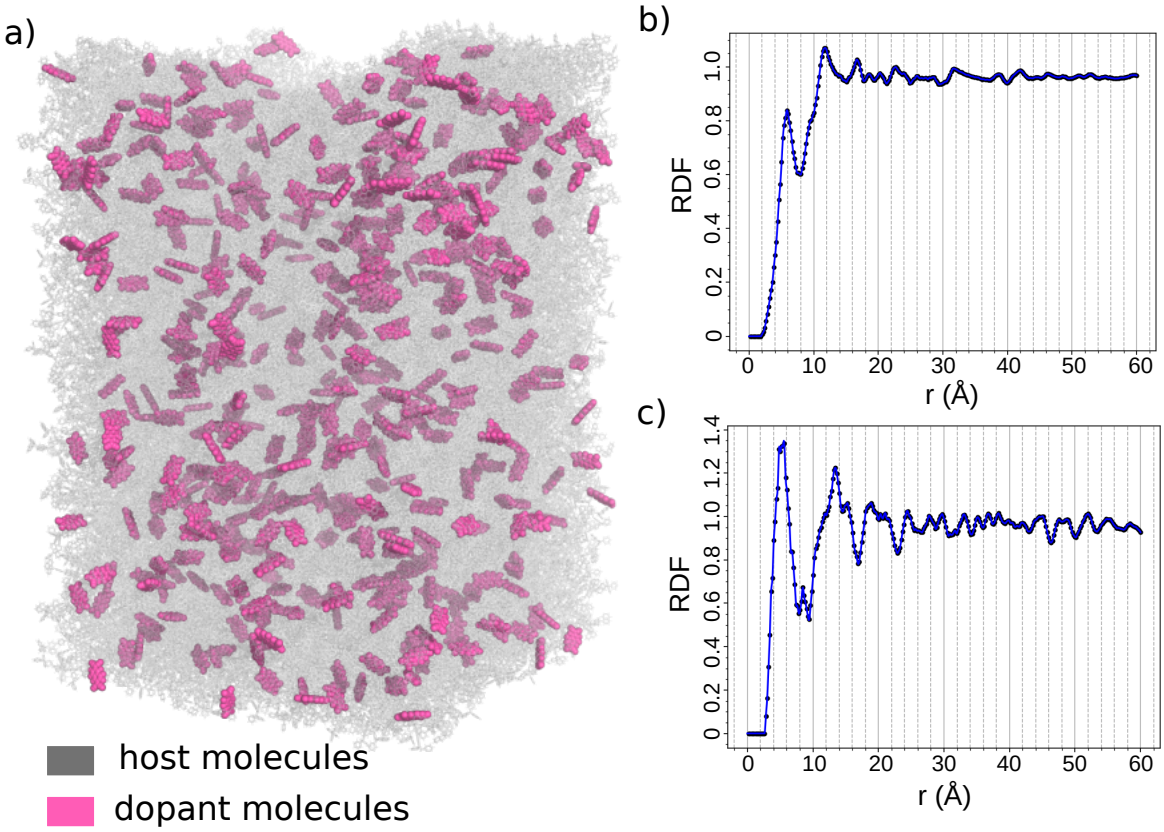

Figure 5.1: a) Morphology of NPB doped with F_6TCNNQ (5%). The Deposit algorithm sequentially places host and dopant molecules according to the DMR. Visualization adapted from Armleder et al. [22], licensed under CC BY 4.0; modified by the author. b) Corresponding RDF between NPB molecules, showing characteristic peaks at 6 Å and 12 Å, consistent with the π-π stacking of NPB [141]. c) RDF between NPB and F_6TCNNQ molecules, exhibiting stronger fluctuations compared to the host-host RDF, suggesting more defined orientations in NPB-F_6TCNNQ molecular pairs.

hosts and dopants deposited at the same distance. The host-dopant distance of $r = 5$ Å allows only the molecular planes to be oriented parallel. The molecular planes refer to the centered benzene or naphthalene group(s), Appendix C.4. This orientation-preferred arrangement has already been experimentally observed for TCNQ derivatives [142, 143]. The RDF between NPB and F_6TCNNQ shows more distinct peaks than the RDF between NPB molecules, suggesting a stronger orientation preference between the host and the dopant than between the host molecules.

5.2 Modeling of the Coulomb interaction of ICTC on short scales

The morphology allows for the calculation of embedded electronic structures, which are a requirement for further charge carrier transport simulations, Section 3.2. The energy

levels and the ICTC binding energy strongly depend on the environment [34, 129], which in turn depends on the molecular structure of the morphology. In the following, the electronic properties of the host and dopant and their relative molecular orientation are analyzed regarding their influence on the ICTC binding energy V_C. For that, a simplified representation of the charge density of the dopant is used on the basis of the monopole and quadrupole moment. A quantum embedding method is used to validate the simplified model. Specifically, V_C is calculated using the quantum embedding method QuantumPatch [122, 123] for host-dopant pairs with different distances to yield reference results. A quantum embedding run encompasses the equilibration of the charge density of molecules within a certain simulation volume, described in more detail in Section 3.2.4.

The charge equilibration of 30 embedded host-dopant pairs is carried out in the neutral and three different charged states, as illustrated in Figure 3.2. The host IP (IP_{host}), dopant EA (EA_{dop}), and the charge transfer energy E_{CT} are obtained. The ICTC binding energy V_C is subsequently computed according to Equation 3.10. Details are given in Section 3.2.4. The relationship between V_C and the inverse distance is shown in Figure 5.2. V_C is compared to the classical Coulomb interaction between two oppositely charged point charges in a polarizable medium with a dielectric permittivity of NPB ($\epsilon_r = 2.7$ [34]). For short distances ($r < 6.7\,\text{Å}$, $r^{-1} > 0.15\,\text{Å}^{-1}$), V_C deviates significantly from the classical Coulomb interaction. Specifically, it becomes almost independent of the distance if $r < 6.7\,\text{Å}$, resulting in a deviation of 0.7–0.9 eV from the classical interaction at $r = 3.3\,\text{Å}$. Consequently, after the ionization of a host-dopant pair, the created hole propagates in a nearly flat electrostatic potential (up to $r = 6.7\,\text{Å}$) rather than being trapped in a deep Coulomb potential near the host cation. This phenomenon is referred to as *short-range overscreening*.

To estimate V_C for a statistically significant number of host-dopant pairs, a method was developed utilizing the multipole representation of the dopant and the partial charge representation of the host molecule: This method was the result of trying various methods, evaluating them, and selecting the optimal method. To that end, various methods have been tested that, while calculating the host-dopant Coulomb interaction at a simplified level, rely only on parameters derived from isolated host and dopant molecules, which are computationally efficient to obtain. Each method incorporates three key components to model the Coulomb interactions: (1) the electrostatics of the host, (2) the electrostatics of the dopant, and (3) the influence of the polarizable environment, such as the organic bulk. The estimation proceeds as follows. The electrostatics of the anionic dopant is described by the first three moments of its multipole expansion: monopole, dipole, and quadrupole moments (the dipole moments of all investigated TCNQ derivatives are negligible). The

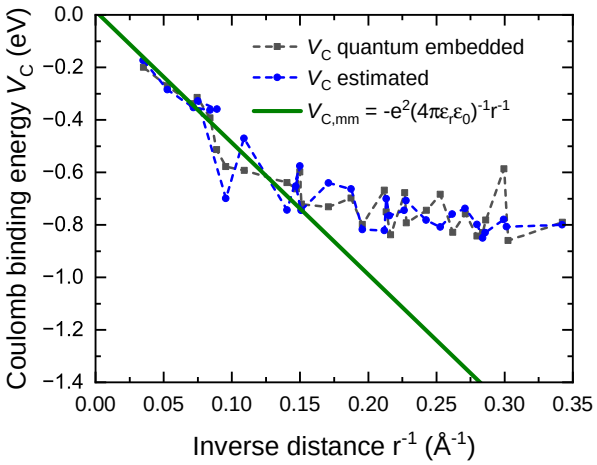

Figure 5.2: Calculation of the ICTC binding energy V_C of host and dopant by the QuantumPatch method (V_C quantum embedding) and the estimation of Equation 5.1 (V_C estimated). For large distances of $r > 15$ Å, the V_C by both methods agree with the Coulomb law that represents the approximation of the two molecules as point-charges with opposite charges. For shorter distances, the point-charge model deviates due to disregarding local field effects. The shallower V_C between two molecules (compared to the $V_{C,mm}$ of point-charges) is denoted as short-range overscreening. Both, QuantumPatch and estimation, agree with each other with deviations being lower than the variation within either method for pairs with similar distance.

cationic host is modeled using ESP partial charges [113]. The polarizable environment is accounted for by describing the interaction between multipoles and partial charges within an effective continuous medium with relative permittivity ϵ_r. This permittivity is computed for the actual morphologies as detailed in 3.2.3. V_C is estimated using the following formula:

$$V_C(\text{estimated}) = \sum_i -\frac{e q_i^h}{4\pi\epsilon_0\epsilon_r r_i} + \frac{q_i^h}{8\pi\epsilon_0\epsilon_r}\frac{\mathbf{r}_i\mathbf{Q}^d\mathbf{r}_i}{r_i^5}. \tag{5.1}$$

e and $\epsilon = \epsilon_0\epsilon_r$ are the elementary charge and the dielectric permittivity, respectively; q_i^h represents the i-th partial charge of the host. The vector $\mathbf{r}_i$ connects the positions of the host partial charges to the dopant center of geometry, and $\mathbf{Q}^d$ denotes the quadrupole tensor of the dopant. To compare the estimation of V_C (Equation 5.1) with the quantum embedding method QuantumPatch, V_C was calculated with the estimator utilizing the quadrupole moment of the anionic F_6TCNNQ (Appendix C.1) and the ESP partial charges of NPB. NPB was geometrically relaxed with DFT (def2-SVP, BP86), and the partial charges were determined by DFT (def2-QZVP and PBE). The comparison, shown in Figure 5.2 (blue and black data, respectively), reveals notable deviations for individual pairs. However, these deviations are within the range of fluctuations observed within

either method for pairs at similar distances. The V_C calculated using the estimator in approximately 100,000 host-dopant pairs is shown in Figure 5.3b. To gain qualitative insights into the dependence of V_C on the separation distance r between the host and dopant, the electrostatic characteristics of the molecules (host and dopant) are represented using monopole and quadrupole moments. Under this approximation, the Coulomb interaction between host cations and dopant anions is expressed as follows:

$$V_C \text{ (multipoles-multipoles)} = V_{mm}^{hd} + V_{mQ}^{hd} + V_{mQ}^{dh} \tag{5.2}$$

where

$$V_{mm}^{hd} = -\frac{e^2}{4\pi\epsilon_0\epsilon_r r} \tag{5.3}$$

is the interaction between the molecule monopoles,

$$V_{mQ}^{hd} = +\frac{e}{8\pi\epsilon_0\epsilon_r}\frac{\mathbf{r}\mathbf{Q}^d\mathbf{r}}{r^5} \tag{5.4}$$

is the interaction between the host monopole and the dopant quadrupole, and

$$V_{mQ}^{dh} = -\frac{e}{8\pi\epsilon_0\epsilon_r}\frac{\mathbf{r}\mathbf{Q}^h\mathbf{r}}{r^5} \tag{5.5}$$

is the interaction between the host quadrupole and the dopant monopole. $\mathbf{Q}^d$ or $\mathbf{Q}^h$ represent the quadrupole tensor of the dopant and host, respectively. The final two components (quadrupole-monopole interactions) are influenced by the relative orientation of the host and dopant molecules. Figure 5.3b depicts V_C(multipoles-multipoles) for three distinct relative orientations of hosts and dopants: along the x, y, and z axes. Here, the x axis corresponds to the direction of the greatest dimensions (long axis) of the molecule, the z axis is normal to the planar structure of the F_6TCNNQ molecule (normal axis), and the y axis is orthogonal to both (short axis), as shown in Appendix C.4. For these orientations, the monopole-multipole interaction described in Equation 5.2 can be simplified to

$$V_{mQ}^{dh}(\alpha\alpha) + V_{mQ}^{hd}(\alpha\alpha) = \frac{e}{8\pi\epsilon_0\epsilon_r}\frac{1}{r^3}(-Q_{\alpha\alpha}^h + Q_{\alpha\alpha}^d) \tag{5.6}$$

with $\alpha = x, y, z$. According to Equation 5.6, V_C varies linearly with the difference in quadrupole moments between the host and dopant. Depending on the signs of these quadrupole moments, the interaction can result in either overscreening or underscreen-

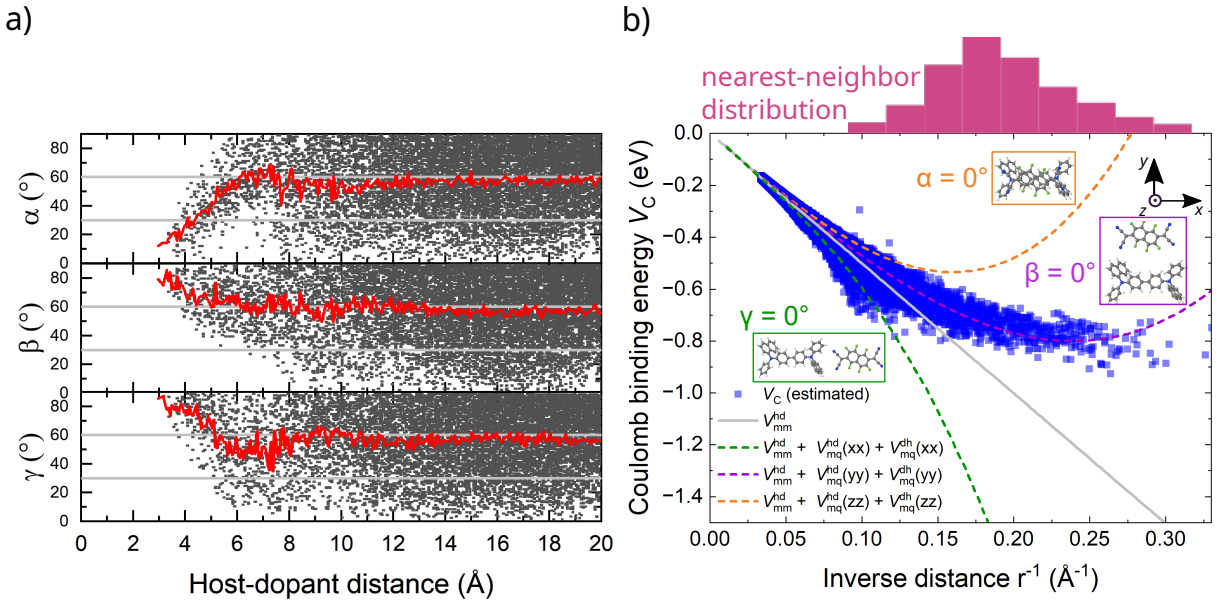

Figure 5.3: a) Angles between the normal (α), short (β), and long (γ) axes of F_6TCNNQ and the vector connecting the center of geometry (COG) of F_6TCNNQ to the COG of an NPB molecule. Each point represents a single host-dopant pair in an NPB:F_6TCNNQ morphology (5% DMR). As a reference, $\alpha = 0$ indicates that the COG of the host is positioned directly above the molecular plane of F_6TCNNQ, with the COG connecting vector aligned along the normal axis of the dopant. b) Calculated Coulomb binding energy V_C from Equation 5.1 as a function of the inverse distance for 100,000 host-dopant pairs. Three analytical lines, obtained using Equation 5.2, represent V_C for dopant-host alignments along the dopant's normal (z), short (y), and long (x) axes, as depicted in the insets. Since a) shows a preferred angle $\alpha = 0$ at short distances, indicating alignment along the z-axis (normal axis) of the dopant, it is concluded that the quadrupole moment in this direction plays the dominant role in the short-range overscreening effect. Insets in b) provide a visual representation of these angles.

ing. For the quadrupole moments of the hosts and dopants examined here (listed in Appendix C.1), overscreening ($V_{\mathrm{mQ}}^{\mathrm{dh}} + V_{\mathrm{mQ}}^{\mathrm{hd}} > 0$) occurs when the relative orientation is along the dopant normal axis (z direction) and, to a lesser degree, along the dopant short axis (y direction), as illustrated in Figure 5.3b. In contrast, alignment along the long axis (x direction) results in underscreening ($V_{\mathrm{mQ}}^{\mathrm{dh}} + V_{\mathrm{mQ}}^{\mathrm{hd}} < 0$). Notably, the calculated V_C in the NPB:F_6TCNNQ morphology follows the trend of z and y alignment. The angles between the host-dopant connecting vector relative to the long (γ), short (β), and normal (α) axes of the neighboring dopants are provided in Figure 5.3a. It shows that for the smallest separations, hosts and dopants tend to align in a stacked configuration, primarily along the z axis. (α is small.) As the host-dopant distance increases, the system transitions to a regime with equal probability of all relative orientations. This can be attributed to the anisotropy of both the host and dopant orientations. The shortest center-of-geometry distance, approximately 3.5 Å, is achieved when the relative orientation

is along the z-axis, whereas the closest approach in the underscreening scenario (alignment along the x-axis) is around 10 Å. Consequently, the V_C distribution at short host-dopant separations is dominated by $V_{mQ}^{dh}(zz)$,$V_{mQ}^{hd}(zz)$, $V_{mQ}^{dh}(yy)$ or $V_{mQ}^{hd}(yy)$ components. This leads to a reduction in $|V_C|$, resulting in a short-range overscreening effect.
To evaluate the significance of the overscreening effect, the distribution of distances between dopants and their nearest host is shown at the top of Figure 5.3b. Notably, 90% of dopants have at least one host within a distance $r < 6.7$ Å, a range where the overscreening effect is pronounced. This implies that 90% of ICTCs, which would traditionally be regarded as deep traps based on classical Coulomb interactions, instead exhibit relatively shallow ICTC binding energies.

5.3 Influence of the ICTC short-range overscreening on the charge carrier mobility

To demonstrate how the overscreening phenomenon can be leveraged to boost the charge carrier mobility, NPB doped with TCNQ, F_4TCNQ, or F_6TCNNQ (5 mol%) was investigated. The corresponding molecular structures are presented in AppendixC.4 and the spatial distribution of F_6TCNNQ within the NPB matrix is visualized in Figure 5.1a. For the dopants TCNQ, F_4TCNQ, and F_6TCNNQ, the Q_{zz} component of the quadrupole tensor is 31.56, 36.79, and 50.98 ea_0^2 respectively (Appendix C.1), highlighting the increasing trend of Q_{zz} with the number of F-atoms. In each of these three systems, the ICTC binding energy was calculated for over one million host-dopant pairs in five morphologies. The distance-resolved averages of these resulting distributions are shown by the colored lines in Figure 5.4b. A stronger overscreening effect is evident with higher Q_{zz}, meaning that as Q_{zz} grows, the magnitude of $|V_C|$ at short distances decreases.
To systematically investigate the response of V_C to changes in the quadrupole moment of the dopant, Q_{zz} in NPB:F_6TCNNQ was artificially adjusted within a range from -200 to $200\,ea_0^2$. In doing so, Q_{xx} and Q_{yy} were scaled in proportion to Q_{zz} to maintain a traceless quadrupole tensor (Figure 5.4a). The resulting distance-dependent averages of V_C were fitted using a third-order polynomial to smooth out minor morphology-related fluctuations, and are shown alongside the data for the real systems in Figure 5.4b. This procedure demonstrates how the modification of the quadrupole tensor of the dopant modifies the profile of $V_C(r)$. Even at $Q_{zz} = -200\,ea_0^2$, the short-range overscreening effect remains partially intact due to the unaltered quadrupole moment of the host (Equation 5.2). In these artificial NPB:F_6TCNNQ systems, the most likely distance between a dopant and its closest host is approximately 5.9 Å (see Figure 5.3b, top). Changing Q_{zz}, V_C at

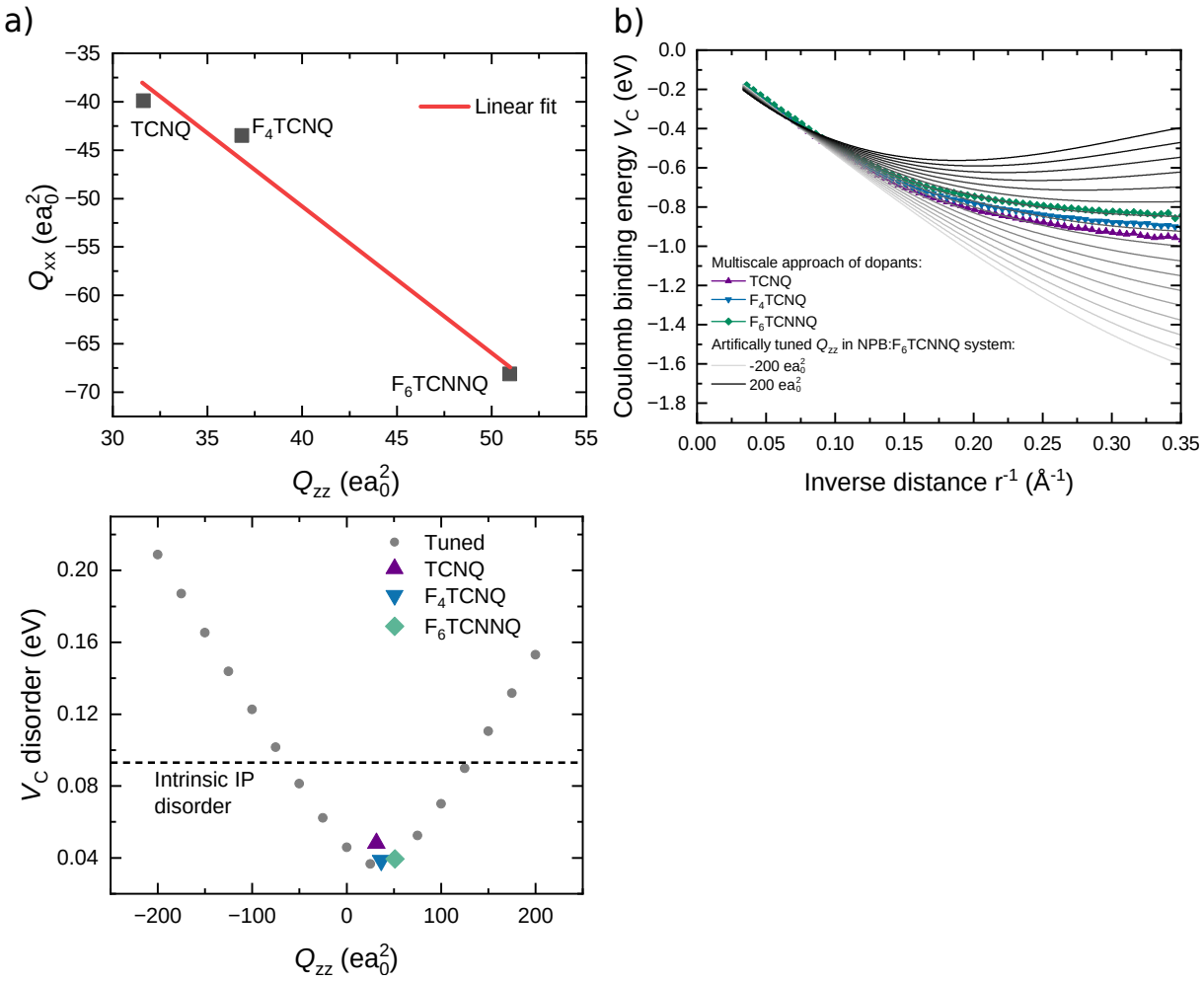

Figure 5.4: a) The quadrupole moment in x-direction of the TCNQ derivatives vs. the component in z-direction. The linear trend is used to keep the ratio of xx and zz component constant for artificial systems in which Q_{zz} is tuned. The y component is then determined so that the quadrupole tensor fullfills its tracelessness. b) The mean of V_C computed by Equation 5.1. The morphology NPB:F_6TCNNQ (5% DMR) is used for the artificial systems, the other components than zz of the dopant quadrupole tensor are adapted to ensure its tracelessness (see text). The real systems use morphologies created by Deposit with the respective dopant. The average Coulomb binding energy V_C increases with increasing Q_{zz}. At host-dopant distances with highest occurrence (NPB:F_6TCNNQ morphology) of 5.9 Å, V_C shows a variation of 0.4 eV in the given Q_{zz}-range. c) The standard deviation of the $V_\mathrm{C}(r)$ distribution at a distance $r = 5.9$ Å, i.e. the $V_\mathrm{C}(r)$ disorder.

this distance can be tuned by approximately 0.4 eV. The relative orientation and micro-electrostatics, particularly the quadrupole moments of the dopant and host molecules, give rise to the short-range overscreening effect. This effect reduces the ICTC binding energy of activated host-dopant pairs at short separations. Contrary to the intuitive assumption that shorter host-dopant distances result in stronger interactions, this effect suggests that reducing the spacing, for example by employing smaller host molecules, does not necessarily enhance Coulomb interactions. In fact, a dopant with a large positive quadrupole moment can further reduce $|V_C|$ at short distances. An increase in the effective dielectric constant at smaller separations between the host and dopant is analogous to the short-range overscreening effect. Figure 5.4c shows the $V_C(r)$ disorder (i.e. the standard deviation of the $V_C(r)$ distribution) at a distance $r = 5.9\,\text{Å}$ being the most probable distance of a dopant to its nearest host in a NPB:F_6TCNNQ morphology. The disorder even exceeds the intrinsic IP disorder of NPB for either low or high Q_{zz} - probably due to high anisotropy induced by high zz component of the quadrupole tensor.
The influence of the dopant quadrupole moment on the charge carrier mobility was examined on NPB doped with TCNQ, F_4TCNQ, and F_6TCNNQ. Kinetic Monte Carlo simulations were employed to model charge carrier transport and doping processes, allowing electrons and holes to hop between molecular sites according to Section 3.3. In particular, hole transport is governed by HOMO to HOMO transport, electron transport by LUMO to LUMO transport, and dopant activation involves electron transfer from the host HOMO to the dopant LUMO. LUMO to LUMO electron transfers were not considered in these simulations, as such processes become significant only at higher doping levels. To evaluate the influence of the dopant quadrupole tensor on the hole mobility, the NPB-based systems doped with TCNQ, F_4TCNQ, and F_6TCNNQ and systems of the morphology of NPB:F_6TCNNQ but a modified dopant Q_{zz} were analyzed. The kMC simulations incorporate material-specific input derived from the multiscale methodology. Transfer integrals were determined as described in 3.2.2 for 300 pairs of molecules using def2-SVP and BP86 as the basis set and functional. Further parameters are found in Appendix C.2. The difference of the host IP and the dopant EA is set to 0.2 eV in all systems (leveraging almost 100% dopant ionization) to decouple the effect of dopant ionization which is not part of this approach. For each combination of dopant and artificial system, five independent morphologies were deposited at a 5% dopant molar ratio. V_C was determined for these systems using Equation 5.2 (Figure 5.4). 20 independent kMC simulations were performed for each morphology.

In Figure 5.5a, the hole mobility is plotted as a function of Q_{zz}. The consistent rise in

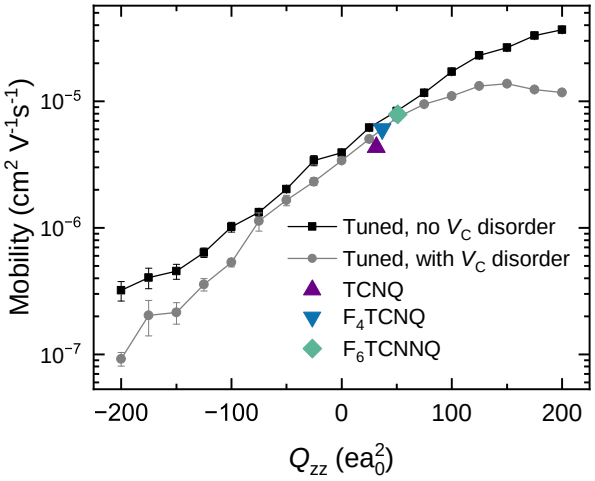

Figure 5.5: Hole mobility vs. Q_{zz} for artificial and real systems. The artificial systems are simulated with and without V_C disorder. The former shows variation over two orders of magnitude stating the importance of Q_{zz} as a design parameter of doped organic semiconductor layers. For small and large Q_{zz}, the V_C disorder increases to a value higher than the intrinsic IP disorder[144] (Figure 5.4b), leading to notable deviations in the mobilities. This reveals a dependence on the V_C disorder. The real system of NPB:TCNQ shows a lower mobility than the comparable artificial systems, most likely due to its higher disorder (Figure 5.4c). The error bars represent the standard error of the mean.

mobility with increasing Q_{zz} demonstrates that tuning Q_{zz} over the considered range enables adjusting mobility by approximately two orders of magnitude. In systems where the dopant quadrupole was artificially varied, the mobility was computed (i) by employing only the mean $V_\mathrm{C}(r)$ ("no V_C disorder") and (ii) by using a Gaussian distribution of V_C at each distance r (labeled "with V_C disorder" in Figure 5.5a). Taking into account the distribution of $V_\mathrm{C}(r)$, as opposed to the mean alone, notably reduces the mobility at higher $|Q_{zz}|$ since increasing the quadrupole component $|Q_{zz}|$ broadens the V_C distribution. This partly suppresses the short-range overscreening effect (the plateau between $Q_{zz} = 75$ and $200\,ea_0^2$, where mobility remains nearly constant despite growing Q_{zz}). These results, together with the role of ICTC binding energy disorder, underscore the importance of explicitly including microelectrostatics in theoretical models of organic semiconductors [145, 146]. In particular, the widths of the distance-resolved V_C distribution (often termed V_C disorder), which so far has been deduced primarily from experiments and shown to correlate with the activation energy [43] — is as critical as the HOMO/LUMO disorder. In general, the microelectrostatic features of organic-semiconductor molecules, in particular the dipole and quadrupole moments, drive phenomena such as mobility or open-circuit voltage losses in organic photovoltaics [21, 147, 148]. The list of microscopic driving mechanisms that influence macroscopic parameters can be expanded by the short-range overscreening effect.

Computational procedures to reliably evaluate ICTC binding energies are an essential requirement in the engineering of effective host-dopant material pairs. In the prototype host-dopant system considered, quadrupole-monopole interactions substantially reduce the binding energy via short-range overscreening. Harnessing this insight could facilitate the design of electronically doped semiconductors by strategically selecting quadrupole moments and forcing molecular orientations. Notably, adjusting the dopant quadrupole moment could modulate the mobility in doped films over orders of magnitude, which is in particular relevant for applications demanding high conductivity (e.g., organic lasers) or specific carrier-transport properties (e.g., transport layers in OLEDs or OSCs).

5.4 Experimental validation on BF-DPB and MeO-TPD

To validate the new V_C description and hence the influence of the short-range overscreening effect, the multiscale workflow with is conducted for the hole transport materials N,N,N',N'-Tetrakis(4-methoxyphenyl)benzidine (MeO-TPD) and N4,N4'-Bis(9,9-dimethyl-9H-fluoren-2-yl)-N4,N4'-diphenylbiphenyl-4,4'-diamine (BF-DPB), shown in Appendix C.4e and f. Morphologies were created according to the Deposit algorithm (3.1). Both host materials are doped with F_6TCNNQ in different DMRs (see Appendix C.3 for the exact numbers). For each DMR, two morphologies were created.

For all pairs separated by less than 30 Å, V_C is obtained using Equation 5.1 together with the quadrupole tensors given in Appendix C.1. The mean and standard deviation of V_C (with the latter describing V_C disorder) are shown in Figure 5.6a, alongside $V_{\mathrm{C,\,mm}}$ (solid lines), which represents the interaction of oppositely charged point charges in a dielectric medium of permittivity ϵ_r (derived as described in Section 3.2.3). At large separations, $V_{\mathrm{C,\,mm}}$ matches V_C, but at shorter distances the short-range overscreening effect appears, reducing the magnitude of $|V_\mathrm{C}|$. Both BF-DPB:F_6TCNNQ and MeO-TPD:F_6TCNNQ yield comparable V_C; however, their ordering differs between $V_\mathrm{C}(r)$ and $V_{\mathrm{C,\,mm}}$, indicating that the orientation and microelectrostatics of individual host-dopant pairs outweigh the macroscopic screening by ϵ_r. Notably, BF-DPB:F_6TCNNQ exhibits a V_C disorder at short distances (about $d = 6$ Å) approximately three times larger than MeO-TPD:F_6TCNNQ (0.15 eV vs. 0.05 eV), and thus surpasses the intrinsic HOMO-level disorder of BF-DPB itself. Figure 5.6b presents the histograms of the distances from the dopant to the closest host, revealing that the dopants in the MeO-TPD:F_6TCNNQ blend are statistically closer to their hosts. At the most frequent dopant-host spacing, V_C in both systems is fairly similar ($V_\mathrm{C} = -0.551$ eV vs. $V_\mathrm{C} = -0.666$ eV, BF-DPB:F_6TCNNQ vs. MeO-TPD:F_6TCNNQ),

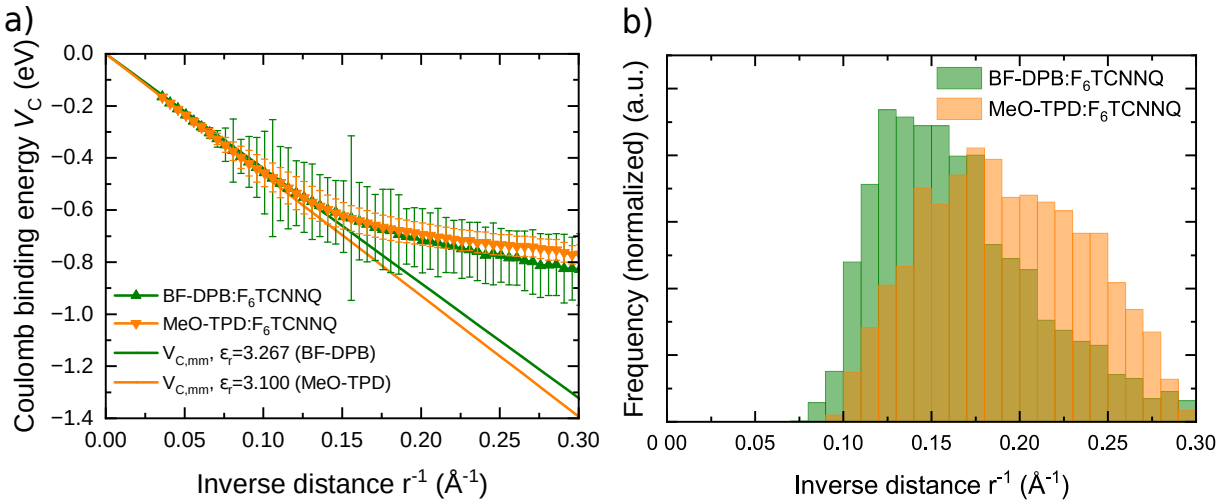

Figure 5.6: a) Coulomb binding energy V_C of BF-DPB and MeO-TPD doped with F_6TCNNQ vs. the inverse pair distance. For reference, V_C of oppositely charged point-charges with the dielectric permittivity ϵ_r of the systems. These systems exhibit the short-range overscreening. For small distances this changes the order of the systems in terms of binding energy magnitude. The error bars represent the standard deviation of the V_C distribution, *i.e.* the V_C disorder. The BF-DPB system shows a V_C disorder four times as large as the V_C disorder of MeO-TPD. b) Histogram of the distances from dopants to their nearest host in BF-DPB and MeO-TPD doped with F_6TCNNQ. The histograms are area-normalized. The expectation value of the distance in BF-DPB is larger than in MeO-TPD leading to a smaller overscreening effect at most probable host-dopant distances.

in contrast to $V_{C,\,mm}$ ($V_{C,mm} = -0.532\,eV$ vs. $V_{C,mm} = -0.817\,eV$). Hence, the short-range overscreening mechanism acts to "flatten" V_C and mitigates the material-to-material variation in these systems.

Based on the distributions of V_C, kMC simulations are used to simulate the conductivity of BF-DPB:F_6TCNNQ and MeO-TPD:F_6TCNNQ depending on different dopant concentrations, and compare the results to experimental data. In these simulations, because of high dopant molar ratios, not only hole transport but also electron transport in the LUMO are considered. The transfer integrals were determined for 300 pairs of molecules with DFT (basis set def2-SVP and functional BP86). The concentration-dependent shifts in IP_{host} and EA_{dop} were incorporated, reflecting notable sensitivity to DMR (Section 5.5). Other precomputed properties necessary to calculate the charge hopping rates are shown in C.2. Since the aim of these simulations is to verify the V_C-based modeling approach, the intrinsic disorder of the host hole-transport level is fitted to experimental mobilities of pure hosts (Appendix C.2 and C.3). For each DMR, two distinct morphologies were generated, and 20 independent kMC simulations were performed for each one.

Figure 5.7 presents the mean and standard error of the simulated conductivity together with the experimental results [149] in panel a and the corresponding simulated mobility

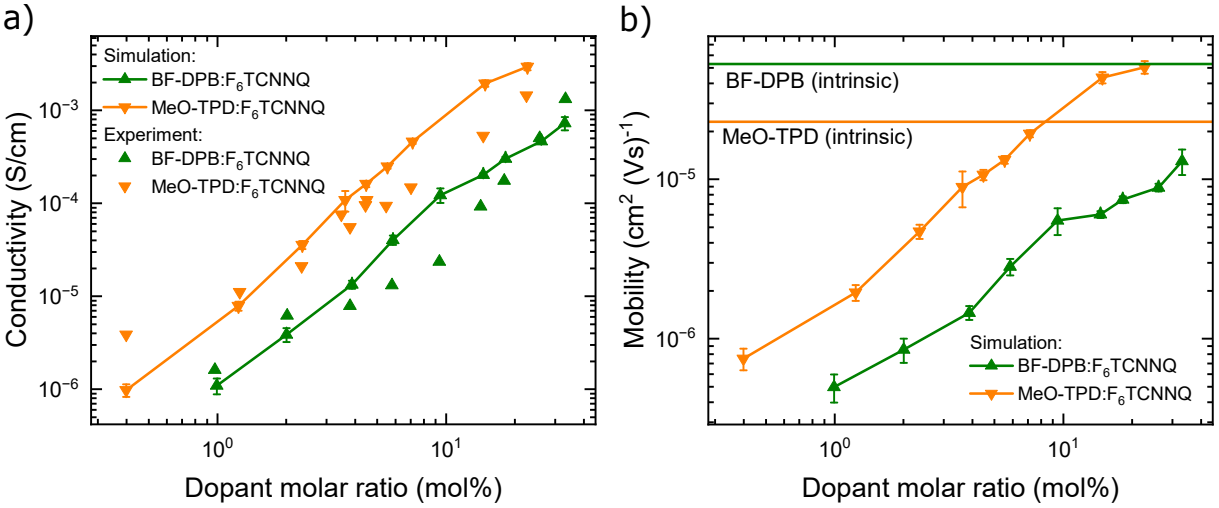

Figure 5.7: a) Simulated conductivities of BF-DPB and MeO-TPD doped with F_6TCNNQ compared with experimental data. The simulations reproduce experimentally observed data. b) Mobility of BF-DPB and MeO-TPD without doping (intrinsic) and doped with F_6TCNNQ. MeO-TPD:F_6TCNNQ shows a higher mobility despite the intrinsic mobility of BF-DPB being higher ($\mu = 5.7 \cdot 10^{-5}\,\mathrm{cm}^2/(\mathrm{Vs})$ vs. $\mu = 2.3 \cdot 10^{-5}\,\mathrm{cm}^2/(\mathrm{Vs})$). The main reason promoting this difference lies in the four times higher V_C disorder in BF-DPB:F_6TCNNQ than MeO-TPD:F_6TCNNQ. This reduces the mobility and conductivity of BF-DPB:F_6TCNNQ compared to MeO-TPD:F_6TCNNQ and leads to the agreement between the experimental and simulated conductivity. The error bars represent the standard error of the mean.

together with the intrinsic mobility in panel b. The dependence of the conductivity on the DMR is reproduced accurately for both material systems, and the absolute conductivities also show good agreement with the measurements. Moreover, the discrepancy between BF-DPB:F_6TCNNQ and MeO-TPD:F_6TCNNQ observed experimentally is reproduced, demonstrating a higher conductivity for MeO-TPD across the entire DMR range. At first glance, this outcome appears counterintuitive because the intrinsic hole mobility of MeO-TPD ($\mu_h = 2.3 \cdot 10^{-5}\,\mathrm{cm}^2/(\mathrm{Vs})$) is lower than the mobility of BF-DPB ($\mu_h = 5.7 \cdot 10^{-5}\,\mathrm{cm}^2/(\mathrm{Vs})$) [149], both semiconductors have comparable bulk densities, and the ionization fraction of dopants in both systems remains high. Specifically, in the low and medium doping range (DMR $< 10\,\%$), the fraction of ionized dopants in MeO-TPD exceeds $90\,\%$, while in BF-DPB it is above $75\,\%$ (Figure 5.9).

One reason is the distance-dependent V_C disorder (Figure 5.6a). In BF-DPB it can exceed the V_C disorder of MeO-TPD by a factor of up to four at certain distances, and the additional disorder surpasses the intrinsic HOMO disorder of BF-DPB itself. Consequently, it is a substantial contribution to the total disorder[14] and lowers the mobility of the doped BF-DPB below the mobility of the doped MeO-TPD, reversing the order implied by the intrinsic mobilities. Comparisons with a purely classical point-charge treatment

of $V_C(r)$ [14, 42, 150] in Appendix C.1 show very similar conductivity for the two doped semiconductors, thus failing to reproduce the experimental observation that doped MeO-TPD has higher conductivity. This highlights the necessity of incorporating short-range overscreening into doping-induced electrostatics, since the disorder introduced by realistic microelectrostatic effects distinguishes these two doped semiconductors.

In summary, the width of the ICTC binding energy distribution at a given distance can be as influential as the conventional HOMO/LUMO disorder. In the current analysis, a strong material dependence of $V_C(r)$ disorder can invert the relative conductivity of BF-DPB and MeO-TPD upon doping. The excellent match to experimental conductivity data of both semiconductors confirms the importance of including this disorder in the description of charge transport in doped organic semiconductors. The multiscale protocol outlined here determines the mean and variance of V_C while taking into account molecular orientations and polarization on molecular length scales. Since ICTC binding energies directly influence doping performance, this approach provides an efficient and robust way to optimize the properties of doped organic semiconductors *in silico*.

5.5 Influence of the dopant concentration on the dopant ionization

This section examines how the dopant concentration affects the dopant ionization ratio, which strongly influences the charge carrier transport in a doped layer. This also explains why, in the previous section, the difference between the host IP and the dopant EA was not fixed but instead calculated in dependence of the dopant molar ratio.
In p-doped organic semiconductors, the ionization rate of the dopant depends on the energy difference between the host IP and the dopant EA (Equation 3.17). This offset energy, $\Delta_{\mathrm{IP_h,EA_d}} = \mathrm{IP_{host}} - \mathrm{EA_{dopant}}$, is influenced by both, properties of standalone host/dopant molecules and the surrounding environment. Many models assume a fixed $\Delta_{\mathrm{IP_h,EA_d}}$, ignoring its dependence on dopant concentration [14, 39]. However, studies show that the energy levels in donor-acceptor systems shift depending on the mixing ratio [151, 152].

To analyze the implications of a fixed $\Delta_{\mathrm{IP_h,EA_d}}$, kMC simulations are conducted on the system BF-DPB:F_6TCNNQ. The underlying parameters are the same as in Section 5.4, except that $\mathrm{IP_{host}}$ and $\mathrm{EA_{dopant}}$ are kept constant. For each DMR, two distinct morphologies were generated, and 40 independent kMC simulations were performed for each morphology.

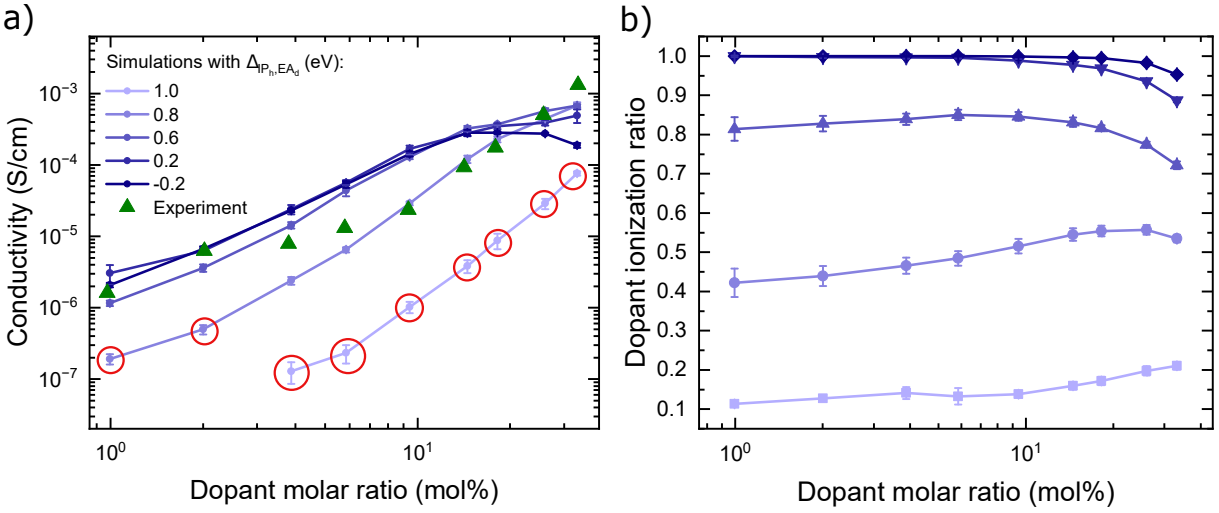

Figure 5.8: a) Mean and standard error of the conductivity of BF-DPB:F_6TCNNQ systems with fixed Δ_{IP_h,EA_d} compared to experimental data [149]. Good agreement is obtained when a smaller Δ_{IP_h,EA_d} is used at low dopant molar ratio (DMR) and a larger Δ_{IP_h,EA_d} at high DMR, indicating that Δ_{IP_h,EA_d} increases with DMR. b) Corresponding DIR for different Δ_{IP_h,EA_d}.

Figure 5.8a shows the simulated conductivity of BF-DPB:F_6TCNNQ. The experimental conductivity [149] is shown for reference. Simulations with only partly converged replicas (3 day convergence time limit) are marked by a red circle describing an upper limit since simulations with higher mobility generally converge faster. Up to a DMR of 10 mol%, decreasing Δ_{IP_h,EA_d} increases conductivity. Interestingly, this trend inverts for higher DMR. At low DMR, the experimental data align with low Δ_{IP_h,EA_d} and at high DMR, the experimental data align with high Δ_{IP_h,EA_d}. Between these extremes, it falls within the range of simulated conductivities of low and high Δ_{IP_h,EA_d}. The conductivity of hole transport is $\sigma = en\mu_h$, with e and E as the elementary charge and electric field, kept constant throughout all simulations. n and μ_h are the charge carrier density and hole mobility, both being influenced by the dopant ionization ratio (DIR), which is shown in Figure 5.8b. A large Δ_{IP_h,EA_d} of 1 eV exhibits only a DIR$<20\,\%$, often referred to as "weak dopants". At the condition $V_C < -\Delta_{IP_h,EA_d}$, dopants are referred to as "strong dopants" [39]. For a somewhat similar class of materials, the charge-transfer salts, this condition corresponds to the point of turnover where the conductivity suddenly increases by an order of magnitude [153]. In organic semiconductors, however, their inherent disorder and distinct charge transport mechanisms make this turnover less abrupt but more gradual and steady. The greatest gradients of DIR with respect to Δ_{IP_h,EA_d} correspond to the point $\Delta_{IP_h,EA_d} = V_C = 0.7\,eV$.

At low DMR, the mobility in Appendix C.5 shows an increase with decreasing Δ_{IP_h,EA_d}. A large Δ_{IP_h,EA_d} activates only a few dopants, which act as Coulomb traps and cause lower

mobilities than the intrinsic mobility. A lower $\Delta_{\mathrm{IP_h,EA_d}}$, leads to more activated dopants, filling the tail states of the HOMO of the host and leading to smaller distances between Coulomb traps and thus enables hopping from one Coulomb trap to another, increasing the mobility [14, 154]. Thus, n and μ_h both explain the rise in conductivity at low DMR. At high DMR, the saturating or even decreasing conductivity upon decreasing $\Delta_{\mathrm{IP_h,EA_d}}$ is explained by the saturating/decreasing mobility. Lower $\Delta_{\mathrm{IP_h,EA_d}}$ increases the number of activated dopants, *i.e.*, charge carriers, increasing the energetic disorder. In addition, the number of unoccupied host molecules decreases, reducing the available percolation pathways for transport, and thereby lowering the mobility.

In the following a quantum embedding and kMC simulations are described which were used to compute the influence of $\Delta_{\mathrm{IP_h,EA_d}}$ on the ionized dopant fractions in the systems BF-DPB:F_6TCNNQ and MeO-TPD:F_6TCNNQ. With the procedure described in 3.2.3, $\Delta_{\mathrm{IP_h,EA_d}}$ is simulated for embedded molecules in the systems BF-DPB:F_6TCNNQ and MeO-TPD:F_6TCNNQ with different DMR. This requires (1) the $\mathrm{IP_{host}}$ and $\mathrm{EA_{dopant}}$ of vacuum-equilibrated molecules and (2) the polarization energies $P^{(+)}$ of the embedded host and $P^{(-)}$ of the embedded dopant. The former does not depend on the DMR and is computed only once for each type of molecule. The polarization energy depends on the polarizing environment of the embedded molecule of interest, and so it depends on the morphology and the DMR. Morphologies with low, medium and high DMR are chosen. In BF-DPB:F_6TCNNQ, the DMRs are 0.99, 5.85, and 33.03 mol%; in MeO-TPD:F_6TCNNQ, they are 0.40, 5.54, and 22.69 mol%. For each morphology, $\mathrm{IP_{host}}$ and $\mathrm{EA_{dopant}}$ are calculated for five molecules.

Figure 5.9a shows the vacuum values of $\Delta_{\mathrm{IP_h,EA_d}}$ (calculated for isolated host and dopant molecules using GW) and the corresponding embedded values obtained by correcting the vacuum values with the polarization energy (simulations by Artem Fediai). It is observed that for both BF-DPB:F_6TCNNQ and MeO-TPD:F_6TCNNQ, $\Delta_{\mathrm{IP_h,EA_d}}$ of embedded host and dopant is at least 0.9 eV smaller than the value for host and dopant in vacuum. Increasing the DMR reduces the polarization energy, hence increasing $\Delta_{\mathrm{IP_h,EA_d}}$. Between the lowest and highest DMR, the $\Delta_{\mathrm{IP_h,EA_d}}$ increases by more than 0.2 eV. Increasing the dopant concentration changes the polarizing environment, which, in turn, changes the energy levels of IP and EA. In [151], a shift in IP by the addition of an acceptor molecule was attributed to the difference in the electrostatic moment and the polarization of the host and acceptor molecule. In [40] a strong dependence of the dopant's energy levels on its host medium was observed.

A linear interpolation of these $\Delta_{\mathrm{IP_h,EA_d}}$ yields the values shown in Appendix C.3. These

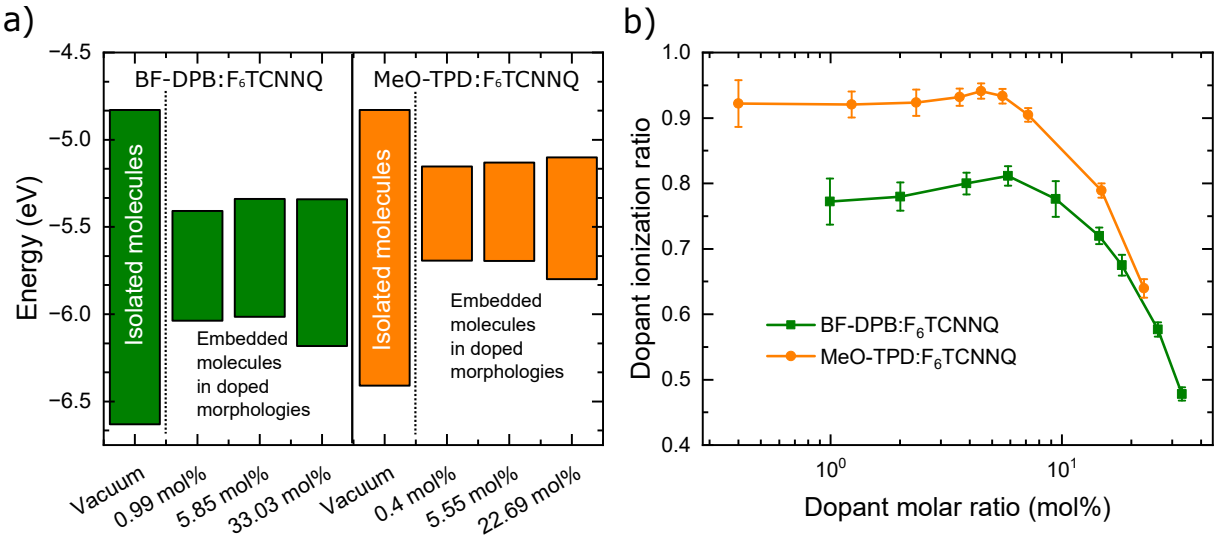

Figure 5.9: a) $\Delta_{\mathrm{IP_h,EA_d}}$ for BF-DPB and MeO-TPD doped with F_6TCNNQ: The lower edge represents the IP of the host, while the upper edge corresponds to the EA of F_6TCNNQ. The energy levels are shown for vacuum conditions and for an embedded host/dopant pair in low, medium, and highly doped morphologies. A significant shift is observed when transitioning from vacuum to embedded conditions, which can be attributed to the embedding polarization energy. b) Higher DMRs result in an increased $\Delta_{\mathrm{IP_h,EA_d}}$, which in turn reduces the dopant ionization ratio. The error bars represent the standard deviation.

were used in the kMC simulations in Section 5.4. Figure 5.9b shows the corresponding DIRs. Generally, BF-DPB:F_6TCNNQ has a lower DIR due to its larger $\Delta_{\mathrm{IP_h,EA_d}}$. The increase in the dopant ionization ratio when the dopant concentration increases to a medium dopant molar ratio of DMR= 6% is explained by the energetic disorder of the system [14]: Upon doping, the doping-induced disorder increases the broadening of the host HOMO and dopant LUMO energetic distributions, making the dopant ionization ratio energetically more favorable. Additionally, a higher structural disorder in more doped morphologies could broaden the energetic distributions. The decrease in the dopant ionization ratio at high dopant concentrations is explained by the larger $\Delta_{\mathrm{IP_h,EA_d}}$.

6 Determination of the polaron yield efficiency in organic dispersions from the deconvolution of UV-Vis absorbance spectra

Recently, efforts have been made to stabilize organic nanoparticles by electronic p-doping instead of using surfactants [13, 73]. A high polaron yield efficiency, *i.e.*, the number of charges transferred from the dopant to the host versus the maximum number available for the transfer, increases the nanoparticle surface charge. However, the activation of p-dopants is an intricate effect depending on the host IP, dopant EA, the integer charge transfer binding energy, and the polarizable environment (Section 2.1.4), which makes the PYE difficult to predict from the individual parameters of the material, but requires experimental characterization. UV-Vis, being a versatile and facile method to determine PYE, is commonly used in layers. Either the polaron absorbance is evaluated, or the superimposed absorbance is fitted by individual contributions [155]. However, both methods require information: the polaron molar extinction coefficient or the pure host (neutral, cation) absorbance, which are generally not known for new materials in dispersions. This section elaborates on a new approach using the deconvolution of the doped dispersion absorbance, a superposition of the host (neutral, cation) and dopant (neutral, anion) absorbance. The method uses the isosbestic points (IBPs) of a cobalt salt bis(2,6-di(1H-pyrazol-1-yl)pyridine)cobalt(III) tri[bis(trifluoromethane)sulfonimide ($CoTFSI_3$) upon doping and its concentration in the dispersion.
By doping the polymer J71, $CoTFSI_3$ is then used to stabilize dispersions to fabricate OSCs.

6.1 UV-Vis deconvolution method

The deconvolution of the superimposed absorption spectrum of the dispersion is based on the IBPs of the dopant. In this study, $CoTFSI_3$ was chosen due to its high doping strength, with a reduction potential of 0.58 V vs. Fc^+/Fc [156], compared to F_4TCNQ at 0.1 V [157]. In addition, $CoTFSI_3$ exhibits several IBPs. The method is applied to dispersions using the semiconductor J71 as the host.

6.1.1 Isosbestic points of the absorbance of the dopant

If species A changes into another species B by a chemical reaction, and they have overlapping absorbances, then IBPs appear in the spectrum [158]. At these points, the absorbance depends only on the combined concentration of A and B and not on the ratio between them. This is a direct consequence of the Beer-Lambert law. It is important that no third species absorbs at the wavelength of the IBP. An organic semiconductor that is electronically doped can undergo a transition of one species (neutral) to another (charged) and, therefore, exhibit one or several IBPs as the total concentration of neutral plus charged species prevails. Similarly, dopants that change their charged state upon doping also show IBPs if the respective absorbances overlap. The absorbance at the IBPs of the dopants is only governed by the total dopant concentration, independent of the ionization ratio.

To measure the IBPs of the dopant $CoTFSI_3$ upon ionization to $CoTFSI_3^{-1}$, the doping process was mimicked by mixing $CoTFSI_3$ and $Li^+CoTFSI_3^-$ in CH_3CN and measuring its absorbance. $CoTFSI_3$ is commercially available and was dissolved in CH_3CN ($3.78 \cdot 10^{-5}\,\mathrm{mol\,L^{-1}} = 50\,\mathrm{mg\,L^{-1}}$). $Li^+CoTFSI_3^-$ can be produced by combining equal molar amounts of commercially available (2,6-di(1H-pyrazol-1-yl)pyridine)cobalt(II) di[bis(trifluoromethane)sulfonimide] ($CoTFSI_2$) and Li^+TFSI^-. Li^+ has previously served as the counterion in measurements involving the anionic forms of p-type dopants [157]. Importantly, the molar extinction coefficient of a species is influenced by the solvent, and therefore, the IBPs vary among different solvents.

Figure 6.1 shows the molar extinction coefficients ε of mixtures of $CoTFSI_3$ and $Li^+CoTFSI_3^-$ at different ratios, clearly showing five IBPs between 252 and 345 nm. IBPs only occur for a transition between two components (here, $CoTFSI_3$ and $CoTFSI_3^-$). If a third component (e.g. Li^+) absorbs, the ε would not coincide for varying ratios in IBPs. Consequently, the fact that all spectra intersect at the same points makes it unlikely that an additional component absorbs within the examined wavelength range. Across all wavelengths lying between the IBPs, the molar extinction coefficient varies with the proportion of $CoTFSI_3$ and $Li^+CoTFSI_3^-$. Table 6.1 shows the IBPs of $CoTFSI_3$ upon ionization.

6.1.2 Superimposed dispersion absorbance

When strong acceptors are introduced into the dispersion at a concentration of c_{dopant}, electrons move from the host to the dopant molecules (integer charge transfer), creating

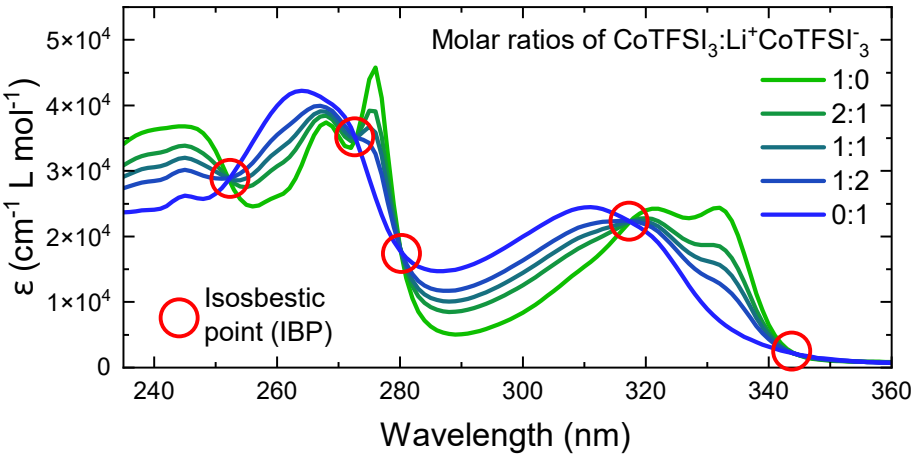

Figure 6.1: Molar extinction coefficient ε of the dopant $CoTFSI_3$ upon ionization in CH_3CN. The anionic species are counter-charged by Li^+. The molar concentration refers to the number of $CoTFSI_3$ species. At the IBPs the molar extinction coefficient coincides and shows the same value independent of the ionization ratio. In the spectral regimes between the IBPs, ε depends on the ionization ratio.

Table 6.1: Measured IBPs of $CoTFSI_3$ upon ionization to $CoTFSI_3^-$ in CH_3CN by extracting the points of intersection of Figure 6.1. Values are given as mean ± standard deviation.

Wavelength (nm)	ε (L cm^{-1}mol^{-1})
344.4 ± 0.3	$(2.1 \pm 0.1) \cdot 10^3$
317.5 ± 0.1	$(2.229 \pm 0.004) \cdot 10^4$
280.1 ± 0.1	$(1.78 \pm 0.03) \cdot 10^4$
272.8 ± 0.1	$(3.51 \pm 0.01) \cdot 10^4$
252.1 ± 0.1	$(2.887 \pm 0.008) \cdot 10^4$

positive charges (polarons) on the host with a concentration of c^+_{host}. The PYE of the doped dispersions is then defined as

$$\text{PYE} = \frac{c^+_{\text{host}}}{c_{\text{dopant}}}. \tag{6.1}$$

Therefore, determining the PYE necessitates knowing the concentration of positive charges present on the host. In the absence of charge transfer involving any additional species, in particular, that no reaction with the dispersion medium occurs, c^+_{host} is identical to the concentration of ionized (anionic) dopants, c^-_{dopant}, and the PYE is equal to the dopant ionization ratio (DIR).

$$\text{PYE} = \frac{c^+_{\text{host}}}{c_{\text{dopant}}} = \text{DIR} = \frac{c^-_{\text{dopant}}}{c_{\text{dopant}}}. \tag{6.2}$$

Qualitative indications of p-doping in organic semiconductors using strong molecular acceptors appear in the absorbance spectra, where a characteristic polaron band develops, indicating the presence of c^+_{host}. However, without calibration, the intensity of this band cannot yield quantitative information about c^+_{host} and, consequently, the PYE. Instead, in the following analysis, c^-_{dopant} will be determined by deconvoluting the absorbance spectrum of the doped dispersion. Based on Equation 6.2 c^-_{dopant} enables the calculation of the DIR and, given the absence of side reactions discussed earlier, the PYE as well. The concentration of a species c can be estimated from its absorbance $A(\lambda)$ according to the Lambert-Beer law:

$$A(\lambda) = c \cdot l \cdot \varepsilon(\lambda), \tag{6.3}$$

l denotes the optical path length of the measurement, corresponding to the path length through the cuvette (1 cm), and $\varepsilon(\lambda)$ represents the molar extinction coefficient of the respective species. If single-electron integer charge transfer takes place between the host and the dopant, the dispersion comprises four species: the neutral host, the positively charged host, the neutral dopant, and the dopant anion. Each of these species contributes to the overall absorbance of the dispersion. By separating their individual contributions through spectral deconvolution, the absorbance of the dopant anion, $A^-_{\mathrm{dopant}}(\lambda)$, can be determined, and consequently the concentration of dopant anions, c^-_{dopant}.
First, the absorbance spectra of the doped host dispersions are decomposed into contributions from the host and the dopant using the IBPs of the dopant. Figure 6.2 illustrates the total absorbance $A_{\mathrm{total}}(\lambda)$ of a J71 dispersion doped with $CoTFSI_3$ (60 mol%). Because the dopant absorbance at the IBPs does not depend on its ionization state, the total absorbance at these points can be separated into the contributions of the dopant, Adopant(λ) (neutral and anionic) and the host, $A_{\mathrm{host}}(\lambda)$ (neutral and cationic). As the total dopant concentration c_{dopant} in the dispersion is known from its preparation, the absorbance of the dopant in IBPs can be calculated using the molar extinction coefficients shown in Figure 6.1 and Equation 6.3. Subtracting the dopant absorbance (indicated by arrows in Figure 6.2a) from the total absorbance $A_{\mathrm{total}}(\lambda)$ yields the absorbance of both the neutral and cationic host, $A_{\mathrm{host}}(\lambda)$ (circles in Figure 6.2a), at the IBPs. Between the IBP wavelengths, the host absorbance is approximated by linear interpolation. This procedure provides the separated absorbance spectra $A_{\mathrm{host}}(\lambda)$ and $A_{\mathrm{dopant}}(\lambda)$.
Second, $A_{\mathrm{dopant}}(\lambda)$ is decomposed into $A^-_{\mathrm{dopant}}(\lambda)$ and $A^0_{\mathrm{dopant}}(\lambda)$, which then is used to transform using the Lambert-Beer law (Equation 6.3) to:

$$A_{\mathrm{dopant}}(\lambda) = A^-_{\mathrm{dopant}}(\lambda) + A^0_{\mathrm{dopant}}(\lambda) = c^-_{\mathrm{dopant}} \cdot l \cdot \varepsilon^-_{\mathrm{dopant}}(\lambda) + c^0_{\mathrm{dopant}} \cdot l \cdot \varepsilon^0_{\mathrm{dopant}}(\lambda), \tag{6.4}$$

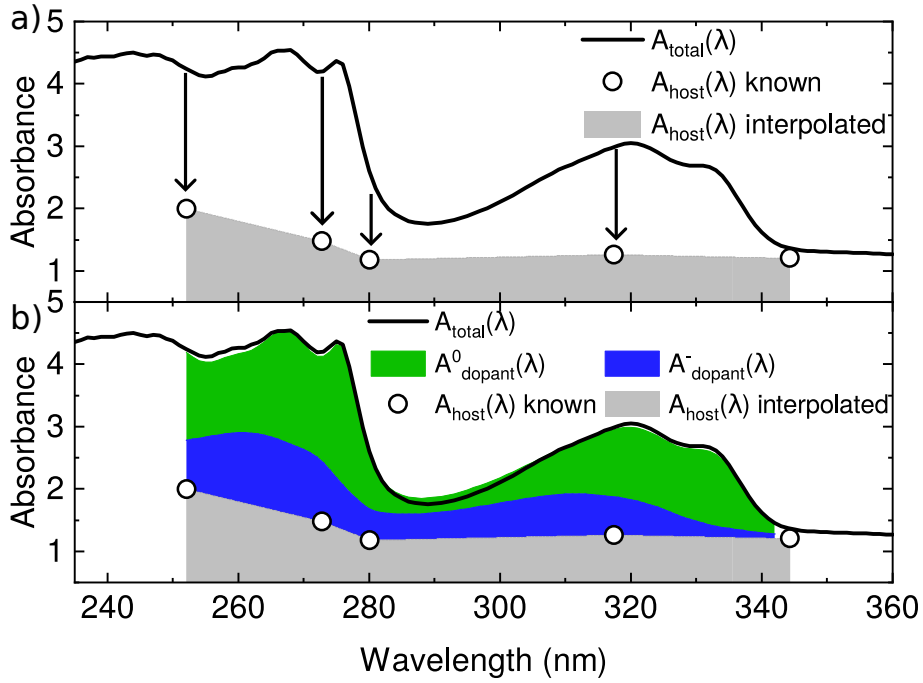

Figure 6.2: a) The absorbance of a p-doped J71 dispersion, A_{total}, is a superposition of the absorbance contributions from the host species (neutral and cationic) and the dopant species (neutral and anionic). At the dopant IBPs, the absorbance contribution of the dopants can be determined based on their known concentration, allowing for the extraction of the host absorbance. A linear interpolation is employed to estimate the absorbance of the host in the wavelength range between the IBPs. b) By subtracting the interpolated host absorbance from the total absorbance, the dopant absorbance is isolated across the entire spectral range. This allows for the disentanglement of contributions from neutral $CoTFSI_3$ and its anionic form, $CoTFSI_3^-$.

Equation 6.4 shows that $A_{\text{dopant}}(\lambda)$ depends on the concentrations of the anionic dopant c^-_{dopant}, and neutral dopant c^0_{dopant}. According to the definition of DIR, it applies:

$$c^-_{\text{dopant}} = \text{DIR} \cdot c_{\text{dopant}}, \tag{6.5}$$

$$c^0_{\text{dopant}} = (1 - \text{DIR}) \cdot c_{\text{dopant}}. \tag{6.6}$$

The insertion of Equation 6.5 and Equation 6.6 into Equation 6.4 and solving for c^-_{dopant} yields an estimator for c^-_{dopant}:

$$\hat{c}^-_{\text{dopant}}(\lambda) = \frac{A_{\text{dopant}}(\lambda) - c_{\text{dopant}} \cdot l \cdot \varepsilon^0_{\text{dopant}}(\lambda)}{l \cdot (\varepsilon^-_{\text{dopant}}(\lambda) - \varepsilon^0_{\text{dopant}}(\lambda))}. \tag{6.7}$$

Using this relation (the detailed derivation of the transformation is presented in Appendix C.0.1), c^-_{dopant} can be derived from the experimental measurements, where c_{dopant} denotes the known total dopant concentration. This procedure appears to introduce a

wavelength dependence of $\hat{c}^-_{\mathrm{dopant}}$ and consequently of the DIR. In an ideal case, $\hat{c}^-_{\mathrm{dopant}}$ should be consistent across all wavelengths. However, in practice, variations arise due to the interpolation of the host absorbance $A_{\mathrm{host}}(\lambda)$, as discussed above. To approximate the actual c^-_{dopant} in the dispersion, $\hat{c}^-_{\mathrm{dopant}}$ is averaged over the entire wavelength range. For the calculation of the standard error, each interpolated regime between the IBPs is considered a separate measurement. It is noted that $\hat{c}^-_{\mathrm{dopant}}(\lambda)$ cannot be obtained at the IBP, since the neutral and anionic dopant signals are indistinguishable there.

6.1.3 PYE in J71 dispersions

A set of J71 dispersions was prepared for the application of the UV–Vis deconvolution technique. J71 was first dissolved in $CHCl_3$ ($0.5\,\mathrm{g\,L^{-1}}$) and stirred under ambient conditions for more than 20 minutes. The dopant $CoTFSI_3$ was initially dissolved in CH_3CN ($30\,\mathrm{g\,L^{-1}}$) at room temperature. Lower dopant concentrations, used to obtain reduced doping ratios, were prepared by diluting this stock solution with CH_3CN. The J71 solutions were subsequently doped by adding the appropriate volume of the $CoTFSI_3$ solution in CH_3CN. The resulting p-doped semiconductor solutions were briefly heated (50 °C, 2–3 min). Organic nanoparticle dispersions were produced by nanoprecipitation following established procedures from the literature [73]. In particular, $CHCl_3$ solutions of J71 ($0.5\,\mathrm{g\,L^{-1}}$, 0.5 mL) and the dopant at the desired concentration were nanoprecipitated into the nonsolvent CH_3CN (3.5 mL) under stirring in a beaker. During injection, the nonsolvent was illuminated with a COB LED. The dispersions were then heated (50 °C, 30–60 min) until $CHCl_3$ had completely evaporated and the dispersion volume reached 1 mL. Finally, an Eppendorf MiniSpin plus was used to remove agglomerates by centrifugation (14,500 rpm, 2 min).

Figure 6.3a shows the nanoparticle sizes of the respective dispersions after nanoprecipitation and after volume reduction. Toward the mid-doping (30-40 mol%) regime, a minimum of the nanoparticle sizes is visible. Generally, in all dispersions, the nanoparticles were small, enabling UV-Vis measurements and neglecting the influence of scattering effects on particles.

Figure 6.3b shows the respective UV-Vis absorbance spectra of the dispersions at a concentration of $62.5\,\mathrm{mg\,L^{-1}}$. Upon doping, the spectral regime in which the dopant absorbs increases, the main peak of J71 decreases, and in the near-infrared, a polaron band emerges. This can be explained by the standard polaron band model, which predicts a change in the density of states within the $\pi - \pi^*$ gap. The original absorption transitions become less frequent, leading to a decrease in the main peak. The new sub-gap states

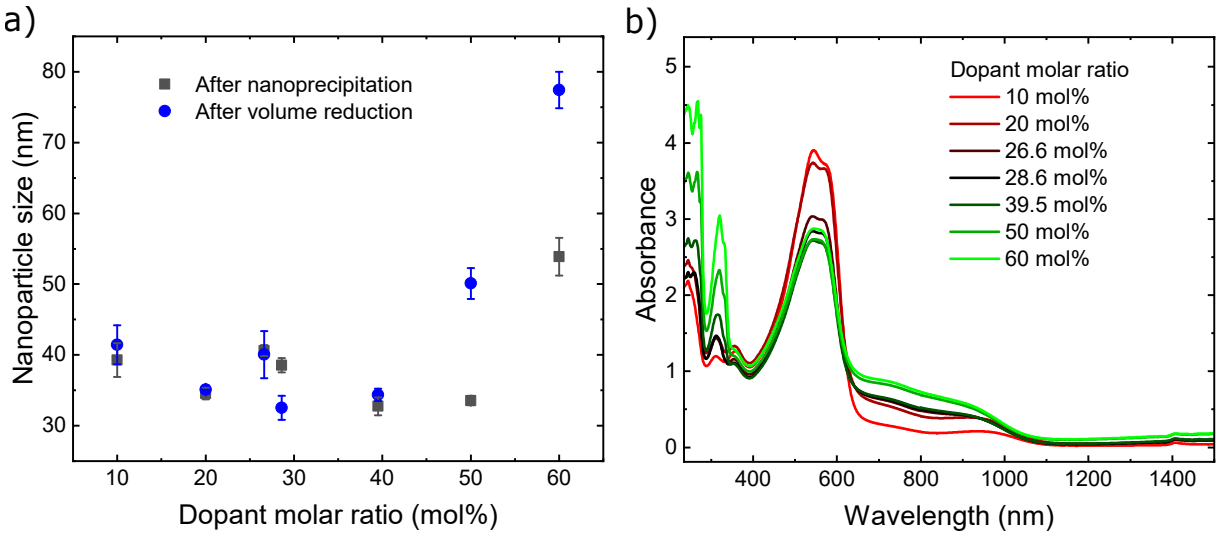

Figure 6.3: Characteristics of J71 dispersions doped with $CoTFSI_3$. a) Nanoparticle sizes after nanoprecipitation and volume reduction. A trend toward smaller nanoparticles is observed in the mid-DMR (30-40 mol%) regime, reaching a minimum at 39.5 mol%. The significant growth in the nanoparticle size between the two measurements for high DMRs of 50 and 60 mol% indicates that these dispersions are less stable compared to those with lower DMRs. The error bars represent the standard deviation of separate DLS measurements on the same sample. b) Absorbance spectra of the dispersions, which represent a superposition of contributions from the host (both neutral and cationic) and $CoTFSI_3$ (both neutral and anionic). Upon adding the dopant, an increased absorbance is observed in its primary absorbance regime below 400 nm. In addition, at wavelengths larger than 650 nm, a polaron band emerges.

absorb at longer wavelengths, resulting in polaron bands.

In Appendix C.6, it is shown that the dopant $CoTFSI_3$ does not react with any of the solvents during the nanoprecipitation process. Hence, the deconvolution of the absorbance spectra allows quantification of the PYE of J71 dispersions doped with $CoTFSI_3$ at different total dopant concentrations c_{dopant}.

Figure 6.4 presents the PYEs for dispersions with DMRs ranging from 10 mol% to 60 mol%. The error bars represent the standard error of the mean. At dopant molar ratios below 30 mol%, the PYEs are nearly unity. As c_{dopant} increases, the PYE declines, reaching approximately 32% at DMR = 60 mol%. This reduction in PYE aligns with earlier observations in doped thin films [17, 159–161]. The decrease is an intrinsic statistical effect in p-doped systems: with increasing dopant concentration, the Fermi level shifts toward the HOMO energy of the host and eventually approaches the dopant LUMO level, thus reducing the efficiency of electron transfer from the host to the dopant [162]. Furthermore, the error estimates are larger at low c_{dopant} and diminish at higher DMRs. The lower uncertainty at elevated DMRs results from the reduced interpolation error as the dopant absorbance becomes more dominant relative to that of the host.

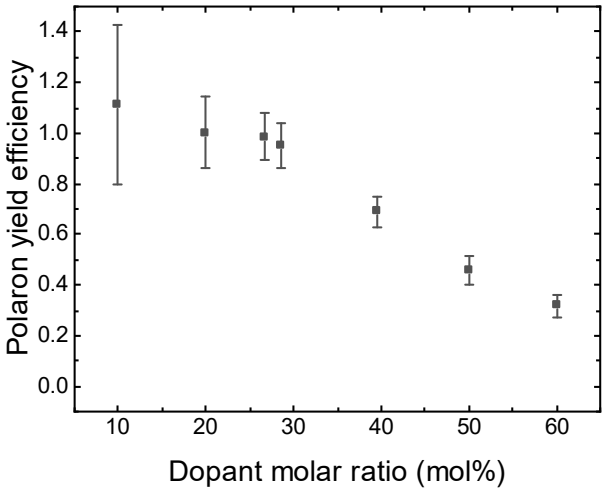

Figure 6.4: a) PYE of J71 dispersions doped with $CoTFSI_3$, calculated using the UV-Vis deconvolution and Equation 6.7 divided by the total dopant concentration versus the dopant molar ratio. The decreasing of the PYE upon increasing dopant molar ratio aligns with earlier observations in doped thin films [17, 159–161].

6.2 Connection of the polaron absorbance to the polaron yield efficiency

A polaron band emerges in the absorbance spectrum of J71 upon doping. The deconvolution of the spectrum allows gauging a model to describe the polaron band, and hence determining the relation between polaron band absorbance and positive charges created by doping.

6.2.1 Relation between polaron absorbance and doping concentration

Up to this point, the intensity of the polaron absorption between 700 nm and 1000 nm (peaking at approximately 730 nm) could not be employed to determine c^+_{host} and, consequently, the PYE. Figure 6.5a depicts the polaron absorbance $A_{\mathrm{polaron}} = A^+_{\mathrm{host}}(\lambda = 730\,\mathrm{nm})$ as a function of the total dopant concentration c_{dopant} (black squares). The observed sublinear increase of the polaron absorbance with rising dopant concentration is consistent with the previously discussed reduction in PYE at higher doping levels, where a fraction of dopant molecules do not generate polarons. The UV-Vis deconvolution enables the determination of c^-_{dopant} and thus allows the correlation between A_{polaron} and c^-_{dopant} to be established (green circles in Figure 6.5a). A clear linear relationship is observed between the polaron absorbance A_{polaron} and c^-_{dopant}. The corresponding linear fit is shown in green. According to the Beer-Lambert law (Equation 6.3), the polaron absorbance A_{polaron} scales linearly with the polaron concentration c^+_{host} and, consequently, with c^-_{dopant}. The proportionality

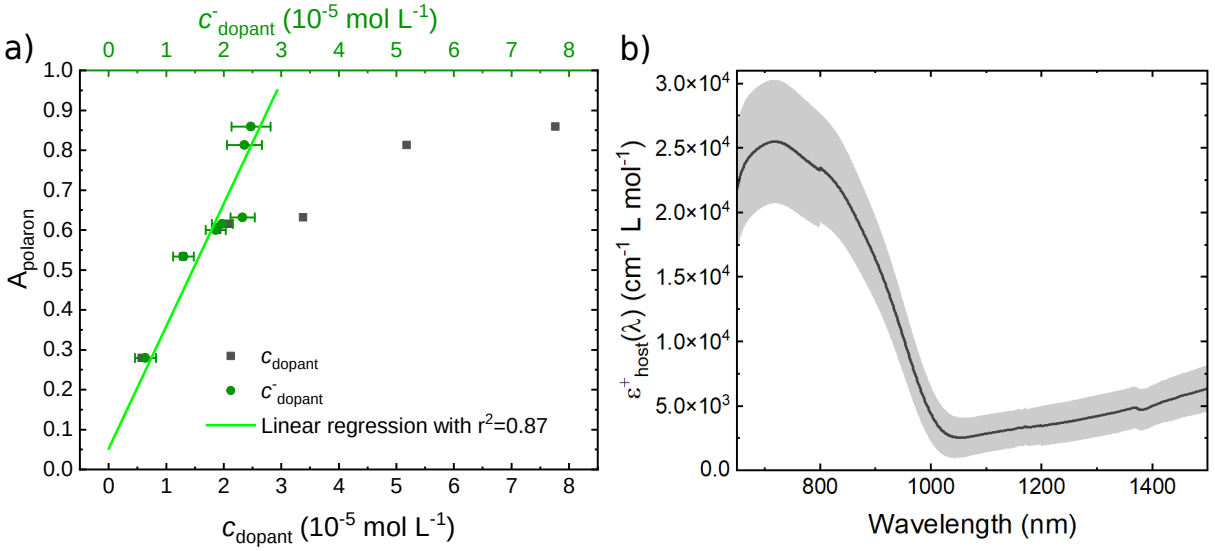

Figure 6.5: a) Polaron absorbance A_{polaron} of J71 dispersions at 730 nm plotted against the total dopant concentration c_{dopant} in the dispersion (black) and against the anion concentration c^-_{dopant} (green, Equation 6.7). As c_{dopant} increases, the polaron absorbance follows a sublinear trend due to the decline in PYE to well below 100%. However, when plotted against c^-_{dopant}, the polaron absorbance increases linearly proving consistency between the UV-Vis deconvolution method and polaron absorbance measurements. The error bars represent the standard error of the mean. b) Computed molar extinction coefficient of the host J71 $\varepsilon^+_{\text{host}}(\lambda)$ by the UV-Vis deconvolution method. The shaded region indicates the propagated standard error of the mean.

factor is the molar extinction coefficient of the polaron band, $\varepsilon_{\text{polaron}} = \varepsilon^+_{\text{host}}(\lambda = 730\,\text{nm})$. The resulting linear regression model is given by

$$A_{\text{polaron}} = c^+_{\text{host}} \varepsilon_{\text{polaron}} l + A_{\text{offset}}, \tag{6.8}$$

with A_{offset} being an offset of the absorbance at $c^+_{\text{host}} = 0\,\text{mol}\,\text{L}^{-1}$, l being the cuvette path length of 1 cm. The goodness of the linear regression with Equation 6.8 serves as an indicator of the precision of the UV-Vis deconvolution. The coefficient of determination, $r^2 = 0.87$, demonstrates a strong linear correlation. Deviations from an ideal regression ($r^2 = 1$) are likely due to experimental uncertainties in the UV–Vis deconvolution process or in the measured polaron absorbance. The robustness of the regression line is further supported by its extrapolation to $c^-_{\text{dopant}} = 0\,\text{mol}\,\text{L}^{-1}$, where the polaron absorbance approaches zero, *i.e.* $A_{\text{offset}} = 0$. This finding is consistent with experimental UV–Vis spectra of undoped J71 layers (used as a reference, since J71 does not form nanoparticles

without the dopant) [163]. As the relation between $A^{+}_{\mathrm{host}}(\lambda)$ and c^{-}_{dopant} is valid across all wavelengths within the polaron absorption range, Equation 6.8 can be generalized to

$$A^{+}_{\mathrm{host}}(\lambda) = c^{+}_{\mathrm{host}} \cdot \varepsilon^{+}_{\mathrm{host}}(\lambda) l + A_{\mathrm{offset}}(\lambda). \tag{6.9}$$

Figure 6.5b presents $\varepsilon^{+}_{\mathrm{host}}(\lambda)$ evaluated over a range of wavelengths. The relative uncertainty in $\varepsilon^{+}_{\mathrm{host}}(\lambda)$ is minimal at the absorbance maximum of 730 nm. It is important to note that this analysis of A_{polaron} is feasible only because neither the neutral host J71 nor the dopant $CoTFSI_3$ exhibits any absorption in the spectral range associated with polarons (Appendix C.7) [163]. The maximum value of $\varepsilon_{\mathrm{polaron}}$ is $(2.5 \pm 0.5) \times 10^4\,\mathrm{L\,mol^{-1}\,cm^{-1}}$ at 730 nm, which aligns well with the polaron molar extinction coefficients reported in the literature for organic molecules, typically on the order of 10^4-$10^5\,\mathrm{L\,mol^{-1}\,cm^{-1}}$ [164–166]. With known $\varepsilon^{+}_{\mathrm{host}}(\lambda)$, the PYE of other dopants, forming ICTC with the host, without IBPs can be determined for this particular host. A characteristic feature of this method is that the relative error decreases with increasing dopant concentration compared to the host. This behavior arises because the uncertainty in interpolating the host absorbance becomes more significant when the host contribution dominates over that of the dopant. Consequently, at low dopant concentrations, such as those typically employed in organic thin films below 10 wt%, reliable analysis is not feasible. Even at a dopant molar ratio of 10 mol%, the PYE exhibits an error of approximately 33%. However, in dispersions, substantially higher dopant concentrations are commonly used than in solid films. For instance, Manger *et al.* [73] reported dopant weight ratios of up to 55 wt% iodine.
Notably, in the wavelength regime in which the deconvolution is performed, the absorbance within the spectrometer's linear range (depending on the spectrometer). This constrains the concentrations of both the host and the dopant, as neither can be too high. In practice, the doped J71 dispersion can only be of the order of $\mathcal{O}(10\,\mathrm{mg\,L^{-1}})$ to deconvolute their spectra.

6.2.2 Determination of the polaron yield efficiency by the polaron band

The limitation described above can be addressed by determining the polaron concentration of a dispersion using the gauged linear regression model (Equation 6.8). In practice, Equation 6.8 is solved for c^{+}_{host}, with the known $\varepsilon_{\mathrm{polaron}}$ and A_{offset} that have been determined beforehand using the UV-Vis deconvolution method. In this approach, two main sources of error are introduced: (i) The uncertainty of the linear regression model, *i.e.* the error of the molar extinction coefficient $\varepsilon^{+}_{\mathrm{polaron}}$ and the absorbance offset A_{offset}. The resulting error in the PYE derived from this model was evaluated, showing that the uncertainty in

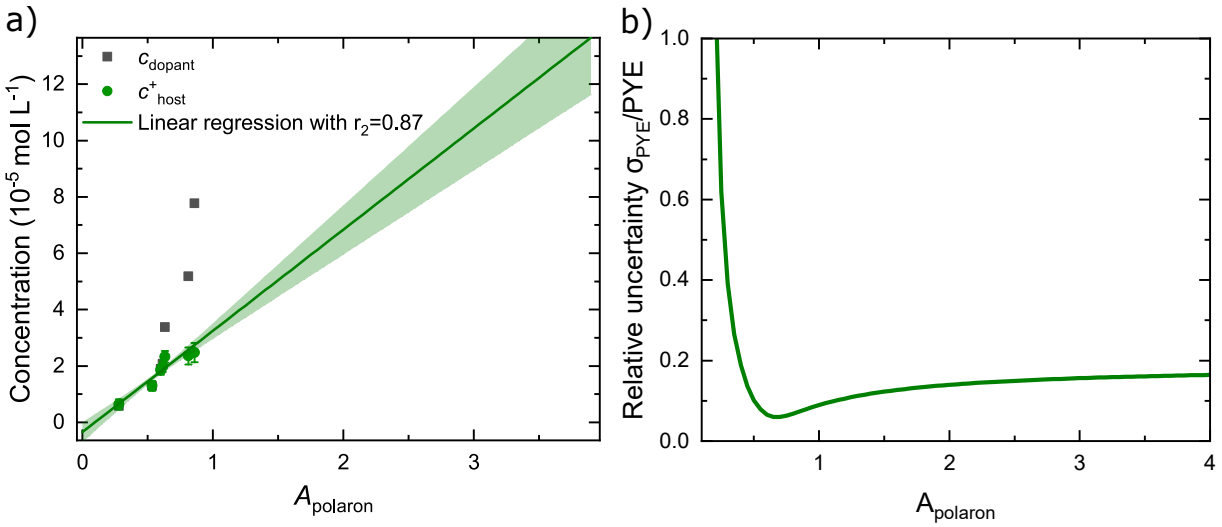

Figure 6.6: a) The green solid line represents the predicted concentration, c^+_{host}, based on the polaron absorbance at 730 nm of J71 dispersions, A_{polaron}. The shaded area indicates the propagated standard error. b) The propagated error of the PYE versus A^+_{polaron} is displayed. Notably, the error saturates below 20 %, allowing for accurate PYE determinations in dispersions with high A^+_{polaron}, which can be achieved not only by high dopant molar ratios but also high dispersion concentrations.

the calculated PYEs depends only on the uncertainties of the model parameters and the magnitude of the measured polaron absorbance (the complete derivation is provided in Appendix C.0.2). (ii) The measurement uncertainty of the UV–Vis polaron absorbance, which is significantly lower than the model uncertainty and, therefore, neglected. For dispersions with strong polaron absorbance (e.g., resulting from a high J71 concentration), the overall error can remain small even at low DMRs, as illustrated in Figure 6.6a: The uncertainty of the linear regression model propagates into c^+_{host}, and the corresponding relative error of PYE is shown in the Figure 6.6b. At low polaron absorbance, the uncertainty in the PYE becomes substantial. However, increasing the dopant concentration reduces this error and leads to saturation at approximately 16% for strong polaron signals. This demonstrates a viable strategy for determining the PYE in dispersions: the UV–Vis deconvolution is first used to extract the regression parameters of the linear model from a dispersion with relatively low host concentration and moderately high DMR. The calibrated regression model can then be applied to dispersions with higher host concentrations to obtain PYEs with lower uncertainty, even at low DMRs. It should be noted that the uncertainties shown in Figure 6.6 depend on the specific host material, as they are affected by the UV-Vis deconvolution.

6.2.3 Limitations

The deconvolution approach, which separates the absorbance spectra into contributions from the neutral and ionized species of both the host and the dopant, requires the presence of multiple IBPs. This condition makes $CoTFSI_3$ particularly suitable for determining the PYE, while other dopants such as F_4TCNQ are less advantageous in this regard. However, $CoTFSI_3$ can be employed to quantify the molar extinction coefficient of the host polaron, which allows the determination of the PYE for systems doped with other dopants as well. The method further depends on a dispersion medium that is chemically inert toward the dopant. Otherwise, the PYE would no longer be equivalent to the DIR. It is also essential to emphasize that for this specific host-dopant combination, it was achieved only to apply the UV-Vis deconvolution for nanoparticle dispersions but not for dissolved material. This is because common solvents for J71, such as halogenated or aromatic solvents, exhibit strong absorption in the spectral range in which the dopant has its IBP. While a mathematical extension of the method to solid layers might, in principle, be feasible, it would require extremely precise thickness determination and the fabrication of highly doped layers, which are challenging to produce experimentally.

6.3 Nanoparticle dispersions stabilized by the p-dopant $CoTFSI_3$ for OSCs

The high PYE of $CoTFSI_3$ in combination with the host polymer J71 makes it a promising candidate for the stabilization of J71:Y6 nanoparticle dispersions. In this work, OSCs are fabricated to evaluate the practical utilization of $CoTFSI_3$ to stabilize dispersions for the production of absorber layers. It is compared with iodine-doped J71:Y6 nanoparticle dispersions [73]. The results have also been discussed in the Master's thesis of Raphael Hörner.

6.3.1 Optimization of the nanoparticle dispersions

An initial series of measurements was performed to determine the minimum dopant concentration required to stabilize a J71:Y6 dispersion and produce small nanoparticles. J71 and Y6 were dissolved in $CHCl_3$ at $c_S = 0.2\,g\,L^{-1}$, and $CoTFSI_3$ dissolved in CH_3CN was added in dopant molar ratios of 5-20 mol%. Then, 0.5 mL of the doped solutions were nanoprecipitated in 3.5 mL of CH_3CN according to the method in Section 4.1.1. A COB LED illuminated the nonsolvent during injection. Afterward, the dispersion volume was reduced to 1 mL, followed by centrifugation (14,500 rpm, 2 min). The measured nanoparticle sizes are shown in Figure 6.7a. At DMRs of 5 mol% and 7.5 mol%, the nanoparticles were

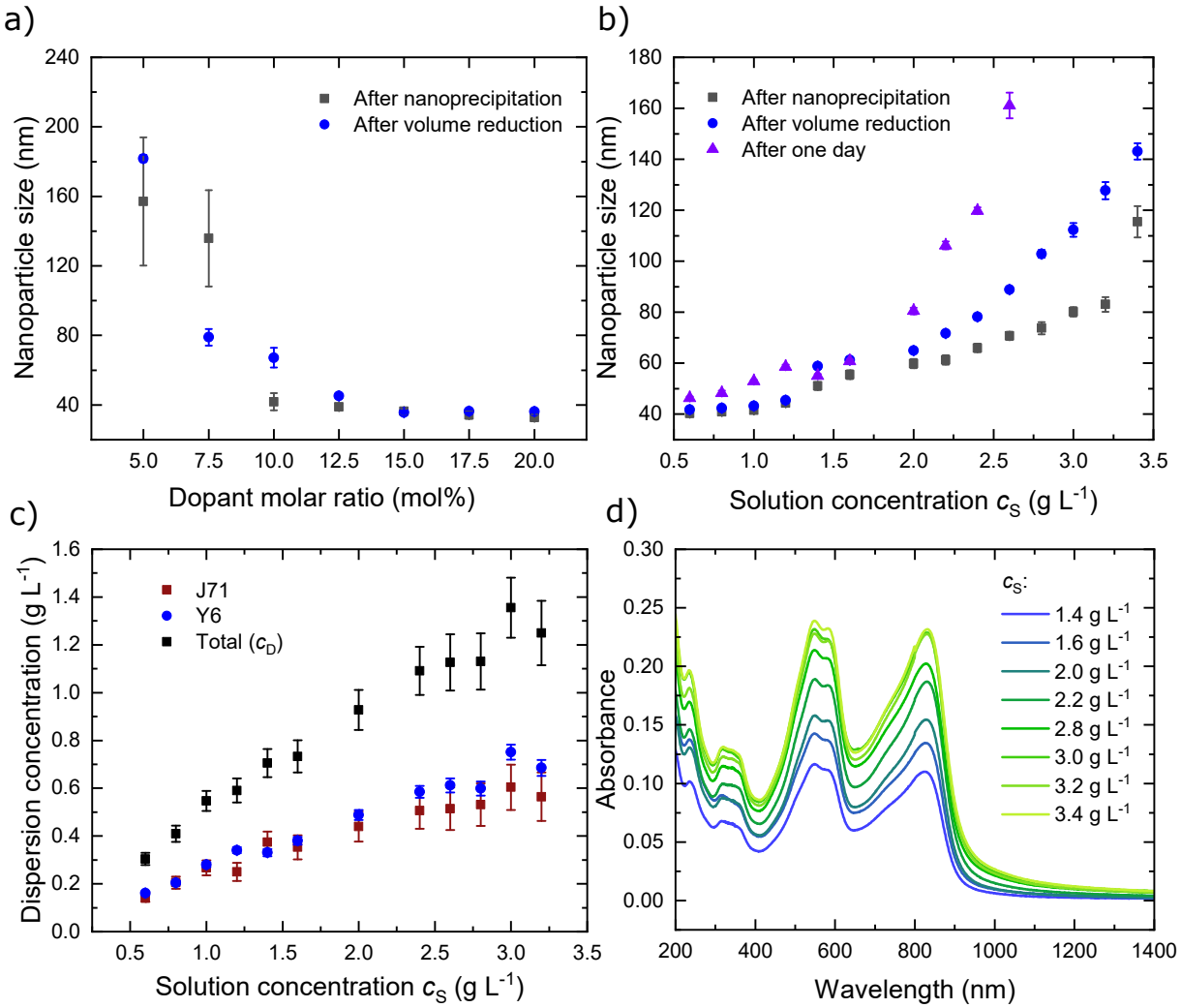

Figure 6.7: Characteristics of J71:Y6 dispersions doped by $CoTFSI_3$. J71:Y6 (1:1 w/w, $CHCl_3$ solution, concentration c_S, 0.5 mL) was nanoprecipitated into the dispersion medium (CH_3CN, 3.5 mL). A volume-reduction to 1 mL and centrifugation followed. a) Nanoparticle size for varying the DMR at constant $c_S = 0.2\,g\,L^{-1}$. b-c) Nanoparticle size and dispersion concentration c_D for varying c_S (constant DMR= 15 mol%) d) Absorbance of layers spincoated by dispersions with varying c_S.

relatively large and exhibited strong fluctuations in the DLS measurements, as indicated by the large error bars. At 10 and 12.5 mol%, the particles were initially smaller but grew during volume reduction. Above a DMR of 15 mol%, the mean particle size remained consistently small (minimum of 36 nm), so 15 mol% was chosen for further experiments. The error bars in the figure represent the standard deviation of separate DLS measurements on the same sample.

For the following experiment, J71:Y6 solutions were prepared with a fixed DMR of 15 mol% and varying initial solution concentrations c_S of 1.4-3.4 $g\,L^{-1}$ to increase the dispersion

concentration and enable thin-film processing with fewer deposition steps. $CoTFSI_3$ was added to the J71:Y6 solutions ($CHCl_3$), after which 0.5 mL of the doped solutions were nanoprecipitated in 3.5 mL of CH_3CN according to the method in Section 4.1.1. A COB LED illuminated the nonsolvent during injection. The dispersion volume was then reduced to 1 mL, followed by centrifugation (14,500 rpm, 2 min).

Figure 6.7b shows that the nanoparticle size increases with increasing c_S. After volume reduction and for $c_S > 2.6\,g\,L^{-1}$, the nanoparticle sizes exceeded 100 nm. For $c_S > 2\,g\,L^{-1}$, the particles also exhibited more pronounced growth during the first day of storage. As these dispersions are intended for the deposition of thin films with thicknesses of approximately 100 nm, large nanoparticles could result in significant surface roughness relative to the layer thickness.

To measure the concentration of Y6 in the dispersion, a small volume (on the order of several tens of µL) was taken, the dispersion medium was evaporated, and the remaining semiconductor was redissolved in $CHCl_3$. The J71 and Y6 peaks in the UV-Vis absorbance spectra of these redissolved nanoparticle dispersions were compared to reference solutions with known concentrations to determine the dispersion concentration c_D (Figure 6.7c). Higher initial solution concentrations led to an increase in c_D, although the relative gain diminished at larger c_S. The ratio of J71 to Y6 incorporated into the dispersion remained identical to the ratio present in solution prior to nanoprecipitation. A maximum dispersion concentration of $c_D = 1.2\,g\,L^{-1}$ was achieved, which exceeds the total J71:Y6 concentration reported for iodine-stabilized dispersions ($0.7\,g\,L^{-1}$) [73]. Thus, $CoTFSI_3$ stabilizes nearly twice the J71:Y6 concentration compared to iodine. In this work, only 16.2 wt% dopant was required to reach $c_D = 1.2\,g\,L^{-1}$, whereas 44.5 wt% iodine was necessary to obtain $c_D = 0.7\,g\,L^{-1}$. The considerably stronger reduction potential of $CoTFSI_3$ (0.58 V [156]) compared to iodine (−0.11 V[1] [167] vs. Fc^+/Fc) contributes to this enhanced stabilization and lowers the required dopant amount.

Some of the dispersions shown in Figure 6.7c were used for spincoating layers (8 deposition steps at 1000 rpm, dynamic mode), as shown in Figure 6.7d. With increasing c_S, the layers exhibited higher absorbance, indicating increased film thickness. The corresponding thickness measurements using a Bruker Dektak XT are summarized in Table 6.2. However, only a slight increase in thickness is observed for $c_S \geq 3\,g\,L^{-1}$. At $c_S = 3.4\,g\,L^{-1}$, a thickness increment of 4.9 nm per deposition step is obtained.

[1] I_2/I^- in CH_3CN

Table 6.2: Thickness per deposition step, d_{DS}, for J71:Y6 dispersions varying c_S. The dispersions were spincoated 8 times on glass substrates for thickness measurements with a Bruker Dektak XT.

c_S ($g\,L^{-1}$)	d_{DS} (nm)
1.4	2.5
1.6	3.0
2.0	3.5
2.8	4.0
3.0	4.8
3.4	4.9

6.3.2 Organic solar cells

The previous section demonstrated that J71:Y6 dispersions can be stabilized with $CoTFSI_3$ at sufficiently high concentrations to allow the deposition of thin films. The next step is to evaluate whether these dispersions are not only stable but can also be used to process device-ready photoactive layers. Therefore, in this section, organic solar cells are fabricated with the photoactive layer processed from $CoTFSI_3$-stabilized J71:Y6 nanoparticle dispersions, in order to assess their suitability for device integration and to benchmark their photovoltaic performance against solution-processed references.

The following architecture is used for the OSCs: ITO/PEDOT:PSS/photoactive layer/ZnO/Ag, as this stack has previously yielded PCEs above 10 % with J71 and Y6 processed from nanoparticle dispersions [73]. The pre-structured ITO substrates were treated with oxygen plasma (2 min). A PEDOT:PSS hole transport layer was spincoated in air. Appendix C.4 summarizes the exact processing parameters for PEDOT:PSS and the subsequent layers. All following steps were carried out in a nitrogen glovebox ($O_2 < 1$ ppm, $H_2O < 1$ ppm). J71:Y6 photoactive layers were fabricated using dispersions of two different initial concentrations ($2.0\,g\,L^{-1}$ and $3.4\,g\,L^{-1}$), each containing 15 mol% $CoTFSI_3$. Five nanoprecipitations were carried out with $c_S = 2.0\,g\,L^{-1}$ and four with $c_S = 3.4\,g\,L^{-1}$. Three reference devices with J71:Y6 (1:1 w/w) were spincoated from chlorobenzene solution ($c_S = 26\,g\,L^{-1}$). After the photoactive layer ZnO was deposited.

The silver top electrode (100 nm) was thermally evaporated in high vacuum (base pressure $\leq 1 \cdot 10^{-6}$ mbar).

Table 6.3 lists the solar cell performance metrics. The thicknesses d of the nanoparticle-processed photoactive layers were calculated based on the deposition steps and data from Table 6.2, while the solution-processed layers were measured directly by profilometry.

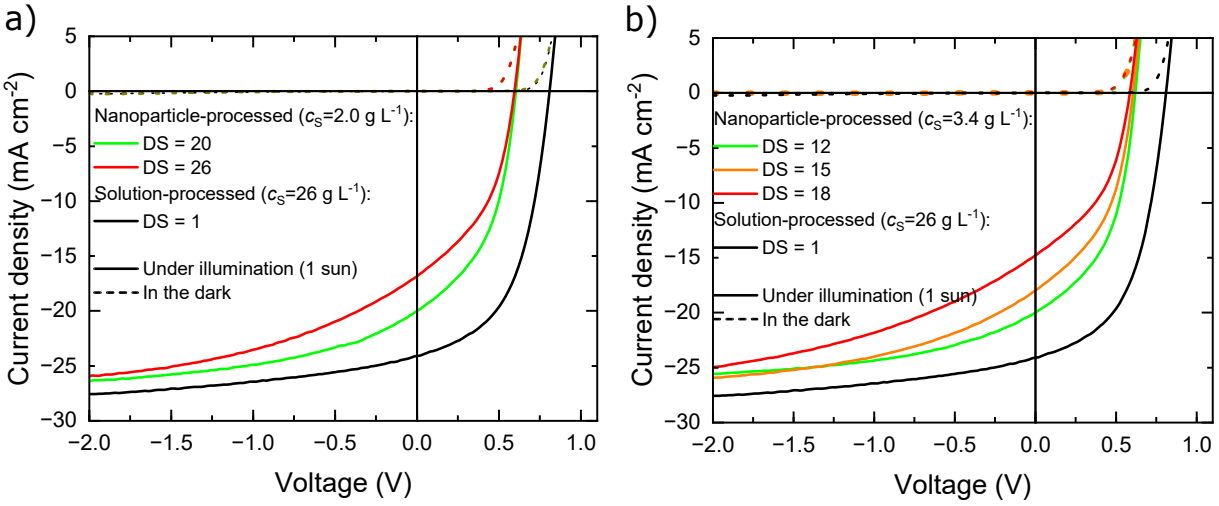

Figure 6.8: J-V curves of J71:Y6 OSCs with nanoparticle- and solution-processed photoactive layer. Applying a reverse voltage increases the extracted photocurrent from devices with nanoparticle-processed photoactive layers. OSCs with thicker nanoparticle-processed photoactive layers exhibit lower short-circuit current density.

Figures 6.8a and 6.8b show the corresponding J-V curves.

The devices with a nanoparticle-processed photoactive layer showed lower efficiencies than those with solution-processed layers. The best OSCs with nanoparticulate photoactive layers reached about 80 % of the short-circuit current density and 75 % of the open-circuit

Table 6.3: Characteristics of J71:Y6 OSCs. The solution concentration before the nanoprecipitation c_S and the number of deposition steps (DS) are varied. The highest efficiency achieved is shown in brackets in each case. The highest efficiency is achieved for only 12 spincoating steps with $c_S = 3.4\,\mathrm{g\,L^{-1}}$. Values are given as mean ± standard deviation.

c_S ($\mathrm{g\,L^{-1}}$)	DS	d (nm)	J_{SC} ($\mathrm{mA/cm^2}$)	V_{OC} (mV)	FF (%)	PCE (%)	Yield[a]
2.0	20	70±5	19.5 ± 0.3	604 ± 2	46.0 ± 0.2	5.4 ± 0.1 (5.6)	6/8
2.0	26	91±6	16.3 ± 0.4	593 ± 3	43.7 ± 0.2	4.2 ± 0.1 (4.4)	8/8
3.4	12	59±5	19.8 ± 0.2	618 ± 3	47.1 ± 0.4	5.7 ± 0.1 (5.9)	3/4
3.4	15	73±6	17.8 ± 0.1	607 ± 1	44.6 ± 0.3	4.8 ± 0.1 (4.9)	4/4
3.4	18	88±7	14.6 ± 0.2	583 ± 4	43.3 ± 0.5	3.7 ± 0.1 (3.8)	4/4
(Nanoparticle-processed photoactive layer)							
26	1	90±5	24.6 ± 0.8	803 ± 6	51.9 ± 0.8	10.1 ± 0.2 (10.4)	12/12
(Solution-processed photoactive layer)							

[a] indicates the number of functioning samples compared to the total number produced.

voltage of the reference cells processed from solution. As shown in the J–V curves measured in the dark (Figure 6.8), all nanoparticle-based devices exhibited good reverse-bias blocking. With increasing applied reverse bias, the photocurrent density also increases, which may indicate a less favorable microstructure in which carrier extraction benefits from an externally applied field. The higher photocurrent observed in thinner layers supports this interpretation. Furthermore, if residual dopant remains in the layer, doping-induced recombination losses could additionally reduce J_{SC} [168]. EQE spectra (Appendix C.8) confirmed that all nanoparticle-based devices maintain the spectral shape of the reference OSCs but exhibit lower peak EQEs. Devices with thinner nanoparticle-processed photoactive layers reached higher EQE values than thicker ones, consistent with the corresponding trend in J_{SC}. The best device still exhibits an SMCF-corrected PCE of 5.4 %.

These results confirm that $CoTFSI_3$ can stabilize nanoparticle inks at concentrations suitable for device fabrication. The achieved SMCF-corrected PCE of 5.4 % already exceeds the performance of OSCs reported with nanoparticle-processed photoactive layers based on P3HT or PTB7 [11, 13, 169, 170]. Iodine-stabilized J71:Y6 inks have reached PCEs above 10 % [73]. A likely contributing factor is the evaporation of iodine during thermal annealing, reducing the residual dopant content in the film. In contrast, due to its molecular size, $CoTFSI_3$ is unlikely to evaporate under typical annealing conditions, and the dopant may remain embedded in the layer, which could disturb the microstructure and increase recombination losses.

7 High-detectivity organic photodiodes from eco-friendly nanoparticle dispersions

Organic photodiodes can match or even exceed the specific detectivity D^* of silicon and indium gallium arsenide photodetectors. As described in Section 2.3.2 blocking layers are known to improve D^* in OPDs [107–110]. In regular device architectures, the electron blocking layer (EBL) lies beneath the photoactive layer, but depositing subsequent layers without dissolving the EBL is challenging due to solvent incompatibility. Instead of solvents, this work has used nonsolvents, such as ethanol or 2-propanol, in which organic semiconductors are dispersed. The insolubility of most organic EBL materials expands the number of EBLs usable in a regular architecture.

First, the device architecture of the OPD employing P3HT:$PC_{71}BM$ as the photoactive layer is optimized. Several materials are screened as hole-blocking cathode interlayers (CILs). Then, poly[bis(4-phenyl)(2,4,6-trimethylphenyl)amine] (PTAA), which has a shallow electron affinity, is investigated as an EBL. The insolubility of PTAA in the solvents used for nanoparticle deposition enables its successful integration into the regular device stack.

A common limitation of OPDs is their reduced detectivity in the near-infrared region [171]. Although most OPDs are narrowband, broadband variants with SRs up to 2500 nm have been reported [172]. The OPD response is mainly governed by the absorption spectrum of the semiconductors in the photoactive layer [173–177]. However, a broadening of the photoresponse can also be achieved in narrowband OPDs by increasing the photoactive layer thickness [99, 111, 178]. In contrast to solutions, nanoparticle dispersions decouple the achievable film thickness from solubility and ink concentration, allowing layer thickness to be built up additively by repeated coating. Accordingly, thick photoactive layers, on the order of 1000 nm, processed from nanoparticle dispersions are employed.

7.1 Blocking holes with cathode interlayers

Several materials were tested as cathode interlayers for their ability to block holes in OPDs based on the standard semiconductors P3HT and $PC_{71}BM$ in photoactive layers. Devices consisting of the regular architecture ITO/PTAA/P3HT:$PC_{71}BM$/CIL/Ag were fabricated.

By selecting the ideal CIL, the shot noise is suppressed by inhibiting hole injection from the Ag electrode into the photoactive layer, as detailed in Section 2.3.2. In total, three different materials were investigated for their suitability as a CIL in the architecture mentioned above. 3-phenyl-4(1′-naphthyl)-5-phenyl-1,2,4-triazole (TAZ) has already been used as a CIL in [107] to decrease the dark current under reverse bias. Calcium (Ca) makes a good electrode in lab-scale OPDs [107, 179]. The ETL zinc oxide (ZnO) is chosen as it yields good OSCs with P3HT and PCBM with good charge carrier selectivity [180, 181]. For the fabrication of OPDs, pre-structured ITO glass substrates were first treated with an oxygen plasma (2 min). PTAA was dissolved in a toluene (0.6 g L^{-1}) and desposited by spincoating at 3000 rpm. The nanoparticle dispersions for the deposition of the photoactive layer were synthesized as follows: The semiconductor solution in $CHCl_3$ (P3HT:$PC_{71}BM$, 1 mL, 1:0.8, 8 g L^{-1}) was nanoprecipitated into EtOH (4 mL). $CHCl_3$ and a portion of the dispersion medium were evaporated at 70 °C, resulting in 1 mL nanoparticle dispersion in EtOH. The dispersions (up to 8 g L^{-1}) were spincoated six times dynamically (every 20 s) onto the substrate at 1000 rpm (20 s drying time between spincoating steps), producing a layer with a thickness of (213 ± 5) nm. The CIL was then deposited. The electrode calcium (Ca) was deposited by thermal sublimation (20 nm, 0.5 Å s^{-1}) under high vacuum (base pressure $\leq 1 \cdot 10^{-6}$ mbar). ZnO (10 nm) was spincoated (2000 rpm, 40 s) from ZnO nanoparticles (1 wt%, in butanol), and the substrates were subsequently annealed at 120 °C (10 min). TAZ (EtOH solution, 0.5 g L^{-1}) was spincoated (4000 rpm, 40 s) with subsequent annealing at 80 °C (10 min). In the end, the silver top electrode (100 nm) was thermally evaporated in high vacuum (base pressure $\leq 1 \cdot 10^{-6}$ mbar). Three substrates were produced for each CIL. For ZnO and TAZ as CIL, large shunt currents were observed for one sample, respectively, and were not considered in the further evaluation because these could be attributed to other factors than those investigated here.

Figure 7.1a shows the *J-V* curve for the different CIL configurations. Devices with Ca as CIL yield the highest FF. The ETL ZnO or omitting the CIL show a very similar curve. TAZ shows the smallest extracted current densities in the 4th quadrant, which may result from the relatively shallow LUMO of -2.7 eV [182], compared to $PC_{71}BM$ at -4.2 eV [183], leading to an extraction barrier for electrons. However, the differences in the *J-V* curves are comparably small.

Because OPDs are commonly operated under reverse bias, differences in the photocurrent are not expected to strongly influence the specific detectivity. To examine whether the shot noise depends on the CIL, the dark current is measured with a Keithley 2420 SMU (compare with Equation 2.20). The results are shown in Figure 7.1b (bias voltage of -1 V). The lower limit of the dark current that the Keithley 2420 can detect is discussed in

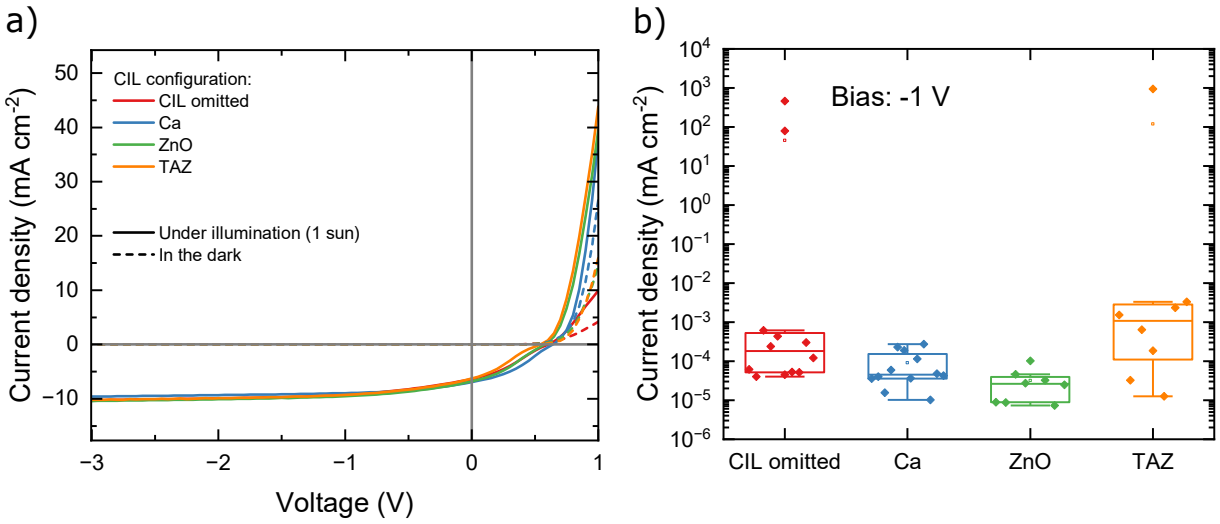

Figure 7.1: a) J–V curves of OPDs with an ITO/PTAA/P3HT:$PC_{71}BM$/CIL/Ag architecture for different cathode interlayer configurations: CIL omitted, Ca, ZnO, and TAZ. The photocurrent differs among the devices in the fourth quadrant; however, under reverse bias, where OPDs are typically operated, these differences largely disappear. b) Dark current densities at a bias voltage of −1 V. OPDs with Ca or ZnO exhibit the lowest dark currents, indicating their effectiveness in blocking holes.

Section 7.2.1. In the subsequent paragraph, it is discussed that the devices comprising ZnO show a decreased dark current upon illumination, which is why they were light-soaked for 120 s under one sun. Comparison of the dark current densities shows the trend of decreasing median in the following order of CIL configurations: TAZ, CIL omitted, Ca and ZnO. The configurations with Ca and ZnO, in this work, have a dark current density median of $5 \cdot 10^{-5}\,\mathrm{mA\,cm^{-2}}$ and $3 \cdot 10^{-5}\,\mathrm{mA\,cm^{-2}}$, which is lower than previously reported dark current densities of OPDs with the photoactive layer material P3HT:$PC_{71}BM$ [106]. As the light-soaking effect for ZnO is well-known [184], the impact of illumination of the devices was tested for all CIL configurations. The influence of light-soaking on the dark current density was investigated. Four devices for ZnO and TAZ as CIL, and three devices for Ca as CIL were measured directly after fabrication before and after illumination under one sun (120 s). The respective dark current densities are shown in Figure 7.2a. For the CIL configurations Ca, TAZ, and omitted CIL the devices show very similar dark current densities before and after illumination. For ZnO as CIL, all devices exhibit lower dark current densities after illumination. Figure 7.2b shows the measured current densities of two samples (six devices in total) depending on the illumination time under one sun. The dark current density decreases by approximately an order of magnitude from 0 s to 120 s. A possible explanation is the light-soaking process of ZnO. Manor *et al.* describe improved n-type selectivity upon UV irradiation of ZnO due to oxygen desorption, which

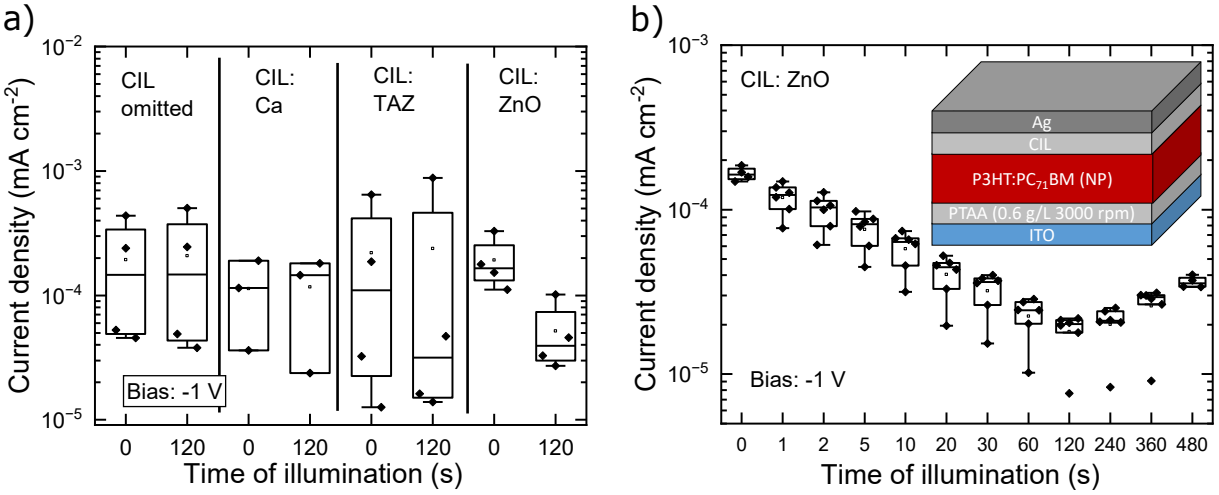

Figure 7.2: a) Dark current density (at −1 V) of OPDs with an ITO/PTAA/P3HT:$PC_{71}BM$/CIL/Ag architecture for different cathode interlayer configurations: CIL omitted, Ca, TAZ, and ZnO. The first measurement was performed directly after device fabrication (within 30 min of top electrode evaporation) without prior illumination, and the second after 120 s of one-sun illumination. Except for ZnO, no notable change in dark current is observed upon illumination. For ZnO, the blocking properties improve after illumination, which is attributed to light-soaking of ZnO [184, 185]. b) Dark current densities for ZnO as CIL as a function of illumination duration.

increases the n-type doping of ZnO and decreases the number of minority charge carriers (holes) [185]. The thus increased hole-blocking properties upon illumination would explain the observed reduction in dark current density. After longer illumination times, an increase in the dark current density is observed. In addition, the effect of enhanced hole selectivity was tested regarding its reversibility over time: Four devices with ZnO as CIL had a dark current density of $(8 \pm 3) \cdot 10^{-5}\,\mathrm{mA\,cm^{-2}}$ within 30 minutes after device fabrication and after 120 s illumination under one sun (measured within 30 min after evaporation). After five days of storing these samples without illumination, the dark current density increased by over one order of magnitude to $(2.0 \pm 0.2) \cdot 10^{-3}\,\mathrm{mA\,cm^{-2}}$. Illumination for five minutes under one sun decreased it again to $(2.5 \pm 0.4) \cdot 10^{-5}\,\mathrm{mA\,cm^{-2}}$. This shows that storing the samples without illumination reverses the effect of reduced dark current. Illumination of the samples triggers the effect again. In addition, the reversibility of the light-soaking effect is observed in the literature and explained by the re-adsorption of oxygen [185, 186]. This makes it difficult to use architectures with ZnO as CIL to investigate changes in other parts of the device (e.g., the photoactive layer), as the dark current depends on the history of the ZnO layer.

Since Ca as a CIL also yields very low dark currents and is not influenced by illumination, it is used for further studies of nanoparticle OPDs. However, Ca also requires careful

handling: It is sensitive to moisture, making it necessary to use protective barriers with low water vapor transmission rates if used outside of gloveboxes [187]. In this work, it is only used in gloveboxes under inert conditions.

7.2 Blocking electrons with PTAA

As discussed in Section 2.3.2, a blocking layer can decrease the dark current and therefore increase the detectivity of an OPD. An important consideration here is the question of orthogonal solvents, as spincoating on top of an already deposited layer can redissolve and remove it. In a regular architecture, the photoactive layer is deposited on top of an electron blocking layer (EBL). Due to the polar nature of the dispersion medium EtOH, it is an orthogonal solvent for many organic semiconductors. In this work PTAA is chosen as a potentially good EBL material due to its low EA of 1.8 eV (measured by IPES) [188], which should be very suitable for blocking electrons. This work expands the previous work done in [189]. OPDs with ITO/AIL/P3HT:$PC_{71}BM$/ZnO/Ag architecture were built, where AIL abbreviates the anode interlayer. Four devices with the interface-modifier MeO-2PACz and four devices with the EBL PTAA as AIL were fabricated. P3HT:$PC_{71}BM$ was spincoated from nanoparticles dispersed in EtOH to keep the AIL, in particular PTAA, intact. Devices with the EBL PTAA as the AIL showed higher reproducibility and lower mean dark current density compared to devices with MeO-2PACz as AIL. However, the small sample size complicates generalizations, especially since one device with MeO-2PACz as AIL shows large dark currents associated with shunts. In addition, a device with MeO-2PACz as AIL shows the same dark current density as the best-performing device with PTAA as AIL. Given the small sample number of 4 and the fact that the best devices of both AILs show the same dark current, there is no conclusive evidence that PTAA improves the blocking in the given architecture. To address the problem of low sample size in [189], this section investigates whether PTAA as electron blocking layer can reduce the dark current in a regular architecture with more statistics. In addition, PTAA is tested against omitting an AIL as some materials, such as PEDOT:PSS, even tend to increase the dark current of OPDs [111].

First, it was examined whether the PTAA layer remains intact when EtOH is spincoated on top of it. Therefore, two PTAA layers with a thickness of 12 nm were deposited, annealed at 80 °C, measured by UV-Vis absorbance spectrometry. After spincoating EtOH on top of it (six times with 1000 rpm), the samples were characterized again. The UV-Vis absorbance measurements are shown in Figure 7.3. The absorbance of the PTAA layers remains almost unchanged after the EtOH washing. The peaks change by less than 3%,

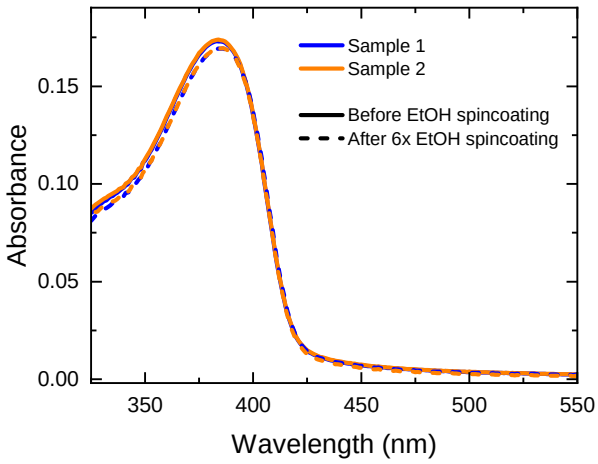

Figure 7.3: UV-Vis recording of a 12 nm PTAA layer on glass before and after washing with EtOH. The EtOH washing simulates the spincoating process of a nanoparticle layer dispersed in EtOH onto PTAA (1000 rpm, dynamically). The absorbance of the PTAA layers remains unaffected by the EtOH washing.

and also examinations by an optical microscope Smartzoom 5 from Carl Zeiss AG did not show layer inhomogeneities by redissolved and agglomerated material after EtOH spincoating. Therefore, it is concluded that PTAA remains intact when spincoating EtOH on top of it. However, UV-Vis spectrometry and optical microscopy primarily detect macroscopic changes in the layer, not, for example, pinholes on a small scale.

7.2.1 Measurement setup for dark currents with high accuracy

The dark currents of solar cells can be measured using a solar simulator setup. The illumination on the OSC is turned off, and a cap is placed on the holder to block ambient illumination. However, for OPDs, where an exact measurement of the dark current is important, this may not be sufficient to ensure true dark conditions. Organic photodiodes typically exhibit dark currents at the lower measurable limit of the solar simulator (introduced in Section 4.3.1), so a new setup and corresponding software (Figure 7.4) were designed and tested for measuring low dark currents with the electrometer Keithley 6517B from Tektronix.

The motivation is to lower the measurement limit of the dark current compared to the solar simulator with the Keithley 2420. The Keithley 2420 is specified to have an accuracy of 0.029% of the displayed current plus 700 pA [190]. Thus, the highest possible accuracy is 700 pA. For a substrate with an area of 0.105 cm^2, this translates to $J = 7 \cdot 10^{-6}\,\mathrm{mA\ cm^{-2}}$. By measuring without a DUT, the noise floor of J is of the order of $\mathcal{O}(10^{-6}\,\mathrm{mA\ cm^{-2}})$, which fits the accuracy limit specified for the Keithley 2420. In Section 7.2, OPDs

a) b)

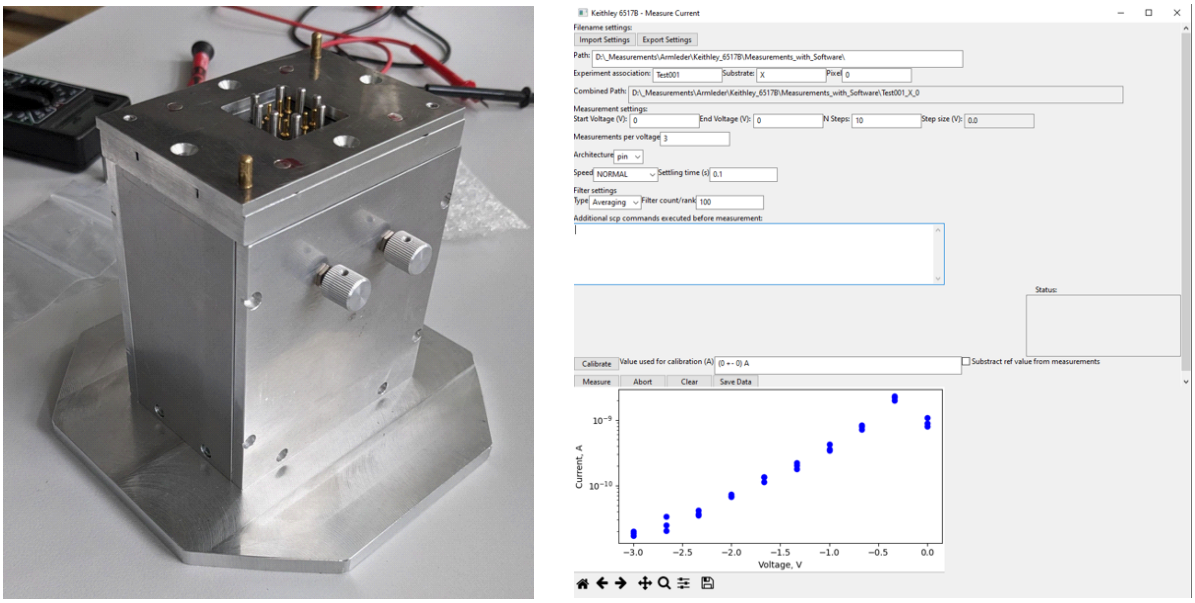

Figure 7.4: a) Photo of the low-noise sample holder developed in this work. The samples are placed on top of the pins. A metallic plate, held in place by magnets, presses the samples onto the pins, while an aluminum lid covers the assembly for electromagnetic shielding. b) Measurement software interface for controlling the Keithley 6517B electrometer.

characterized with this setup exhibit dark currents that reach the noise floor. This made it unclear whether lower dark currents are achievable, and this led to the design of a new setup.

The Keithley 6517B electrometer has an accuracy of 3 fA under optimal conditions [191]. For the devices investigated in this work (A=0.105 cm^2) this leads to a hypothetically lowest J of $2.85 \cdot 10^{-11}$ mA cm^{-2}. The design goal was to build a substrate holder for the device structure, shown in Figure 4.3, that allows low-noise current measurements. To reduce electromagnetic interference near the DUT, a grounded aluminum case fully encloses the substrate and unshielded cables. The manual switches control which anode and cathode of the four devices on the substrate are connected. In comparison, in the measurement setup of the solar simulator, only the anode is switched while all cathodes remain connected to the power source, increasing possible lateral leakage current.

To shield the connection between the case and the electrometer, coaxial/triaxial cables are used. In a coaxial cable the inner conductor transports the signal and the outer conductor is set to ground. To minimize current leakage, triaxial cables consist of three conductors: the inner conductor transports the signal, the inner shielding conductor is driven to the signal potential, and the outer conductor is set to ground. To match the triaxial and coaxial input of the electrometer, a triaxial cable (Tektronix, Keithley 7078-TRX-12) is

used in "high-resistance meter connection" [192]. The center contact connects the DUT and the electrometer. To ensure proper dark conditions, the top of the case is closed by an aluminum lid. To further reduce the scattered light, two layers of polyurethane coating on woven nylon fabric from Thorlabs are put over the whole measurement setup.
Measurement of the noise floor yields currents of the order of $\mathcal{O}(1\,\mathrm{pA})$, which translates to $J = 10^{-8}\,\mathrm{mA\ cm^{-2}}$ ($A = 0.105\,\mathrm{cm^2}$) for devices of this work. This is two orders of magnitude lower than the results obtained using the Keithley 2420. However, it is still three orders of magnitude larger than the stated accuracy limit in the datasheet of the Keithley 6517B. The reasons could include the relatively long cable length (triaxial cable 3 m, coaxial cable 2 m) and the fact that a driven guard is only used in the triaxial cable. A Python-based measurement software was developed to automatically perform a voltage sweep. In this work, always three data points were recorded for each set voltage. The median is then used for the evaluation. The integration time is set to HIACCURACY [192]. After applying a voltage, a settling time of 1 s was granted before measuring the current.

7.2.2 PTAA in regular architecture

To test the influence of the electron blocking layer, PTAA, in OPDs, the architecture ITO/EBL/P3HT:$PC_{71}BM$/Ca/Ag was chosen. The photoactive layer is processed from nanoparticles dispersed in EtOH. $CHCl_3$ semiconductor solution (P3HT:$PC_{71}BM$ 1:0.8, 1 mL, $8\,\mathrm{g\,L^{-1}}$) was nanoprecipitated into EtOH (4 mL). The $CHCl_3$ and part of the dispersion medium were evaporated at 70 °C, resulting in 1 mL nanoparticle dispersion in EtOH. The P3HT:$PC_{71}BM$ (1:0.8) dispersions (up to $8\,\mathrm{g\,L^{-1}}$, EtOH) were dynamically spincoated six times (every 20 s) onto the substrate at 1000 rpm, reaching a thickness of (253 ± 10) nm.
The EBL was varied in four configurations: (i) EBL omitted; (ii) PTAA (spincoated, $1\,\mathrm{g\,L^{-1}}$, 3000 rpm); (iii) PTAA (spincoated, $1\,\mathrm{g\,L^{-1}}$, 1500 rpm); (iv) PTAA (spincoated, $2\,\mathrm{g\,L^{-1}}$, 1500 rpm). For each configuration, four substrates (carrying each four devices) were fabricated. The corresponding thicknesses are 4 nm, 5 nm and 9 nm.
Figure 7.5a shows the median (solid line) and interquartile range [25,75]% (shaded area, barely visible) of the *J-V* curves, where thicker PTAA layers result in reduced photocurrent extracted in the fourth quadrant and also under reverse bias. At a bias of -2.5 V, the *J-V* curves coincide and show a saturated photocurrent. Introducing PTAA as the EBL leads to a lower extracted photocurrent. Increasing the thickness of the PTAA reduces the photocurrent even further. The hole mobility of PTAA ($\mu_\mathrm{h} = 4 \cdot 10^{-3}\,\mathrm{cm^2(Vs)^{-1}}$ [193])

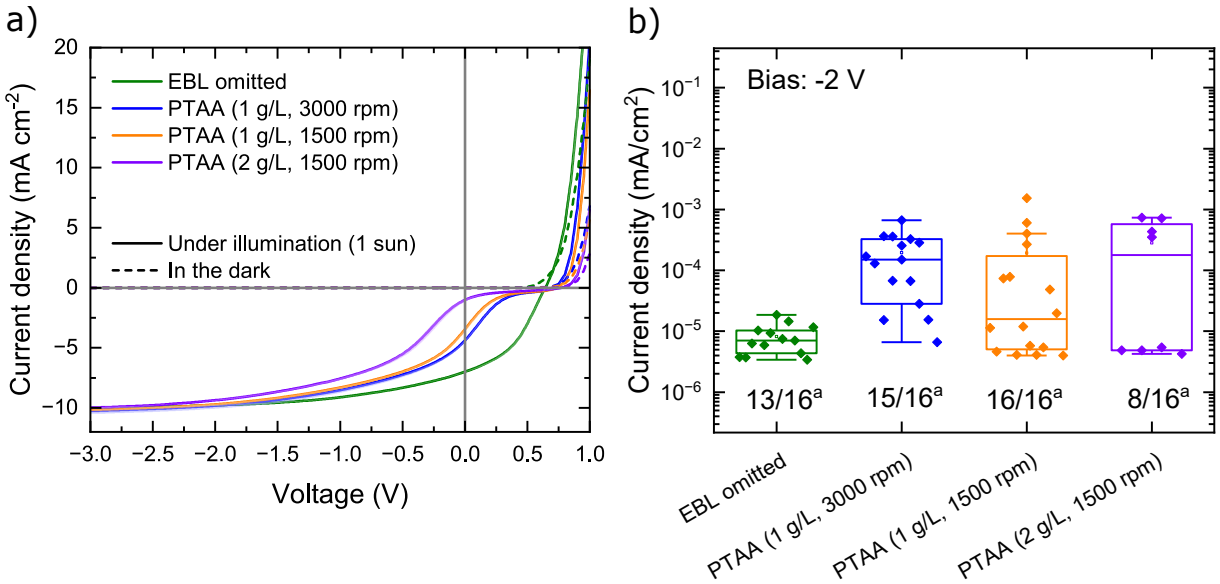

Figure 7.5: OPDs fabricated with the architecture ITO/EBL/P3HT:$PC_{71}BM$/Ca/Ag, varying only the electron blocking layer: EBL omitted and three different PTAA thicknesses. The photoactive layer was processed from a nanoparticle dispersion.a) Median J–V characteristics (solid line) with the interquartile range (25–75 %) indicated as a shaded area. b) Dark current density measured at a bias of −2 V. The device without an EBL exhibits the lowest dark current, indicating that the use of PTAA does not improve blocking performance. Furthermore, although the photocurrent of OPDs containing PTAA is highly reproducible, their dark current densities show substantial device-to-device variation.
[a] Devices with dark currents below 10^0 mA cm^{-2}. Devices with higher dark current densities are shunt-limited, typically exhibit artifacts under illumination and were excluded from the evaluation.

is reported to be lower than the mobility of P3HT (μ_h = 0.1 cm^2(Vs)$^{-1}$ [194]), which may cause charge accumulation, bimolecular recombination, and hence the reduced FF. In addition, because ionization energy (5.1 eV) is larger than that of P3HT (4.9 eV), the ITO/PTAA/P3HT stack can exhibit a hole-extraction barrier [189].

The J-V curves under illumination exhibit low variations, indicated by the barely visible shaded area that represents the interquartile range [25,75]%. Figure 7.5b displays the dark current density of the OPDs at a bias voltage of -2 V, measured with the Keithley 6517B. OPDs with PTAA show greater variation than the devices without PTAA; despite all having high reproducibility under illumination. Since the dark current is much smaller, it is more susceptible to defects, pinholes, and shunts. Comparing the best-performing devices (*i.e.*, those with the lowest dark current) across each EBL configuration provides a more reliable comparison. The lowest dark current densities of each EBL configuration fall within the same order of magnitude (this also occurs for other bias voltages, Appendix C.9). The sample with the lowest dark current corresponds to an architecture without an EBL. The large sample number of 16 devices per EBL configuration and the improved measurement

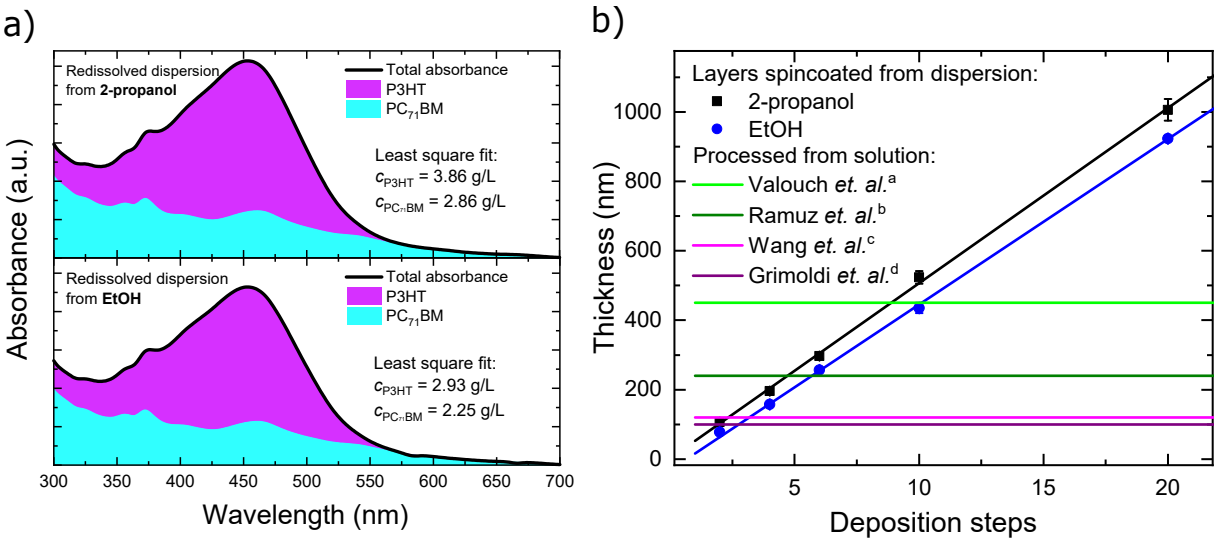

Figure 7.6: a) Absorbance of redissolved P3HT:$PC_{71}BM$ nanoparticles in $CHCl_3$ that were originally dispersed in EtOH and 2-propanol. A least-squares fit determines the semiconductor concentration, which is 18% higher in 2-propanol than in EtOH. b) Thickness of layers deposited from dispersions. The linearity confirms no loss of already deposited semiconductor. On average, layers deposited from 2-propanol are 21% thicker. The horizontal lines show photoactive layer thicknesses of OPDs in the literature with P3HT:PCBM as photoactive layer, processed from solution. In [a], a solution with $80\,g\,L^{-1}$ was used, demonstrating the advantages of nanoparticle processing over solution processing by decoupling the final thickness from the semiconductor concentration.
[a] [107], [b] [111], [c] [106], [d] [108].

setup using the Keithley 6517B support the hypothesis that using PTAA as an EBL does not decrease the dark current density in this architecture.

7.3 Influence of the photoactive layer thickness on the detectivity

To compare the film thicknesses obtained from the nanoparticle dispersions and solutions, the nanoparticle synthesis route was applied twice in the nonsolvents ethanol and 2-propanol, respectively. $CHCl_3$ semiconductor solution (P3HT:$PC_{71}BM$ 1:0.8, 1 mL, $8\,g\,L^{-1}$) was nanoprecipitated into the nonsolvent (4 mL). $CHCl_3$ and a portion of the dispersion medium were evaporated at 70 °C, resulting in 1 mL of the semiconductor dispersed in EtOH. The actual concentrations were determined by evaporating the solvent from 7.5 µL of dispersion, redissolving the remaining semiconductor material in $CHCl_3$, and quantifying it using UV-Vis absorbance spectrometry (Figure 7.6a). A least-squares fit with calibration solutions of known concentrations was used to extract the concentrations of both semiconductor components. If no material was lost through agglomeration and sedimentation during nanoprecipitation or volume reduction, the final dispersions would retain the theoretical concentration of $8\,g\,L^{-1}$. However, as shown in Figure 7.6a, this

concentration was not achieved, indicating material loss. Visible agglomeration and sedimentation occurred in the beakers used for nanoprecipitation and volume reduction, as well as in the centrifugation tubes. Such material losses in dispersions with concentrations on the order of $\mathrm{g\,L^{-1}}$ are well known and have been previously reported in Section 6.3 and in the literature [73, 81].

The 2-propanol-based dispersion exhibited a concentration 18 % higher than that of the ethanol-based dispersion. In addition, the nanoparticle sizes differed slightly, measuring $(73 \pm 2)\,\mathrm{nm}$ in 2-propanol and $(81 \pm 2)\,\mathrm{nm}$ in EtOH. Figure 7.6b shows the total film thickness after successive spincoating steps from each dispersion. The linear increase confirms that previously deposited semiconductor layers remain and are not redissolved or washed during subsequent coating.

Vertical lines in Figure 7.6b indicate thicknesses of solution-processed photoactive layers; label ^{a} corresponds to a 450 nm layer spin-coated from a molecular solution of $80\,\mathrm{g\,L^{-1}}$. High concentrations lead to increased viscosity as well as molecular aggregation or partial precipitation, which hinders homogeneous film formation and results in poor film quality. These results illustrate the advantage of nanoparticle-based processing, where the final layer thickness is decoupled from semiconductor solubility and solution concentration. Films deposited from 2-propanol dispersions are consistently thicker than those from EtOH, with average single-step thicknesses of $(51 \pm 2)\,\mathrm{nm}$ and $(42 \pm 3)\,\mathrm{nm}$, respectively, corresponding to an increase of 21 %. This difference arises both from the higher concentration of the 2-propanol dispersion and from the higher viscosity of 2-propanol, as described by Meyerhofer's relation [195], which links film thickness to solution viscosity. That is why 2-propanol is used for the fabrication of OPDs in further sections.

7.3.1 J-V curves

To investigate the influence of the photoactive layer thickness on the device performance, OPDs with varying photoactive layer thicknesses were fabricated. The device architecture was ITO/P3HT:$PC_{71}BM$ (1:0.8)/Ca/Ag. Nanoparticles were synthesized as described in Section 7.3, using 2-propanol as nonsolvent. The P3HT:$PC_{71}BM$ (1:0.8) dispersions were dynamically spincoated onto the ITO electrode. To minimize variability introduced by a spincoated CIL such as ZnO, a thermally evaporated Ca layer (20 nm, $0.5\,\mathrm{Å\,}s^{-1}$) was employed as the CIL.

Dispersions were processed from 2-propanol to reduce the number of deposition steps. Figure 7.7a shows the median dark current density as a function of applied bias voltage, with the shaded area indicating the interquartile range ($[25, 75]\%$). The interquartile

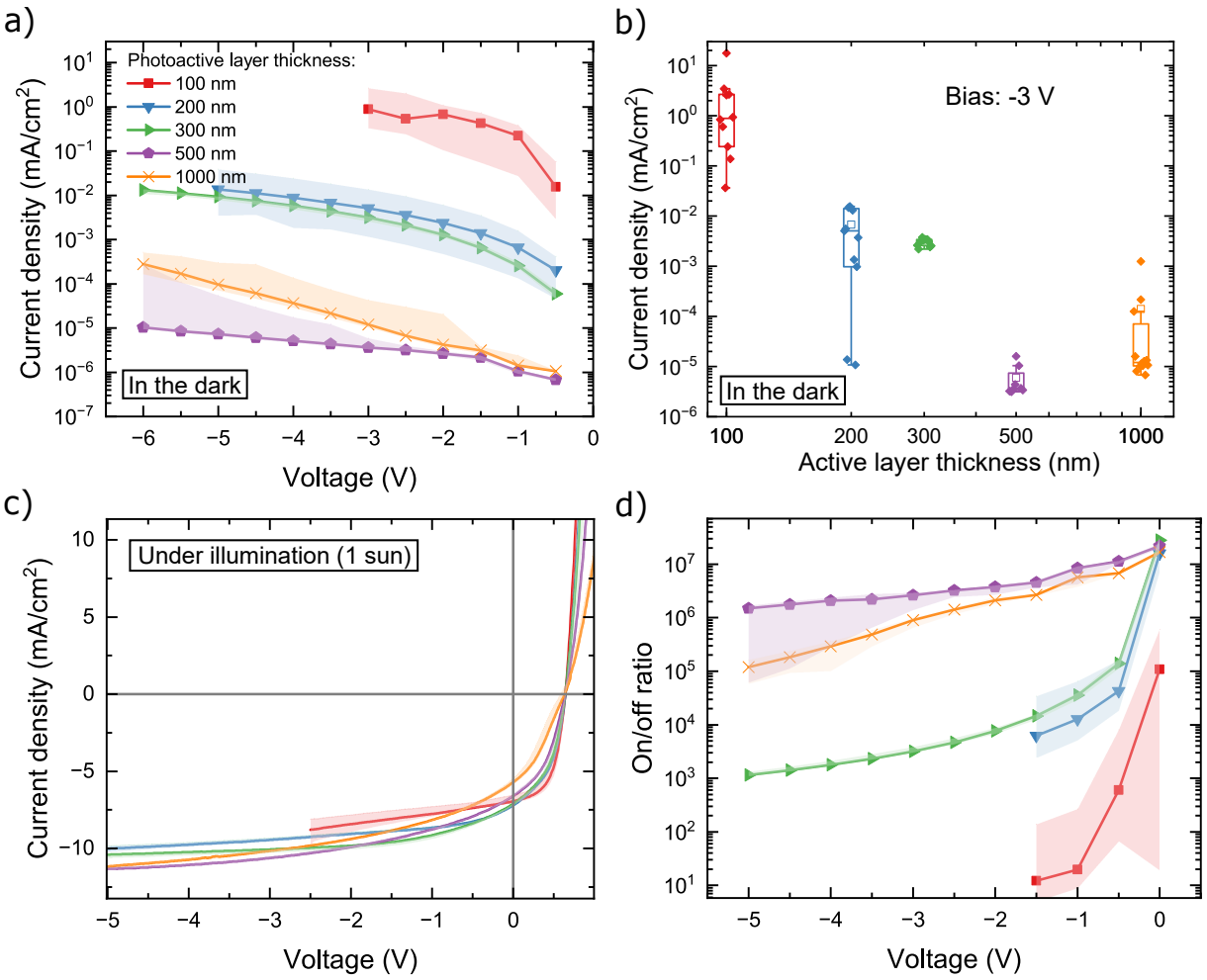

Figure 7.7: a) J-V curves in the dark of OPDs with ITO/P3HT:$PC_{71}BM$/Ca/Ag architecture and different photoactive layer thicknesses. Increasing the photoactive layer thickness between 100 nm and 500 nm reduces the dark current. At 1000 nm, the dark current is approximately the same as the dark current at 500 nm at low bias but shows increasing discrepancy at higher bias voltage. b) Dark current of devices at a bias voltage of -3 V. c) J-V curves under illumination. Thicker layers lead to a reduced FF in the fourth quadrant. d) On/off ratio. For a photoactive layer thickness of 500 nm at -0.5 V, an on/off ratio of 10^7 is achieved.

ranges generally span about one order of magnitude, except for the 300 nm thick layers, where the spread is smaller. Increasing the photoactive layer thickness from 100 nm to 500 nm agrees with previous reports, which show that the dark current decreases with thicker photoactive layers [99]. At a thickness of 1000 nm, however, the dark current density increases, particularly at higher negative bias voltages. The reduction in dark current for thicker photoactive layers is commonly attributed to a lower pinhole density and a corresponding increase in shunt resistance [99].

For a thickness of 500 nm, the dark current appears to reach saturation, as indicated by the nearly identical dark current densities for the 500 nm and 1000 nm layers at moderately negative bias. The slight increase observed at 1000 nm under strong reverse bias is unlikely to result from the layer thickness itself, as there is no physical mechanism by which a thicker photoactive layer would intrinsically worsen the blocking behavior. Instead, this deviation is most likely caused by batch-to-batch variability in the nanoparticle dispersion or stochastic differences in film formation during spincoating, to which the dark current is highly sensitive.

Figure 7.7b shows the dark current density at a bias voltage of -3 V. In contrast to Figure 7.7a, outliers are also visible. Interestingly, some devices with four deposition steps exhibit dark current densities almost as low as those with ten deposition steps. If the reduction in dark current for thicker photoactive layers primarily arises from a lower probability of shunt formation, then well-defined thin photoactive layers should also be capable of achieving similarly low dark currents. This assumption is supported by two outliers corresponding to photoactive layers of 200 nm thickness, which show dark current densities comparable to those of 500 nm-thick layers. However, to achieve a higher reproducibility in attaining low dark currents, thicker photoactive layers are preferable.

Figure 7.7c shows the J-V characteristics under illumination (one sun). Notably, devices with all photoactive layer thicknesses exhibit high reproducibility under illumination. In contrast, the reproducibility of the dark current is smaller. As the dark current is much smaller, it is more susceptible to defects, pinholes, and shunts. Increasing the thickness of the photoactive layer reduces the extracted short-circuit current density. In general, none of the devices exhibit a fully saturated photocurrent at short-circuit conditions. The applied bias range up to -5 V was insufficient to reach saturation for all photoactive layer thicknesses. At a bias voltage of -3 V, the photocurrent increases with the photoactive layer thickness, except for the thickest devices, which have not yet reached saturation. At -3 V the photocurrents stay within the same order of magnitude, differing by less than 20 % for OPDs with different photoactive layer thicknesses.

The on/off ratio in Figure 7.7d is calculated by the ratio of the current densities under

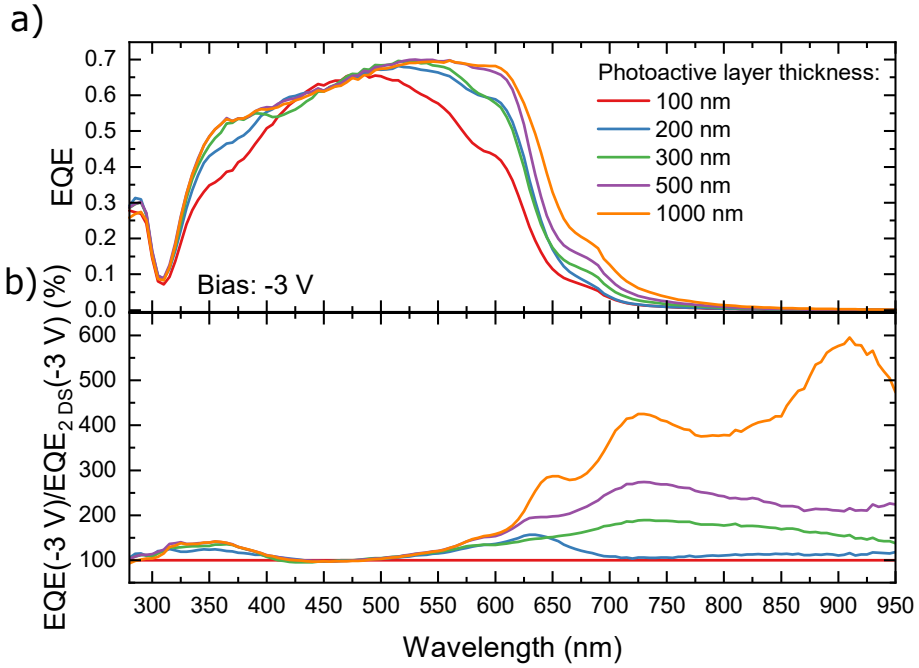

Figure 7.8: Spectral broadening of the EQE with increasing photoactive layer thickness. a) EQE for different numbers of deposition steps. Increasing the photoactive layer thickness flattens the EQE spectrum and leads to a significant increase in the infrared region. b) Relative increase in EQE for the photoactive layer thickness 200 nm, 300 nm, 500 nm and 1000 nm vs. the EQE for a photoactive layer thickness of 100 nm at a bias voltage -3 V.

illumination and in the dark. Especially, at a photoactive layer thickness of 500 nm, on/off ratios of 10^6 to 10^7 are reached, achieving state-of-the-art values [102, 106, 111, 196, 197]. A more thorough positioning of the OPDs with nanoparticulate photoactive layer within the literature is provided below, based on the specific detectivity.

7.4 Spectral broadening and detectivity

Figure 7.8a shows the EQE for different photoactive layer thicknesses at a bias voltage of -3 V. For a photoactive layer thickness of 100 nm, which is the typical thickness used for OSCs in this system, the EQE peaks at 480 nm. At both shorter and longer wavelengths, the EQE decreases. Increasing the thicknesses results in a flattening of the EQE around this maximum. In particular, for wavelengths greater than 650 nm, a significant increase in the EQE tail is observed. At 675 nm, the EQE increases from 7% to 20% between the samples with photoactive layer thicknesses of 100 nm and 1000 nm corresponding to a ratio of 285%.

Figure 7.8b shows the ratio of the EQE of OPDs with photoactive layer thicknesses of 200, 300, 500 and 1000 nm to the EQE of OPDs with photoactive layer thickness of 100 nm

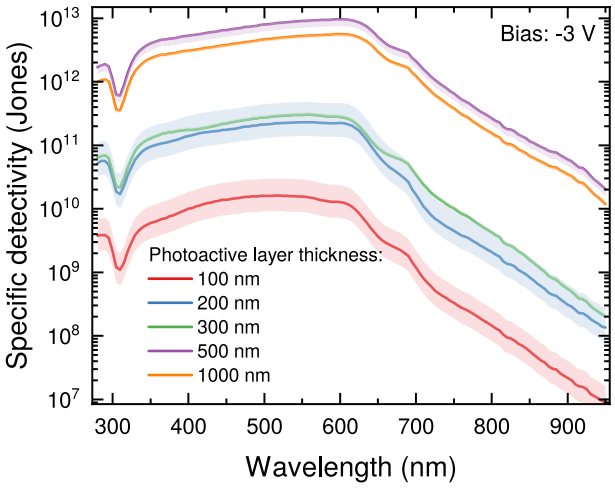

Figure 7.9: Median shot noise-limited specific detectivity of OPDs at a bias of -3 V. With increasing photoactive layer thickness up to 500 nm, the dark current decreases, and the EQE broadens, leading to higher and broader specific detectivity for thicker layers. For a photoactive layer thickness of 500 nm at a wavelength of 600 nm, a hero specific detectivity of $1.03 \cdot 10^{13}$ Jones is achieved, surpassing the reported literature value of $1.2 \cdot 10^{12}$ Jones for the reported value of P3HT:PC_{71}BM at -0.5 V bias voltage [106]. This is especially astounding as a larger reverse bias in this work has been applied.

at -3 V bias voltage. At longer wavelengths, the increase is more pronounced, reaching a maximum improvement of 590% at 910 nm within the recorded range of 280–950 nm. This shows that organic photodiodes with photoactive layers processed by nanoparticle dispersion exhibit spectral broadening by increasing the photoactive layer thickness as already observed for other processing techniques such as spray-coating, spincoating by solution as well as in simulations [99, 111, 178].

Figure 7.9 represents the specific detectivity D^* at a bias voltage of -3 V. The solid line represents the median, while the shaded area indicates the interquartile range [25,75]%. The specific detectivity increases with increasing photoactive layer thickness between 100 nm and 500 nm. In addition, a broadening of the specific detectivity is observed. At a photoactive layer thickness of 300 nm, a specific detectivity over 10^{11} Jones is achieved within the range of 335–648 nm. In comparison, for a thickness of 500 nm, the upper bound extends to 855 nm, representing a broadening of over 200 nm. Only devices with photoactive layer thickness of 500 nm or 1000 nm are capable of achieving a D^* of 10^{12} Jones, with the latter exhibiting a lower specific detectivity. The observed trend is primarily driven by differences in the dark current. The effect of EQE broadening upon increasing the photoactive layer thickness can be seen by comparing D^* for the photoactive layer thicknesses 200 nm and 300 nm, as their dark current medians are similar. The increasing D^* for the thickness of 300 nm at longer wavelengths results from the EQE broadening in

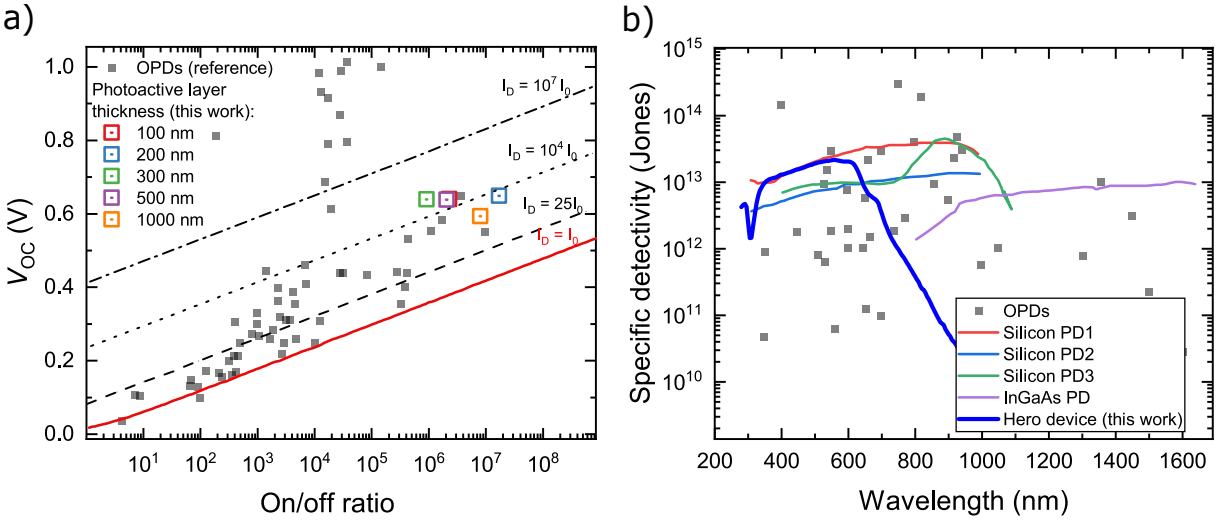

Figure 7.10: a) OPDs of this work and literature in a V_{OC} vs. the on/off ratio diagram. The on/off ratio, being the ratio of the photocurrent I_{ph} and dark current I_D, are given at a bias voltage of -0.1 V. The red line marks the intrinsic lower limit due to thermodynamic generation of charge carriers that would result in a current I_0. With a V_{OC} of approximately 0.6 V, the OPDs in this work exhibit a similar on/off ratio as OPDs in the literature. Reference data taken from [198]. b) shows the highest-performing OPD from this work (photoactive layer thickness 500 nm) at a bias voltage of -0.5 V, compared to OPDs in the literature. Reference data taken from [171].

thicker photoactive layers.

The hero detectivity for a photoactive layer thickness of 500 nm is $1 \cdot 10^{13}$ Jones at a bias voltage of -3 V. At -0.5 V, it increases to $2.1 \cdot 10^{13}$ Jones. This is one order of magnitude higher than the reported value of P3HT:$PC_{71}BM$ at a bias voltage of -0.5 V[106]. In the literature, no OPD was found with a photoactive layer of P3HT mixed with either ([6,6]phenyl-C_{61}-butyric acid methyl ester) $PC_{61}BM$ or $PC_{71}BM$ that surpass the highest-performing OPD of this work (see Table C.5). However, care must be taken, as only the shot noise limited detectivity (Equation 2.20) is measured in this work (four out of five publications in Table C.5 do the same). A discussion of the validity of comparing the shot noise limited values is found in Section 2.3.2.

Figure 7.10a presents the V_{OC} vs. the on/off ratio at a bias voltage of -0.1 V for OPDs in the literature and this work [198]. The on/off ratio is primarily determined by the dark current density, as the photocurrent is generally within the same order of magnitude across OPDs. The red line represents the intrinsic limit of the achievable on/off ratio for a given V_{OC}, based on the thermally generated dark current. Given the V_{OC} of OPDs in this work, they align with OPDs from other studies, although their dark current is not as low as the intrinsic limit.

Figure 7.10b compares the detectivity of the hero device (10 times spincoating) at -0.5 V

with OPDs in the literature. In the spectral range of 350-500 nm, the OPD can compete with silicon photodetectors and outperform many OPDs. However, for wavelengths larger than approximately 700 nm, higher detectivities can only be reached if other photoactive semiconductor combinations than P3HT:$PC_{71}BM$ with broader absorption spectra are employed.

8 Stabilization of Y6 dispersions by n-doping and their application in organic solar cells

OSCs made from P3HT:fullerene nanoparticle dispersions have demonstrated PCEs that exceed 4% [11]. Later, these dispersions were found to be intrinsically positively charged [12], prompting efforts to enhance charge carrier concentration through extrinsic p-doping for OSC fabrication [13, 73]. However, some semiconductors have a deep IP, making it difficult to p-dope them efficiently. In contrast, typical acceptors in OSCs have a deep EA, allowing them to easily accept electrons from other molecules and become negatively charged, undergoing n-doping. Following an extensive literature survey, no prior reports were identified that use n-doping to stabilize organic nanoparticle dispersions for subsequent device fabrication. The work presented here introduces the processing of an OSC photoactive layer from an n-doped organic nanoparticle dispersion, demonstrating that electrostatic stabilization via n-doping can be exploited as an alternative to p-dopant–based approaches.

First, the air stability of the n-dopants $(\text{N-DMBI})_2$ and pentamethylcyclopentadienyl mesitylene ruthenium dimer $((\text{RuCp*mes})_2)$ is examined, along with that of n-doped acceptors. Furthermore, it is demonstrated that Y6 can form stable nanoparticle dispersions when n-doped with $(\text{N-DMBI})_2$. It is investigated whether donors can be integrated into stabilized, n-doped Y6 nanoparticle dispersions. Finally, OSCs are fabricated using n-doped Y6 dispersions, together with the donor PIDT-T8BT. By counteracting n-doping in the photoactive layer and applying thermal annealing, a PCE of 0.8% is achieved.

8.1 Examination of n-dopants as stabilizing agents for nanoparticle dispersions

Figure 8.1a shows the stability of n-dopants, $(\text{N-DMBI})_2$ and $(\text{RuCp*mes})_2$, dissolved in CB at a concentration of $c_S = 19.6\,\text{mg}\,\text{L}^{-1}$ under inert conditions (N_2 atmosphere). The dopants are introduced in Section 2.1.5. The solution was placed into cuvettes in a glovebox, sealed with Parafilm, and measured using UV-Vis absorbance spectrometry. Afterward, the dopant solutions were exposed to air, and a pipette was used to flush air through the solution five times (0.2 mL per flush). The samples were then stored for 85

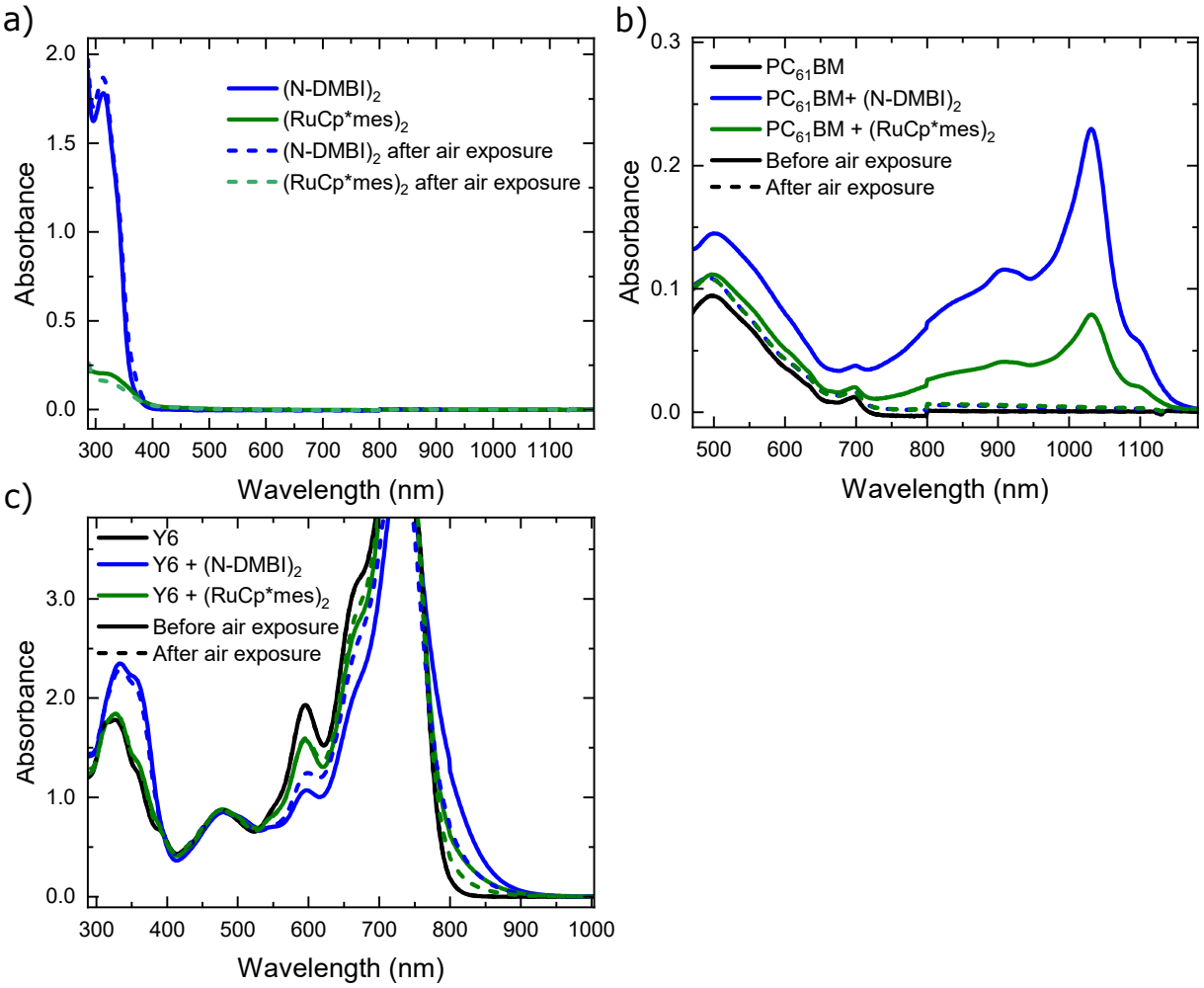

Figure 8.1: Absorbance spectra of dopants and semiconductors dissolved in CB under inert conditions and after exposure to air are shown in a)–c). a) The spectra of the dimeric n-dopants $(N\text{-}DMBI)_2$ and $(RuCp^*mes)_2$ remain unchanged after air exposure, consistent with previous reports [199, 200]. b) The emergence of a new absorbance band between 700 nm and 1150 nm upon mixing $PC_{61}BM$ with the dopants confirms successful n-doping, as this feature is absent in both the pure dopant and pure $PC_{61}BM$ solutions and is attributed to $PC_{61}BM^-$ [201]. After exposure to air, this band disappears, showing that n-doping of $PC_{61}BM$ in CB is not stable in ambient conditions. c) Similarly, Y6 exhibits characteristic spectral changes upon addition of the n-dopants, comparable to those seen in n-doped Y6 thin films [202]. These changes diminish after exposure to air, indicating that n-doping of Y6 in CB is likewise not stable under ambient conditions.

minutes and remeasured. The results show almost no change in the absorbance spectrum, confirming that the dopant in its dimer form remains stable against air exposure.
Figure 8.1b and c examine the air stability of n-doped $PC_{61}BM$ and Y6. Both acceptors were dissolved in CB at $23.8\,mg\,L^{-1}$ in a glovebox, and the dopants $(N\text{-}DMBI)_2$ and $(RuCp^*mes)_2$ were added ($5\,\mu L$ from solution, $0.5\,g\,L^{-1}$). The cuvettes were sealed with parafilm and measured using UV-Vis absorbance spectrometry. Afterward, air was flushed through the solution (five times, 0.2 mL per flush), and the samples were stored for 85 minutes before remeasuring. Before air exposure, $PC_{61}BM$ exhibited a polaron absorbance feature with a peak at 1030 nm [201]. However, after air exposure, these polaron bands disappeared, indicating that n-doping of $PC_{61}BM$ is not air stable. Y6 exhibits spectral changes upon the addition of the n-dopants, resembling the changes observed in n-doped thin films of Y6 [202] (Appendix C.11). Upon air exposure, these spectral changes decreased but did not vanish entirely, suggesting that n-doping on Y6 is more air stable compared to $PC_{61}BM$. A commonly accepted explanation for air sensitivity is the existence of an energy level associated with the LUMO in air and moisture, estimated between -3.6 and -4.0 eV [203, 204]. N-doped materials with a LUMO shallower than this range tend to lose electrons, making their n-doping unstable. Conversely, materials with a more negative LUMO are air stable, as their electrons already occupy the lowest available energy level. $PC_{61}BM$ has a LUMO of -3.7 eV [205], while Y6 has a LUMO of -4.1 eV [206]. This aligns with the experimental results, where $PC_{61}BM$ showed greater air sensitivity compared to Y6. However, it is important to note that energy levels depend on the measurement method and molecular environment. Y6 was chosen for further experiments. As $(N\text{-}DMBI)_2$ leads to stronger changes associated with n-doping in the absorbance of $PC_{61}BM$ and Y6 than $(RuCp^*mes)_2$, it was chosen for further investigation.
Nanoprecipitations from $CHCl_3$ are performed in ambient air to prevent damage to the glovebox filters caused by gaseous $CHCl_3$. Therefore, the stability of the dopant, $(N\text{-}DMBI)_2$, in $CHCl_3$ under ambient conditions was investigated. When freshly dissolved, $(N\text{-}DMBI)_2$ is transparent; however, it reacts with $CHCl_3$, turning yellow in 20-30 minutes. This behavior has also been observed in [207]. To prevent $(N\text{-}DMBI)_2$ from reacting with the solvent, one approach is to weigh the exact required amount of dopant. However, precise weighing can be challenging. A more practical method was to dissolve the dopant in dichloromethane (DCM) inside a glovebox, pipette the required amount into a vial, and let the DCM evaporate. DCM is preferred because of its low boiling point at 39.6 °C, allowing for rapid evaporation and minimizing the exposure of the dopant to solvent. However, $(N\text{-}DMBI)_2$ also reacts with DCM in 10-20 minutes, turning yellow. Therefore, evaporation should be completed in 1-2 minutes. This can be achieved by increasing

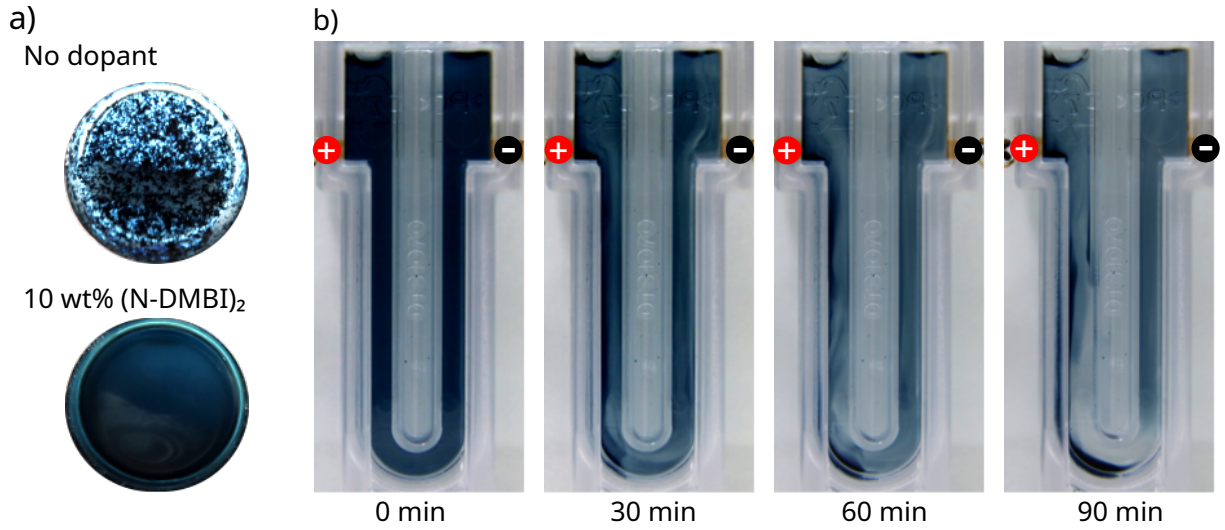

Figure 8.2: a) Picture of the beakers after nanoprecipitation of Y6 solution ($2\,\mathrm{g\,L^{-1}}$, $CHCl_3$) in EtOH, without dopant (top) and with the n-dopant ($(N\text{-}DMBI)_2$, 10 wt%) (bottom). Without the dopant, Y6 agglomerates immediately after nanoprecipitation, leading to visible flocculation. In contrast, adding the dopant to Y6 results in a homogeneously distributed dispersion. DLS measurements confirm a nanoparticle size of (25±2) nm for the doped dispersion, whereas undoped Y6 forms particles on the order of $\mathcal{O}(\mu m)$. b) Time series of a Y6:$(N\text{-}DMBI)_2$ dispersion under an applied voltage. Over 90 minutes, the initially uniform distribution of Y6 migrates toward the positively charged electrode, indicating that the nanoparticles carry a negative charge.

the concentration of $(N\text{-}DMBI)_2$ in DCM. Once the solvent has evaporated, the dopant can be stored without degradation, as there is no contact with solvents, oxygen, or moisture. With the method described above, the Y6 solutions are doped. Y6 ($2\,\mathrm{g\,L^{-1}}$, $CHCl_3$) is added to a vial in which an $(N\text{-}DMBI)_2$ DCM solution was previously pipetted and the DCM evaporated. This results in a Y6 solution with a dopant weight ratio of 10 wt% $(N\text{-}DMBI)_2$. The solution is left for three minutes at room temperature to allow Y6 doping by the dopant. The 0.5 mL solution is then nanoprecipitated by injecting it into 3.5 mL of EtOH under stirring with a magnetic stir bar (800 rpm), following the nanoprecipitation method described in Section 4.1.1. This achieves a stable nanoparticle dispersion (Figure 8.2a, bottom). DLS measurements yield a particle size of (25 ± 2) nm. In contrast, without the addition of the dopant to the Y6 solution, strong flocculation are visible, indicating the formation of large agglomerates (Figure 8.2a, top). This also confirms the insolubility of Y6 in EtOH. The volume of the dispersions is then reduced to 1 mL to remove $CHCl_3$ and increase the concentration. Agglomerates are removed by centrifugation (14,500 rpm, 2 min). Only dispersions prepared with freshly dissolved $(N\text{-}DMBI)_2$ in $CHCl_3$ or $(N\text{-}DMBI)_2$ from an evaporated DCM solution, as described above, can undergo volume reduction, meaning that $CHCl_3$ and part of the dispersion

medium EtOH are evaporated until the volume is reduced to 1 mL. However, dispersions prepared with a reacted (N-DMBI)$_2$ solution in $CHCl_3$ (yellow tint) flocculate during volume reduction, indicating insufficient stabilization. Two nanoparticle dispersions of Y6 doped with (N-DMBI)$_2$ from the evaporated DCM solution at 10 wt% were analyzed using DLS. The measured nanoparticle size of (25 ± 2) nm immediately after nanoprecipitation increased to (67 ± 3) nm after volume reduction in a water bath at 50 °C (errors denote the standard deviation of individual DLS measurements). After six days, the nanoparticle size further increased to (155 ± 17) nm.
Dimethyl sulfoxide (DMSO) was also tested as a dispersion medium, but flocculation occurred immediately after nanoprecipitation. CH_3CN as a dispersion medium was tested under the same conditions, yielding nanoparticle sizes of (27 ± 1) nm, (38 ± 4) nm, and (49 ± 3) nm immediately after nanoprecipitation, after volume reduction, and after six days, respectively. Although the nanoparticle sizes were smaller in CH_3CN, EtOH is preferred due to its environmentally friendly classification [54, 57]. EtOH is less toxic, and its biodegradability allows for cheaper disposal costs [208].
Furthermore, solvents were examined as potential storage media for the dopant. The dopant was dissolved in $CHCl_3$, CH_3CN, and CB at a concentration of $5\,\mathrm{g\,L^{-1}}$ and stored for one week. The $CHCl_3$ solution was stored in air, while CH_3CN and CB solutions were stored under inert conditions (N_2 atmosphere). A nanoprecipitation of Y6 with 10 wt% (N-DMBI)$_2$, stored in $CHCl_3$, immediately resulted in flocculation under the same nanoprecipitation parameters as described above. In contrast, dopants stored in CH_3CN and CB yielded small nanoparticles with sizes of (25 ± 1) nm and (41 ± 5) nm, respectively. The volume-reduced nanoparticle dispersions maintained sizes below 100 nm. However, it is important to note that the dopant did not fully dissolve in CH_3CN even after a week, making it less practical for further use. CB has a higher boiling point (131.7 °C) than $CHCl_3$ and commonly used dispersion media (such as EtOH, IPA, and CH_3CN), making it difficult to remove from the dispersion. Therefore, the DCM evaporation method, as described above, was chosen for further experiments.

To determine whether positive or negative charges stabilize the nanoparticle dispersions, an electrophoresis experiment was conducted. A Y6 dispersion doped with (N-DMBI)$_2$ (10 wt%) in EtOH dispersion, with a concentration of $c_D = 0.75\,\mathrm{g\,L^{-1}}$, was diluted by a factor of 10 and filled into a U-shaped cuvette with two electrodes positioned at the upper edges of each end (see Figure 8.2b). A voltage of 50 V was applied. Over time, a density gradient formed, indicating that the particles migrated toward the positively charged

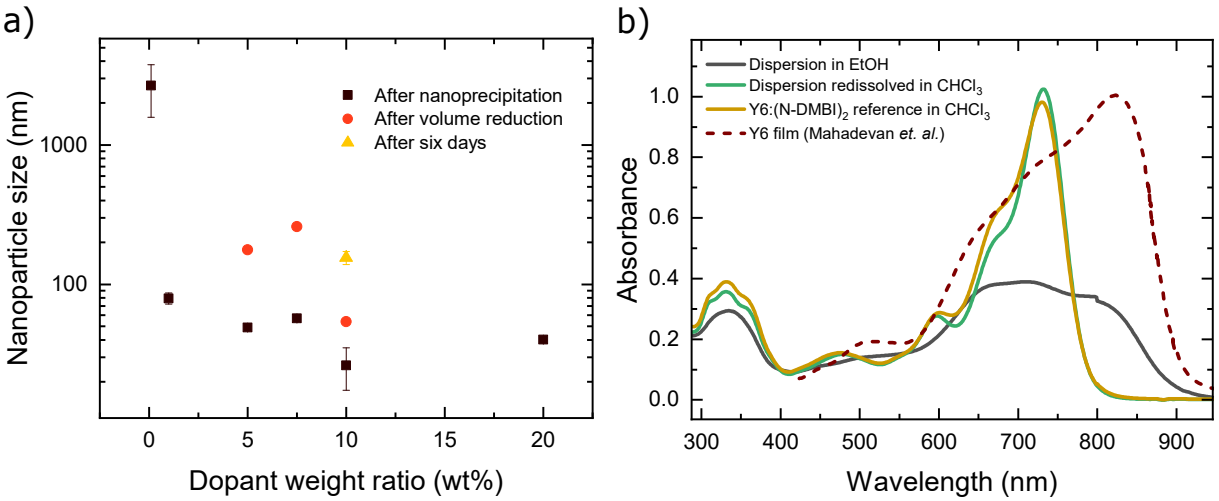

Figure 8.3: a) Nanoparticle sizes of Y6 doped with different concentrations of $(N\text{-}DMBI)_2$. The amount of dopant determines if dispersions can undergo volume reduction. In this series, volume reduction was only possible for dispersions with 5, 7.5, and 10 wt% DWR. The error bars represent the standard deviation of separate DLS measurements on the same sample. b) UV-Vis absorbance spectra of Y6 doped with $(N\text{-}DMBI)_2$ (10 wt%): dissolved in $CHCl_3$, as a nanoprecipitated dispersion in EtOH (volume-reduced), and redissolved dispersion in $CHCl_3$. For comparison, the absorbance of a Y6 thin film (Mahadevan *et. al.*) is shown [209].

electrode. This observation leads to the conclusion that the nanoparticles carry a negative charge.

8.2 Y6 dispersions for layer deposition

In the following, the amount of dopant required to stabilize the Y6 dispersions is described. Therefore, Y6 dispersions were synthesized with a varying dopant weight ratio. $(N\text{-}DMBI)_2$ was dissolved in DCM (5 g L^{-1}) inside a glovebox. Different amounts were added to vials, and the DCM was evaporated. Then, 0.7 mL of Y6 solution (2 g L^{-1} in $CHCl_3$) was added. The specific amounts of $(N\text{-}DMBI)_2$ were adjusted relative to Y6 to achieve DWRs of 0.1, 1, 5, 7.5, 10, and 20 wt%. $(N\text{-}DMBI)_2$ remained in contact with Y6 and $CHCl_3$ for 3 minutes. Then, 0.5 mL of this solution was nanoprecipitated into 3.5 mL of EtOH, as described above. The volume reduction was performed in a water bath at 50 °C until a volume of 1 mL was reached. Agglomerates were removed by centrifugation (14,500 rpm, 2 min).

Figure 8.3a shows the nanoparticle sizes as a function of the DWR. All dispersions, except for the dispersion with the lowest DWR, exhibited nanoparticle sizes below 100 nm. However, only the dispersions with DWRs of 5 wt%, 7.5 wt%, and 10 wt% remained stable during volume reduction. Among these, only the 10 wt% dispersion remained stable after

six days, while the other dispersions flocculated. Therefore, a DWR of 10 wt% was chosen for further experiments.

Figure 8.3b shows the absorbance spectra of Y6 doped with 10 wt% $(N\text{-}DMBI)_2$ in different configurations: as a solution, as a dispersion and as a redissolved dispersion, where the dispersion medium (EtOH) was evaporated and the semiconductor material was redissolved in $CHCl_3$. In addition, the absorbance spectrum of a Y6 film is shown [209]. The Y6 film exhibits a red-shifted peak compared to the solution, attributed to the changes of the packed molecules in a solid compared to the isolated molecules in solution [210]. The absorbance spectrum of the dispersion differs significantly from that of the solution phase, exhibiting a broader absorption spectrum with increased intensity in the infrared range. Because nanoparticles represent solid structures surrounded by a dispersion medium, the molecular packing in the nanoparticles may explain the observed infrared shift in their absorbance. Previously, the absorbance shift from solution to nanoparticle dispersion in P3HT material had been shown to be similar to the shift observed from solution to solid films [74].

In the following, the Y6 concentration of the initial solution used for the nanoprecipitation is increased to investigate its effect on the final dispersion concentration. $(N\text{-}DMBI)_2$ was dissolved in DCM inside a glovebox. Different amounts were added to vials, and the DCM was evaporated. Then, 0.7 mL of Y6 solution with $c_S = 1\,g\,L^{-1}$ to $c_S = 4\,g\,L^{-1}$ in $CHCl_3$ was added. The DWR is kept constant at 10 wt%. $(N\text{-}DMBI)_2$ remained in contact with Y6 and $CHCl_3$ for 3 minutes. Then, 0.5 mL of this solution was nanoprecipitated into 3.5 mL of EtOH, as described above. The volume reduction was performed in a water bath at 50 °C until a volume of 1 mL is reached. Agglomerates were removed by centrifugation (14,500 rpm, 2 min).

Figure 8.4a and b show the nanoparticle size and dispersion concentration versus the initial Y6 concentration c_S in $CHCl_3$. Increasing the Y6 concentration leads to larger nanoparticle sizes. After nanoprecipitation, this change is relatively small, but after volume reduction, it becomes more pronounced.

Constrained by the procedure of nanoparticle synthesis the dispersion concentration, c_D, can maximally achieve half of c_S. However, because of agglomeration and sedimentation, the real value is often lower. Figure 8.4b presents the dispersion concentration c_D. For its determination, 60 µL of the dispersion was placed in a vial, the dispersion medium was evaporated, and the remaining semiconductor was redissolved in $CHCl_3$. The absorbance was then measured and compared to a reference Y6:$(N\text{-}DMBI)_2$ (10 wt%) solution with a known concentration. Up to an initial $CHCl_3$ concentration of $c_S = 3\,g\,L^{-1}$, the dispersion concentration increases slightly sublinearly. However, at $c_S = 4\,g\,L^{-1}$, a sharp decrease is

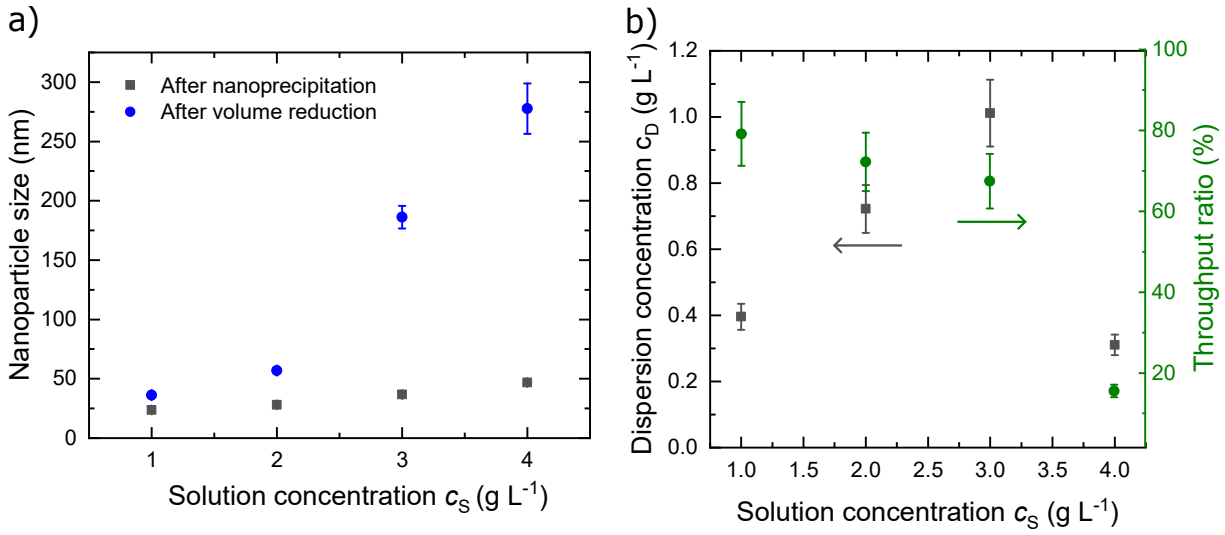

Figure 8.4: a) Nanoparticle size of Y6:(N-DMBI)$_2$ (10 wt%) as a function of the initial Y6 concentration in $CHCl_3$ solution. Increasing the initial concentration, c_S, results in a notable increase in nanoparticle size, particularly after volume reduction. The error bars represent the standard deviation of separate DLS measurements on the same sample. b) Dispersion concentration and throughput ratio (see text for definition) of the volume-reduced dispersions. Increasing the initial Y6 $CHCl_3$ concentration up to $c_S = 3\,\mathrm{g\,L^{-1}}$ leads to a higher dispersion concentration while maintaining a relatively constant throughput ratio of approximately 80%. $c_S = 4\,\mathrm{g\,L^{-1}}$ leads not only to very large particles after volume reduction but also to low dispersion concentrations.

observed. The ratio of the actual dispersion concentration c_D to the maximally possible dispersion concentration $c_{D,max}$, hereinafter called throughput ratio η, is defined by

$$\eta = \frac{c_D}{c_{D,max}}. \tag{8.1}$$

It describes the fraction of semiconductor that undergoes the transformation from dissolved to dispersed and is optimally high for the application of layer deposition. Figure 8.4b shows that up to $c_S = 3\,\mathrm{g\,L^{-1}}$ the throughput ratio slightly decreased, followed by a sharp drop.

These dispersions are intended for the deposition of thin-film layers with thicknesses of approximately 100 nm. Large nanoparticles could introduce large surface roughness relative to the actual layer thickness. Furthermore, the throughput ratio η should be high to avoid loss of Y6 during nanoparticle synthesis. Therefore, a solution concentration of $c_S = 2\,\mathrm{g\,L^{-1}}$ is chosen for further experiments as a trade-off, yielding a dispersion concentration of nearly $c_D = 0.8\,\mathrm{g\,L^{-1}}$.

8.3 Co-stabilization of donors in Y6 dispersions

For the fabrication of OSCs, Y6 must be mixed with donors to enable efficient exciton dissociation. PM6, poly[(thiophene)-alt-(6,7-difluoro-2-(2-hexyldecyloxy)quinoxaline)] (PTQ10), J71, and P3HT were mixed with Y6 in a 1:1 ratio, with a total concentration of $c_S = 0.5\,g\,L^{-1}$ in $CHCl_3$, doped with 10 wt% $(N\text{-}DMBI)_2$. The dopant weight ratio is defined with respect to the total mass of Y6 and dopant only (excluding the donor). The nanoprecipitations with the first three donors, PM6, PTQ10 and J71, resulted in strong flocculation, with no significant dispersion after volume reduction. The nanoprecipitation with P3HT achieved an η of approximately 40% for Y6 and 30% for P3HT in the volume-reduced dispersion.

It has already been observed that the incorporation of acceptors in (intrinsically) p-doped P3HT nanoparticles, such as fullerenes, poses a challenge when aiming for stable nanoparticle dispersions [170]. Therefore, in the following experiments, a donor-acceptor mixture with a higher Y6:donor ratio is pursued. Dolan *et al.* demonstrated that the polymer poly[2,1,3-benzothiadiazole-4,7-diyl(4-hexyl-2,5-thiophenediyl)[4,4,9,9-tetrakis(4-hexylphenyl)-4,9-dihydro-s-indaceno[1,2-b:5,6-b′]dithiophene-2,7-diyl](3-hexyl-2,5-thiophenediyl)] (PIDT-T8BT) can be used together with Y6 in efficient OSCs [211]. For a donor-acceptor ratio of 1:10, a PCE exceeding 10% was achieved.

The observation that only small amounts of donor are required suggests co-stabilizing PIDT-T8BT in n-doped Y6 dispersions. PIDT-T8BT was mixed with Y6 in acceptor-donor ratios of 9:1 (w/w) and 8:2 (w/w) at a total concentration of $c_S = 2\,g\,L^{-1}$ in $CHCl_3$. A reference containing only Y6 at $c_S = 2\,g\,L^{-1}$ was also prepared. A volume of 0.5 mL of each $CHCl_3$ solution was nanoprecipitated in a beaker containing 3.5 mL of EtOH while stirring at 800 rpm. A water bath at 50 °C was employed to evaporate $CHCl_3$ and reduce the dispersion volume to 1 mL. Agglomerates were removed by centrifugation (14,500 rpm, 2 min).

Figure 8.5a shows the nanoparticle size resulting from these experiments. Increasing the PIDT-T8BT fraction leads to larger nanoparticles after nanoprecipitation and volume reduction. At an 8:2 acceptor-donor ratio, the nanoparticle size in the volume-reduced dispersion reaches 150 nm, which is relatively large for thin-film processing. However, the size at a 9:1 (w/w) acceptor-donor ratio remains within the range previously used for nanoparticle-based OSCs [11, 73, 134].

To confirm the presence of PIDT-T8BT in the dispersion, the volume-reduced dispersions were redissolved and analyzed using UV-Vis absorbance spectrometry. Specifically, a small fraction of the dispersion (60 µL) was separated, the dispersion medium was evaporated

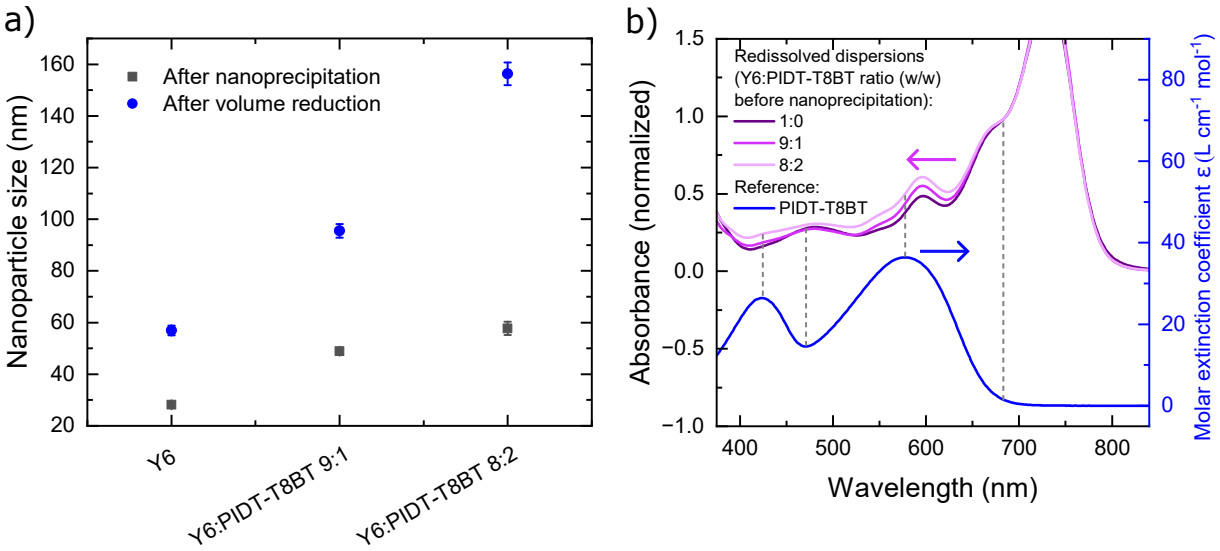

Figure 8.5: Y6:PIDT-T8BT solution ($c_S = 2\,g\,L^{-1}$, $CHCl_3$) nanoprecipitated in EtOH. a) Nanoparticle sizes. Increasing the PIDT-T8BT ratio increases the nanoparticle size. The error bars represent the standard deviation of separate DLS measurements on the same sample. b) Absorbance of redissolved dispersions, normalized to the Y6 IBP at 686 nm. Increasing the PIDT-T8BT concentration in dispersion, an increased absorbance is observed in the range where PIDT-T8BT absorbs (compare with the blue reference). This indicates that PIDT-T8BT is incorporated into the nanoparticle dispersion.

and the remaining material was redissolved in 1.6 mL $CHCl_3$. Figure 8.5b shows the corresponding UV-Vis absorbance spectra, normalized to the Y6 concentration (by normalizing them to the IBP of Y6 at 686 nm). As a reference, the molar extinction coefficient of PIDT-T8BT is also displayed. In the spectral range where PIDT-T8BT absorbs, clear differences appear in the spectra corresponding to different Y6:PIDT-T8BT ratios before nanoprecipitation. Notably, the largest differences occur at the wavelength at which the absorbance peak of PIDT-T8BT is located.

Determining the exact concentration of PIDT-T8BT in the dispersion is challenging, as fitting the total absorbance with spectra from Y6:$(N\text{-}DMBI)_2$ (10 wt%) and PIDT-T8BT reference solutions does not capture all spectral characteristics. This discrepancy arises because the fit would assume the same doping efficiency for the redissolved dispersion and the reference, which is not necessarily the case. However, estimating the concentration of Y6 from its IBP yields $0.72\,g\,L^{-1}$, $0.65\,g\,L^{-1}$, $0.56\,g\,L^{-1}$ for the 1:0, 9:1 (w/w), and 8:2 (w/w) Y6:PIDT-T8BT ratios, respectively. Similarly, estimating the concentration of PIDT-T8BT from its molar extinction coefficient peak at 578 nm results in $0\,g\,L^{-1}$, $0.08\,g\,L^{-1}$, $0.14\,g\,L^{-1}$ for the respective ratios.

These results indicate that the nanoprecipitation process achieves a throughput ratio

slightly above 70% for both Y6 and PIDT-T8BT, and the initial acceptor-donor ratio before nanoprecipitation is retained in the final dispersion. Due to its smaller nanoparticle size, the 9:1 (w/w) acceptor-donor ratio is selected to fabricate OSC photoactive layers from n-doped nanoparticle dispersions in the following section.

8.4 Organic solar cells

In the previous section, it was demonstrated that nanoparticle dispersions can be synthesized using n-doped Y6. Furthermore, the acceptor-donor mixture Y6:PIDT-T8BT, which has already been used as a photoactive layer material in OSCs, was shown to form nanoparticles with acceptable sizes and dispersion concentrations. In this section, these dispersions are utilized as inks to process the photoactive layer of OSCs.

8.4.1 Effect of n-doping on OSC

The following architecture was chosen for OSCs, ITO/ZnO/photoactive layer/MoO_x/Ag, as the architecture had been shown to yield good efficiencies with Y6 and PIDT-T8BT as photoactive layer semiconductors [211]. The pre-structured ITO glass substrates were treated with an oxygen plasma (2 min). The following steps were done in a glovebox ($O_2 < 1$ ppm, $H_2O < 1$ ppm). ZnO was spincoated (2000 rpm, 40 s) from zinc oxide nanoparticles (1 wt%, in butanol), the substrates were subsequently annealed at 120 °C (10 min). MoO_x and Ag were evaporated at a pressure of $1 \cdot 10^{-6}$ mbar, MoO_x with a rate < 1 Ås^{-1} (10 nm) and Ag (1 Å s^{-1}, 10 nm and 2.5 Å s^{-1}, 90 nm).
First, OSCs with Y6:PIDT-T8BT photoactive layers processed from solution were fabricated to analyze the influence of n-doping. The photoactive layer was spincoated (2000 rpm, 1 min) from a 9:1 (w/w) Y6:PIDT-T8BT solution (20 g L^{-1}, $CHCl_3$) and annealed at 150 °C for 10 minutes. The thickness was measured to be 200 ± 15 nm (mean and standard deviation of individual measurements on the same sample) by a Bruker Dektak XT tactile profiler. Devices with undoped and n-doped, 0.4 wt% and 0.8 wt%, photoactive layer were prepared. A doping concentration of 10 wt%, as used for nanoparticles, would be more comparable, but is not possible because Y6 loses its solubility in $CHCl_3$ upon n-doping.
Two substrates (each with four devices) were fabricated for each variation. Before recording the J-V curves, the substrates were light-soaked for 120 s using a xenon solar simulator. The resulting J-V curves are shown in Figure 8.6a, and the corresponding OSC characteristics are summarized in Table 8.1. Upon n-doping, V_{OC} decreases. However, several studies have shown that introducing small dopant concentrations into bulk-heterojunctions do not affect, or can even increase the V_{OC}. This behavior is attributed to an increase in charge

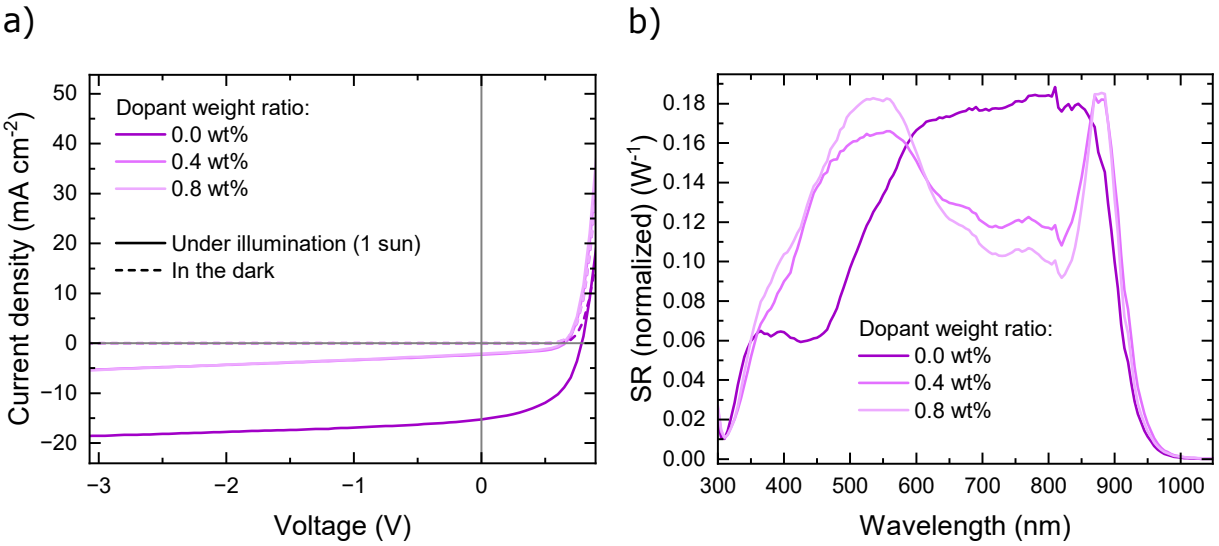

Figure 8.6: Characteristics of OSCs with solution-processed Y6:PIDT-T8BT (9:1 w/w) photoactive layers for different n-doping ratios. a) shows that the current density upon n-doping the photoactive layer is strongly reduced. Applying a negative voltage increases J. b) Upon n-doping, the normalized SR, showing the relative SR contribution to J_{SC}, changes - there is less contribution in the wavelength regime in which Y6 (films) absorbs, compare with Figure 8.3.

Table 8.1: Solar cell characteristics of OSCs with solution-processed Y6:PIDT-T8BT (9:1 w/w) photoactive layers at different dopant weight ratios. Upon n-doping V_{OC}, J_{SC}, FF and PCE decrease. Reported values represent mean ± standard deviation.

DWR	V_{OC} (mV)	J_{SC} (mA cm^{-2})	FF (%)	PCE (%)	N
0 wt%	789 ± 2	15.1 ± 0.2	51.7 ± 0.7	6.17 ± 0.15	8
0.4 wt%	683 ± 8	2.38 ± 0.18	49 ± 1.2	0.797 ± 0.081	8
0.8 wt%	641 ± 7	2.01 ± 0.05	45.5 ± 0.2	0.585 ± 0.014	8

carrier concentration and mobility, as well as favorable morphological modifications [202, 212]. Optimal dopant concentrations that improve device performance were reported to be of the order of $\mathcal{O}(10^{-3}\,\text{wt\%})$ to $\mathcal{O}(10^{-2}\,\text{wt\%})$ for n-dopants such as N-DMBI [202, 213]. At higher dopant concentrations, the V_{OC} decreases strongly, which is commonly attributed to excessive shifts in energy levels within the OSC and an increased density of trap states [14, 214–216]. This decrease typically begins at concentrations on the order of $\mathcal{O}(10^{-1}\,\text{wt\%})$, corresponding to the range used to fabricate the OSCs presented in Table 8.1 and Figure 8.6 [202, 212, 214].

Figure 8.6b shows the normalized SR (SR divided by short-circuit current) to compare the spectral contributions to J_{SC}. In the n-doped OSCs, most of the response is located in the short-wavelength regime, leading to photons with wavelengths $< 550\,\text{nm}$

to contribute more to J_{SC} than longer-wavelength photons. In contrast, the undoped OSC exhibits a high SR plateau at longer wavelengths (600 nm $< \lambda <$ 900 nm). This suggests that n-doping relatively reduces the contribution to J_{SC} in the absorption range of Y6 while increasing the contribution in the absorption range of PIDT-T8BT. The effect increases for higher doping weight ratios. A lower internal quantum efficiency in the absorbance range of the acceptor was also observed when n-doping BHJ with PM6 and 3,9-bis(2-methylene-((3-(1,1-dicyanomethylene)-6,7-difluoro)-indanone))-5,5,11,11-tetrakis(4-hexylphenyl)-dithieno[2,3-d:2',3'-d']-s-indaceno[1,2-b:5,6-b']dithiophene (ITIC-4F). Additional electrons introduced by n-doping on the acceptor may lead to a lower exciton generation rate of the acceptor domains [216].
The short-circuit current density, J_{SC}, is significantly reduced in the doped devices. However, applying a negative voltage increases their current density. At -3 V, the current density increases by a factor of more than two, indicating that charge carriers are generated but require an electric field for efficient extraction. This suggests an unfavorable microstructure, which may hinder exciton separation or reduce percolation pathways for free charge carriers. Doping alters the electrostatics of materials and can induce morphological changes such as aggregation of the doped material [215, 217, 218]. This could also affect miscibility with PIDT-T8BT. Moreover, simulations show that introducing n- or p-type doping into otherwise optimized OSCs could lower J_{SC} by increasing recombination: doping-induced space charge concentrates the electric field near the cathode or anode interfaces but flattens it across the bulk of the photoactive layer, where the weak field promotes recombination [168]. In OSCs with Y6:donor photoactive layers, it has been shown that small amounts of dopant (on the order of 10^{-3} wt%) can improve the microstructure and increase J_{SC}, but higher doping concentrations reduce it [216]. In Section 8.4.3, it is observed that annealing of these doped OSCs at higher temperatures significantly increases J_{SC}.

8.4.2 OSCs fabricated from n-doped Y6:PIDT-T8BT dispersions

For OSCs fabricated from n-doped Y6:PIDT-T8BT dispersions, the device architecture was identical to that described in Section 8.4.1. A volume of 0.5 mL Y6:PIDT-T8BT (9:1 w/w) solution ($CHCl_3$, 2 g L^{-1}) was nanoprecipitated into a beaker containing 3.5 mL of EtOH while stirring at 800 rpm. A water bath at 50 °C was employed to evaporate $CHCl_3$ and reduce the dispersion volume to 1 mL. Agglomerates were removed by centrifugation (14,500 rpm, 2 min). As examined in Section 8.2, this yields a dispersion concentration of approximately 0.7 g L^{-1}. For the photoactive layer, one substrate was spincoated (1000 rpm) with 30 dynamic deposition steps and another with 40 steps, having a 20 s

Table 8.2: OSCs with photoactive layers fabricated from Y6:PIDT-T8BT (9:1 w/w) 10 wt% $(N\text{-}DMBI)_2$ dispersions. t_{steps} is the number of deposition steps of the photoactive layer. The column Treatment describes if the photoactive layer has been treated with the p-dopant F_4TCNQ to reduce the effect of n-doping in the layer (see the text for the whole process). N is the number of devices. Reported values represent mean ± standard deviation.

t_{steps}	Treatment	V_{OC} (mV)	J_{SC} (mA cm^{-2})	FF (%)	PCE (%)	N
30	None	333 ± 11	0.54 ± 0.01	33.1 ± 0.5	0.059 ± 0.002	4
40	None	470 ± 3	0.405 ± 0.005	29.0 ± 0.1	0.055 ± 0.001	4
40	F_4TCNQ	684 ± 4	1.08 ± 0.01	27.3 ± 0.1	0.202 ± 0.003	3

drying time between the deposition steps. The films were annealed at 150 °C. The other layers of the stack are prepared as explained in Section 8.4.1. The dispersion was also spincoated 20 times onto a glass substrate, yielding a thickness of 4.2 ± 0.15 nm per deposition step (mean ± standard deviation), as measured with a Bruker Dektak XT tactile profiler. Accordingly, a photoactive layer processed with 30 spincoating steps results in a thickness of 125 ± 5 nm, and 40 steps yield 168 ± 6 nm.

Figure 8.7a shows the *J-V* curves of devices with nanoparticulate photoactive layers, and Figure 8.7b presents the normalized SR. The corresponding device parameters are listed in Table 8.2. The *J-V* characteristics confirm that OSCs with a photoactive layer can be fabricated using n-doped Y6:PIDT-T8BT nanoparticle dispersions. However, the PCE is low. Compared to the reference with photoactive layer processed from an undoped solution in Section 8.4.1, the reduced performance arises from lower V_{OC}, J_{SC}, and FF. While V_{OC} and FF are of comparable magnitude to the reference, J_{SC} is roughly two orders of magnitude smaller.

Several observations indicate that Y6 remains n-doped in the nanoparticulate photoactive layer. 1) The V_{OC} is lower than in the solution-processed reference with undoped photoactive layer, consistent with the behavior discussed in Section 8.4.1. 2) The normalized SR closely matches that of solution-processed OSCs with n-doped photoactive layer and differs strongly from the reference with undoped photoactive layer. 3) The organic stack was redissolved in $CHCl_3$ and measured by UV-Vis absorbance spectrometry (Figure 8.7). Spectra were normalized to the Y6 concentration via the IBP position at 686 nm, where the absorbance of Y6 in $CHCl_3$ is independent of doping concentration (Appendix C.11). The main absorbance peak of the redissolved film lies between those of neat Y6 and Y6:$(N\text{-}DMBI)_2$ (10 wt%), indicating that the deposited layer remained doped. Below 650 nm, the redissolved film exhibits higher absorbance than either Y6 or Y6:$(N\text{-}DMBI)_2$

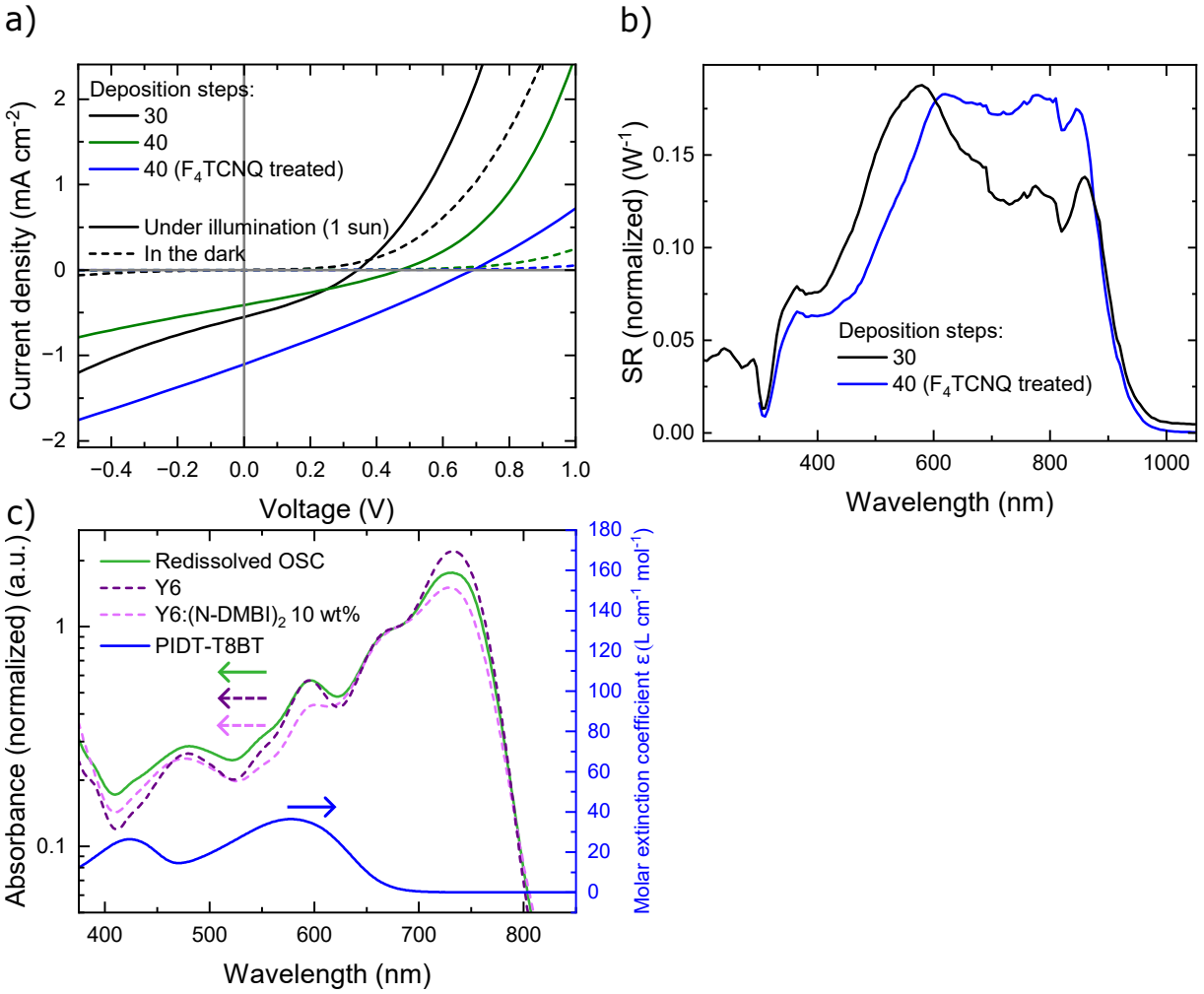

Figure 8.7: OSCs with photoactive layer fabricated by Y6:PIDT-T8BT (9:1 w/w) 10 wt% $(N\text{-}DMBI)_2$ dispersions. a) J-V curves. b) Normalized SR. The J-V curves and recorded SR show that it is possible to process OSCs from n-doped Y6:PIDT-T8BT dispersions. To counteract the effect of n-doping in the photoactive layer, a device is fabricated in which F_4TCNQ solution (in CH_3CN) is deposited between dispersion deposition steps ("F_4TCNQ treated"). This increases both V_{OC} as J_{SC}. c) Absorbance of a redissolved OSC with photoactive layer fabricated by dispersion compared with neat Y6, Y6 10 wt% $(N\text{-}DMBI)_2$ normalized to the Y6 concentration. Blue shows the molar extinction coefficient of PIDT-T8BT. The Y6 peak at 730 nm has an absorbance between the reference Y6 solution (undoped and 10 wt%) which indicates that the dopant is still nested in the OSC. In the wavelength range, in which PIDT-T8BT absorbs, the redissolved OSC solution absorbs equally or more than the reference Y6 solutions (undoped and 10 wt%) indicating that PIDT-T8BT is incorporated into the layer.

(10 wt%), consistent with a third absorber - most likely PIDT-T8BT - which dominates in this spectral region. An identical outcome was obtained in a control experiment where the photoactive layer was deposited on glass.
These observations strongly suggest that $(N\text{-}DMBI)_2$ and PIDT-T8BT remain in the photoactive layer of the OSC. The presence of n-doping directly reduces OSC performance by lowering V_{OC}, J_{SC} and FF which leads to a low efficiency.

The following paragraph addresses strategies to counteract the poor performance of the OSCs above by deactivating or removing the dopant from the photoactive layer. The core idea is to introduce the p-dopant F_4TCNQ into the layer to neutralize the monomeric n-dopant N-DMBI. Additional electrons from n-dopants occupy the LUMO of Y6. When an electron-affine molecule such as F_4TCNQ is introduced, electrons from the Y6 LUMO can transfer to the F_4TCNQ LUMO. Depending on the mobilities of F_4TCNQ and N-DMBI, the oppositely charged dopants may diffuse through the layer and form dipolar charge-transfer complexes, effectively reducing their electrostatic influence. To evaluate this approach, the device architecture was chosen to be that described above, but the photoactive layer processing was modified as follows: The dispersion was dynamically spin-coated (1000 rpm) 40 times. In addition, an F_4TCNQ solution (0.2 g L^{-1} in CH_3CN) was spin-coated (1000 rpm) after every second dispersion deposition step (20 F_4TCNQ treatments in total). A delay of 20 s elapsed between each deposition step. The dispersion was nanoprecipitated with 10 wt% of $(N\text{-}DMBI)_2$, corresponding to a nominal dopant concentration of approximately 0.1 g L^{-1} in the deposited ink. Since F_4TCNQ is applied every second deposition step at 0.2 g L^{-1}, the delivered masses per two-step cycle are of similar magnitude. Given that the molar masses of F_4TCNQ (276.15 g mol^{-1}) and the monomeric equivalent of N-DMBI (267.37 g mol^{-1}) are very similar, the nominal molar quantities of p- and n-dopant introduced during processing are comparable, assuming similar uptake. It should be noted that the solvents differ (EtOH for the dispersion and CH_3CN for F_4TCNQ), so this comparison is not an exact stoichiometric matching but rather an estimate to verify whether the p-dopant can counteract the n-doping effect in the layer.
Figure 8.7a presents the *J-V* curves of the devices treated with F_4TCNQ ("F_4TCNQ treated"), while Table 8.2 summarizes the corresponding OSC parameters. The F_4TCNQ treatment significantly increases both V_{OC} and J_{SC}. Previously, n-doping was shown to decrease these parameters in OSCs with solution-processed photoactive layers. Thus, the observed increase in V_{OC} and J_{SC} suggests that the p-dopant helped to counteract the effect of the n-dopant.

Figure 8.7b compares the normalized SR of the F_4TCNQ-treated OSC with that of the previously presented untreated device (30 deposition steps). Notably, the treated device exhibits a stronger SR at longer wavelengths, further supporting the hypothesis that F_4TCNQ reduces the influence of n-doping, which was previously shown to suppress the response at these wavelengths (see Figure 8.6). Thus, a plausible explanation for the improved OSC performance and increased PCE following F_4TCNQ treatment is the reduction of n-doping within the photoactive layer. However, despite these improvements, the performance of OSC with nanoparticle-processed photoactive layers is significantly lower than OSCs with undoped, solution-processed photoactive layers.

8.4.3 Improving OSC characteristics by annealing

Another reason for the reduced performance of OSCs with photoactive layers from nanoparticle dispersions compared to OSCs with photoactive layers from solution-processed devices is the microstructure of the nanoparticulate layers [169]. Fullerenes were shown to spatially reorganize in P3HT:fullerene layers, reducing the roughness of deposited layers from nanoparticle dispersions [81]. OSCs fabricated from PTB7:$PC_{71}BM$ dispersions stabilized by F_4TCNQ exhibited poor device characteristics compared to their solution-processed counterparts. This was attributed to a potentially unfavorable microstructure [13]. Nanoparticles tend to form a highly porous layer upon deposition, particularly in the absence of post-processing treatments, such as annealing. The porosity of these layers can lead to suboptimal charge transport properties and increased recombination losses. To mitigate these issues, thermal annealing is commonly applied to promote the fusion of individual nanoparticles, thereby reducing porosity and improving the film morphology.
The OSCs with solution-processed photoactive layers, introduced in Section 8.4.1, were post-built annealed at 180 °C for 10 minutes. Table 8.3 presents the OSC characteristics after post-built annealing (compare with Table 8.1 before post-annealing). The doped devices exhibit a significant increase in J_{SC}, FF, and PCE after post-annealing. Figure 8.8a displays the normalized SR. After post-annealing, the spectral shape of both undoped and doped samples becomes more similar, indicating a higher contribution to photocurrent generation in the wavelength range corresponding to Y6 absorption.
Figure 8.8b shows post-built annealing experiments on the F_4TCNQ-treated nanoparticle-processed OSCs. The entire device stack was annealed at specific temperatures, as indicated in the legend. Annealing at 200 °C for 2 minutes increased both J_{SC} and FF, while V_{OC} remained unchanged, resulting in a peak PCE of 0.88%. This still yields an SMCF-corrected PCE of 0.83%. This represents the highest PCE for OSCs with

Table 8.3: Characteristics of OSC with photoactive layer processed by solution (*sol.*) and OSCs with photoactive layer by nanoparticle (*NP*) dispersion for different annealing temperatures. T_{last} thereby describes the last annealing temperature at which either the photoactive layer during fabrication[a] or the whole stack[b] was annealed. There are eight devices for the devices with solution-processed photoactive layer and three devices for the nanoparticle-processed photoactive layers. Reported values represent mean ± standard deviation.

Config.	T_{last}	V_{OC} (mV)	J_{SC} (mA cm^{-2})	FF (%)	PCE (%)
sol. 0 wt%	180 °C, 10 min[b]	757 ± 1	14.4 ± 0.2	41.6 ± 0.2	4.54 ± 0.08
sol. 0.4 wt%	180 °C, 10 min[b]	682 ± 9	13.1 ± 0.3	38.8 ± 0.7	3.5 ± 0.2
sol. 0.8 wt%	180 °C, 10 min[b]	628 ± 7	11.1 ± 0.2	37.9 ± 0.6	2.6 ± 0.1
NP F_4TCNQ	150 °C, 10 min[a]	684 ± 4	1.08 ± 0.01	27.3 ± 0.1	0.202 ± 0.003
NP F_4TCNQ	180 °C, 10 min[b]	630 ± 2	2.79 ± 0.06	32 ± 0.2	0.56 ± 0.02
NP F_4TCNQ	200 °C, 2 min[b]	630 ± 3	4.25 ± 0.03	32.5 ± 0.2	0.88 ± 0.01
NP F_4TCNQ	200 °C, 10 min[b]	552 ± 3	4.16 ± 0.05	32.5 ± 0.2	0.75 ± 0.01

[a] Annealing during device fabrication after deposition of the photoactive layer.

[b] Annealing of the final stack.

photoactive layers deposited from n-doped organic nanoparticle dispersions in this work. Further annealing at 200 °C for 10 minutes led to a decrease in V_{OC}, J_{SC}, and PCE. The decline in performance after extended annealing may be attributed to increased activation of previously dimerized n-dopants. As discussed earlier, $(\text{N-DMBI})_2$ is activated by heat. If residual unactivated dopants remain in the layer in their dimer form, prolonged heating at 200 °C may further enhance doping. This is supported by the experiment described in Appendix C.12, where Y6:PIDT-T8BT layers doped with $(\text{N-DMBI})_2$ (10 wt%) were annealed at different temperatures, redissolved in $CHCl_3$, and analyzed using UV-Vis absorbance spectrometry to estimate their doping concentration.

Figure 8.9 presents AFM tapping-mode images of nanoparticle-processed layers subjected to various annealing temperatures, alongside a reference image of a solution-processed film. The dispersions were prepared under the same conditions as the dispersions for OSC fabrication: a 0.5 mL of a Y6:PIDT-T8BT (9:1 w/w) solution (2 g L^{-1}, $CHCl_3$) was nanoprecipitated in 3.5 mL EtOH under stirring (800 rpm). The solution-processed reference layer was fabricated using the same method as the undoped reference OSC, which achieved a PCE exceeding 6% in Section 8.4.1.
At 150 °C for 10 minutes, clusters form, but individual nanoparticles remain distinguishable.

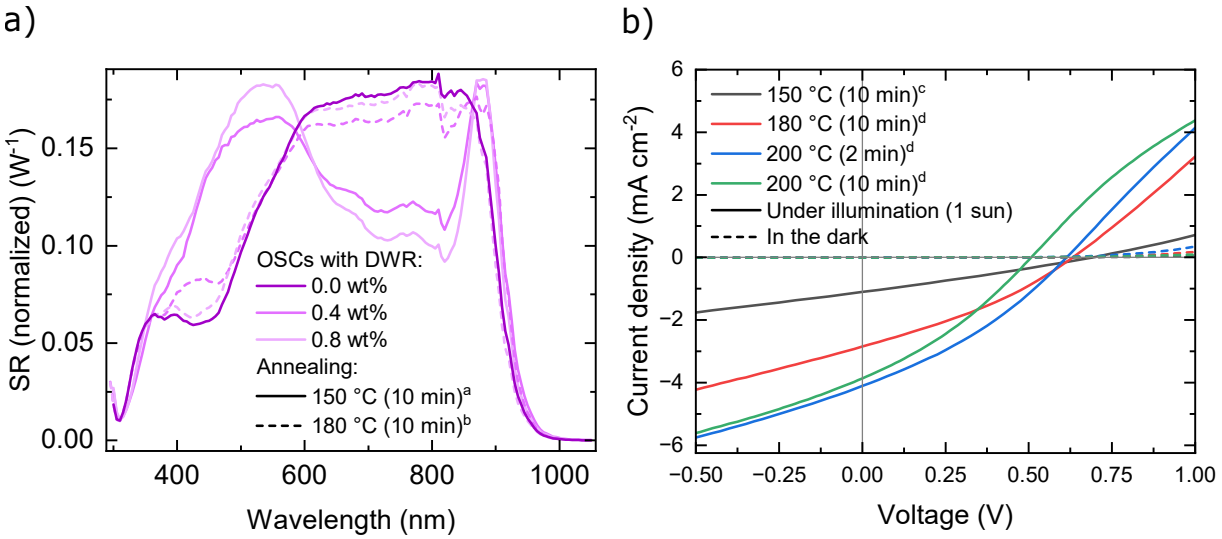

Figure 8.8: a) Normalized SR of solution-processed OSC for different annealing temperatures. Annealing changed the shape of the SR of doped devices, increasing the current in the spectral range, in which typically Y6 (film) absorbs (Figure 8.3). By additionally annealing the doped devices at 180 °C, the shape got closer to the undoped device. b) *J-V* curves of one dispersion-processed OSC by Y6:PIDT-T8BT (9:1 w/w) 10 wt% $(N\text{-}DMBI)_2$ treated with F_4TCNQ for different subsequent annealing steps (from top to bottom). Additional annealing steps increase the V_{OC} until 200 °C (2 min). Longer annealing at 200 °C decreases the J_{SC}.
[a] Annealing during device fabrication after deposition of the photoactive layer.
[b] Annealing of the final stack.
[c] F_4TCNQ treated device as shown in Figure 8.7.
[d] All curves result from the same device of the same substrate. Annealing processes were done subsequently.

At 200 °C, a more continuous film is observed, where individual nanoparticles are no longer discernible. Compared to P3HT:$IC_{60}BA$ nanoparticle layers, which typically fuse between 120-150 °C [81] and are annealed at 150 °C in OSC applications, Y6:PIDT-T8BT nanoparticles require higher annealing temperatures to achieve film formation. Despite the reduction in roughness at higher temperatures, even after annealing at 200 °C, the film remains significantly rougher than the solution-processed reference layer, with approximately twice the surface roughness. In addition, visible voids remain in the layer, potentially extending through its entire thickness. The solution-processed reference exhibits a uniform nanostructure with lower height variations, whereas the annealed nanoparticle-processed layers show agglomerated material in specific regions, forming structures on the scale of half a micrometer. This suggests that even after high-temperature annealing, the microstructure of the nanoparticle-processed layers does not reach the same level of homogeneity as solution-processed films.

In summary, this work demonstrates the fabrication of organic solar cells whose photoac-

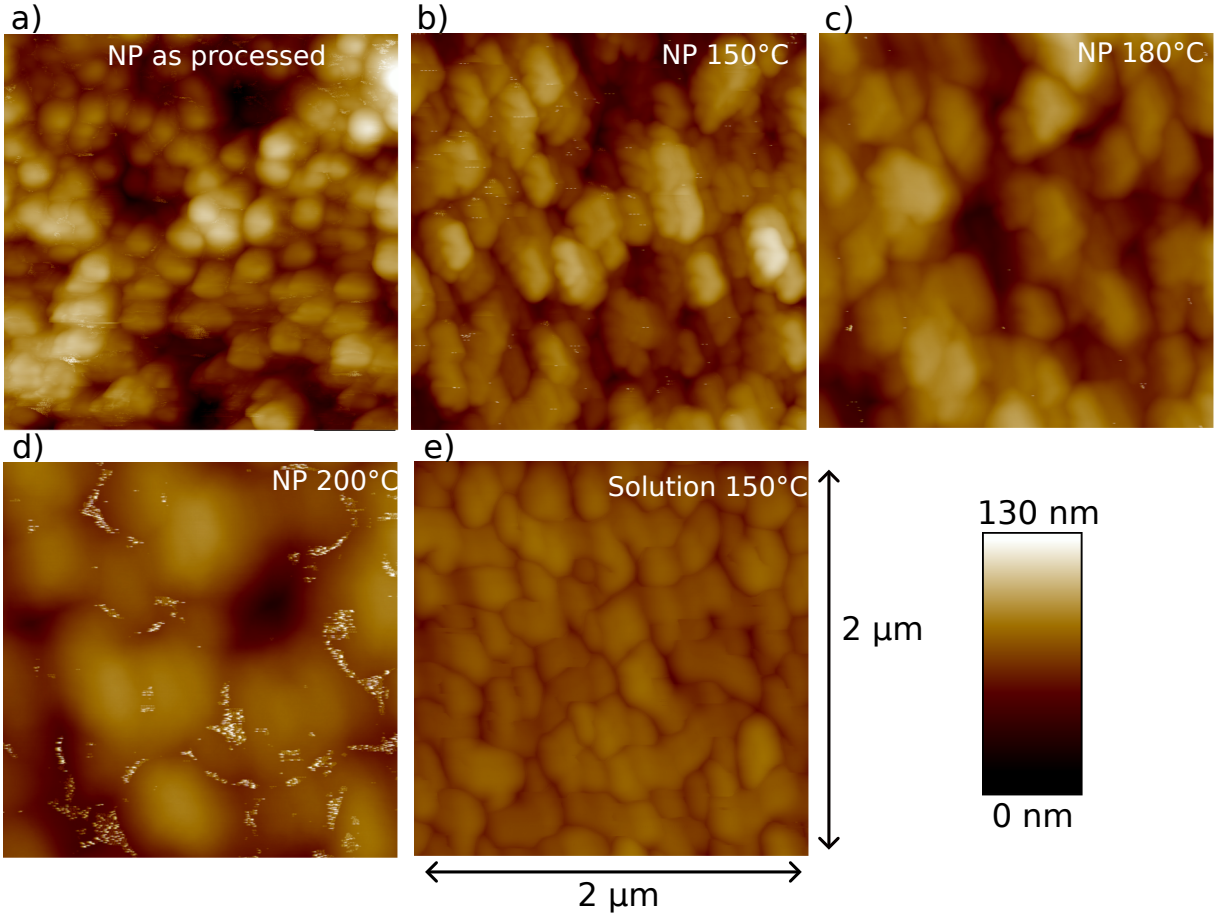

Figure 8.9: AFM tapping-mode images of nanoparticle-processed layers from Y6:PIDT-T8BT (9:1, w/w) 10 wt% $(N\text{-}DMBI)_2$ dispersions at different annealing temperatures and a solution-processed reference layer from Y6:PIDT-T8BT (9:1, w/w) annealed at 150 °C. The root mean square roughnesses in height (evaluated over the whole area, $2 \times 2\,\mu m^2$) are a) 18.3 nm, b) 11.1 nm, c) 10.2 nm, d) 8.74 nm and e) 4.14 nm. The recordings and decrease in roughness show the fusing of nanoparticles by annealing. The roughness of the solution-processed reference cannot be reached via annealing of the nanoparticle-processed layers.

tive layers are processed from n-doped, electrostatically stabilized organic nanoparticle dispersions. The power conversion efficiency corrected by the spectral mismatch correction factor exceeds 0.8% which demonstrates the viability of this novel ink-based processing approach. Nevertheless, residual doping in the deposited layers and indications of a non-optimized microstructure suggest considerable room for further optimization.

9 Conclusion

This work advances both the fundamental understanding and practical implementation of molecular doping in organic semiconductors and nanoparticle dispersions. The main objectives were: (i) To investigate how local electrostatic interactions of integer charge transfer complexes (ICTCs) determine their binding energy and, in turn, charge transport in organic semiconductors. (ii) To develop a method for quantifying the polaron yield efficiency (PYE) from dopants in electrostatically stabilized dispersions, *i.e.* the actual number of charges transferred between the dopant and the host vs. the maximum number of charges available for transfer. (iii) To investigate whether organic nanoparticle dispersions can be stabilized by introducing negative surface charges through n-doping, and whether such n-doped dispersions are suitable for processing the photoactive layers of organic solar cells (OSCs). In addition, to explore organic photodetectors architectures based on nanoparticle-processed layers and benchmark them against state-of-the-art devices.

Computational modeling of doped organic semiconductor layers revealed that the quadrupole moment of the dopant can significantly influence charge carrier mobility, potentially by over two orders of magnitude. An estimator was developed to describe the ICTC binding energy V_C based on the dopant multipoles and host partial charges. This allows the calculation of V_C across a statistically relevant number of ICTCs. The orientation between nearby host and dopant molecules was identified as a key factor in the so-called short-range overscreening effect, where $|V_\mathrm{C}(r)|$ is lower than expected from the commonly used monopole (point-charge) Coulomb approximation. This effect leads to a particularly strong influence of the anionic quadrupole moment component of the dopant perpendicular to the molecular plane. By tuning this component, V_C and charge carrier mobility can be systematically adjusted. Additionally, it was shown that V_C disorder, *i.e.*, variations in ICTC binding energy within a semiconductor, has a measurable impact on charge transport properties. Since the ICTC binding energy is a key metric for assessing host–dopant compatibility, this approach provides an efficient and reliable means to systematically evaluate doping performance and to support the rational *in-silico* design of materials for doped organic semiconductors.

A method was developed to determine the PYE in doped dispersions using the isosbestic absorbance points of the dopant. This approach has the advantage of not requiring host absorbance spectra, enabling faster analysis of stabilized dispersions with different host materials. Once the relationship between polaron absorbance and polaron concentration is established for a given host material, PYE can be determined from the polaron absorbance for various dopants and at different dispersion concentrations. The facileness of this method makes it applicable to other organic semiconductor systems with high dopant concentrations, provided the concentration and molar absorption properties of the dopant are known. The findings contribute to understanding the stability of organic nanoparticle dispersions and identifying factors that influence their stabilization. This method is easy to implement and cost-effective, making it suitable for broader use, including high-throughput screening.

Organic photodetectors (OPDs) based on nanoparticle (NP) dispersions were shown to achieve detectivities comparable to state-of-the-art OPDs. They also surpass previously reported OPDs using the same photoactive layer composition (P3HT:$PC_{71}BM$) or similar architectures (P3HT:$PC_{61}BM$) [100, 106–108, 111]. Since P3HT is a well-established and cost-effective material, and NP dispersions allow fabrication with reduced use of harmful solvents, this approach presents an alternative for processing OPDs. Additionally, NP-based processing enables the formation of thicker films, which reduces shunting pathways and can enhance detectivity. The study also explored the introduction of electron blocking layers (EBLs) via NP dispersions. While PTAA was tested as an EBL without success, the ability to introduce such interlayers through NP processing could be valuable for other material systems.

OSCs were fabricated with photoactive layers processed from organic nanoparticle dispersions stabilized by n-doping. It was demonstrated that stable nanoparticle dispersions can be synthesized from n-doped Y6, with an electrophoresis experiment confirming that the nanoparticles carry a negative charge. Additionally, the polymer PIDT-T8BT was successfully co-stabilized with Y6, enabling the formation of n-doped acceptor-donor dispersions. The dispersion concentrations achieved were sufficient for processing organic semiconductor devices. As a proof of concept, the dispersions were used as inks for fabricating bulk-heterojunction OSCs, yielding a power conversion efficiency of 0.8%. Notably, this was achieved using ethanol as an eco-friendly dispersion medium, whereas previous studies on Y6:PIDT-T8BT typically relied on dissolving the materials in environmentally harmful solvents for depositing the photoactive layer [211, 219]. However, the deposited layers remained doped, and there were indications of a nonoptimized microstructure, suggesting room for further improvements. These results open a new route of processing

organic semiconductors as nanoparticle dispersions, with the potential to extend the range of semiconductors that can be accessed beyond those accessible by p-doping.
In summary, the field of doping organic electronics and organic nanoparticles was advanced by achieving the above goals. The improvement of a computational workflow to predict macroscopic properties of doped organic materials and the method development of a UV-Vis spectrometry method to determine the PYE form important utilities to be used by other researchers. Both of these advancements could also help either computational or experimental high-throughput screening to automatically drive the research of new material combinations of doped materials. Organic photodetectors with photoactive layers from nanoparticle dispersions having detectivities comparable to state-of-the-art photodetectors provide an eco-friendly alternative to today's conventional devices. The findings on short-range overscreening as a means to tune mobility, together with the demonstration of the photoactive layer of OSC fabricated from n-doped nanoparticle dispersions, provide promising directions for future research, particularly regarding fabrication routes and improved control of charge transport in organic optoelectronic devices.

A Materials

Donors

- P3HT (Rieke Metals), regioregularity $\geq$ 90%, 4002-EE, Mw = 50-70 kg/mol
  Poly(3-hexylthiophene-2,5-diyl)
- PTB7 (1-Material)
  (poly[[4,8-bis[(2-ethylhexyl)oxy]benzo[1,2-b:4,5-b′]dithiophene-2,6-diyl][3-fluoro-2-[(2-ethylhexyl)carbonyl]thieno[3,4-b]thiophenediyl]]
- PIDT-T8BT (Mats R. Andersson, Flinders Institute for Nanoscale Science and Technology, Flinders University, Bedford Park, Australia)
  Poly[2,1,3-benzothiadiazole-4,7-diyl(4-hexyl-2,5-thiophenediyl)[4,4,9,9-tetrakis(4-hexylphenyl)-4,9-dihydro-s-indaceno[1,2-b:5,6-b′]dithiophene-2,7-diyl](3-hexyl-2,5-thiophenediyl)]
- J71 (Ossila)
  Poly[[5,6-difluoro-2-(2-hexyldecyl)-2H-benzotriazole-4,7-diyl]-2,5-thiophenediyl[4,8-bis[5-(tripropylsilyl)-2-thienyl]benzo[1,2-b:4,5-b'] dithiophene-2,6-diyl]-2,5-thiophenediyl]
- PM6 (1-Material)
  Poly[(2,6-(4,8-bis(5-(2-ethylhexyl-3-fluoro)thiophen-2-yl)-benzo[1,2-b:4,5- b']dithiophen))-alt-(5,5-(1',3'-di-2-thienyl-5',7'-bis(2-ethylhexyl)benzo[1',2'-c:4',5'- c']dithiophen-4,8-dion)] also known as PBDB-T-2F
- PTQ10 (1-Material)
  poly[(thiophene)-alt-(6,7-difluoro-2-(2-hexyldecyloxy)quinoxaline)]

Acceptors

- Y6 (1-Material)
  2,2′-((2Z,2′Z)-((12,13-bis(2-ethylhexyl)-3,9-diundecyl-12,13-dihydro-[1,2,5]thiadiazolo[3,4-e]thieno[2′,3′′:4′,5′]thieno[2′,3′:4,5]pyrrolo[3,2-g]thieno[2′,3′:4,5]thieno[3,2-b]indole-2,10-diyl)bis(methanylylidene))bis(5,6-difluoro-3-oxo-2,3-dihydro-1H-indene-2,1-diylidene))dimalo
  nonitrile

- $PC_{71}BM$ (Lumtec)
  [6, 6]phenyl-C_{71}-butyric acid methyl ester

Dopants

- F_4TCNQ (Ossila)
  2,3,5,6-Tetrafluoro-7,7,8,8-tetracyanoquinodimethane
- $(RuCp^*mes)_2$ (Seth R. Marder, School of Chemistry and Biochemistry, and Center for Organic Photonics and Electronics, Georgia Institute of Technology, Atlanta, USA)
  pentamethylcyclopentadienyl mesitylene ruthenium dimer (pentamethylcyclopentadienyl)(1,3,5-trimethylbenzene)ruthenium dimer
- $(N\text{-}DMBI)_2$ (Seth R. Marder, School of Chemistry and Biochemistry, and Center for Organic Photonics and Electronics, Georgia Institute of Technology, Atlanta, USA)
  (pentamethylcyclopentadienyl)(1,3,5-trimethylbenzene)ruthenium dimer
- $CoTFSI_3$ (greatcellsolar)
  bis(2,6-di(1H-pyrazol-1-yl)pyridine)cobalt tri[bis(trifluoromethane)sulfonimide
- $CoTFSI_2$ (greatcellsolar)
  (2,6-di(1H-pyrazol-1-yl)pyridine)cobalt(II) di[bis(trifluoromethane)sulfonimide]

Others

- PTAA (Sigma-Aldrich)
  poly[bis(4-phenyl)(2,4,6-trimethylphenyl)amine]
- TAZ (Lumtec)
  3-phenyl-4(1′-naphthyl)-5-phenyl-1,2,4-triazole
- Zinc oxide (ZnO) as nanoparticle dispersion (1 wt% butanol), synthesized according to [220]
- PEDOT:PSS (Heraeus, VP AI 4083)
  Poly(3,4-ethylenedioxythiophene):Polystyrene sulfonate
- Li^+TFSI^{-1} (Alfa Aesar)
  Lithium bis(trifluoromethanesulfonyl)imide

B Acronyms

a.u.	Arbitrary unit
AFM	Atomic force microscopy
AM	Air mass
BF-DPB	N4,N4'-Bis(9,9-dimethyl-9H-fluoren-2-yl)-N4,N4'-diphenyl-biphenyl-4,4'-d iamine
C_{60}	Buckminster fullerene with 60 carbon atoms
C8-BTBT	2,7-dioctyl[1]benzothieno[3,2-b][1]benzothiophene
Ca	Calcium
CB	Chlorobenzene
CDFT	Constrained density functional theory
CH_3CN	Acetonitrile
$CHCl_3$	Chloroform
COB	Chip-on-board
CNT	Classical nucleation theory
DIR	Dopant ionization ratio
DLS	Dynamic light scattering
DLVO	Derjaguin-Landau-Verwey-Overbeek
DMSO	Dimethyl sulfoxide
DMR	Dopant molar ratio
DUT	Device under test
DWR	Dopant weight ratio

DFT	Density functional theory
DS	Deposition step
EA	Electron affinity
EQE	External quantum efficiency
ETL	Electron transport layer
EtOH	Ethanol
F_6TCNNQ	1,3,4,5,7,8-hexafluorotetracyanonaphthoquinodimethane
FF	Fill factor
HTL	Hole transport layer
HOMO	Highest occupied molecular orbital
IBP	Isosbestic point
ICBA	Indene-C60 bisadduct
ICTC	Integer charge transfer complex
IP	Ionization potential
ITO	Indium tin oxide
LCAO	Linear combination of atomic orbitals
LED	Light-emitting diode
LUMO	Lowest unoccupied molecular orbital
MeO-TPD	N,N,N',N'-Tetrakis(4-methoxyphenyl)benzidine
MM	Molecular mechanics
MPP	Maximum power point
NEP	Noise-equivalent power
NP	Nanoparticle
NPB	N,N′-Di(1-naphthyl)-N,N′-diphenyl-(1,1′-biphenyl)-4,4′-diamine
NSD	Noise spectral density

OLED	Organic light-emitting diodes
OPD	Organic photodiode
OSC	Organic solar cell
$PC_{61}BM$	[6,6]phenyl-C_{61}-butyric acid methyl ester
PCE	Power conversion efficiency
P(NDI20D-T2)	Poly[N,N′-bis(2-octyldodecyl)-naphthalene-1,4,5,8-bis(dicarboximide)-2,6-diyl]-alt-thiophene-2,5-diyl
PBDB-T	Poly[(2,6-(4,8-bis(5-(2-ethylhexyl)thiophen-2-yl)-benzo[1,2-b:4,5-b']dithiophen))-alt- (5,5-(1',3'-di-2-thienyl-5',7'-bis(2-ethylhexyl)benzo[1',2'-c:4',5'-c']dithiophen-4,8- dion)]
PDI	Polydispersity index
PESA	Photoelectron spectroscopy in air
PHJ	Planar heterjunction
PSD	Power spectral density
PTB7-Th	Poly[4,8-bis(5-(2-ethylhexyl)thiophen-2-yl)benzo[1,2-b;4,5-b']dithiophen-2,6-diyl-alt- (4-(2-ethylhexyl)-3-fluorothieno[3,4-b]thiophen-)-2-carboxylat-2-6-diyl)]
PYE	Polaron yield efficiency
QM/MM	Quantum mechanics/molecular mechanics
RDF	Radial distribution function
SA	Simulated annealing
SMCF	Spectral mismatch calculation factor
SMU	Source measure unit
SNR	Signal-to-noise
SR	Spectral response
SSP	Sequentially solution-processed
TCNQ	Tetracyanoquinodimethane

UV-Vis	Ultraviolet-visible

C Supporting data and derivations

Controlling charge transport by tuning the electrostatics of p-doped organic semiconductors

This section is based on work previously published in Armleder et al. [22]. The results are included here as part of the dissertation.

Table C.1: Quadrupole tensor Q components computed by for cationic host molecules (+1 e): NPB, MeO-TPD, BF-DPB and anionic dopant molecules (-1 e): TCNQ, F_4TCNQ, F_6TCNNQ. The conformation of the molecules was relaxed (with the respective additional charge) with DFT (def2-SVP and BP86), for these conformations the quadrupole moments were computed using DFT (def2-QZVP and PBE). The simulations were conducted by Jorge Enrique Olivares Peña [22].

Q in $(e_0^2 a_0)$	NPB^+	$TCNQ^-$	F_4TCNQ^-	F_6TCNNQ^-	MeO-TPD^+	BF-DPB^+
Q_{xx}	66.548	-39.897	-43.446	-68.215	92.383	103.122
Q_{yy}	-24.344	8.338	6.657	17.236	-23.580	-58.729
Q_{zz}	-42.204	31.559	36.788	50.980	-68.803	-44.393
Q_{xy}	-7.107	0.000	-0.001	-2.799	9.237	-38.379
Q_{xz}	19.825	0.000	0.000	-0.000	3.649	-0.068
Q_{yz}	1.040	0.000	0.000	-0.000	-1.177	-0.144

Table C.2: Simulation parameters of kinetic Monte Carlo simulations with the hosts NPB, BF-DPB and MeO-TPD. The densities of the simulated morphologies are calculated by the summed element masses divided by the respective volume. The density of NPB fits well to the experiment, for the other materials a deviation below 12% is observed. The experimental mobilities for the materials BF-DPB and MeO-TPD are used to fit the disorder of the host charge transport level (in intrinsic systems without doping), see Appendix C.2 and C.3. These are given in the row below. The reorganization energies are calculated for molecules in vacuum by the Nelson's four-point procedure, see 3.2.2. The dielectric permittivity ϵ_r is determined as described in 3.2.3.

Property	NPB	BF-DPB	MeO-TPD
Density of simulated morphologies (g/cm^3)	1.13	1.075	1.11
Experimental density (g/cm^3)	1.14[140]	1.21[140]	1.2[221]
Experimental mobility ($cm^2/(Vs)$)	-	$5.7 \cdot 10^{-5}$[149]	$2.3 \cdot 10^{-5}$ [149]
Disorder of the hole charge transport levels (eV) ($\sigma_{\mathrm{IP,\ host}}$)	0.093[144]	0.105	0.118
Reorganization energy of electrons (eV) (vacuum) ($\lambda_{\mathrm{electron}}$)	0.148	0.247	0.612
Reorganization energy of holes (eV) (vacuum) (λ_{hole})	0.282	0.207	0.211
Relative dielectric permittivity (ϵ_r)	2.730	3.267	3.100

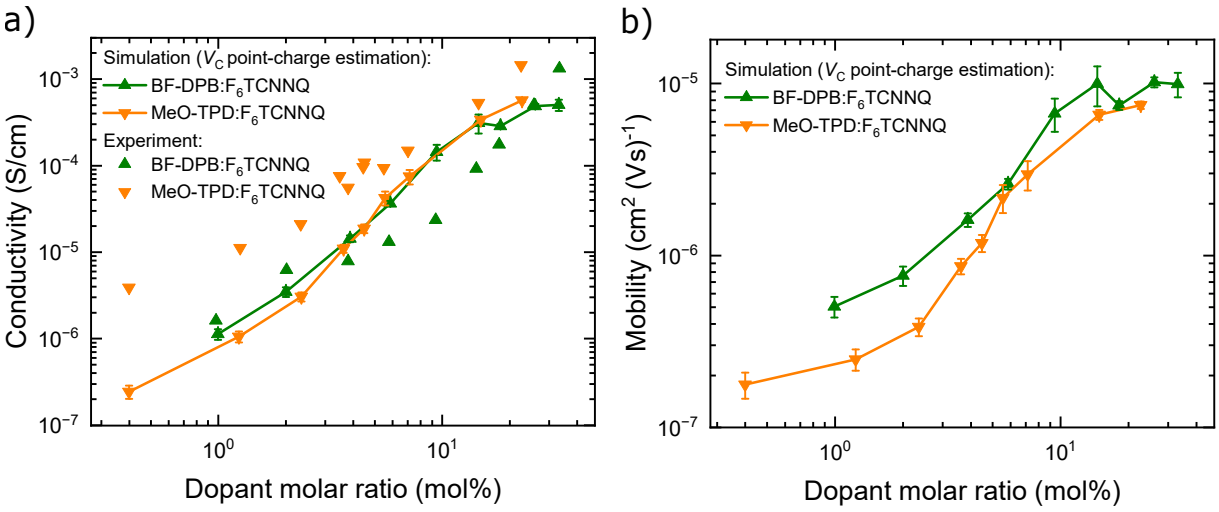

Figure C.1: Simulated conductivity and mobility of the systems BF-DPB and MeO-TPD doped with F_6TCNNQ as described in Section 5.4. Here, V_C is estimated by point-charge, *i.e.* host and dopant are treated as oppositely charged monopoles that interact via Coulomb interaction.

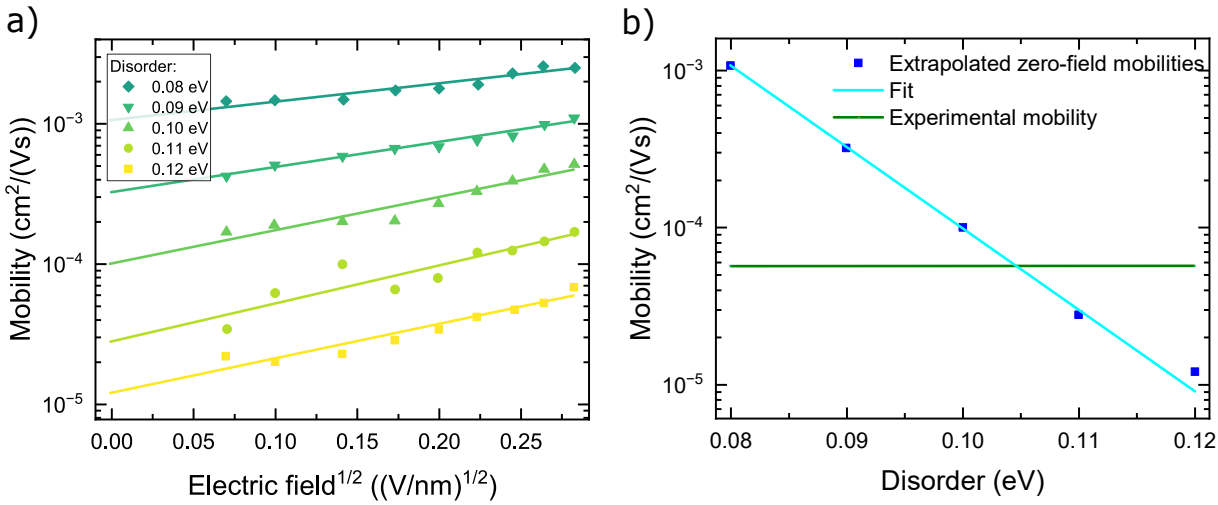

Figure C.2: a) Determination of zero-field mobilities from kMC simulations for undoped BF-DPB with parameters given in Appendix C.2. b) The disorder is fitted to the experimental mobility of intrinsic BF-DPB [149].

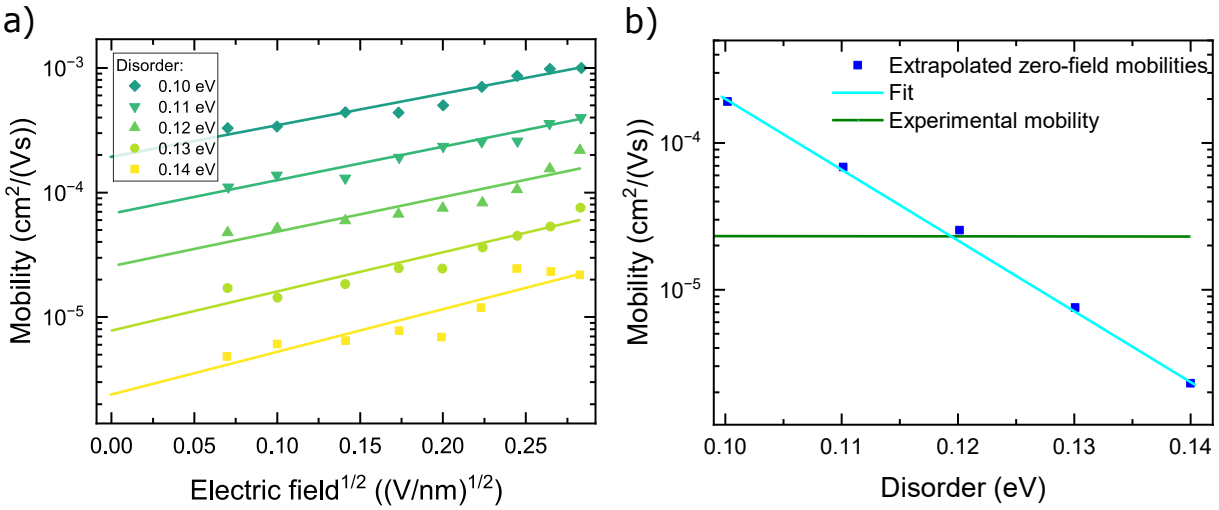

Figure C.3: a) Determination of zero-field mobilities from kMC simulations for undoped MeO-TPD with parameters given in Appendix C.2. b) The disorder is fitted to the experimental mobility of intrinsic MeO-TPD [149].

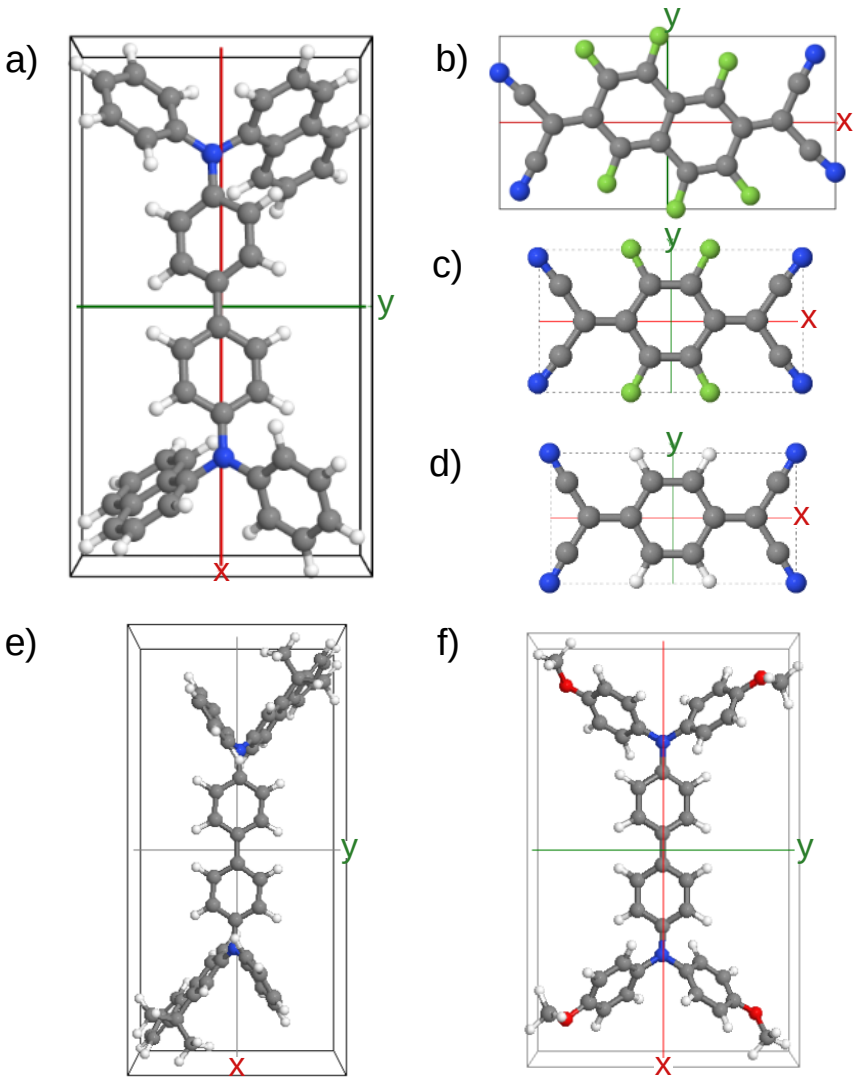

Figure C.4: Orientations of the molecules used in Section 5. a) NPB, b) F_6TCNNQ, c) F_4TCNQ, d) TCNQ, e) BF-DPB and f) MeO-TPD. Visualization adapted from Armleder et al. [22], licensed under CC BY 4.0; modified by the author.

Table C.3: Dopant molar ratios of the simulated host-dopant systems, BF-DPB:F_6TCNNQ and MeO-TPD:F_6TCNNQ, with the used difference in IP of the host and EA of the dopant (Δ_{IP_h,EA_d}).

BF-DPB:F_6TCNNQ		MeO-TPD:F_6TCNNQ	
DMR (mol%)	Δ_{IP_h,EA_d} (eV)	DMR (mol%)	Δ_{IP_h,EA_d} (eV)
0.994	0.629	0.4	0.534
2.002	0.630	1.236	0.529
3.872	0.630	2.349	0.523
5.851	0.631	3.623	0.516
9.425	0.659	4.474	0.511
14.523	0.698	5.547	0.522
18.209	0.726	7.146	0.538
26.050	0.787	14.838	0.617
33.093	0.841	22.694	0.698

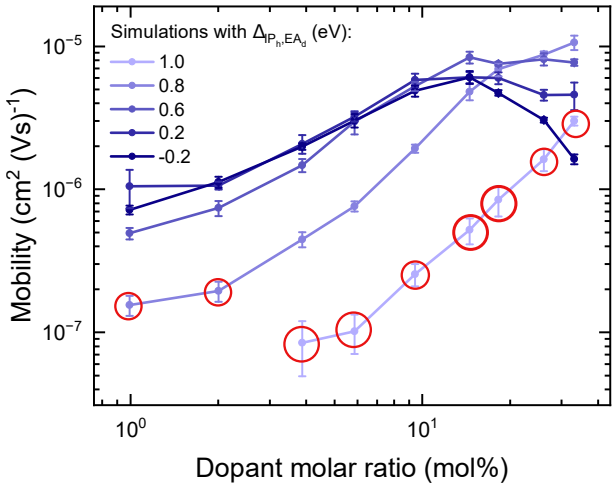

Figure C.5: Mobilities corresponding to the simulations with the conductivities shown in Figure 5.8. Simulations with only partly converged replicas (3 day convergence time limit) are marked by a red circle describing an upper limit since simulations with higher mobility generally converge faster.

Determination of the polaron yield efficiency in organic dispersions from the deconvolution of UV-Vis absorbance spectra

C.0.1 Derivation of PYE estimator

The total dopant absorbance $A_{\text{dopant}}(\lambda)$ is given by the superposition of the neutral species $A^0_{\text{dopant}}(\lambda)$ and the anionic species $A^-_{\text{dopant}}(\lambda)$, as shown in Equation 6.4. The Beer-Lambert law is applied to express $A_{\text{dopant}}(\lambda)$ in terms of the known molar extinction coefficients $\varepsilon^0_{\text{dopant}}$ and $\varepsilon^-_{\text{dopant}}$ and the corresponding (unknown) concentrations of the neutral and anionic dopant species, c^0_{dopant} and c^-_{dopant}, respectively.

$$A_{\text{dopant}}(\lambda) = A^-_{\text{dopant}}(\lambda) + A^0_{\text{dopant}}(\lambda) = c^-_{\text{dopant}} \cdot l \cdot \varepsilon^-_{\text{dopant}}(\lambda) + c^0_{\text{dopant}} \cdot l \cdot \varepsilon^0_{\text{dopant}}(\lambda). \quad \text{(C.1)}$$

Using Equations 6.5 and 6.6 leads to:

$$A_{\text{dopant}}(\lambda) = l \cdot \text{DIR} \cdot c_{\text{dopant}} \cdot (\varepsilon^-_{\text{dopant}}(\lambda) - \varepsilon^0_{\text{dopant}}(\lambda)) + l \cdot c_{\text{dopant}} \cdot \varepsilon^0_{\text{dopant}}(\lambda). \quad \text{(C.2)}$$

Solving for DIR yields:

$$\text{DIR}(\lambda) = \frac{A_{\text{dopant}}(\lambda) - l \cdot c_{\text{dopant}} \cdot \varepsilon^0_{\text{dopant}}(\lambda)}{l \cdot c_{\text{dopant}} \cdot (\varepsilon^-_{\text{dopant}}(\lambda) - \varepsilon^0_{\text{dopant}}(\lambda))}. \quad \text{(C.3)}$$

Together with $c^-_{\text{dopant}} = \text{DIR} \cdot c_{\text{dopant}}$, Equation C.2 is solved as:

$$c^-_{\text{dopant}}(\lambda) = \frac{A_{\text{dopant}}(\lambda) - l \cdot c_{\text{dopant}} \cdot \varepsilon^0_{\text{dopant}}(\lambda)}{l \cdot (\varepsilon^-_{\text{dopant}}(\lambda) - \varepsilon^0_{\text{dopant}}(\lambda))}. \quad \text{(C.4)}$$

C.0.2 PYE from polaron absorbance - error considerations

Once the molar extinction coefficient of the polaron absorbance of the host molecule is found, it can be used to calculate The error of the PYE calculated by the linear regression model (Equation 6.8) is given by:

$$\sigma_{\text{PYE}} = \frac{\sigma_{c^+_{\text{host}}}}{c_{\text{dopant}}}, \quad \text{(C.5)}$$

where $\sigma_{c^+_{\text{host}}}$ is the error of the polaron absorbance.

$$c^+_{\text{host}} = \frac{1}{l \cdot \varepsilon^+_{\text{host}}}(A_{\text{polaron}} - A_{\text{offset}}). \quad \text{(C.6)}$$

Using error propagation as an estimate for the error leads to:

$$\sigma_{c^+_{\mathrm{host}}} = \frac{1}{l \cdot \varepsilon^+_{\mathrm{host}}}(A_{\mathrm{polaron}} - A_{\mathrm{offset}}) \sqrt{\begin{aligned}&\left(\frac{1}{\varepsilon^+_{\mathrm{host}}}\sigma_{\varepsilon^+_{\mathrm{host}}}\right)^2 + 2 \cdot \frac{1}{(A_{\mathrm{polaron}} - A_{\mathrm{offset}})} \frac{1}{\varepsilon^+_{\mathrm{host}}}\sigma_{\varepsilon^+_{\mathrm{host}}, A_{\mathrm{offset}}} \\ &+ \left(\frac{1}{A_{\mathrm{polaron}} - A_{\mathrm{offset}}}\sigma_{A_{\mathrm{offset}}}\right)^2\end{aligned}} \tag{C.7}$$

Inserting Equation C.6 yields the relative error on $\sigma_{c^+_{\mathrm{host}}}$:

$$\frac{\sigma_{c^+_{\mathrm{host}}}}{c^+_{\mathrm{host}}} = \sqrt{\left(\frac{1}{\varepsilon^+_{\mathrm{host}}}\sigma_{\varepsilon^+_{\mathrm{host}}}\right)^2 + 2 \cdot \frac{1}{(A_{\mathrm{polaron}} - A_{\mathrm{offset}})} \frac{1}{\varepsilon^+_{\mathrm{host}}}\sigma_{\varepsilon^+_{\mathrm{host}}, A_{\mathrm{offset}}} + \left(\frac{1}{A_{\mathrm{polaron}} - A_{\mathrm{offset}}}\sigma_{A_{\mathrm{offset}}}\right)^2}. \tag{C.8}$$

Inserting this into Equation C.5 and using the definition of DE yields the relative error on the DE:

$$\frac{\sigma_{\mathrm{DE}}}{\mathrm{DE}} = \sqrt{\left(\frac{1}{\varepsilon^+_{\mathrm{host}}}\sigma_{\varepsilon^+_{\mathrm{host}}}\right)^2 + 2 \cdot \frac{1}{(A_{\mathrm{polaron}} - A_{\mathrm{offset}})} \frac{1}{\varepsilon^+_{\mathrm{host}}}\sigma_{\varepsilon^+_{\mathrm{host}}, A_{\mathrm{offset}}} + \left(\frac{1}{A_{\mathrm{polaron}} - A_{\mathrm{offset}}}\sigma_{A_{\mathrm{offset}}}\right)^2}. \tag{C.9}$$

Equations C.8 and C.9 show that the relative error of c^+_{host} and DE will decrease with increasing A_{polaron}, and it will saturate to the following values:

$$\frac{\sigma_{c^+_{\mathrm{host}}}}{c^+_{\mathrm{host}}} = \sqrt{\left(\frac{1}{\varepsilon^+_{\mathrm{host}}}\sigma_{\varepsilon^+_{\mathrm{host}}}\right)^2}, \quad \frac{\sigma_{\mathrm{DE}}}{\mathrm{DE}} = \sqrt{\left(\frac{1}{\varepsilon^+_{\mathrm{host}}}\sigma_{\varepsilon^+_{\mathrm{host}}}\right)^2}. \tag{C.10}$$

These values depend only on the measurements of the polaron band. The errors do not depend on the host-dopant ratio as in the UV-Vis deconvolution method. Hence, a low error can be achieved by having a high polaron absorbance, *i.e.*, a dispersion with a small DMR but a high host concentration.

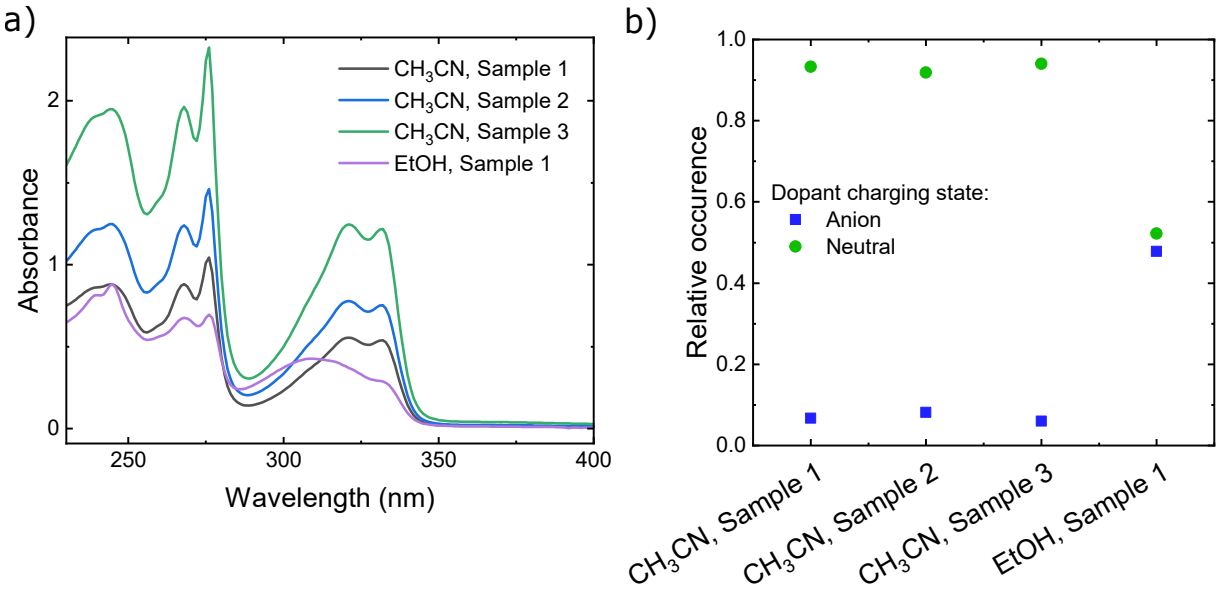

Figure C.6: a) Absorbance spectra of $CoTFSI_3$ obtained after mimicking the nanoprecipitation process described in Section 6.1.3, but without a host polymer, in order to examine whether the dopant remains inert to the solvents during nanoprecipitation. The dopant was first dissolved at a high concentration ($30\,g\,L^{-1}$) in CH_3CN and subsequently added to $CHCl_3$, thereby mimicking the doping of the host polymer in $CHCl_3$. A volume of 0.5 mL of this dopant solution in $CHCl_3$ was then injected, under stirring and illumination, into 3.5 mL of either CH_3CN or EtOH. Afterwards, the total volume was reduced to 1 mL. The process parameters were identical to those described in Section 6.2.1, except that no J71 host was used. The amount of dopant corresponds to the quantity typically used for doping a host polymer at approximately $\mathcal{O}(10\,wt\%)$. b) Relative occurrences of the dopant species after the process, determined by fitting the spectra from panel a) with reference spectra of the neutral and anionic dopant species (see Figure C.7 for the spectra in CH_3CN). The results indicate that $CoTFSI_3$ is not inert during nanoprecipitation into EtOH, in contrast to its behavior during nanoprecipitation into CH_3CN.

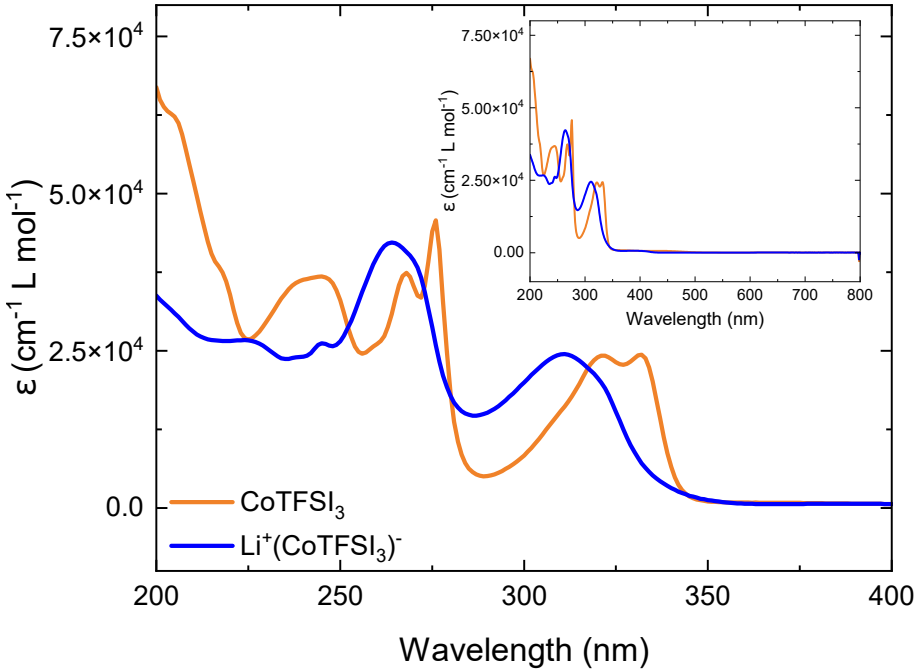

Figure C.7: Molar extinction coefficient of the neutral and anionic $CoTFSI_3$ recorded in CH_3CN.

Table C.4: Processing parameters of OSCs in Section 6.3.2. Spincoating volume is the volume of solution or dispersion used in the spincoating process with the rotational speed v_R for a period of time t_R, followed by an annealing step at temperature T_A for a period of time t_A.

Material	Spincoating volume (µL)	v_R (min^{-1})	t_R (s)	T_A (°C)	t_A (min)
PEDOT:PSS	80	5000	30	150	10
J71:Y6 dispersions	40	1000	20	180	10
J71:Y6 solution	50	1400	30	180	10
ZnO	50	2000	40	120	10

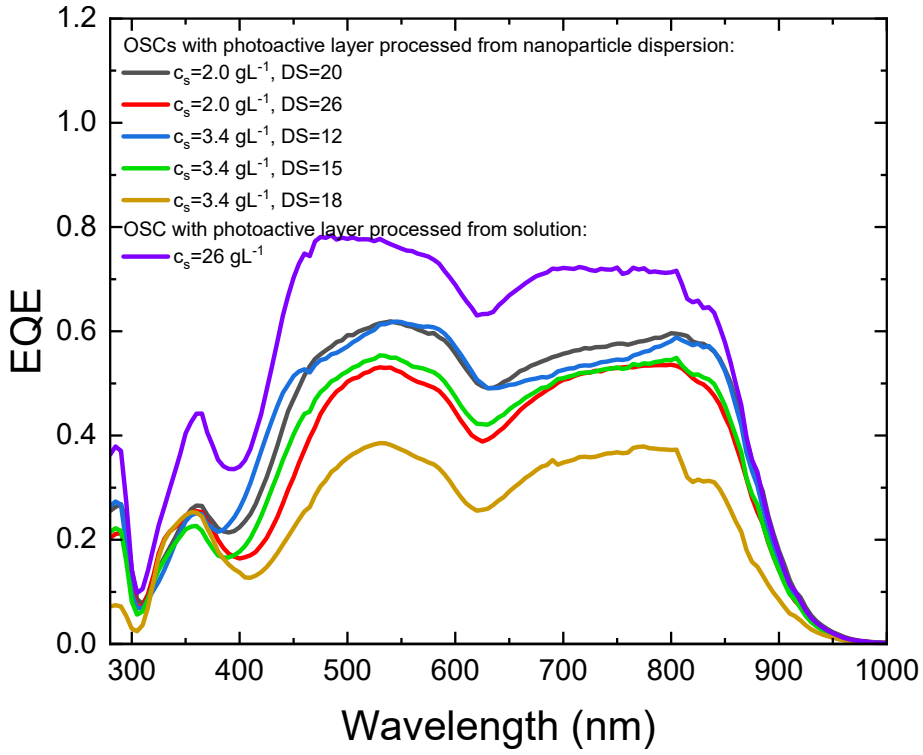

Figure C.8: External quantum efficiency of J71:Y6 OSCs with photoactive layer fabricated from nanoparticle dispersion and solution as described in Section 6.3.2. c_S is the concentration of the semiconductor solution used for the nanoprecipitation and DS the number of deposition steps.

Organic photodiodes processed from nanoparticle dispersions

Table C.5: Dark currents, J_D, and specific detectivities, D^*, of P3HT:$PC_{61/71}BM$ OPDs in the literature.

Photoactive layer	EBL	HBL	J_D (mA/cm^2)	D^* (10^{12} Jones)	Literature
P3HT:$PC_{71}BM$	-	-	$2.0 \cdot 10^{-4}$	1.2[a]	[106]
P3HT:$PC_{61}BM$	-	-	$5.0 \cdot 10^{-6}$	7.0[a]	[111]
P3HT:$PC_{61}BM$	poly-PT	-	$2.5 \cdot 10^{-5}$	2.2[a]	[108]
P3HT:$PC_{61}BM$	-	TAZ	$4.5 \cdot 10^{-5}$	3.0[a]	[107]
P3HT:$PC_{61}BM$	-	C_{60}	$1.3 \cdot 10^{-5}$	2.4[b]	[100]

[a] Shot noise limited specific detectivity.

[b] Specific detectivity based on measured noise density.

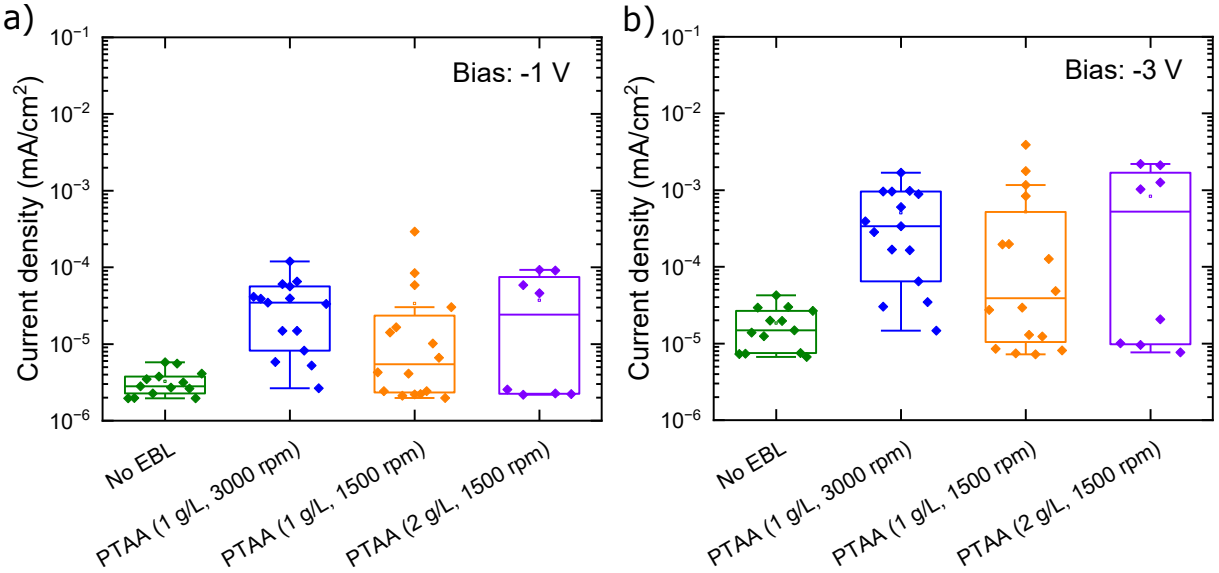

Figure C.9: OSCs fabricated with the architecture ITO/HTL/P3HT:$PC_{71}BM$/Ca/Ag, varying the electron blocking layer: no EBL and three different PTAA thicknesses. The photoactive layer was processed from nanoparticle dispersion. The dark current density is shown at a bias voltage of -1 V and -3 V. The lowest dark current is observed in a device without an EBL, indicating no improvement from PTAA. Additionally, OPDs with PTAA exhibit significant variation in the dark current.

Stabilization of Y6 dispersions by n-doping and their application in organic solar cells

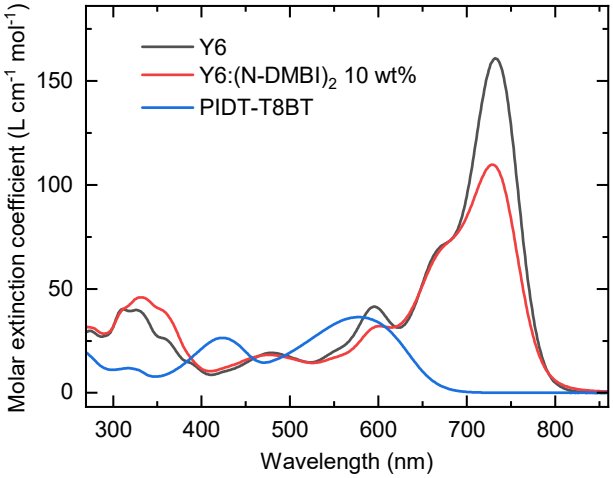

Figure C.10: Molar extinction coefficients of Y6, Y6 doped with $(N\text{-}DMBI)_2$ (10 wt%) and PIDT-T8BT in $CHCl_3$.

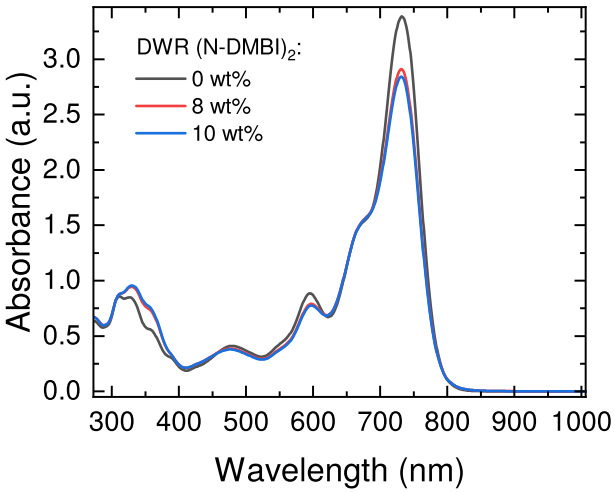

Figure C.11: Absorbance spectra of Y6 upon n-doping with $(N\text{-}DMBI)_2$.

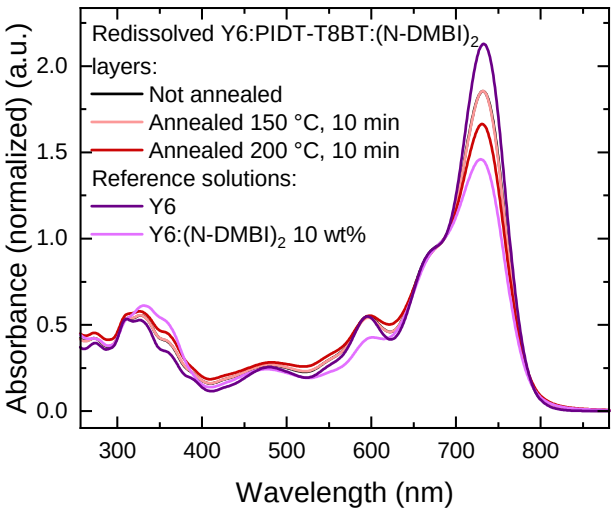

Figure C.12: Absorbance spectra of Y6:PIDT-T8BT doped with $(N\text{-}DMBI)_2$ (10 wt%) layers annealed at different temperatures, dissolved in $CHCl_3$. Reference spectra of Y6 and Y6:$(N\text{-}DMBI)_2$ solutions in $CHCl_3$ are included for comparison. While annealing at 150 °C did not change the absorbance spectrum compared to not annealed layers, annealing at 200 °C shifts the main peak of the redissolved Y6:$(N\text{-}DMBI)_2$ layer downwards indicating an increase of doping in the layer. This could be attributed to residual unactivated dopants that remained in the layer in their dimer form and are activated by layer annealing of 200 °C but not 150 °C.

Bibliography

(1) Ling, H.; Liu, S.; Zheng, Z.; Yan, F. Organic flexible electronics. *Small Methods* **2018**, *2*, 1800070.

(2) Zhu, L.; Zhang, M.; Zhou, G.; Wang, Z.; Zhong, W.; Zhuang, J.; Zhou, Z.; Gao, X.; Kan, L.; Hao, B.; Han, F.; Zeng, R.; Xue, X.; Xu, S.; Jing, H.; Xiao, B.; Zhu, H.; Zhang, Y.; Liu, F. Achieving 20.8% organic solar cells via additive-assisted layer-by-layer fabrication with bulk p-i-n structure and improved optical management. *Joule* **2024**, *8*, 3153–3168.

(3) Brabec, C. J.; Hauch, J. A.; Schilinsky, P.; Waldauf, C. Production aspects of organic photovoltaics and their impact on the commercialization of devices. *MRS Bull.* **2005**, *30*, 50–52.

(4) García-Valverde, R.; Cherni, J. A.; Urbina, A. Life cycle analysis of organic photovoltaic technologies. *Prog. Photovoltaics* **2010**, *18*, 535–558.

(5) Saïd, A.; Rahmat, M. K.; Rozlan, M. H. H. M. Organic solar cells: Recent advances and challenges. *IOP Conf. Ser.: Earth Environ. Sci.* **2023**, *1261*, 012019.

(6) Li, Q.; Monticelli, C.; Zanelli, A. Life cycle assessment of organic solar cells and perovskite solar cells with graphene transparent electrodes. *Renewable Energy* **2022**, *195*, 906–917.

(7) Jansen-van Vuuren, R. D.; Armin, A.; Pandey, A. K.; Burn, P. L.; Meredith, P. Organic photodiodes: The future of full color detection and image sensing. *Adv. Mater.* **2016**, *28*, 4766–4802.

(8) Simone, G.; Dyson, M. J.; Weijtens, C. H. L.; Meskers, S. C. J.; Coehoorn, R.; Janssen, R. A. J.; Gelinck, G. H. On the origin of dark current in organic photodiodes. *Adv. Opt. Mater.* **2020**, *8*, 1901568.

(9) Eslamian, M. Inorganic and organic solution-processed thin film devices. *Nano-Micro Lett.* **2017**, *9*, 3.

(10) Guo, J.; Min, J. A cost analysis of fully solution-processed ITO-free organic solar modules. *Adv. Energy Mater.* **2019**, *9*, 1802521.

(11) Gärtner, S.; Christmann, M.; Sankaran, S.; Röhm, H.; Prinz, E.-M.; Penth, F.; Pütz, A.; Türeli, A. E.; Penth, B.; Baumstümmler, B.; Colsmann, A. Eco-friendly fabrication of 4% efficient organic solar cells from surfactant-free P3HT:ICBA nanoparticle dispersions. *Adv. Mater.* **2014**, *26*, 6653–6657.

(12) Marlow, P.; Manger, F.; Fischer, K.; Sprau, C.; Colsmann, A. Eco-friendly fabrication of organic solar cells: electrostatic stabilization of surfactant-free organic nanoparticle dispersions by illumination. *Nanoscale* **2022**, *14*, 5569–5578.

(13) Manger, F.; Marlow, P.; Fischer, K.; Nöller, M.; Sprau, C.; Colsmann, A. Organic solar cells: Electrostatic stabilization of organic semiconductor nanoparticle dispersions by electrical doping. *Adv. Funct. Mater.* **2022**, *32*, 2202566.

(14) Fediai, A.; Symalla, F.; Friederich, P.; Wenzel, W. Disorder compensation controls doping efficiency in organic semiconductors. *Nat. Commun.* **2019**, *10*, 4547.

(15) Olthof, S.; Mehraeen, S.; Mohapatra, S. K.; Barlow, S.; Coropceanu, V.; Brédas, J. L.; Marder, S. R.; Kahn, A. Ultralow doping in organic semiconductors: Evidence of trap filling. *Phys. Rev. Lett.* **2012**, *109*, 176601.

(16) Lüssem, B.; Riede, M.; Leo, K. Doping of organic semiconductors. *Phys. Status Solidi A* **2013**, *210*, 9–43.

(17) Jacobs, I. E.; Moulé, A. J. Controlling molecular doping in organic semiconductors. *Adv. Mater.* **2017**, *29*, 1703063.

(18) Arkhipov, V. I.; Heremans, P.; Emelianova, E. V.; Bässler, H. Effect of doping on the density-of-states distribution and carrier hopping in disordered organic semiconductors. *Phys. Rev. B* **2005**, *71*, 045214.

(19) Özdemir, A. D.; Kaiser, S.; Neumann, T.; Symalla, F.; Wenzel, W. Systematic kMC study of doped hole injection layers in organic electronics. *Front. Chem.* **2022**, *9*, 809415.

(20) Gaul, C.; Hutsch, S.; Schwarze, M.; Schellhammer, K. S.; Bussolotti, F.; Kera, S.; Cuniberti, G.; Leo, K.; Ortmann, F. Insight into doping efficiency of organic semiconductors from the analysis of the density of states in n-doped C_{60} and ZnPc. *Nat. Mater.* **2018**, *17*, 439–444.

(21) Privitera, A.; Londi, G.; Riede, M.; D'Avino, G.; Beljonne, D. Molecular quadrupole moments promote ground-state charge generation in doped organic semiconductors. *Adv. Funct. Mater.* **2020**, *30*, 2004600.

(22) Armleder, J.; Neumann, T.; Symalla, F.; Strunk, T.; Olivares Peña, J. E.; Wenzel, W.; Fediai, A. Controlling doping efficiency in organic semiconductors by tuning short-range overscreening. *Nat. Commun.* **2023**, *14*, 1356.

(23) Biskup, T. Doping of organic semiconductors: Insights from EPR spectroscopy. *Appl. Phys. Lett.* **2021**, *119*, 010503.

(24) Arvind, M.; Tait, C. E.; Guerrini, M.; Krumland, J.; Valencia, A. M.; Cocchi, C.; Mansour, A. E.; Koch, N.; Barlow, S.; Marder, S. R.; Behrends, J.; Neher, D. Quantitative analysis of doping-induced polarons and charge-transfer complexes of poly(3-hexylthiophene) in solution. *J. Phys. Chem. B* **2020**, *124*, 7694–7708.

(25) Karpov, Y.; Erdmann, T.; Raguzin, I.; Al-Hussein, M.; Binner, M.; Lappan, U.; Stamm, M.; Gerasimov, K. L.; Beryozkina, T.; Bakulev, V.; Anokhin, D. V.; Ivanov, D. A.; Günther, F.; Gemming, S.; Seifert, G.; Voit, B.; Pietro, R. D.; Kiriy, A. High conductivity in molecularly p-Doped diketopyrrolopyrrole-based polymer: The impact of a high dopant strength and good structural order. *Adv. Mater.* **2016**, *28*, 6003–6010.

(26) Köhler, A.; Bässler, H., *Electronic processes in organic semiconductors: An introduction*; John Wiley & Sons: 2015.

(27) Tress, W., *Organic Solar Cells: Theory, Experiment, and Device Simulation*; Springer Cham: 2014.

(28) Schwenn, P. E.; Burn, P. L.; Powell, B. J. Calculation of solid state molecular ionisation energies and electron affinities for organic semiconductors. *Organic Electronics* **2011**, *12*, 394–403.

(29) Duhm, S.; Heimel, G.; Salzmann, I.; Glowatzki, H.; Johnson, R. L.; Vollmer, A.; Rabe, J. P.; Koch, N. Orientation-dependent ionization energies and interface dipoles in ordered molecular assemblies. *Nat. Mater.* **2008**, *7*, 326–332.

(30) Chen, W.; Huang, H.; Chen, S.; Huang, Y. L.; Gao, X. Y.; Wee, A. T. S. Molecular orientation-dependent ionization potential of organic thin films. *Chem. Mater.* **2008**, *20*, 7017–7021.

(31) Bounds, P. J.; Munn, R. W. Polarization energy of a localized charge in a molecular crystal. *Chem. Phys.* **1979**, *44*, 103–112.

(32) Bounds, P. J.; Munn, R. W. Polarization energy of a localized charge in a molecular crystal. II. Charge-quadrupole energy. *Chem. Phys.* **1981**, *59*, 41–45.

(33) D'Avino, G.; Muccioli, L.; Castet, F.; Poelking, C.; Andrienko, D.; Soos, Z. G.; Cornil, J.; Beljonne, D. Electrostatic phenomena in organic semiconductors: fundamentals and implications for photovoltaics. *J. Phys.: Condens. Matter* **2016**, *28*, 433002.

(34) Armleder, J.; Strunk, T.; Symalla, F.; Friederich, P.; Peña, J. E. O.; Neumann, T.; Wenzel, W.; Fediai, A. Computing charging and polarization energies of small organic molecules embedded into amorphous materials with quantum accuracy. *J. Chem. Theory Comput.* **2021**, *17*, 3727–3738.

(35) Schwoerer, M.; Wolf, H. C., *Organic Molecular Solids*; John Wiley & Sons: 2007.

(36) Salzmann, I.; Heimel, G.; Oehzelt, M.; Winkler, S.; Koch, N. Molecular electrical doping of organic semiconductors: Fundamental mechanisms and emerging dopant design rules. *Acc. Chem. Res.* **2016**, *49*, 370–378.

(37) Méndez, H.; Heimel, G.; Winkler, S.; Frisch, J.; Opitz, A.; Sauer, K.; Wegner, B.; Oehzelt, M.; Röthel, C.; Duhm, S.; Többens, D.; Koch, N.; Salzmann, I. Charge-transfer crystallites as molecular electrical dopants. *Nat. Commun.* **2015**, *6*, 8560.

(38) Lifschitz, A. M.; Young, R. M.; Mendez-Arroyo, J.; Stern, C. L.; McGuirk, C. M.; Wasielewski, M. R.; Mirkin, C. A. An allosteric photoredox catalyst inspired by photosynthetic machinery. *Nat. Commun.* **2015**, *6*, 6541.

(39) Fediai, A.; Emering, A.; Symalla, F.; Wenzel, W. Disorder-driven doping activation in organic semiconductors. *Phys. Chem. Chem. Phys.* **2020**, *22*, 10256–10264.

(40) Li, J.; Duchemin, I.; Roscioni, O. M.; Friederich, P.; Anderson, M.; Como, E. D.; Kociok-Köhn, G.; Wenzel, W.; Zannoni, C.; Beljonne, D.; Blase, X.; D'Avino, G. Host dependence of the electron affinity of molecular dopants. *Mater. Horiz.* **2019**, *6*, 107–114.

(41) Mityashin, A.; Olivier, Y.; Regemorter, T. V.; Rolin, C.; Verlaak, S.; Martinelli, N. G.; Beljonne, D.; Cornil, J.; Genoe, J.; Heremans, P. Unraveling the mechanism of molecular doping in organic semiconductors. *Adv. Mater.* **2012**, *24*, 1535–1539.

(42) Tietze, M. L.; Benduhn, J.; Pahner, P.; Nell, B.; Schwarze, M.; Kleemann, H.; Krammer, M.; Zojer, K.; Vandewal, K.; Leo, K. Elementary steps in electrical doping of organic semiconductors. *Nat. Commun.* **2018**, *9*, 1182.

(43) Schwarze, M.; Gaul, C.; Scholz, R.; Bussolotti, F.; Hofacker, A.; Schellhammer, K. S.; Nell, B.; Naab, B. D.; Bao, Z.; Spoltore, D.; Vandewal, K.; Widmer, J.; Kera, S.; Ueno, N.; Ortmann, F.; Leo, K. Molecular parameters responsible for thermally activated transport in doped organic semiconductors. *Nat. Mater.* **2019**, *18*, 242–248.

(44) Comin, M.; Fratini, S.; Blase, X.; D'Avino, G. Doping-induced dielectric catastrophe prompts free-carrier release in organic semiconductors. *Adv. Mater.* **2022**, *34*, 2105376.

(45) Yoshida, H.; Yamada, K.; Tsutsumi, J.; Sato, N. Complete description of ionization energy and electron affinity in organic solids: determining contributions from electronic polarization, energy band dispersion, and molecular orientation. *Phys. Rev. B* **2015**, *92*, 075145.

(46) Barrett, B. J.; Katz, H. E.; Bragg, A. E. Permittivity threshold and thermodynamics of integer charge-transfer complexation for an organic donor–acceptor pair. *J. Phys. Chem. B* **2023**, *127*, 2792–2800.

(47) Ivory, D. M.; Miller, G. G.; Sowa, J. M.; Shacklette, L. W.; Chance, R. R.; Baughman, R. H. Highly conducting charge-transfer complexes of poly(*p*-phenylene). *J. Chem. Phys.* **1979**, *71*, 1506–1507.

(48) Parthasarathy, G.; Shen, C.; Kahn, A.; Forrest, S. R. Lithium doping of semiconducting organic charge transport materials. *J. Appl. Phys.* **2001**, *89*, 4986–4992.

(49) D'Andrade, B. W.; Forrest, S. R.; Chwang, A. B. Operational stability of electrophosphorescent devices containing p and n doped transport layers. *Appl. Phys. Lett.* **2003**, *83*, 3858–3860.

(50) Kido, J.; Matsumoto, T. Bright organic electroluminescent devices having a metal-doped electron-injecting layer. *Appl. Phys. Lett.* **1998**, *73*, 2866–2868.

(51) Nollau, A.; Pfeiffer, M.; Fritz, T.; Leo, K. Controlled n-type doping of a molecular organic semiconductor: Naphthalenetetracarboxylic dianhydride (NTCDA) doped with bis(ethylenedithio)-tetrathiafulvalene (BEDT-TTF). *J. Appl. Phys.* **2000**, *87*, 4340–4343.

(52) Werner, A.; Li, F.; Harada, K.; Pfeiffer, M.; Fritz, T.; Leo, K.; Machill, S. n-Type doping of organic thin films using cationic dyes. *Adv. Funct. Mater.* **2004**, *14*, 255–260.

(53) Werner, A. G.; Li, F.; Harada, K.; Pfeiffer, M.; Fritz, T.; Leo, K. Pyronin B as a donor for n-type doping of organic thin films. *Appl. Phys. Lett.* **2003**, *82*, 4495–4497.

(54) Alfonsi, K.; Colberg, J.; Dunn, P. J.; Fevig, T.; Jennings, S.; Johnson, T. A.; Kleine, H. P.; Knight, C.; Nagy, M. A.; Perry, D. A.; Stefaniak, M. Green chemistry tools to influence a medicinal chemistry and research chemistry based organisation. *Green Chem.* **2008**, *10*, 31–36.

(55) Herzig, E. M.; Gao, F.; Bergqvist, J.; Loi, M. A.; Meier, S. B. Harmonizing organic photovoltaics research and development among academia and industry. *Joule* **2024**, *8*, 2171–2178.

(56) Prat, D.; Pardigon, O.; Flemming, H. W.; Letestu, S.; Ducandas, V.; Isnard, P.; Guntrum, E.; Senac, T.; Ruisseau, S.; Cruciani, P.; Hosek, P. Sanofi's solvent selection guide: A step toward more sustainable processes. *Org. Process Res. Dev.* **2013**, *17*, 1517–1525.

(57) Henderson, R. K.; Jiménez-González, C.; Constable, D. J. C.; Alston, S. R.; Inglis, G. G. A.; Fisher, G.; Sherwood, J.; Binks, S. P.; Curzons, A. D. Expanding GSK's solvent selection guide – embedding sustainability into solvent selection starting at medicinal chemistry. *Green Chem.* **2011**, *13*, 854–862.

(58) Karthika, S.; Radhakrishnan, T. K.; Kalaichelvi, P. A review of classical and nonclassical nucleation theories. *Cryst. Growth Des.* **2016**, *16*, 6663–6681.

(59) Thanh, N. T. K.; Maclean, N.; Mahiddine, S. Mechanisms of nucleation and growth of nanoparticles in solution. *Chem. Rev.* **2014**, *114*, 7610–7630.

(60) Davey, R. J.; Schroeder, S. L. M.; ter Horst, J. H. Nucleation of organic crystals—A molecular perspective. *Angew. Chem. Int. Ed.* **2013**, *52*, 2166–2179.

(61) Jones, R. A. L., *Soft condensed matter*; Oxford Univ. Press: 2002.

(62) Oxtoby, D. W. Nucleation of first-order phase transitions. *Acc. Chem. Res.* **1998**, *31*, 91–97.

(63) Zhang, C.; Pansare, V. J.; Prud'homme, R. K.; Priestley, R. D. Flash nanoprecipitation of polystyrene nanoparticles. *Soft Matter* **2012**, *8*, 86–93.

(64) Li, N.; Nikoubashman, A.; Panagiotopoulos, A. Z. Multi-scale simulations of polymeric nanoparticle aggregation during rapid solvent exchange. *J. Chem. Phys.* **2018**, *149*, 084904.

(65) Aubry, J.; Ganachaud, F.; Addad, J.-P. C.; Cabane, B. Nanoprecipitation of polymethylmethacrylate by solvent shifting: 1. Boundaries. *Langmuir* **2009**, *25*, 1970–1979.

(66) Nikoubashman, A.; Lee, V. E.; Sosa, C.; Prud'homme, R. K.; Priestley, R. D.; Panagiotopoulos, A. Z. Directed assembly of soft colloids through rapid solvent exchange. *ACS Nano* **2016**, *10*, 1425–1433.

(67) Sharratt, W. N.; Lee, V. E.; Priestley, R. D.; Cabral, J. T. Precision polymer particles by flash nanoprecipitation and microfluidic droplet extraction. *ACS Appl. Polym. Mater.* **2021**, *3*, 4746–4768.

(68) Tadros, T. F., *Nanodispersions*; De Gruyter: 2016.

(69) Solans, C.; Izquierdo, P.; Nolla, J.; Azemar, N.; Garcia-Celma, M. J. Nano-emulsions. *Curr. Opin. Colloid Interface Sci.* **2005**, *10*, 102–110.

(70) Shvets, A. A.; Semenov, A. N. Effective interactions between solid particles mediated by free polymer in solution. *J. Chem. Phys.* **2013**, *139*, 054905.

(71) Ameri, M.; Al-Mudhaffer, M. F.; Almyahi, F.; Fardell, G. C.; Marks, M.; Al-Ahmad, A.; Fahy, A.; Andersen, T.; Elkington, D. C.; Feron, K.; Dickinson, M.; Samavat, F.; Dastoor, P. C.; Griffith, M. J. Role of stabilizing surfactants on capacitance and charge and and ion transport in organic nanoparticle-based electronic devices. *ACS Appl. Mater. Interfaces* **2019**, *11*, 10074–10088.

(72) Cao, Z.; Tsai, S. N.; Zuo, Y. Y. An optical method for quantitatively determining the surface free energy of micro- and nanoparticles. *Anal. Chem.* **2019**, *91*, 12819–12826.

(73) Manger, F.; Fischer, K.; Marlow, P.; Röhm, H.; Sprau, C.; Colsmann, A. Iodine-stabilized organic nanoparticle dispersions for the fabrication of 10% efficient non-fullerene solar cells. *Adv. Energy Mater.* **2023**, *13*, 2202820.

(74) Marlow, P. Organische Solarzellen: Synthese und Stabilisierung tensidfreier organischer Halbleiterdispersionen, Ph.D. Thesis, Karlsruher Institut für Technologie (KIT), 2021.

(75) Schwoerer, M., Organische Elektronik In *Physik im 21. Jahrhundert*, Martienssen, W., Röß, D., Eds.; Springer Berlin Heidelberg: 2011.

(76) Colberts, F. J. M.; Wienk, M. M.; Janssen, R. A. J. Aqueous nanoparticle polymer solar cells: Effects of surfactant concentration and processing on device performance. *ACS Appl. Mater. Interfaces* **2017**, *9*, 13380–13389.

(77) Moulé, A. J. Power from plastic. *Curr. Opin. Solid State Mater. Sci.* **2010**, *14*, 123–130.

(78) Fukuda, K.; Yu, K.; Someya, T. The future of flexible organic solar cells. *Adv. Energy Mater.* **2020**, *10*, 2000765.

(79) Hu, Z.; Wang, J.; Ma, X.; Gao, J.; Xu, C.; Yang, K.; Wang, Z.; Zhang, J.; Zhang, F. A critical review on semitransparent organic solar cells. *Nano Energy* **2020**, *78*, 105376.

(80) Søndergaard, R.; Hösel, M.; Angmo, D.; Larsen-Olsen, T. T.; Krebs, F. C. Roll-to-roll fabrication of polymer solar cells. *Mater. Today* **2012**, *15*, 36–49.

(81) Fischer, K. Design of P3HT:Fullerene nanoparticle dispersions for the fabrication of organic solar cells, Ph.D. Thesis, Karlsruher Institut für Technologie (KIT), 2023.

(82) Lochner, C. M.; Khan, Y.; Pierre, A.; Arias, A. C. All-organic optoelectronic sensor for pulse oximetry. *Nat. Commun.* **2014**, *5*, 5745.

(83) Ng, T. N.; Wong, W. S.; Chabinyc, M. L.; Sambandan, S.; Street, R. A. Flexible image sensor array with bulk heterojunction organic photodiode. *Appl. Phys. Lett.* **2008**, *92*, 213303.

(84) Rauch, T.; Böberl, M.; Tedde, S. F.; Fürst, J.; Kovalenko, M. V.; Hesser, G.; Lemmer, U.; Heiss, W.; Hayden, O. Near-infrared imaging with quantum-dot-sensitized organic photodiodes. *Nature Photon* **2009**, *3*, 332–336.

(85) Nau, S.; Wolf, C.; Sax, S.; List-Kratochvil, E. J. W. Organic non-volatile resistive photo-switches for flexible image detector arrays. *Adv. Mater.* **2014**, *27*, 1048–1052.

(86) Fang, Y.; Huang, J. Resolving weak light of sub-picowatt per square centimeter by hybrid perovskite photodetectors enabled by noise reduction. *Adv. Mater.* **2015**, *27*, 2804–2810.

(87) Armin, A.; Jansen-van Vuuren, R. D.; Kopidakis, N.; Burn, P. L.; Meredith, P. Narrowband light detection via internal quantum efficiency manipulation of organic photodiodes. *Nat. Commun.* **2015**, *6*, 6343.

(88) Gong, X.; Tong, M.; Xia, Y.; Cai, W.; Moon, J. S.; Cao, Y.; Yu, G.; Shieh, C.-L.; Nilsson, B.; Heeger, A. J. High-detectivity polymer photodetectors with spectral response from 300 nm to 1450 nm. *Science* **2009**, *325*, 1665–1667.

(89) Azzellino, G.; Grimoldi, A.; Binda, M.; Caironi, M.; Natali, D.; Sampietro, M. Fully inkjet-printed organic photodetectors with high quantum yield. *Adv. Mater.* **2013**, *25*, 6829–6833.

(90) Pace, G.; Grimoldi, A.; Natali, D.; Sampietro, M.; Coughlin, J. E.; Bazan, G. C.; Caironi, M. All-organic and fully-printed semitransparent photodetectors based on narrow bandgap conjugated molecules. *Adv. Mater.* **2014**, *26*, 6773–6777.

(91) Arias, A. C.; MacKenzie, J. D.; McCulloch, I.; Rivnay, J.; Salleo, A. Materials and applications for large area electronics: Solution-based approaches. *Chem. Rev.* **2010**, *110*, 3–24.

(92) Simone, G.; Dyson, M. J.; Meskers, S. C. J.; Janssen, R. A. J.; Gelinck, G. H. Organic photodetectors and their application in large area and flexible image sensors: The role of dark current. *Adv. Funct. Mater.* **2020**, *30*, 1904205.

(93) Yang, D.; Ma, D. Development of organic semiconductor photodetectors: from mechanism to applications. *Adv. Opt. Mater.* **2019**, *7*, 1800522.

(94) Dong, R.; Bi, C.; Dong, Q.; Guo, F.; Yuan, Y.; Fang, Y.; Xiao, Z.; Huang, J. An ultraviolet-to-NIR broad spectral nanocomposite photodetector with gain. *Adv. Opt. Mater.* **2014**, *2*, 549–554.

(95) Kim, I. K.; Jo, J. H.; Lee, J.; Choi, Y. J. Detectivity analysis for organic photodetectors. *Org. Electron.* **2018**, *57*, 89–92.

(96) Guo, F.; Xiao, Z.; Huang, J. Fullerene photodetectors with a linear dynamic range of 90 dB enabled by a cross-linkable buffer layer. *Adv. Opt. Mater.* **2013**, *1*, 289–294.

(97) Yoon, S.; Ha, J.; Cho, J.; Chung, D. S. Nonabsorbing acceptor-based planar heterojunction for color-selective and high-detectivity polymer photodiodes. *Adv. Opt. Mater.* **2016**, *4*, 1933–1938.

(98) Ha, J. U.; Kim, K.; Yoon, S.; Sim, K. M.; Cho, J.; Chung, D. S. Synergetic effect of a surfactant on the facile fabrication and high detectivity of an inverted organic bulk heterojunction photodiode. *ACS Photonics* **2017**, *4*, 2085–2090.

(99) Armin, A.; Hambsch, M.; Kim, I. K.; Burn, P. L.; Meredith, P.; Namdas, E. B. Thick junction broadband organic photodiodes. *Laser Photonics Rev.* **2014**, *8*, 924–932.

(100) Kim, I. K.; Pal, B. N.; Ullah, M.; Burn, P. L.; Lo, S. C.; Meredith, P.; Namdas, E. B. High-performance, solution-processed non-polymeric organic photodiodes. *Adv. Opt. Mater.* **2015**, *3*, 50–56.

(101) Yao, Y.; Liang, Y.; Shrotriya, V.; Xiao, S.; Yu, L.; Yang, Y. Plastic near-infrared photodetectors utilizing low band gap polymer. *Adv. Mater.* **2007**, *19*, 3979–3983.

(102) Ren, H.; Chen, J.-D.; Li, Y.-Q.; Tang, J.-X. Recent progress in organic photodetectors and their applications. *Adv. Sci.* **2020**, *8*, 2002418.

(103) Shan, T.; Hou, X.; Yin, X.; Guo, X. Organic photodiodes: Device engineering and applications. *Front. Optoelectron.* **2022**, *15*, 49.

(104) Shekhar, H.; Solomeshch, O.; Liraz, D.; Tessler, N. Low dark leakage current in organic planar heterojunction photodiodes. *Appl. Phys. Lett.* **2017**, *111*, 223301.

(105) Agostinelli, T.; Campoy-Quiles, M.; Blakesley, J. C.; Speller, R.; Bradley, D. D. C.; Nelson, J. A polymer/fullerene based photodetector with extremely low dark current for x-ray medical imaging applications. *Appl. Phys. Lett.* **2008**, *93*, 203305.

(106) Wang, H.; Xing, S.; Zheng, Y.; Kong, J.; Yu, J.; Taylor, A. D. Three-phase morphology evolution in sequentially solution-processed polymer photodetector: toward low dark current and high photodetectivity. *ACS Appl. Mater. Interfaces* **2018**, *10*, 3856–3864.

(107) Valouch, S.; Hönes, C.; Kettlitz, S. W.; Christ, N.; Do, H.; Klein, M. F. G.; Kalt, H.; Colsmann, A.; Lemmer, U. Solution processed small molecule organic interfacial layers for low dark current polymer photodiodes. *Organic Electronics* **2012**, *13*, 2727–2732.

(108) Grimoldi, A.; Colella, L.; Monaca, L. L.; Azzellino, G.; Caironi, M.; Bertarelli, C.; Natali, D.; Sampietro, M. Inkjet printed polymeric electron blocking and surface energy modifying layer for low dark current organic photodetectors. *Org. Electron.* **2016**, *36*, 29–34.

(109) Yoon, S.; Cho, J.; Sim, K. M.; Ha, J.; Chung, D. S. Low dark current inverted organic photodiodes using anionic polyelectrolyte as a cathode interlayer. *Appl. Phys. Lett.* **2017**, *110*, 083301.

(110) Zhou, X.; Yang, D.; Ma, D. Extremely low dark current, high responsivity, all-polymer photodetectors with spectral response from 300 nm to 1000 nm. *Adv. Opt. Mater.* **2015**, *3*, 1570–1576.

(111) Ramuz, M.; Bürgi, L.; Winnewisser, C.; Seitz, P. High sensitivity organic photodiodes with low dark currents and increased lifetimes. *Org. Electronics* **2008**, *9*, 369–376.

(112) Neumann, T.; Danilov, D.; Lennartz, C.; Wenzel, W. Modeling disordered morphologies in organic semiconductors. *J. Comput. Chem.* **2013**, *34*, 2716–2725.

(113) Singh, U. C.; Kollman, P. A. An approach to computing electrostatic charges for molecules. *J. Comput. Chem.* **1984**, *5*, 129–145.

(114) Bayly, C. I.; Cieplak, P.; Cornell, W.; Kollman, P. A. A well-behaved electrostatic potential based method using charge restraints for deriving atomic charges: The RESP model. *J. Phys. Chem.* **1993**, *97*, 10269–10280.

(115) Li, Z.; Scheraga, H. A. Monte Carlo-minimization approach to the multiple-minima problem in protein folding. *Proc. Natl. Acad. Sci. U.S.A.* **1987**, *84*, 6611–6615.

(116) Soos, Z. G.; Tsiper, E. V.; Pascal, R. A. Charge redistribution and electronic polarization in organic molecular crystals. *Chem. Phys. Lett.* **2001**, *342*, 652–658.

(117) Tsiper, E. V.; Soos, Z. G. Charge redistribution and polarization energy of organic molecular crystals. *Phys. Rev. B* **2001**, *64*, 195124.

(118) Ishida, T.; Morita, A. Extended treatment of charge response kernel comprising the density functional theory and charge regulation procedures. *J. Chem. Phys.* **2006**, *125*, 074112.

(119) Castet, F.; Aurel, P.; Fritsch, A.; Ducasse, L.; Liotard, D.; Linares, M.; Cornil, J.; Beljonne, D. Electronic polarization effects on charge carriers in anthracene: A valence bond study. *Phys. Rev. B* **2008**, *77*, 115210.

(120) Castet, F.; Ducasse, L.; Fritsch, A. From organic superconductors to DNA: Fragment orbital-based model. *Int. J. Quantum Chem.* **2006**, *106*, 734–746.

(121) Ratcli, L. E.; Danilov, D.; Wenzel, W.; Beljonne, D. Toward fast and accurate evaluation of charge on-site energies and transfer integrals in supramolecular architectures using linear constrained density functional theory (CDFT)-based methods. *J. Chem. Theory Comput.* **2015**, 10.

(122) Friederich, P.; Symalla, F.; Meded, V.; Neumann, T.; Wenzel, W. *Ab initio* treatment of disorder effects in amorphous organic materials: Toward parameter free materials simulation. *J. Chem. Theory Comput.* **2014**, *10*, 3720–3725.

(123) Friederich, P.; Meded, V.; Symalla, F.; Elstner, M.; Wenzel, W. QM/QM approach to model energy disorder in amorphous organic semiconductors. *J. Chem. Theory Comput.* **2015**, *11*, 560–567.

(124) Friederich, P.; Strunk, T.; Wenzel, W.; Kondov, I. Multiscale simulation of organic electronics via smart scheduling of quantum mechanics computations. *Procedia Comput. Sci.* **2016**, *80*, 1244–1254.

(125) Becke, A. D. Density-functional exchange-energy approximation with correct asymptotic behavior. *Phys. Rev. A* **1988**, *38*, 3098–3100.

(126) Adamo, C.; Barone, V. Toward reliable density functional methods without adjustable parameters: The PBE0 model. *J. Chem. Phys.* **1999**, *110*, 6158–6170.

(127) Balasubramani, S. G. et al. TURBOMOLE: Modular program suite for *ab initio* quantum-chemical and condensed-matter simulations. *J. Chem. Phys.* **2020**, *152*, 184107.

(128) Wilhelm, J.; Ben, M. D.; Hutter, J. GW in the gaussian and plane waves scheme with application to linear acenes. *J. Chem. Theory Comput.* **2016**, *12*, 3623–3635.

(129) Symalla, F.; Fediai, A.; Armleder, J.; Kaiser, S.; Strunk, T.; Neumann, T.; Wenzel, W. 43-3: Ab-initio simulation of doped injection layers. *SID Symp. Dig. Tech. Pap.* **2020**, *51*, 630–633.

(130) Rappoport, D.; Furche, F. Property-optimized Gaussian basis sets for molecular response calculations. *J. Chem. Phys.* **2010**, *133*, 134105.

(131) Symalla, F. Modellierung von Ladungs- und Exzitondynamik in amorphen organischen Halbleitern, Ph.D. Thesis, Karlsruhe Institute of Technology, 2018.

(132) Ewald, P. P. Die Berechnung optischer und elektrostatischer Gitterpotentiale. *Ann. Phys.* **1921**, *369*, 253–287.

(133) Bortz, A. B.; Kalos, M. H.; Lebowitz, J. L. A new algorithm for Monte Carlo simulation of Ising spin systems. *J. Comput. Phys.* **1975**, *17*, 10–18.

(134) Gärtner, S.; Clulow, A. J.; Howard, I. A.; Gilbert, E. P.; Burn, P. L.; Gentle, I. R.; Colsmann, A. Relating structure to efficiency in surfactant-free polymer/fullerenes nanoparticle-based organic solar cells. *ACS Appl. Mater. Interfaces* **2017**, *9*, 42986–42995.

(135) Ulum, S.; Holmes, N.; Barr, M.; Kilcoyne, A. L. D.; Gong, B. B.; Zhou, X.; Belcher, W.; Dastoor, P. The role of miscibility in polymer:fullerene nanoparticulate organic photovoltaic devices. *Nano Energy* **2013**, *2*, 897–905.

(136) Bruker Corporation DektakXT Stylus Profiler User Manual; Bruker Corporation, 2011.

(137) Gueymard, C. A.; Myers, D.; Emery, K. Proposed reference irradiance spectra for solar energy systems testing. *Solar Energy* **2002**, *73*, 443–467.

(138) Li, J.; D'Avino, G.; Pershin, A.; Jacquemin, D.; Duchemin, I.; Beljonne, D.; Blase, X. Correlated electron-hole mechanism for molecular doping in organic semiconductors. *Phys. Rev. Mater.* **2017**, *1*, 025602.

(139) Weigend, F.; Ahlrichs, R. Balanced basis sets of split valence, triple zeta valence and quadruple zeta valence quality for H to Rn: design and assessment of accuracy. *Phys. Chem. Chem. Phys.* **2005**, *7*, 3297.

(140) Nell, B.; Ortstein, K.; Boltalina, O. V.; Vandewal, K. Influence of dopant–host energy level offset on thermoelectric properties of doped organic semiconductors. *J. Phys. Chem. C* **2018**, *122*, 11730–11735.

(141) Cheng, J.-A.; Cheng, P.-J. Crystal study of N,N′-diphenyl-N,N′-bis(1-naphthyl)-1,1′-biphenyl-4,4′-diamine. *J. Chem. Crystallogr.* **2010**, *40*, 557–560.

(142) Nagamatsu, S.; Pandey, S. S. Ordered arrangement of F4TCNQ anions in three-dimensionally oriented P3HT thin films. *Sci. Rep.* **2020**, *10*, 20020.

(143) Zhang, Z.; Wang, J.; Liu, D.; Luo, W.; Zhang, M.; Jiang, W.; Zhu, Y. Highly efficient organic photocatalyst with full visible light spectrum through π–π stacking of TCNQ–PTCDI. *ACS Appl. Mater. Interfaces* **2016**, *8*, 30225–30231.

(144) Reiser, P.; Konrad, M.; Fediai, A.; Léon, S.; Wenzel, W.; Friederich, P. Analyzing dynamical disorder for charge transport in organic semiconductors via machine learning. *J. Chem. Theory Comput.* **2021**, *17*, 3750–3759.

(145) Kaiser, S.; Neumann, T.; Symalla, F.; Schlöder, T.; Fediai, A.; Friederich, P.; Wenzel, W. De novo calculation of the charge carrier mobility in amorphous small molecule organic semiconductors. *Front. Chem.* **2021**, *9*.

(146) Andrienko, D., Simulations of morphology and charge transport in supramolecular organic materials In *Supramolecular Materials for Opto-Electronics*, Koch, N., Ed.; The Royal Society of Chemistry: 2014.

(147) Poelking, C.; Tietze, M.; Elschner, C.; Olthof, S.; Hertel, D.; Baumeier, B.; Würthner, F.; Meerholz, K.; Leo, K.; Andrienko, D. Impact of mesoscale order on open-circuit voltage in organic solar cells. *Nat. Mater.* **2015**, *14*, 434–439.

(148) Schwarze, M.; Schellhammer, K.; Ortstein, K.; Benduhn, J.; Gaul, C.; Hinderhofer, A.; Toro, L. P.; Scholz, R.; Kublitski, J.; Roland, S.; Lau, M.; Poelking, C.; Andrienko, D.; Cuniberti, G.; Schreiber, F.; Neher, D.; Vandewal, K.; Ortmann, F.; Leo, K. Impact of molecular quadrupole moments on the energy levels at organic heterojunctions. *Nat. Commun.* **2019**, *10*, 2466.

(149) Menke, T.; Ray, D.; Kleemann, H.; Hein, M. P.; Leo, K.; Riede, M. Highly efficient p-dopants in amorphous hosts. *Org. Electron.* **2014**, *15*, 365–371.

(150) Zuo, G.; Abdalla, H.; Kemerink, M. Impact of doping on the density of states and the mobility in organic semiconductors. *Phys. Rev. B* **2016**, *93*, 235203.

(151) Bag, S.; Friederich, P.; Kondov, I.; Wenzel, W. Concentration dependent energy levels shifts in donor-acceptor mixtures due to intermolecular electrostatic interaction. *Sci. Rep.* **2019**, *9*, 12424.

(152) Graham, K. R.; Ngongang, G. O. N.; Conron, S. M.; Munir, R.; Vandewal, K.; Chen, J. J.; Sweetnam, S.; Thompson, M. E.; Salleo, A.; McGehee, M. D.; Amassian, A. The roles of structural order and intermolecular interactions in determining ionization energies and charge-transfer state energies in organic semiconductors. *Adv. Energy Mater.* **2016**, *6*, 1601211.

(153) Metz, W. D. Organic crystals: Hints of extraordinary conductivity. *Science* **1973**, *180*, 1041–1042.

(154) Zuo, G.; Abdalla, H.; Kemerink, M. Impact of doping on the density of states and the mobility in organic semiconductors. *Phys. Rev. B* **2016**, *93*, 235203.

(155) Müller, L.; Nanova, D.; Glaser, T.; Beck, S.; Pucci, A.; Kast, A. K.; Schröder, R. R.; Mankel, E.; Pingel, P.; Neher, D.; Kowalsky, W.; Lovrincic, R. Charge-transfer–solvent interaction predefines doping efficiency in p-doped P3HT films. *Chem. Mater.* **2016**, *28*, 4432–4439.

(156) Burschka, J.; Kessler, F.; Nazeeruddin, M. K.; Grätzel, M. Co(III) complexes as p-dopants in solid-state dye-sensitized solar cells. *Chem. Mater.* **2013**, *25*, 2986–2990.

(157) Kiefer, D.; Kroon, R.; Hofmann, A. I.; Sun, H.; Liu, X.; Giovannitti, A.; Stegerer, D.; Cano, A.; Hynynen, J.; Yu, L.; Zhang, Y.; Nai, D.; Harrelson, T. F.; Sommer, M.; Moulé, A. J.; Kemerink, M.; Marder, S. R.; McCulloch, I.; Fahlman, M.; Fabiano, S.; Müller, C. Double doping of conjugated polymers with monomer molecular dopants. *Nature Mater.* **2019**, *18*, 149–155.

(158) Cohen, M. D.; Fischer, E. 588. Isosbestic points. *J. Chem. Soc.* **1962**, 3044–3052.

(159) Atallah, T. L.; Gustafsson, M. V.; Schmidt, E.; Frisbie, C. D.; Zhu, X.-Y. Charge saturation and intrinsic doping in electrolyte-gated organic semiconductors. *J. Phys. Chem. Lett.* **2015**, *6*, 4840–4844.

(160) Tietze, M. L.; Pahner, P.; Schmidt, K.; Leo, K.; Lüssem, B. Doped organic semiconductors: Trap-filling, impurity saturation, and reserve regimes. *Adv. Funct. Mater.* **2015**, *25*, 2701–2707.

(161) Scaccabarozzi, A. D.; Basu, A.; Aniés, F.; Liu, J.; Zapata-Arteaga, O.; Warren, R.; Firdaus, Y.; Nugraha, M. I.; Lin, Y.; Campoy-Quiles, M.; Koch, N.; Müller, C.; Tsetseris, L.; Heeney, M.; Anthopoulos, T. D. Doping approaches for organic semiconductors. *Chem. Rev.* **2022**, *122*, 4420–4492.

(162) Tietze, M. L.; Burtone, L.; Riede, M.; Lüssem, B.; Leo, K. Fermi level shift and doping efficiency in p-doped small molecule organic semiconductors: A photoelectron spectroscopy and theoretical study. *Phys. Rev. B* **2012**, *86*, 035320.

(163) Liu, W.; Zhang, J.; Zhou, Z.; Zhang, D.; Zhang, Y.; Xu, S.; Zhu, X. Design of a new fused-ring electron acceptor with excellent compatibility to wide-bandgap polymer donors for high-performance organic photovoltaics. *Adv. Mater.* **2018**, *30*, 1800403.

(164) Dhanker, R.; Gray, C. L.; Mukhopadhyay, S.; Nunez, S.; Cheng, C.-Y.; Sokolov, A. N.; Giebink, N. C. Large bipolaron density at organic semiconductor/electrode interfaces. *Nat. Commun.* **2017**, *8*, 2252.

(165) Kendrick, W. J.; Jirásek, M.; Peeks, M. D.; Greetham, G. M.; Sazanovich, I. V.; Donaldson, P. M.; Towrie, M.; Parker, A. W.; Anderson, H. L. Mechanisms of IR amplification in radical cation polarons. *Chem. Sci.* **2020**, *11*, 2112–2120.

(166) Cheng, C.-Y.; Dhanker, R.; Gray, C. L.; Mukhopadhyay, S.; Kennehan, E. R.; Asbury, J. B.; Sokolov, A.; Giebink, N. C. Charged polaron polaritons in an organic semiconductor microcavity. *Phys. Rev. Lett.* **2018**, *120*, 017402.

(167) Bentley, C. L.; Bond, A. M.; Hollenkamp, A. F.; Mahon, P. J.; Zhang, J. Voltammetric determination of the iodide/iodine formal potential and triiodide stability constant in conventional and ionic liquid media. *J. Phys. Chem. C* **2015**, *119*, 22392–22403.

(168) Trukhanov, V. A.; Bruevich, V. V.; Paraschuk, D. Y. Effect of doping on performance of organic solar cells. *Phys. Rev. B* **2011**, *84*, 205318.

(169) Gärtner, S. Organische Nanopartikel zum Aufbau photoaktiver Schichten Organischer Solarzellen, Ph.D. Thesis, Karlsruher Institut für Technologie (KIT), 2016.

(170) Fischer, K.; Marlow, P.; Bitsch, K.; Sprau, C.; Colsmann, A. The importance of semiconductor miscibility for the formation of light-harvesting polymer:fullerene nanoparticle dispersions. *Sol. RRL* **2024**, *8*, 2400132.

(171) Liu, J.; Gao, M.; Kim, J.; Zhou, Z.; Chung, D. S.; Yin, H.; Ye, L. Challenges and recent advances in photodiodes-based organic photodetectors. *Mater. Today* **2021**, *51*, 475–503.

(172) Zheng, L.; Zhu, T.; Xu, W.; Liu, L.; Zheng, J.; Gong, X.; Wudl, F. Solution-processed broadband polymer photodetectors with a spectral response of up to 2.5 μm by a low bandgap donor–acceptor conjugated copolymer. *J. Mater. Chem. C* **2018**, *6*, 3634–3641.

(173) Hendriks, K. H.; Li, W.; Wienk, M. M.; Janssen, R. A. J. Small-bandgap semiconducting polymers with high near-infrared photoresponse. *J. Am. Chem. Soc.* **2014**, *136*, 12130–12136.

(174) Hu, X.; Dong, Y.; Huang, F.; Gong, X.; Cao, Y. Solution-processed high-detectivity near-infrared polymer photodetectors fabricated by a novel low-bandgap semiconducting polymer. *J. Phys. Chem. C* **2013**, *117*, 6537–6543.

(175) Lee, K.-H.; Leem, D.-S.; Castrucci, J. S.; Park, K.-B.; Bulliard, X.; Kim, K.-S.; Jin, Y. W.; Lee, S.; Bender, T. P.; Park, S. Y. Green-sensitive organic photodetectors with high sensitivity and spectral selectivity using subphthalocyanine derivatives. *ACS Appl. Mater. Interfaces* **2013**, *5*, 13089–13095.

(176) Wang, J.; Wang, J.; Dougherty, D. B. Direct molecular quantification of electronic disorder in N,N ′-Di-[(1-naphthyl)-N,N ′-diphenyl]-1,1′-biphenyl)-4,4′-diamine on Au(111). *J. Vac. Sci. Technol. B* **2020**, *38*, 053401.

(177) Gao, J.; Gao, W.; Ma, X.; Hu, Z.; Xu, C.; Wang, X.; An, Q.; Yang, C.; Zhang, X.; Zhang, F. Over 14.5% efficiency and 71.6% fill factor of ternary organic solar cells with 300 nm thick active layers. *Energy Environ. Sci.* **2020**, *13*, 958–967.

(178) Zhao, Z.; Xu, C.; Niu, L.; Zhang, X.; Zhang, F. Recent progress on broadband organic photodetectors and their applications. *Laser Photon. Rev.* **2020**, *14*, 2000262.

(179) Kettle, J.; Chang, S.-W.; Horie, M. IR sensor based on low bandgap organic photodiode with up-converting phosphor. *IEEE Sensors J.* **2015**, *15*, 3221–3224.

(180) Kim, J. Y.; Noh, S.; Lee, D.; Nayak, P. K.; Hong, Y.; Lee, C. Solution-processable zinc oxide for the polymer solar cell based on P3HT:PCBM. *J. Nanosci. Nanotech.* **2011**, *11*, 5995–6000.

(181) Hau, S. K.; Yip, H.-L.; Baek, N. S.; Zou, J.; O'Malley, K.; Jen, A. K.-Y. Air-stable inverted flexible polymer solar cells using zinc oxide nanoparticles as an electron selective layer. *Appl. Phys. Lett.* **2008**, *92*, 253301.

(182) Li, X.-L.; Ye, H.; Chen, D.-C.; Liu, K.-K.; Xie, G.-Z.; Wang, Y.-F.; Lo, C.-C.; Lien, A.; Peng, J.; Cao, Y.; Su, S.-J. Triazole and pyridine hybrid molecules as electron-transport materials for highly efficient green phosphorescent organic light-emitting diodes. *Isr. J. Chem.* **2014**, *54*, 971–978.

(183) Cai, P.; Xu, X.; Sun, J.; Chen, J.; Cao, Y. Effects of including electron-withdrawing atoms on the physical and photovoltaic properties of indacenodithieno[3,2-b]thiophene-based donor–acceptor polymers: towards an acceptor design for efficient polymer solar cells. *RSC Adv.* **2017**, *7*, 20440–20450.

(184) Jiang, Z.; Soltanian, S.; Gholamkhass, B.; Aljaafari, A.; Servati, P. Light-soaking free organic photovoltaic devices with sol–gel deposited ZnO and AZO electron transport layers. *RSC Adv.* **2018**, *8*, 36542–36548.

(185) Manor, A.; Katz, E. A.; Tromholt, T.; Krebs, F. C. Electrical and photo-induced degradation of ZnO layers in organic photovoltaics. *Adv. Energy Mater.* **2011**, *1*, 836–843.

(186) Günther, M.; Lotfi, S.; Rivas, S. S.; Blätte, D.; Hofmann, J. P.; Bein, T.; Ameri, T. The neglected influence of zinc oxide light-soaking on stability measurements of inverted organic solar cells. *Adv. Funct. Mater.* **2023**, *33*, 2209768.

(187) Klumbies, H. Encapsulations for organic devices and their evaluation using calcium corrosion tests, Ph.D. Thesis, Technische Universität Dresden, 2013.

(188) Endres, J.; Kulbak, M.; Zhao, L.; Rand, B. P.; Cahen, D.; Hodes, G.; Kahn, A. Electronic structure of the $CsPbBr_3$/polytriarylamine (PTAA) system. *J. Appl. Phys.* **2017**, *121*, 035304.

(189) Manger, F. Organische Solarzellen: Kolloidale Stabilisierung von organischen Nanopartikeldispersionen durch elektrische Dotierung, Ph.D. Thesis, Karlsruher Institut für Technologie (KIT), 2022.

(190) Tektronix *Series 2400 SourceMeter® SMU Instruments Datasheet*; Datasheet; Keithley Instruments, 2021.

(191) Tektronix *6517B Electrometer/High Resistance Meter Datasheet*; Datasheet; Keithley Instruments, 2022.

(192) Keithley Instruments Model 6517B Electrometer User's Manual; Keithley Instruments, LLC, 2022.

(193) Wang, Y.; Duan, L.; Zhang, M.; Hameiri, Z.; Liu, X.; Bai, Y.; Hao, X. PTAA as efficient hole transport materials in perovskite solar cells: a review. *Solar RRL* **2022**, *6*, 2200234.

(194) Yang, X.; Luo, M.; Zhang, Q.; Huang, H.; Yao, Y.; Yang, Y.; Li, Y.; Cheng, W.; Li, P. Simultaneously enhancing the efficiency and stability of perovskite solar cells by using P3HT/PEDOT:PSS as a double hole transport layer. *Nanomaterials* **2024**, *14*, 1476.

(195) Kistler, S. F.; Schweizer, P. M., *Liquid film coating: scientific principles and their technological implications*; Springer Science & Business Media: 2012.

(196) Yıldırım, F.; Bacaksız, E.; Türüt, A.; Aydoğan, Ş. Self-driven, stable broadband photodetector based on GaAs:CdS heterojunction with ultrahigh on/off ratio and detectivity. *Surf. Interfaces* **2024**, *44*, 103709.

(197) Han, X.; Han, C.; He, M.; Han, J.; Yu, H.; Gou, J.; Wang, J. Ultralow turn-on voltage organic upconversion devices for high-resolution imaging based on near-infrared homotandem photodetector. *Laser Photonics Rev.* **2025**, *19*, 2401375.

(198) Gielen, S.; Kaiser, C.; Verstraeten, F.; Kublitski, J.; Benduhn, J.; Spoltore, D.; Verstappen, P.; Maes, W.; Meredith, P.; Armin, A.; Vandewal, K. Intrinsic detectivity limits of organic near-infrared photodetectors. *Adv. Mater.* **2020**, *32*, 2003818.

(199) Mohapatra, S. K.; Marder, S. R.; Barlow, S. Organometallic and organic dimers: Moderately air-stable, yet highly reducing, n-dopants. *Acc. Chem. Res.* **2022**, *55*, 319–332.

(200) Guo, S.; Kim, S. B.; Mohapatra, S. K.; Qi, Y.; Sajoto, T.; Kahn, A.; Marder, S. R.; Barlow, S. n-doping of organic electronic materials using air-stable organometallics. *Adv. Mater.* **2012**, *24*, 699–703.

(201) Naab, B. D.; Guo, S.; Olthof, S.; Evans, E. G. B.; Wei, P.; Millhauser, G. L.; Kahn, A.; Barlow, S.; Marder, S. R.; Bao, Z. Mechanistic study on the solution-phase n-doping of 1,3-Dimethyl-2-aryl-2,3-dihydro-1H-benzoimidazole derivatives. *J. Am. Chem. Soc.* **2013**, *135*, 15018–15025.

(202) Xie, J.; Lin, W.; Bazan, G. C.; Pullerits, T.; Zheng, K.; Liang, Z. N-doping of nonfullerene bulk-heterojunction organic solar cells strengthens photogeneration and exciton dissociation. *J. Mater. Chem. A* **2022**, *10*, 18845–18855.

(203) Yuan, D.; Liu, W.; Zhu, X. Efficient and air-stable n-type doping in organic semiconductors. *Chem. Soc. Rev.* **2023**, *52*, 3842–3872.

(204) Schwarze, M.; Tietze, M. L.; Ortmann, F.; Kleemann, H.; Leo, K. Universal limit for air-stable molecular n-doping in organic semiconductors. *ACS Appl. Mater. Interfaces* **2020**, *12*, 40566–40571.

(205) Hauff, E. V.; Dyakonov, V.; Parisi, J. Study of field effect mobility in PCBM films and P3HT:PCBM blends. *Solar Energy Mater. Sol. Cells* **2005**, *87*, 149–156.

(206) Yuan, J.; Zhang, Y.; Zhou, L.; Zhang, G.; Yip, H.-L.; Lau, T.-K.; Lu, X.; Zhu, C.; Peng, H.; Johnson, P. A.; Leclerc, M.; Cao, Y.; Ulanski, J.; Li, Y.; Zou, Y. Single-junction organic solar cell with over 15% efficiency using fused-ring acceptor with electron-deficient core. *Joule* **2019**, *3*, 1140–1151.

(207) Tam, T. L. D.; Xu, J. Strategies and concepts in n-doped conjugated polymer thermoelectrics. *J. Mater. Chem. A* **2021**, *9*, 5149–5163.

(208) Pereira, A.; David, F.; Vanhoenacker, G.; Sandra, K.; Sandra, P. Green chromatography (Part 1): Introduction and liquid chromatography. *LCGC Europe* **2010**, *23*, 242–259.

(209) Mahadevan, S.; Liu, T.; Pratik, S. M.; Li, Y.; Ho, H. Y.; Ouyang, S.; Lu, X.; Yip, H.-L.; Chow, P. C. Y.; Brédas, J.-L.; Coropceanu, V.; So, S. K.; Tsang, S.-W. Assessing intra- and inter-molecular charge transfer excitations in non-fullerene acceptors using electroabsorption spectroscopy. *Nat. Commun.* **2024**, *15*, 2393.

(210) Meng, P.; Lau, A.; Miyajima, D.; Zhao, Z.; Alam, P.; Qiu, Z.; Tang, B. Z. Modulating molecular aggregation of luminogens: Bridging the gap between solutions and solids. *Appl. Phys. Lett.* **2024**, *124*, 100501.

(211) Dolan, A.; Pan, X.; Griffith, M. J.; Sharma, A.; Perrelle, J. M. D. L.; Baran, D.; Metha, G. F.; Huang, D. M.; Kee, T. W.; Andersson, M. R. Enhanced photocatalytic and photovoltaic performance arising from unconventionally low donor–Y6 ratios. *Adv. Mater.* **2024**, *36*, 2309672.

(212) Chen, Q.; Xu, X.; Bo, Z. Application of n-type or p-type dopants in organic photovoltaics. *ChemSusChem* **2025**, *18*, e202402525.

(213) Lin, Y.; Nugraha, M. I.; Firdaus, Y.; Scaccabarozzi, A. D.; Aniés, F.; Emwas, A.-H.; Yengel, E.; Zheng, X.; Liu, J.; Wahyudi, W.; Yarali, E.; Faber, H.; Bakr, O. M.; Tsetseris, L.; Heeney, M.; Anthopoulos, T. D. A simple n-dopant derived from diquat boosts the efficiency of organic solar cells to 18.3%. *ACS Energy Lett.* **2020**, *5*, 3663–3671.

(214) Chen, Q.; Huang, H.; Ran, G.; Zhang, C.; Hu, D.; Xu, X.; Zhang, W.; Yang, C.; Wu, Y.; Bo, Z. Improving the performance of layer-by-layer organic solar cells by n-doping of the acceptor layer. *ACS Appl. Mater. Interfaces* **2023**, *15*, 46138–46147.

(215) Xiong, Y.; Ye, L.; Gadisa, A.; Zhang, Q.; Rech, J. J.; You, W.; Ade, H. Revealing the impact of F4-TCNQ as additive on morphology and performance of high-efficiency nonfullerene organic solar cells. *Adv. Funct. Mater.* **2019**, *29*, 1806262.

(216) Lin, Y.; Firdaus, Y.; Nugraha, M. I.; Liu, F.; Karuthedath, S.; Emwas, A.-H.; Zhang, W.; Seitkhan, A.; Neophytou, M.; Faber, H.; Yengel, E.; McCulloch, I.; Tsetseris, L.; Laquai, F.; Anthopoulos, T. D. 17.1% efficient single-junction organic solar cells enabled by n-type doping of the bulk-heterojunction. *Adv. Sci.* **2020**, *7*, 1903419.

(217) Shang, Z.; Heumueller, T.; Prasanna, R.; Burkhard, G. F.; Naab, B. D.; Bao, Z.; McGehee, M. D.; Salleo, A. Trade-off between trap filling, trap creation, and charge recombination results in performance increase at ultralow doping levels in bulk heterojunction solar cells. *Adv. Energy Mater.* **2016**, *6*, 1601149.

(218) Duong, D. T.; Phan, H.; Hanifi, D.; Jo, P. S.; Nguyen, T.-Q.; Salleo, A. Direct observation of doping sites in temperature-controlled, p-doped P3HT thin films by conducting atomic force microscopy. *Adv. Mater.* **2014**, *26*, 6069–6073.

(219) Pan, X.; Bjuggren, J. M.; Jevric, M.; Tan, W. L.; McNeill, C. R.; Andersson, M. R. Achieving high-efficiency organic photovoltaics from a new completely amorphous donor polymer. *Chem. Mater.* **2022**, *34*, 5103–5115.

(220) Sun, B.; Sirringhaus, H. Solution-processed zinc oxide field-effect transistors based on self-assembly of colloidal nanorods. *Nano Lett.* **2005**, *5*, 2408–2413.

(221) Li, J.; Rochester, C. W.; Jacobs, I. E.; Friedrich, S.; Stroeve, P.; Riede, M.; Moulé, A. J. Measurement of small molecular dopant F4TCNQ and C60F36 diffusion in organic bilayer architectures. *ACS Appl. Mater. Interfaces* **2015**, *7*, 28420–28428.

Danksagung

Ich bin dankbar für alle Menschen, die mich während meiner Promotion begleitet, unterstützt und damit diese Arbeit möglich gemacht haben.
Zunächst möchte ich apl. Prof. Dr. Alexander Colsmann und Prof. Dr. Wolfgang Wenzel für ihr Vertrauen und die kompetente Betreuung danken. Ich bin ihnen dankbar für die herzliche Aufnahme in ihren Gruppen sowie für die Möglichkeit, in meiner Promotion sowohl experimentell als auch simulativ zu arbeiten.
Besonderer Dank gilt apl. Prof. Dr. Alexander Colsmann, mit dem ich stets anregende und konstruktive wissenschaftliche Diskussionen führen konnte. Sein ausgeprägtes internationales Netzwerk hat mir zahlreiche Einblicke und Kontakte ermöglicht, die für den Fortschritt dieser Arbeit von großem Wert waren. Darüber hinaus schätze ich sehr, dass er auch außerhalb des regulären Arbeitsumfelds jederzeit für wissenschaftlichen Austausch offen war. Sein effizientes Management der vielen parallel laufenden Projekte und sein Gespür dafür, die jeweils Beteiligten zusammenzubringen, haben wesentlich zu einer gut funktionierenden Arbeitsumgebung beigetragen.
Ich möchte mich insbesondere bei Prof. Dr. Wolfgang Wenzel für die Übernahme des Korreferats bedanken sowie dafür, dass er mich direkt nach meiner Masterarbeit in seine Gruppe aufgenommen und mir die Möglichkeit gegeben hat, die spannenden Themen im Bereich der organischen Elektronik weiterzuführen. Die Finanzierung in den ersten drei Jahren hat diese Arbeit wesentlich ermöglicht. Der hohe wissenschaftliche Standard in seiner Gruppe hat mich fachlich stark geprägt, und seine in gemeinsamen Projekten stets ermutigend formulierten Mails haben besonders in anspruchsvollen Phasen motiviert.

Mein besonderer Dank gilt Dr. Artem Fediai, dessen Fähigkeit, visionäre Ideen in konkrete Perspektiven zu überführen, mich fachlich stark geprägt haben. Die spontanen und oft minutenaktuellen Diskussionen über Simulationsergebnisse – nicht selten bereits während des Rechnens im Chat – haben einen wichtigen Beitrag zum Fortschritt dieser Arbeit geleistet.
Ein großes Danke an das Team der Nanomatch GmbH, die mir immer schnell und unkompliziert geholfen haben, wenn ich Fragen zu ihrem Simulationscode hatte. Mein besonderer Dank gilt auch dem “Team Nano” mit Dr. Karen Fischer, Jan Bruder und Dr. Felix

Manger sowie allen Studentinnen und Studenten, die an diesem Thema mitgewirkt haben. Durch die enge Zusammenarbeit und die gemeinsamen Diskussionen entstand nicht nur ein produktiver wissenschaftlicher Austausch, sondern auch eine nette Gemeinschaft. Ebenso danke ich Dr. Holger Röhm und Dr. Christian Sprau, die durch vielfältige Gespräche zahlreiche neue Ideen eingebracht haben.
Darüber hinaus möchte ich mich für die wertvollen Kooperationen bedanken, die zum Fortschritt dieser Arbeit beigetragen haben. Besonders danke ich Prof. Dr. Mats R. Andersson für die Bereitstellung des Polymers PIDT-T8BT sowie Prof. Dr. Seth Marder für die zur Verfügung gestellten n-Dotierstoffe. Ihre Unterstützung hat entscheidend dazu beigetragen, zentrale Experimente dieser Arbeit zu ermöglichen.
Allen früheren und aktuellen Kolleginnen und Kollegen der OPV-Gruppe und der AG Wenzel danke ich für die tolle Zusammenarbeit und den inspirierenden Austausch über Wissenschaft und darüber hinaus. Leon Salomon, Sebastian Coen, Yunan Chen, Sven Fischer, Marcel Habrik, Kerstin Märkle, Dr. Alexander Schulz, Dr. Simon Petrick, Dr. Malte Martens, Dr. Ali Özdemir und Dr. Anna Mauri haben mit ihrer Offenheit und Hilfsbereitschaft für eine großartige Arbeitsatmosphäre gesorgt. Auch gemeinsame Freizeitaktivitäten wie Klettern, ein Feierabendbier oder Radausflüge trugen zu einem angenehmen Miteinander und einem starken Zusammenhalt bei.
Ebenso ist auch den Studierenden Nils Bischof, Nils Klein und Raphael Hörner zu danken, deren engagierte Mitarbeit entscheidend zum Gelingen dieser Arbeit beigetragen hat.
Mein Dank richtet sich zudem an Mario Sütsch, Hans Vögele und Klaus Ochs aus der Werkstatt des LTI, die mich bei der Anfertigung eines Messhalters für Photodioden tatkräftig unterstützt haben.
Abschließend danke ich meinen Freunden und meinem Partner Lunes, die mir geholfen haben, die stressige Zeiten der Promotionszeit zu meistern. Von Herzen danke ich auch meiner Mutter, die mich immer unterstützt hat, sowie meinem Vater, der früh mein technisches und naturwissenschaftliches Interesse geweckt hat. Meinem Bruder danke ich dafür, dass ich mit ihm immer über alles mögliche philosophieren konnte, was mir oft neue Perspektiven eröffnet hat.